Division of Biomedical Engineering

Department of Human Biology

University of Cape Town

Computational Model of Thrombosis in Cerebral Aneurysms for Predicting Clotting Outcomes in Flow Diverter Treated Patient-Derived Geometries Validated with Novel PIV-Based In Vitro Clotting Flow Experiment

Struan Robertson Hume

HMXSTR001

SUBMITTED TO THE UNIVERSITY OF CAPE TOWN

In fulfilment of the requirements for the degree:

Ph.D. in Biomedical Engineering

Faculty of Health Sciences

UNIVERSITY OF CAPE TOWN

The Centre for Research in Computational and Applied Mechanics (CERECAM)

Supervised by:

Associate Professor Malebogo Ngoepe & Associate Professor Wei Hua Ho

Department of Mechanical Engineering
Faculty of Engineering & the Built Environment
UCT

DECLARATION

I, Struan Hume, hereby declare that the work on which this dissertation/thesis is based is my original work (except where acknowledgements indicate otherwise) and that neither the whole work nor any part of it has been, is being, or is to be submitted for another degree in this or any other university.

I empower the university to reproduce for the purpose of research either the whole or any portion of the contents in any manner whatsoever.

Signed by candidate

Signature: ……

Date: 18/02/2024

Dedication

To family, it underpins every achievement.

Abstract

There are a growing number of computational models of thrombosis in cerebral aneurysms designed with consideration towards clinical use and research. Many thrombosis models include complicated clotting mechanisms, which can be computationally expensive, and present a challenge to comprehensively validate in vitro due in part to the complexity of adequately measuring the ongoing interaction between flow and clot-growth; a key factor in predicting aneurysm-occlusion after surgical placement of a stent.

To this end, a pulsatile-flow direct thrombosis-model has been developed towards use in a clinical environment to predict thrombosis outcomes in patient-specific cerebral aneurysm cases with and without a flow diverter, and is validated at each 0.05s timestep using a novel PIV-based (Particle Image Velocimetry) in vitro clotting flow experiment that simultaneously captures motion of a fibrin clot strand and surrounding flow within an idealized aneurysm flow vessel.

The validated pulsatile-flow fibrin clot-model produces plausible clotting outcomes in each of the patient-specific cerebral aneurysm cases, with and without flow diverters, dependent upon the classification and size of cerebral aneurysm in question. The novel PIV-based in vitro clotting flow experiment demonstrates that fibrin clotting and flow may be measured simultaneously using PIV techniques.

In cross-referencing the results of multiple simulations and flow experiments performed for this thesis with one another and to literature, the combined studies indicate two potentially important considerations for future direct thrombosis models of cerebral aneurysms. These include directional clot growth in accordance with the alignment of fibrin strands due to periodically high physiological flow rates, and the significance of the non-Newtonian features of blood for the modelling of physiological flow and wall boundaries in major cerebral arteries, although the results of a small sample of experiments is far from conclusive and further study in these areas is required.

Acknowledgements

I would like to express my gratitude to my advisors Associate Professor Malebogo Ngoepe and Associate Professor Wei Hua Ho, both of whom offered continuous guidance and encouragement in my studies. Without their expertise and insights, this work would not have been possible.

I am also grateful to Jemitias Chivavava and the Crystallization and Precipitation Research Unit at UCT, who graciously provided access to Particle Image Velocimetry equipment crucial to this research.

Special thanks to my colleague, Qudus Jimoh-Taiwo, for our engaging discussions that have propelled my work forward.

I would also like to acknowledge the financial support provided by the South African National Research Foundation, which have made this research possible.

Finally, I owe a deep debt of gratitude to my family, whose unwavering support has been the foundation of this journey. My father has been an invaluable sounding board, always ready to discuss my ideas and offer thoughtful insights. My mother has been a constant source of comfort, providing encouragement when things did not go as planned.

Most importantly, I am deeply thankful to my wife, whose patience and unwavering support allowed me to focus on my work, even as she balanced a growing career and the joy of raising our little boy. I am particularly grateful for her unwavering support and understanding during the final stretch that made all the difference.

Contents

List of Figures

List of Tables

Solution Reference Variables

v	velocity scalar
$\vec{v}$	velocity vector
$\frac{dv}{dn}$	velocity gradient
ρ	fluid density
μ	dynamic fluid viscosity
τ	shear stress
ϕ	general scalar variable
t	time

1. Introduction

1.1. Risk, Treatment, and Diagnosis of Unruptured Cerebral Aneurysms

Cerebral aneurysms denote focal dilations within the cerebral arteries. The rupture of cerebral aneurysms precipitates subarachnoid hemorrhage, leading to the occurrence of hemorrhagic stroke and potentially ischemic stroke consequent to cerebral vasospasm [1].

Typical surgical interventions for the treatment of cerebral aneurysms encompass surgical clipping, endovascular coiling, and flow diversion techniques. Surgical clipping necessitates craniotomy for access to the aneurysm, enabling the placement of a metallic clip at its neck to impede blood ingress. Endovascular coiling entails the insertion of a catheter into an arterial vessel, which is then navigated to the site of the aneurysm, facilitating the deployment of a wire that coils within the aneurysmal sac, subsequently reinforced by the deployment of a stent or flow diverter to induce clot formation and sealing. Flow diversion employs a similar methodology, where a catheter is guided to position a flow diverter across the neck of an unruptured aneurysm, thus attenuating blood flow into the aneurysmal sac. Endovascular coiling is notably less invasive than surgical clipping and is deemed reasonably safe for patients presenting with either ruptured or unruptured aneurysms [2]. The most precarious aspect of endovascular coiling pertains to the catheter insertion phase into the aneurysm, which entails a potential hazard of inadvertent aneurysm rupture. Consequently, exclusive utilization of a flow diverter represents an efficacious treatment modality, particularly in scenarios where alternative approaches encounter challenges [3]. When considering several meta analyses of ICA (Intracranial Cerebral Artery) aneurysm surgical intervention data, collectively spanning from three decades ago to the present, serious morbidity (including death and permanent dependency) for neurosurgical clipping and endovascular surgical interventions are 6% and 3%, respectively [4–6].

Invasive surgical interventions of unruptured aneurysms can reduce the risk of subarachnoid hemorrhaging, but carry risk of significant complications [4–8]. This presents a challenge with consideration that unruptured cerebral aneurysms are common in roughly 3% of the population, and are often asymptomatic with only a small proportion that rupture [9,10]. These factors coupled with the often-prohibitive expense of radiological imaging to the average patient limit consideration for screening of asymptomatic unruptured aneurysms primarily to those with comorbidities and family history of vascular and related diseases [10].

Unruptured cerebral aneurysms are more prevalent in women than men, and significantly higher in people >30 years old by comparison to those <30 [9]. Even if most cerebral aneurysms do not develop

a risk of rupture, between 1 in 200 to 400 will [10]. While this accounts for only 5% of strokes, hemorrhagic stroke as a result of cerebral aneurysm rupture affects a relatively young cohort of the population by comparison to other diseases (>30 yrs) and has a case fatality of 50%, including 10 to 15% of patients that die outside of a hospital [7,9,11–13]. 50% of survivors develop lifelong dependency, and of the 50% of survivors capable of maintaining independent lives, only 25% recover without neurological or psychosocial deficits [13,14].

The complicated relationship between the potential for negative outcomes of surgical intervention and the uncommon but highly severe case of cerebral aneurysm rupture creates a dilemma of how best to approach treatment. Proactive screening and treatment of unruptured cerebral aneurysms is seemingly favorable, but surgical intervention carries a non-negligible risk of inadvertently inducing complications it is meant to prevent [10,11]. To date, consideration towards patient history and comorbidities paired with morphological factors of aneurysms such as location, size, shape, bottle-neck factor, and aspect ratio are applied when gauging the necessity of treatment [10,15]. These items, however, are mostly qualitative in nature and are based on mean ranges derived from meta-analyses of broadly categorized RCA cases that, importantly, may disagree with one another concerning morphological risk factors [10,15].

Flow diverter devices are amongst the safest endovascular devices and are well-regarded for frequently producing complete occlusion, particularly in small (87%), large and giant aneurysms (95%) according to a study of 108 patients who underwent PED placement for ICA aneurysms [6,16–18]. This study demonstrates major ipsilateral stroke or neurologic death in 5.6% of patients at one year [17]. However, flow diverter device interventions in less common types of aneurysms, such as distal and bifurcation aneurysms, yield varied occlusion and complication rates [18].

While consideration of morphological factors and patient history presents a natural starting point for determining aneurysm risk of rupture and endovascular treatment approach, in isolation it is a low-resolution approach for predicting broad outcomes. The nature of a cerebral aneurysm is patient-specific, and the variability between cases is not adequately accommodated by mean outcomes.

To meaningfully minimize complications and improve clinical outcomes for cerebral aneurysm healthcare, accurate and precise predictions accounting for critical factors such as localized rheology and biochemistry on a patient-specific basis are required.

1.2. Thrombosis in Cerebral Aneurysms

Thrombosis is a process characterized by the formation of blood clots within vasculature. Thrombosis exhibits a significant association with cerebral aneurysms and holds pivotal importance in determining the efficacy of endovascular interventions [1].

Thrombosis can manifest irrespective of the rupture status of an aneurysm [19–21]. In cases where rupture has not transpired, thrombosis may lead to aneurysm stabilization. Conversely, thrombosis can also cause ischemic stroke, and potentially rupture resulting from inflammation as a result of endothelial dysfunction driven by aberrant flow patterns caused by a luminal thrombus [22]. These outcomes may ensue from either endogenous clot formation or induced clot formation facilitated by implanted devices [23].

Following vascular injury, Von Willebrand's factor (VWF) is released, prompting thrombin generation and facilitating platelet adhesion to the subendothelial collagen layer of the blood vessel [24,25]. In the context of cerebral aneurysms, significant sections of the vessel wall are damaged. This damage creates large areas of exposed subendothelial layer, which is ideal for clot initiation [26,27].

Endothelial restoration is facilitated through platelet recruitment to the site of vascular injury, thereby preventing further blood extravasation. The transportation and interaction of platelets near the injured vessel wall are influenced by a combination of blood cellular components and local hemodynamic conditions [28]. Thrombosis entails four distinct stages of platelet involvement: deposition, activation, adhesion, and aggregation [29]. During deposition, filaments are extruded from the injury site onto the surface of deposited platelets. Subsequently, the activation phase ensues, wherein interaction between the GP Ib platelet receptors and VWF leads to robust yet reversible adhesion facilitated by the activation of platelet integrin α_IIB β_3. The adhesion stage is characterized by significant growth of the platelet aggregate. Upon interaction with activated integrin, VWF fosters the establishment of irreversible bond adhesions, marking the adhesion phase. This culminates in the aggregation phase, where activated platelets further promote platelet recruitment, ultimately resulting in the formation of a platelet plug.

Concurrently with platelet activity, a sequence of reactions referred to as the coagulation cascade unfolds, culminating in the generation of a fibrin mesh to fortify the platelet plug, which persists throughout the healing process. The coagulation cascade comprises of three stages; clot initiation, amplification, and propagation [30–32]. In the initiation phase, the injury site is exposed to tissue factor, triggering a subsequent reaction and yielding a small amount of thrombin[33]. This initiates the amplification phase, during which thrombin activates platelets, co-factor V, and co-factor VIII [31]. The propagation phase follows from the activation of these components, accelerating platelet

recruitment and thrombin production. Thrombin assumes a pivotal role in platelet activation and serves as a critical enzyme in the pathway leading to fibrin formation. Given that numerous coagulation reactions occur on platelet membranes, platelets also facilitate several vital enzyme-mediated reactions crucial for fibrin mesh generation [34,35].

Substantial evidence indicates distinct thrombosis mechanisms within cerebral aneurysms compared to typical physiological clotting [23]. While blood-related factors, such as platelet involvement and interactions with coagulation proteins, remain largely consistent between both processes[30,36–39], thrombosis and physiological clotting differ regarding vascular endothelium and geometry-related local hemodynamics, which alter the initiation phase of the coagulation cascade [23,26,40].

Irrespective of the specific etiology, the initiation of clotting reactions leading to the formation of the fibrin mesh necessitates the involvement of tissue factor. Conjecture surrounds the source of tissue factor in thrombosis associated with cerebral aneurysms as differing from that in standard clotting [23,31,39,41–46]. For clotting initiation, tissue factor present in the subendothelium must typically be exposed, often resulting from vascular wall injuries. Notably however, extensive sections of the vessel wall in cerebral aneurysms lack a subendothelial layer [26]. Evidence suggests that in the absence of exposed subendothelium, endothelial damage within the aneurysm plays a significant role in initiating clot formation [27]. Research has validated the presence of blood-borne tissue factor involved in clotting processes [47–49]. Consensus holds that this circulating tissue factor exerts its effects in response to abnormal stimuli, although the precise role of tissue factor remains a subject of speculation [23,33,44,49–52]. The existence of this blood-borne tissue factor is significant, given that cerebral aneurysms create an environment characterized by complex hemodynamics and varying shear rates [53].

The hemodynamic conditions and platelet dynamics within aneurysmal settings markedly deviate from those observed in physiological clotting scenarios. Platelet activation may arise in aberrant blood flow patterns and under conditions of elevated shear stress, as encountered in arterial stenosis induced by vascular diseases [54]. Within aneurysms, platelets are drawn to activated platelets, leading to the formation of platelet plugs. The prevalence of recirculation in this environment promotes a heightened presence of coagulation proteins, fostering an environment conducive to fibrin formation [53,55–57].

The hemodynamics and biochemistry involved in thrombosis play a crucial role in endovascular treatment outcomes for cerebral aneurysms and are a crucial consideration for accurate and precise prediction of patient-specific cerebral aneurysm interventions.

1.3. Direct Cerebral Aneurysm Thrombosis Models

Direct thrombosis models utilize physiological models to predict clotting outcomes by integrating these models directly into their solutions. These physiological models mathematically delineate subsystems of the entire clotting process, thereby enabling direct thrombosis models to simulate clot growth directly and forecast the evolution of clot development [58].

In direct thrombosis models, local hemodynamics are integrated with components of physiological clotting [23]. These models directly consider activity involving either one or both blood platelets and surrounding biochemical reactions, enabling the prediction of clot growth based on local hemodynamics. Certain models incorporate the biomechanical characteristics of a developing clot, allowing the clot to have an effect surrounding flow and vice versa.

One of the pioneering models in this category was proposed by Bedekar et al., which incorporates hemodynamic considerations within anatomically accurate aneurysm geometries derived from patient-specific data, while also integrating platelet activity and coagulation proteins [59]. This model is the first to amalgamate these factors within a realistic patient-derived geometry obtained from computed tomography angiography (CTA). Hemodynamics are modeled using the Navier-Stokes equations, while the shifting concentrations of coagulation and platelet species are captured through convection-diffusion-reaction equations. The platelet activity and coagulation protein reaction components of the model are based on an integrated physiological model developed by Sorenson et al. [60].

An influential computational model of thrombosis proposed by Ouared et al. is noteworthy for its innovative development of approaches applied within thrombosis potential models [61] Specifically, this model introduces a methodology whereby clot growth influences the flow field, and conversely, the flow field impacts clot growth. This is achieved through the implementation of a shear regulation mechanism, wherein the local shear rate is computed, and clotting is initiated when the shear rate falls below 100 s^{-1}. Following clot formation, the clot region solidifies, impeding flow passage. To model blood flow, a lattice Boltzmann numerical approach for hydrodynamics is employed, wherein force calculations are conducted based on particle movement and collisions within a discrete space-time framework.

Ngoepe et al. further extend the model originally proposed by Bedekar et al., incorporating biochemical reactions and hemodynamic factors within cerebral aneurysm geometries derived from patient angiography data [23,53,57,59]. This refined model encompasses the placement of flow diverter geometries, where clot growth is simulated by adjusting porosity and permeability parameters. Adjustments in momentum and continuity equations are made to account for variations

in porosity and permeability, distinguishing between blood plasma and the developing clot. A level-set method is employed to track the expanding clot's surface, with clot initiation regulated by shear rate thresholds and thrombin concentration influencing clot growth. Consequently, Ngoepe et al.'s model enables the prediction of clotting outcomes before and after flow diverter placement [23,57]. Flow dynamics are governed by the Navier-Stokes equations, with blood modeled as a Newtonian, incompressible fluid of constant density and velocity. Protein transportation within the clot development area is altered by an effective diffusivity equation, which is derived from biochemical reaction and reaction rate equations sourced from previous models by Hockin et al. and Wagenvoord et al. [23,57,62,63].

Ou et al. present a computational model predicting thrombus formation post-flow-diversion treatment [64]. This model addresses stasis-induced thrombosis, where an expression for blood-borne tissue factor is applied, and controls fibrin generation inside a flow-diverted aneurysm. Coagulation factors are modeled as a transport species, and its transport, generation and depletion are modeled by a convection-diffusion-reaction equation. Stable clot formation is assumed where fibrin concentration exceeds a threshold value. The computational results were validated using an experimental rat model with a ligated right common carotid artery, wherein a thrombus formed due to flow stasis, and fibrin distribution was measured.

Sarrami-Foroushani et al. address a shortcoming in previous models and develop a computational model predicting thrombus stability and platelet composition [65]. This model couples a thrombosis model with a CFD model. Within the thrombosis model there are four coupled biochemical events that culminate in a clot of fibrin mesh and aggregated platelets; thrombin generation, fibrin generation, platelet activation, and platelet aggregation. This model also introduces a flow induced platelet index, indicating the difference in platelet concentration between a closed and open system, which is used to measure clot stability. The model is validated against PIV measurements in work by Gester et al., and presents similar clotting and platelet composition [66]. Sarrami-Foroushani et al. have further applied this model to predict flow diversion clotting outcomes in patient-specific cerebral aneurysms by comparison to real clotting outcomes [67].

Direct cerebral aneurysm thrombosis models are a promising tool for interventional planning of cerebral aneurysms. Towards this end, many direct thrombosis models apply reasonable assumptions to simplify boundary conditions, fluid properties, and biochemistry to offset high computation times. However, the required level of model detail for accurate prediction of patient-specific clotting outcomes is not clearly understood, arising from limitations towards evaluating model accuracy due to a near lack of suitable direct validation techniques [58,68]. As such there is a need for a

comprehensive method of direct validation for direct thrombosis models of cerebral aneurysms, such that model assumptions and clotting outcomes may be more adequately assessed.

1.4. *In Vitro* Flow Experiments and Validation of Direct Thrombosis Models

Particle image velocimetry (PIV) serves as a technique employed for the acquisition of instantaneous velocity vectors within a fluid in motion, constituting a method for the validation of computational flow models [69].

This process involves the integration of microparticles into the fluid medium, which while traversing a transparent geometric space are captured across multiple images acquired rapidly by a stationary camera. To enhance the visibility of these microparticles relative to the surrounding fluid, a laser source is directed towards the transparent geometry within a controlled darkened environment, facilitating light reflection off the microparticles. Achieving precise spatial registration of the microparticles necessitates adjusting the refractive index of the fluid medium to match that of the transparent geometry. Subsequently, computational algorithms are applied to compare successive image pairs, enabling the determination of microparticle displacement over time, thereby yielding comprehensive velocity field representations. Given the capacity of high-quality microparticles to faithfully follow the flow-patterns of the fluid within which they are mixed, this methodology is generally esteemed for its high degree of accuracy [70].

PIV has been used to validate flow patterns simulated in thrombosis models [65,68,69,71]. Mulder et al. present a study of flow patterns in cerebral aneurysms based upon vortex identification, involving a CFD study and accompanying PIV validation study, which applies steady flow through a silicone idealized aneurysm flow phantom with a 30 wt% electrolyte solution of calcium chloride and magnesium chloride to minimize difference in refraction indices [69]. Gester et al. present an experiment wherein flow of a water-glycerol mixture mimicking the Newtonian fluid properties of blood is measured through an idealized aneurysm flow vessel with and without a flow diverter installed using PIV methods, which is then drained and replaced with blood so thrombus growth may be measured over the course of several hours using doppler sonography and inference can be made to determine the effects of flow upon clotting [68].

Clot validation and the effect of flow on biochemistry, however, are crucial concerns for thrombosis models. Towards this end, Clauser et al. present an experiment using a novel plasma-based PIV fluid to measure flow within an idealized aneurysm vessel to compare the effects of aneurysmal flow with and without a flow diverter installed and attempt to measure flow while inducing a clot, although the method of clot induction combined with the flow phantom material resulted in full occlusion of the vessel within seconds [72]. A flow experiment with similar characteristics is presented by Ngoepe et

al. to qualitatively measure the effects of steady flow on clot development in a macroscopic idealized cerebral aneurysm flow phantom, which is adapted from a geometry used by Mulder et al. and additive manufacturing and processing techniques by Ho et al. [69,73,74]. In this study, a fibrinogen-saline solution is applied as the operating fluid under steady flow within the flow phantom, where thrombin-saline solution is injected from the top of the aneurysm and resulting fibrin clot growth is qualitatively measured under the steady flow conditions. Jimoh-Taiwo et al. apply the materials and methods of Ngoepe et al. to form a fibrin clot in a straight channel to validate clotting outcomes of a CFD mechano-chemical deep-vein thrombosis model [73,75].

To date, there do not appear to be any *in vitro* validation experiments for macroscale vessels that can comprehensively validate direct thrombosis models via simultaneous capture of high-resolution flow and clot growth. However, the experiments by Clauser et al. and Ngoepe et al. indicate that this is possible [72,73]. This kind of experiment would present a valuable comprehensive validation tool for direct thrombosis models that addresses the impact of flow on clot development and vice versa, particularly as they relate to the many assumptions made for thrombosis models to simplify the modelling of blood in physiological flow.

1.4.1. Modelling of Physiological Flow Patterns

Pulsatile flow most accurately represents the periodic nature of blood flow *in-vivo*, and there are many models that directly link the volume and mass flow rate of blood to the rate of thrombin generation, fibrin deposition, and growth of thrombi [76]. Despite this, many computational cerebral aneurysm thrombosis models do not account for the effects of pulsatile flow.

Pulsatile flow as it relates to clotting has been explored in experimental and computational flow models. Corbett et al. present a 2D CFD study applying varying pulsatility and velocity to a step-wall transition with varying height [77]. Blood is approximated as a non-Newtonian fluid, and the model is validated with an experimental flow-loop and demonstrates that flow stagnation decreases with increase in pulsatility. Hume & Tshimanga et al. present a validated flow model that demonstrates pulsatile flow has a significant effect on retention of clotting reagents within an idealized cerebral aneurysm, and that use of pulsatility over steady flow may alter clotting outcomes [71]. Study of this phenomenon as it relates to the non-Newtonian properties of human blood and its flow interaction with wall boundaries in macroscale vessels has yet to be explored in detail, however.

1.4.2. Wall Boundary Conditions and Non-Newtonian Properties of Blood

The no-slip condition was first proposed by Osborne Reynolds, and is applied to viscous fluids at solid boundaries, such that velocity approaches zero near them [78]. This standard assumption is considered to hold where adhesion forces are stronger than cohesion forces for fluid particles near a

fluid-solid interface, which is a standard consideration for the modelling of most Newtonian fluid flows [79].

A no-slip wall boundary condition is used in many macroscale CFD thrombosis and clotting models and is a standard assumption in modelling flow that is considered applicable in most cases of laminar flow in sufficiently large and rough-walled vessels [57,64,65,71,75,77,80–89]. This is partially due to the Newtonian assumption for blood, which has been demonstrated to be a reasonable approximation for determining distribution of wall shear stress in arteries, an important indicator for sites of clot development [90]. The Newtonian assumption for blood has also been demonstrated not to significantly alter flow patterns in cerebral aneurysms, though it may lead to the overprediction of wall shear stress [91,92].

Blood flow at the near-wall region is complex, and presents a significant challenge in hemodynamics modelling research [93,94]. Vahid et al. presents a sensitivity study of Newtonian and non-Newtonian rheological models, with varying flow profiles across different aneurysms; describing the near-wall region in terms of shear stress [93]. Ngwenya et al. explores vortical structures in cerebral aneurysms as they influence fibrin clot formation [95]. Mazzi et al. present a unified theory of cardiovascular flow disturbances at the blood-vessel wall interface by linking wall shear-stress and surface vortices [94].

Full blood is a colloidal suspension that is a non-Newtonian shear-thinning fluid that is viscoelastic and thixotropic [96–99]. The no-slip condition is considered a questionable assumption by some for modelling non-Newtonian fluids such as blood, which demonstrates slip behavior at solid boundaries [86,100,101]. The non-Newtonian properties of blood are demonstrated to be significant for stenosed arteries and small vessels [102]. As such some small vessel models apply a partial-slip boundary condition, such that velocity at a fluid-solid interface is non-zero [103–106].

However, there are a growing number of models demonstrating that some of these non-Newtonian effects are significant even in large vessels with predominantly high shear rates [83]. Slip can even occur for Newtonian fluids dependent upon flow rates and surface roughness [86,101]. While some of these properties have been explored in clotting of cerebral aneurysms, slip has not been explored in a macrovascular setting [91].

Given these factors, and a lack of high resolution in-vitro measurement of the non-Newtonian effects of human blood under physiological flow rates, there are grounds to explore the approximation of the no-slip condition for macroscale physiological flows.

2. Aims, Objectives, and Thesis Roadmap

Computational models of direct thrombosis of cerebral aneurysms have the potential to be powerful clinical diagnostic tools that can significantly reduce mortality and morbidity associated with endovascular treatment. However, direct validation of computational models of direct thrombosis presents a challenge due to a variety of factors. Blood analogs have been applied in PIV studies to validate flow, but they are nearly all inorganic, and there is an almost total lack of *in vitro* flow macroscale vessel experiments using full-blood or blood-derived fluids to evaluate the extent to which these blood analogs are fully representative of blood in a macrovascular flow environment. Inorganic blood analogs are furthermore incapable of directly validating clot growth, and critically there is a complete absence of macroscale *in vitro* flow experiments applying human blood-derived operating fluids containing human-derived clotting proteins important to the final stages of coagulation, wherein the development of a growing clot is measured simultaneously relative to a periodic physiologically accurate high-resolution flow field.

The problem this introduces is two-fold. It prevents direct assessment of real-time biochemical interactions as they relate to the surrounding physiological flow environment, and it also prevents direct assessment of common simplifications and assumptions for flow behavior, boundary conditions and fluid properties of blood in macro vessels under physiological flow. This limits the potential to accurately validate flow distributions and the consequent clotting outcomes.

With the aim of creating a direct thrombosis model that is directly validated *in vitro*, this thesis presents a direct thrombosis model and an accompanying validation *in vitro* flow clotting experiment to achieve the following objectives:

1. Create a direct thrombosis model of cerebral aneurysms that predicts realistic clotting outcomes in patient-specific aneurysm geometries with and without flow diverter intervention under physiologically accurate flow conditions, using a porosity-based clotting model activated dependent upon local shear rates and fibrin-concentration generated from a reduced biochemical model of thrombin and fibrinogen.
2. Create a PIV-based idealized cerebral aneurysm *in vitro* flow experiment capable of using fibrinogen-saline solution as an operating fluid, that can accurately capture flow fields under physiological flow conditions simultaneously to fibrin clot growth induced by the addition of a controlled injection of thrombin-saline solution.
3. Directly validate the direct thrombosis model of cerebral aneurysms with the PIV-based idealized cerebral aneurysm *in vitro* flow experiment via a direct comparison of clotting and flow.

Importantly, the fluids applied for the PIV-based idealized cerebral aneurysm *in vitro* flow experiment described in the 2nd objective does not contain blood cells, platelets, or all of the proteins present in full-blood, but contains the proteins of critical to the final stages of coagulation for the formation of a fibrin clot; allowing direct base comparison to a computational thrombosis model clotting applying identical material properties and proteins.

Given the scope of the aim and objectives, this thesis is broken down into three studies, each of which includes study-specific methodologies, results analysis, and comparison to literature. The first study explores the development and flow/clotting results of the PIV-based thrombin-fibrinogen *in vitro* flow experiment and its prototype PIV-based water-gelatin *in vitro* flow experiment. The second study presents validation simulations of the direct thrombosis model of cerebral aneurysms and a comparison of results to the PIV-based *in vitro* flow experiments of the first study. The third and final study applies the validated direct thrombosis model of cerebral aneurysms to predict clotting outcomes in patient-specific aneurysm geometries with and without flow diverter intervention.

2.1. Thesis Roadmap

For clarity, the overall structure of the thesis is the following:

The dissertation consists of one PIV-based study and two CFD studies with slightly differing methodologies. An introduction is presented, followed by aims and objectives, a broad methodology, a chapter for each study, and conclusion.

The broad methodology begins with a section describing the CFD methods common to both CFD studies, followed by a section concerning the PIV methods common to each experiment performed as part of the PIV-based study. The first study presented is the PIV-based study, followed by a CFD validation study, and a CFD prediction study. Each study is concluded by a section of discussion of results as they relate and compare to literature.

The PIV-based study introduces a section for each experiment inclusive of experiment-specific methods, results and analysis.

The CFD studies each introduce a section for study-specific methodology. The CFD validation study follows with two sections comparing CFD results to PIV-based experiment results. The CFD prediction study includes a results section for individual cases.

The conclusion chapter summarizes the overall findings, implications, and overall contribution of the three studies.

3. Methodology

The computational model applied in this study is built upon a computational model applied in previous research as well as work by Ngoepe et al. and Jimoh-Taiwo et al. [57,71,75]. A pulsatile-flow direct thrombosis of cerebral aneurysms model has been created in ANSYS® Fluent using a transient-solution implicit pressure-based solver, wherein a series of aneurysm geometries are applied, with data-derived pulsatile volumetric flow and pressure functions supplied at the inlet and outlet respectively. User-defined-scalars representing thrombin, fibrinogen, and fibrin concentrations are generated from the aneurysm, the velocity inlet, and the interaction between thrombin and fibrinogen, respectively. A Michaelis-Menten formulation is used to generate fibrin. A porosity function is activated and gradually increases in areas with sufficiently low shear rate and fibrin-concentration scalar value up to a threshold value. In porous areas where this threshold value is reached, viscous resistance increases drastically in that region, simulating the formation of a permanent clot.

The flow experiments applied in this study are built upon a previous PIV validation experiment, as well as work performed by Ngoepe et al. and Jimoh-Taiwo et al. [71,73,75]. These flow experiments apply a PIV-based framework with certain design considerations to allow the measurement of a flow field simultaneously to monitoring the growth of a clot, or introduction of another substance into the flow field. Broadly, these experiments include an idealized cerebral aneurysm flow phantom, through which a fluid subject to a physiologically realistic periodic flow pattern is applied, wherein vector flow fields are captured throughout the duration of flow, during which time a substance is injected into the aneurysm via an injection port.

3.1. CFD Methodology

3.1.1. Computational Approach

For simplicity, flow is considered Newtonian and incompressible. It is governed by the following Navier-Stokes derived transport equations:

Mass Conservation Equation:

$$\nabla \cdot \vec{v} = 0 \tag{1}$$

Momentum Conservation Equation:

$$\rho \frac{\partial \vec{v}}{\partial t} + \rho \vec{v} \cdot \nabla \vec{v} + \nabla \mathrm{P} = \mu \nabla^2 \vec{v} \tag{2}$$

Where $\vec{v}$ is a sample velocity vector, ρ is the fluid density, μ is the dynamic fluid viscosity, and P is pressure.

ANSYS® Academic Research Fluent 2021 R2 is used to implement a porosity-based clotting model into a model developed by Hume & Tshimanga et al. [71]. Geometries are created and processed in SpaceClaim and meshed using ANSYS MESHING. The mesh is imported into ANSYS® Fluent, which calculates the solution using a transient pressure-based solver. ANSYS Post-Processer is used to analyse simulation results, compare them to one another, and results of relevant flow experiments and models in literature.

3.1.2. ANSYS® Fluent Pressure-Based Solver Functionality and Settings

3.1.2.1. Least-Squared Cell-Based Gradient Evaluation

Gradients play a crucial role in a multitude of tasks, such as defining scalar values at cell faces, calculating velocity derivatives, and evaluating secondary diffusion terms. To achieve this, a least-squares cell-based gradient approach is employed due to its comparable accuracy to alternative methods while requiring lower computational resources. In this approach, the solution is assumed to demonstrate linear variation between $c0$ and ci across δr_i, which respectively represent the center of the cell under consideration, the center of an adjacent cell, and the vector distance between them [107].

Considering all cells surrounding a cell in question, the system is defined as the following:

$$[J](\nabla\phi)_{c0} = \Delta\phi \tag{3}$$

Where:

$[J]$ The coefficient matrix which is purely a function of geometry

In the process of minimizing the system in a least-squares fashion, the primary aim is to ascertain the cell gradient. This task is accomplished through the Gram-Schmidt process, which disentangles the coefficient matrix and generates a set of weight matrices corresponding to each cell. Consequently, for each face of cell $c0$, three weight components are derived [107].

3.1.2.2. General Scalar Transport Equation

The general transport equation is used to describe the conservation and movement of various physical quantities in flow. In ANSYS® Fluent, a method grounded in control volumes is utilized to transform the abstract scalar transport equation into a computationally solvable algebraic form. This process involves integrating the transport equation across a defined control volume, resulting in a discrete equation that encapsulates the conservation law centered on the control-volume framework [107].

The general scalar transport equation is as follows:

$$\int_V \frac{\partial \rho \phi}{\partial t} dV + \oint \rho \phi \, \vec{v} \cdot d\vec{A} = \oint \Gamma_\phi \nabla_\phi \cdot d\vec{A} + \int_V S_\phi dV \tag{4}$$

Where:

ρ	density
ϕ	general variable
V	cell volume
$\vec{v}$	velocity vector
$\vec{A}$	surface area vector
Γ_ϕ	diffusion coefficient of ϕ
∇_ϕ	gradient of ϕ
S_ϕ	Source of ϕ per unit volume

3.1.2.3. Standard Gradient Limiter

Second-order upwind discretization schemes utilize gradient limiters to mitigate oscillations within the solution flow field, ensuring that the resulting behavior is more faithful to the true solution [107].

3.1.2.4. Momentum Equation

The momentum equation is used to calculate the velocity field of the fluid. The time-dependent integral-form of the momentum equation for the pressure-based solver is represented as follows [107].

$$\int_V \frac{\partial \rho \vec{v}}{\partial t} dV + \oint \rho \vec{v} \, \vec{v} \cdot d\vec{A} = -\oint p\boldsymbol{I} \cdot d\vec{A} + \oint \bar{\bar{\tau}} \cdot d\vec{A} + \int_V \vec{F} \, dV \tag{5}$$

Where:

$\boldsymbol{I}$	Identity Matrix
$\bar{\bar{\tau}}$	Stress Tensor
$\vec{F}$	Force Vector

Gravity is considered across all cases as -9.81 m/s^2 in the -y direction.

3.1.2.4.1. PRESTO! Pressure Interpolation Scheme

Pressure interpolation is used to determine the pressure values at the cell faces in the computational domain from the pressure values at the cell centers. The PRESTO! (PREssure Staggering Option) pressure interpolation scheme is selected for its recommended use for flows involving porous media. PRESTO! applies a discrete continuity balance for a "staggered" control volume about the face to compute the face pressure [107].

3.1.2.5. PISO Pressure-Velocity Coupling

The pressure-velocity coupling is necessary to couple the continuity and momentum equations such that mass is conserved. Face mass flux J_f is applied to the continuity equation to derive an additional condition for pressure, thereby establishing a pressure-velocity coupling. Among the pressure-velocity coupling methodologies available in ANSYS® Fluent, the PISO algorithm emerges as particularly suitable for the present problem, notably advantageous for transient flow analyses, especially in scenarios where substantial time steps are preferred. Rooted in a predictor-corrector approach, the PISO algorithm belongs to the SIMPLE family of algorithms. [107].

The SIMPLE algorithm family of algorithms employs a relationship between corrections of velocity and pressure to impose mass conservation and acquire the pressure field [107].

If the momentum equation is solved with a guessed pressure field p^*, the face flux J_f^* is as follows:

$$J_f^* = \hat{J}_f^* + d_f(p_{c0}^* - p_{c1}^*) \tag{6}$$

The continuity equation cannot be satisfied by J_f^* alone, so a correction J_f' is added to output the corrected face flux J_f, and in turn satisfy the continuity equation.

The corrected face flux is as follows:

$$J_f = J_f^* + J_f' \tag{7}$$

Where the correction J_f' is as follows:

$$J_f' = d_f(p_{c0}' - p_{c1}') \tag{8}$$

Where:

p' cell pressure correction

The coefficient d_f is defined as a function of $\overline{(a_P - \sum_{nb} a_{nb})}$ for the SIMPLEC and PISO algorithms. Modified in this way, the correction equation accelerates convergence where pressure-velocity coupling deters the acquisition of a solution [107].

The corrected face flux equation is substituted into the discrete continuity equation to yield a discrete equation for the pressure correction p' in the cell [107].

The pressure-correction equation is as follows:

$$a_P p' = \sum_{nb} a_{nb} p'_{nb} + b \tag{9}$$

The net flow rate into the cell, b, is as follows:

$$b = \sum_{f}^{N_{faces}} J_f^* A_f \tag{10}$$

The pressure-correction equation is solved using the algebraic multigrid method, and followed by cell pressure and face flux correction.

The corrected cell pressure is as follows:

$$p = p^* + \alpha_p p' \tag{11}$$

Where:

α_p under-relaxation factor for pressure.

The corrected face flux equation is as follows:

$$J_f = J_f^* + d_f(p'_{c0} - p'_{c1}) \tag{12}$$

The corrected face flux J_f satisfies the discrete continuity equation identically during each iteration.

3.1.2.5.1. Neighbor Correction

The PISO algorithm transfers the iterative computations typically associated with SIMPLE/SIMPLEC into the solution phase of the pressure-correction equation. Following one or more iterations of these integrated PISO loops, the corrected velocities better fulfill the momentum and continuity equations. This mechanism, known as neighbor correction, maintains a default setting of 1, significantly reducing the iteration count necessary for convergence in transient scenarios [107].

3.1.2.5.2. Skewness Correction

Skewness correction entails an iterative process employed to compute pressure-correction gradient components along cell faces. Following the initial solution computation for the pressure-correction equation, the pressure-correction gradient undergoes recalculation, and subsequently updates the mass flux corrections. This methodology is particularly advantageous in skewed meshes where the correlation between mass flux on cell faces and pressure corrections at neighboring cells is intricate, and where the values of pressure-correction gradient components along cell faces are not predetermined. By facilitating easier convergence with distorted meshes, skewness correction enhances computational efficiency [107].

Due to the average skewness of the mesh being satisfactory, the default skewness correction value of 1 was selected.

3.1.2.5.3. Skewness-Neighbor Coupling

Skewness-neighbor coupling is default enabled for the PISO scheme but is disabled for the model presented. This coupling causes the PISO algorithm to apply iterations for skewness correction for each iteration of neighbor correction, usually allowing for a more accurate face mass flux correction based on the normal pressure correction gradient than an uncoupled solution. However, due to an unavoidable level of distortion for some meshes described, the skewness-neighbor coupling is disabled [107].

3.1.2.6. Under-Relaxation

3.1.2.6.1. Under-Relaxation of Variables

In the pressure-based coupled algorithm, explicit under-relaxation is utilized for both momentum and pressure. Under-relaxation of variables is valuable for achieving convergent behaviour in a solution given the nonlinearity of the sets of equations solved within the pressure-based coupled algorithm. Specifically, under-relaxation of variables serves to mitigate abrupt changes in the variable ϕ for each solution iteration in the following form [107]:

$$\phi = \phi_{old} + \alpha \Delta\phi \tag{13}$$

Where:

ϕ_{old}	old ϕ value from previous iteration
α	under-relaxation factor
$\Delta\phi$	computed change in ϕ

Per default ANSYS® Fluent solver settings, only two variables have an under-relaxation factor less than 1. Pressure has an under-relaxation factor of 0.3, and momentum has an under-relaxation factor of 0.7 per program defaults.

3.1.2.6.2. Under-Relaxation of Equations

Every equation addressed by the pressure-based solver incorporates an associated under-relaxation factor, because the update of variables at each iteration is controlled by implicit relaxation to stabilize convergence behavior of outer nonlinear iterations [107].

At a location specific timestep, the under-relaxation factor α changes the discretized equation for scalar ϕ to the following:

$$\frac{a_p \phi}{\alpha} = \sum_{nb} a_{nb} \phi_{nb} + b + \frac{1-\alpha}{\alpha} a_p \phi_{old} \tag{14}$$

3.1.2.7. Time Advancement Algorithm

The flow simulation is time dependent, and in this case ANSYS® Fluent utilizes the following discretized form of the generic transport equation shown in equation (4) [107].

ANSYS® Fluent pressure-based solver uses an implicit discretization of the transport equation. By default, the convective diffusive and source terms are evaluated at time level $n+1$ [107].

$$\int_V \frac{\partial \rho \phi}{\partial t} dV + \oint \rho^{n+1} \phi^{n+1} \vec{v}^{n+1} \cdot d\vec{A} = \oint {\Gamma_\phi}^{n+1} {\nabla_\phi}^{n+1} \cdot d\vec{A} + \int_V {S_\phi}^{n+1} dV \tag{15}$$

Time discretization error is determined by the second-order temporal discretization and the time advancement scheme.

The second-order iterative time advancement scheme is employed in the simulation, wherein equations are solved iteratively for each time-step until the criteria for convergence are met [107].

3.1.2.8. User-Defined Scalars (UDS)

UDS are included in the simulation to represent thrombin, fibrinogen, and fibrin, where all flow volumes comprise the solution zone, and the mass flow rate determines UDS flux. This UDS is solved by ANSYS® Fluent in the same fashion it solves the transport equation for a scalar using the differential form of (4) [107].

3.1.2.9. Algebraic Multigrid Solver (AMG)

The pressure-based implicit solver in ANSYS® Fluent leverages an Algebraic Multigrid (AMG) technique to expedite convergence. AMG operates by iteratively correcting errors on successively coarser grid levels. The underlying premise is that the global error observed on a fine mesh can be encapsulated as local error on a coarser mesh. Consequently, this approach significantly diminishes the required number of iterations and CPU time to attain convergence, as the computational costs decrease exponentially with coarser mesh resolutions [107].

3.1.2.9.1. Multigrid Concept

A discretized set of linear equations is defined as follows [107].

$$\mathrm{A}\phi_e + b = 0 \tag{16}$$

Where:

ϕ_e	Exact Solution
A	Fine level operator

Prior to convergence, the approximate solution ϕ has a defect d.

$$\mathrm{A}\phi + b = d \tag{17}$$

A correction ψ is applied so that the exact solution becomes the following:

$$\phi_e = \phi + \psi \tag{18}$$

Substituting this into the discretized set of linear equations yields:

$$\mathrm{A}(\phi + \psi) + b = 0 \tag{19}$$

$$\mathrm{A}\psi + (\mathrm{A}\phi + b) = 0 \tag{20}$$

Which applied to the approximate solution equation yields the correction equation.

$$\mathrm{A}\psi + d = 0 \tag{21}$$

If the fine level relaxation scheme has damped local errors adequately, the correction will be more successfully solved on the subsequent coarse level.

3.1.2.9.2. Coarse Grid Correction

Corrections are solved via the processes of restriction and prolongation. Restriction is the transfer of a defect from the fine level to the coarse level. Corrections are then computed, and prolongation begins, in which the corrections are transferred back to the fine level from the coarse level [107].

The coarse level correction equation is the following:

$$\mathrm{A}^H\psi^H + Rd = 0 \tag{22}$$

Where:

A^H	Coarse level operator
R	Restriction operator

The fine level solution is as follows:

$$\phi^{new} = \phi + P\psi^H \tag{23}$$

Where P is the prolongation operator. For AMG, the prolongation operator is given as the transpose of the restriction operator [107].

$$P = R^T \tag{24}$$

The coarse level operator A^H is constructed via a Galerkin approach. A new defect associated with the corrected fine level solution must be substituted when transferred back to the coarse level. The expression A^H is derived as follows [107].

$$Rd^{new} = 0 \tag{25}$$

$$R(A\phi^{new} + b) = 0 \quad (26)$$

$$R(A(\phi + \mathrm{P}\psi^{H}) + b) = 0 \quad (27)$$

$$RAP\psi^{H} + R(A\phi + b) = 0 \quad (28)$$

$$RAP\psi^{H} + Rd = 0 \quad (29)$$

Yielding:

$$A^{H} = RAP \quad (30)$$

This coarse level operator effectively is a summation of diagonal and off-diagonal blocks for all cells of a group in the fine grid, which forms the diagonal block of the group's coarse cell.

3.1.2.9.3. V Multigrid Cycle

The V-cycle represents the standard multigrid cycle utilized within the algebraic multigrid framework. It constitutes a recursive procedure implemented at each level of the multigrid hierarchy. The default V-cycle for algebraic multigrid encompasses four sequential steps, outlined as follows [107]:

1. Restriction: The solution at the current grid level is restricted to the subsequent coarser grid level.
2. Multigrid Cycle: A single multigrid cycle is executed, reducing errors on the coarse grid.
3. Interpolation: Corrections computed on the coarse grid are interpolated back to the fine grid using prolongation, resulting in the introduction of some high-frequency error.
4. Post-relaxation: Iterative post-relaxation sweeps are conducted on the fine grid to eliminate the high-frequency error.

3.1.3. Materials

Human blood exhibits non-Newtonian behavior, with its density and viscosity subject to alterations influenced by various factors.

A Newtonian assumption for blood is conventional for many aneurysm CFD studies and is applied for the CFD model [57,64,65,71,75,77,80–89]. This assumption is demonstrated to be a reasonable approximation for determining sites of clot development in sufficiently sized vessels based upon wall shear stress in arteries [90]. To this end blood is modelled as having a density of $\rho = 1000\,kg/m^3$ and a viscosity $\mu = 0.004\,kg/ms$, and is considered laminar and incompressible in the computational model.

The results of the PIV-based experiments explored in Chapter 4 and the validation simulations explored in Chapter 5 call this Newtonian assumption into question. However, the Newtonian material properties of the operating fluid are maintained in favor of exploring the applicability of non-Newtonian behavior of the operating fluid as it relates to the presence of slip at the wall boundary as discussed in Chapter 5. Non-Newtonian flow is explored in this way due to uncertainty concerning the

fluid properties of the operating fluid in the thrombin-fibrinogen flow experiments discussed in sections 4.1.3-4.1.4, and potentially significant rheological changes the operating fluid undergoes during clot formation; both of which are not directly quantified within the experimental framework or in literature. Hence, wall boundary conditions are applied to capture these flow phenomena regardless.

The PIV experiment applies a fluid inclusive of fibrinogen, which roughly represents the fluid properties mentioned above with the exception that viscosity is considered as $\mu = 0.001\, kg/ms$; approximately the same as 0.4% PBS solution. Thrombin is added to this mixture to begin the clotting process within the aneurysmal sac of the geometry. While this solution is not an analog to blood, the proteins involved are applied in research of acute coagulation as it relates to the formation of a fibrin clot, and thereby is relevant for comparison to blood in the context of flow and clotting [73,108].

3.1.4. Michaelis-Menten Model

$$v = \frac{V_{max}\,[S]}{K_m + [S]} \tag{31}$$

The biochemical reactions applied in this model are described by a Michaelis-Menten formulation as shown in equation (31), and are derived from work by Jimoh-Taiwo & Haffejee et al. [75], Where v is the reaction rate, V_{max} is the maximum rate achieved by the system, $[S]$ is the concentration of the substrate, and K_m is the Michaelis constant.

$$Thrombin\ (IIa)\ +\ Fibrinogen\ (I) \rightarrow Fibrin\ (Ia) \tag{32}$$

$$\frac{d[Ia]}{dt} = \frac{k_{cat}\,[IIa][I]}{K_m + [I]} \tag{33}$$

Parameter	Value	Unit
k_{cat}	3540	min^{-1}
K_m	3160	nMol

Table 1: Reduced Michaelis-Menten formulation constants

The Michaelis-Menten formulation is reduced for this model to account solely for the interaction of thrombin (IIa) and Fibrinogen(I) to produce Fibrin (Ia), as shown in equation (32), and takes the form shown in equation (33). Constants shown in equation (33) are defined in Table 1.

Scalar	Diffusivity Coefficient
Thrombin	6.79e-8 (kg/m s)
Fibrinogen	3.25e-08 (kg/m s)
Fibrin	2.59e-08 (kg/m s)
Clot	2.59e-08 (kg/m s)

Table 2: Diffusivity coefficients for reagent UDS

The fibrinogen, thrombin, and fibrin scalars are accounted for in the CFD framework by the transport equation for an arbitrary scalar ϕ_k shown in section 3.1.2.8 and are represented in equation (4). The diffusion coefficients for each scalar are shown in Table 2, and are based upon the diffusion of each respective protein in vivo. A fourth scalar is applied to represent areas that develop a permanent clot per the porosity-based clotting model described in the following section, and it is modelled as having a diffusivity coefficient identical to that of Fibrin.

3.1.5. Porosity-Based Clotting Model

$$porosity = \begin{cases} 1 - \dfrac{fibrin/fibrin_{clot\ threshold}}{4}, & \text{if } fibrin < fibrin_{clot\ threshold} \\ & \dot{\gamma} \leq 100\ s^{-1} \\ 0.75, & \text{if } fibrin_{clot\ threshold} \leq fibrin \\ & \dot{\gamma} \leq 100\ s^{-1} \\ 1, & \text{if } \dot{\gamma} > 100\ s^{-1} \end{cases} \quad (34)$$

$$viscous\ resistance\ coefficient = \begin{cases} 1\text{e}12, & \text{if } fibrin_{clot\ threshold} \leq fibrin \\ & \dot{\gamma} \leq 100\ s^{-1} \\ 1\text{e}-12, & \text{otherwise} \end{cases} \quad (35)$$

The porosity-based clotting model consists of two functions that adjust porosity and viscous resistance shown in equations (34) and (35), respectively, and operate based upon local values of the fibrin-concentration scalar and shear rate $\dot{\gamma}$ in a cell zone.

The porosity function alters porosity on a linear scale from 1 (no porosity) to 0.75 within computational cells where the user-defined fibrin-concentration scalar is present and shear rate $\dot{\gamma}$ is less than 100 s^{-1}, as represented by equation (34). In areas where a porosity of 0.75 is achieved, the viscous resistance becomes 1e12 from 1e-12 as shown in equation (35), and the clotting scalar shown in Table 2.

$$\nabla p = -\frac{\mu}{\alpha}\vec{v} \tag{36}$$

The pressure-drop across the porous medium is represented by Darcy's law as shown in equation (36). In ANSYS Fluent, Darcy's law is written as the following:

$$\Delta p \approx \sum_{j=1}^{3} C_{2_{xj}} \Delta n \frac{1}{2}\rho|v|v_j \tag{37}$$

Where Δn is the thickness of the medium in each Cartesian direction.

The effect of porosity is accounted for with an additional momentum source term in the standard momentum equations. The source term S_i is as follows:

$$S_i = -\left(\sum_{j=1}^{3} D_{ij}\mu v_j + \sum_{j=1}^{3} C_{ij}\frac{1}{2}\rho|v|v_j\right) \tag{38}$$

Where the sums on the right-hand side of the equation are the viscous loss term and the inertial loss term, respectively, where D_{ij} is the viscous resistance coefficient. D and C are matrices and $|v|$ is the velocity magnitude follows [107].

3.1.6. Cell Zone and Boundary Conditions

This section outlines the boundary conditions standard to each simulation, and a brief explanation of how each is calculated in ANSYS Fluent.

3.1.6.1. Artery Zone

The artery zone is the flow-volume of interest for the computational model across all simulations. The artery zone includes the aneurysm and parent artery for each simulation. The porosity-based clotting model only functions in this section of the volume.

3.1.6.2. Inlet/Outlet Zones

The inlet and outlet zones are volume extensions of the surfaces that would otherwise be considered the inlet and outlet of the artery zone. The inlet and outlet zones consist of the velocity inlet and pressure outlet boundaries, respectively, and these cell zones are included so that there is a region without porous media between the inlet/outlet flow boundaries and the artery zone. By preventing porous media from near or at the inlet/outlet flow boundaries, solution stability is increased significantly. Otherwise, the inlet zone allows flow to fully develop between the velocity inlet and artery zone.

3.1.6.3. Velocity Inlet

A velocity inlet boundary condition is applied, where the velocity magnitude is oriented perpendicular to the inlet boundary. Uniform velocity distribution is assumed along the inlet surface, simulating a

flow plug behavior. This flow plug redistributes within the inlet zone and exhibits characteristics resembling Poiseuille Flow before entering the artery zone.

The velocity inlet is also responsible for the distribution of the fibrinogen scalar value described in section 3.1.4, where the value of this scalar is defined separately for each simulation-specific methodology at the beginning of chapters 5 & 6.

ANSYS® Fluent uses velocity components and boundary condition scalar quantities to calculate inlet mass flow rate and momentum fluxes.

It computes the mass flow rate of an adjacent fluid cell to the velocity inlet boundary as follows:

$$\dot{m} = \int \rho \vec{v} \cdot d\vec{A} \tag{39}$$

Where only the component of velocity normal to the face of the control volume is employed in computing the inlet mass flow rate.

3.1.6.4. Pressure Outlet

A pressure outlet boundary condition is implemented. The backflow is set normal to the outlet boundary.

For incompressible flow, the pressure at the face of the outlet boundary P_f is defined as follows:

$$P_f = \frac{P_c + P_e}{2} \tag{40}$$

Where:

P_c Interior cell pressure neighboring the exit face f

P_e Specified exit pressure

3.1.7. Calculation Settings

The convergence criteria for all flow models are that continuity, x-velocity, y-velocity, z-velocity, UDS-0 (thrombin), UDS-1 (fibrinogen) and UDS-2 (fibrin) residuals all fall below 0.001 each timestep.

3.2. Flow Experiment Methodology

The flow experiments applied in this study are built upon a previous PIV validation experiment, as well as work performed by Ngoepe et al. and Jimoh-Taiwo et al. [71,73,75]. These flow experiments apply a PIV-based framework with certain design considerations to allow the measurement of a flow field simultaneously to monitoring the growth of a clot, or introduction of another substance into the flow field. This chapter describes the broad methodology common to all flow experiments performed as part of this study, including design considerations for capturing clotting in a PIV-based

flow experiment, PIV theory, flow phantom design, PIV setup, image pre-processing theory, and image postprocessing theory.

3.2.1. Flow Phantom

3.2.1.1. Design Considerations for Capturing Clotting in PIV

Refractive index matching is a common practice in PIV studies considered important to reduce image distortions [109]. Due to the use of proteins derived from human-blood, traditional methods for refractive index matching for PIV are not suitable for this study. This is due to very few fluids being suitable for changing the refractive index of a fibrinogen-saline mixture without fundamentally altering fibrinogen's interaction with thrombin. The few fluids that meet this criterion, such as glucose-saline mixture, must be added at such a high concentration that the fluid properties of the mixture are significantly different than fibrinogen-saline solution. Similarly, the flow phantom material cannot be feasibly changed since materials with the correct combination of refractive index and clarity are not identifiable outside of experimental materials that were unavailable for this study.

As such, the mismatch of refraction index is addressed geometrically using Snell's Law, described by the following equation:

$$n_1 sin\theta_1 = n_2 sin\theta_2 \tag{41}$$

Where:

n_1 incident index

n_2 refracted index

θ_1 incident angle

θ_2 refracted angle

According to Snell's law, shown in equation (41), there are two ways to eliminate light refraction, or more specifically to make the incident angle of light outside an interface θ_1 equal to the refracted angle through that interface θ_2. The first way is to match the incident index n_1 with the refractive index n_2 such that they are equal, and therefore making θ_1 and θ_2 equal as well; what is referred to as refractive index matching. The second is to ensure that θ_1 contacts the interface at the critical angle 0°, resulting in a refracted angle θ_2 that is also 0°, making both sides of the equation zero. This negates the relevance of the values for incident index n_1 and refractive index n_2 in determining incident angle and refracted angle, effectively removing the requirement for refractive index matching of fluids to remove image distortions.

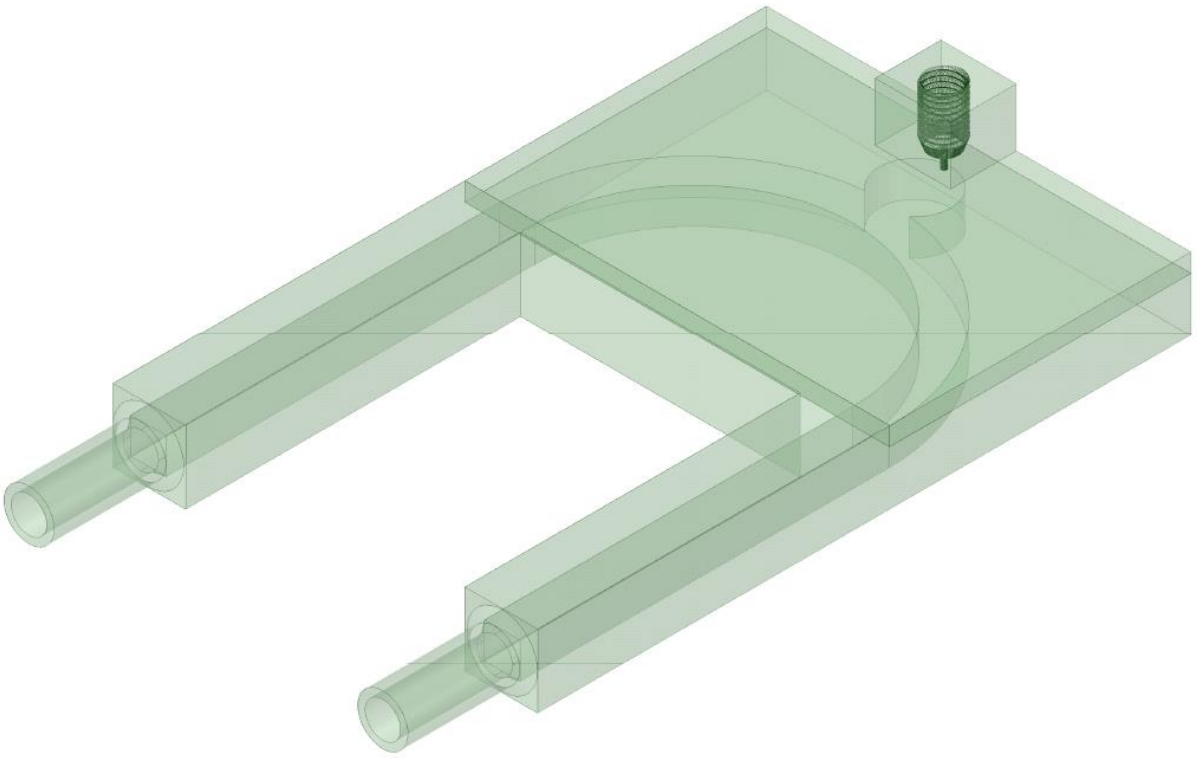

Figure 1: Flow phantom model assembly

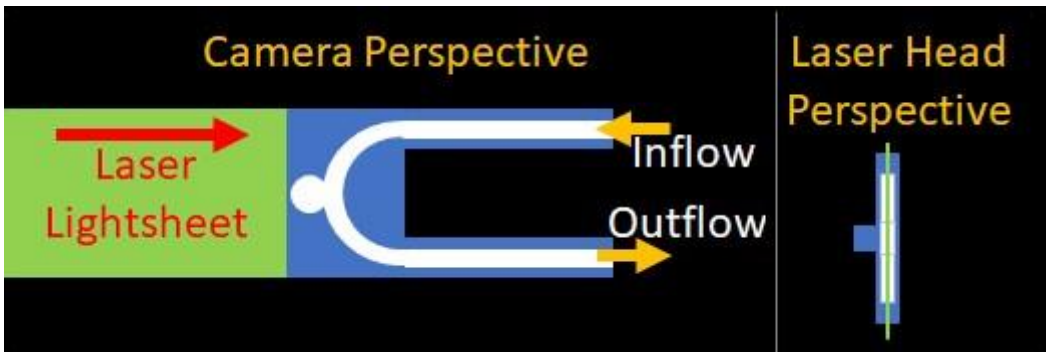

Figure 2: Orientation of flow phantom relative to camera and laser head

As such, a square-channel flow phantom shown in Figure 1 is applied in this study to reduce distortion of particles in absence of refractive index matching between the operating fluid and the flow phantom. As shown in Figure 1, the flow phantom still applies some curved features to create the shape of an idealized aneurysm.

The orientation of the flow phantom shown in Figure 1 relative to the camera is shown in Figure 2, where the broad side of the flow phantom is perpendicular to the direction in which the camera is pointed, and the laser light sheet passes through the center of the narrow edge of the flow phantom; passing through the center of the flow channel parallel to the broad sides of the flow phantom. Referring to Snell's law in equation (41), refraction is not reduced everywhere in the flow phantom

due to the curves in geometry formed by the interior surfaces. However, because these surfaces form planes parallel to the direction in which the camera is pointing, all incident angles θ_1 and refracted angles θ_2 occur along the plane formed by the laser light sheet. Therefore, distortions only occur along the green line representing the laser light sheet from the perspective of the laser head shown in Figure 2 (right), and not in the plane of interest from the camera's perspective (left).

3.2.1.2. Flow Phantom Geometry Design

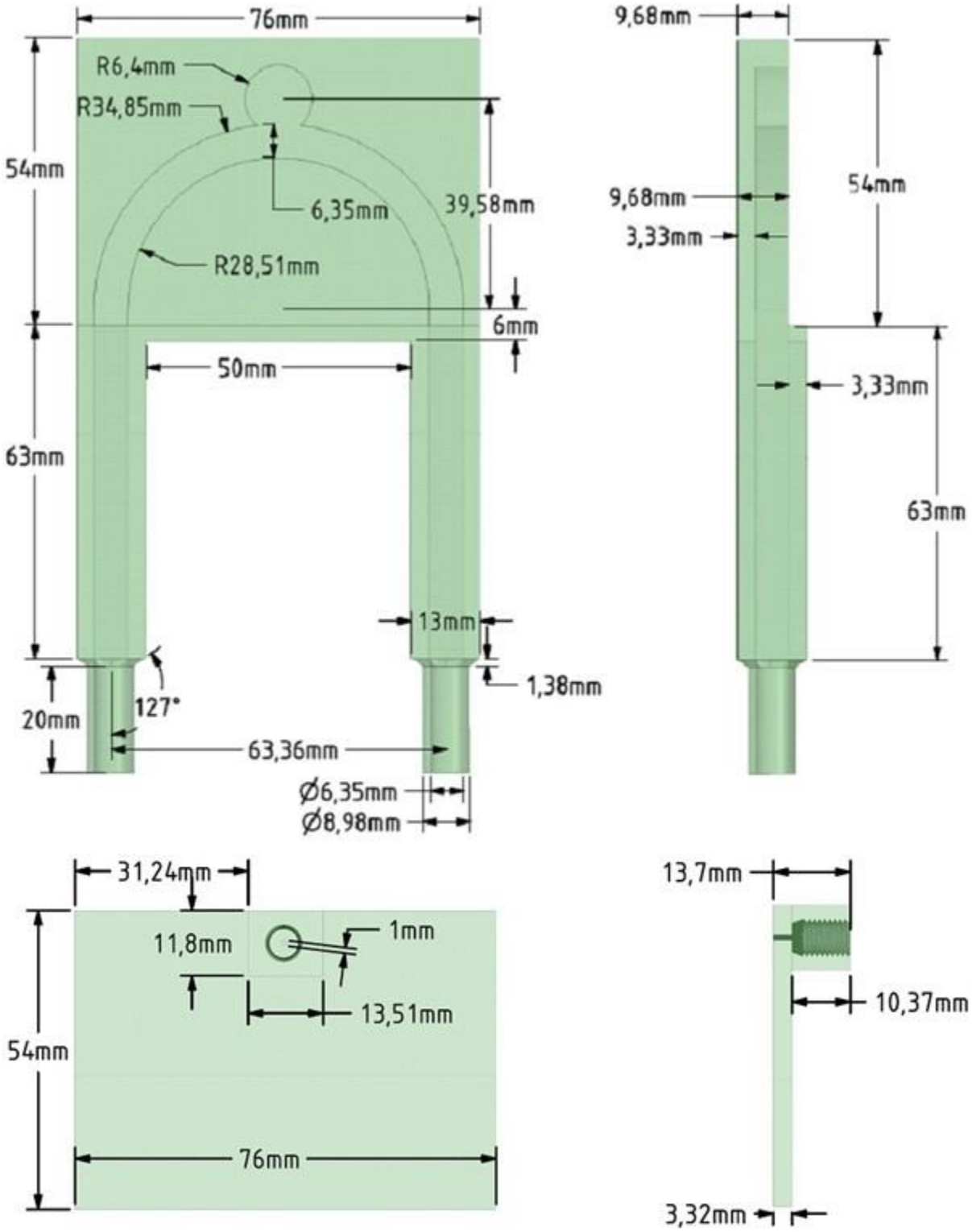

Figure 3: Flow phantom channel (top) and injection panel (bottom) dimensions

The flow phantom is composed of two components; a partially open-faced square channel shown in Figure 3 (top), and a panel with an injection port that fits on top of it (bottom), to allow access to the

channel interior for postprocessing discussed in upcoming section 3.2.1.3. The square channel shown in Figure 2 and Figure 3 is 6.35x6.35 mm with a cylindrical aneurysm of 6.4 mm radius and 6.35 mm height. These flow volume dimensions are used as a rough analog to idealized cerebral aneurysm flow phantoms applied in similar studies [65,66,69,72,73,110,111] and furthermore an analog to realistically sized intracranial saccular aneurysms per the geometrical considerations described by Parlea et al. [112]. Round hoses connect the flow phantom to the pulsatile pump as discussed in upcoming section 3.2.4 of the experiment setup, and subsequently a round to square transition of 1.38 mm in length is applied in the flow phantom near the adaptors internally. The 1mm injection port inlet on the flow phantom injection panel shown in Figure 3 (bottom) aligns to the side of the cylindrical aneurysm shown in Figure 1 so as not to obstruct the laser light sheet shown in Figure 2.

3.2.1.3. Flow Phantom Material and Postprocessing

A Formlab 2 3D printer was used to produce the flow phantom using a clear V4 resin. Clear V4 resin has been applied in similar flow research by Ho et al. and Ngoepe et al., and is determined to be optimal for its clarity [73,74].

The 3D printed flow phantom is post-processed to improve optical clarity specifically via the removal of rough edges and the addition of a clear medium on all surfaces. All flat surfaces are polished with increasingly fine sandpaper up to a fine 2000 grit. Once sanded, parts are coated with clear acrylic spray paint both internally and externally, and the parts are attached.

3.2.2. Discrete Fourier Transform PIV Theory

PIVlab, a broadly acclaimed GUI-based tool for PIV flow analysis, is applied for PIV flow analysis in this study [113–115]. The PIV technique applied is based upon the acquisition of sets of image pairs that are used to derive velocity vectors. The following cross-correlation equation is used to compute these velocity vectors:

$$v = \frac{d}{M\Delta t'} \tag{42}$$

Where:

d distance

M pixel to distance conversion scale factor

Δt separation time

The cross-correlation algorithm used in PIVLab for this study performs a time-resolved analysis with Discrete Fourier Transform (DFT), using decreasing interrogation areas to determine velocity magnitude and direction [116].

This is represented by the following equation:

$$C(m,n) = \sum_i \sum_j A(i,j)B(i-m, j-n) \tag{43}$$

Where:

A interrogation area of first image within image pair

B interrogation area of second image within image pair

C resultant matrix

Where the resultant matrix C is the expected displacement particles traveling from image A to image B, determined by the location of the intensity peak.

In the Discrete Fourier Transform (DFT) method, the interrogation areas for image A and B are identical in size, which creates a degree of error in the correlation matrix. This is mitigated by the reduction of separation time Δt, where Δt is kept at less than 1/3rd the size of the interrogation area. This is further mitigated by performing several passes of the algorithm, refining the interrogation window with each pass [113].

Additionally to maximize quality control of computed results, an 'extreme' correlation robustness is applied, such that cross-correlation is repeated five times with shifted interrogation windows and correlation values that are not present in each of the five correlation matrices are eliminated from the resulting correlation matrix [113,117].

3.2.3. Image Preprocessing and Data Postprocessing

Combinations of the image pre-processing methods described in this section are applied to all images derived for each of the flow visualization experiments.

3.2.3.1. Contrast Limited Adaptive Histogram Equalization (CLAHE)

CLAHE is a standard preprocessing setting used in PIVLab that significantly improves the probability of detecting valid vectors in PIV [114,118]. CLAHE operates by spreading the most common intensities in an image histogram to the full range of intensity data for individual small tiles that cover the flow region of interest. This allows high exposure regions and low exposure regions to be optimized independently of one another.

3.2.3.2. Intensity Highpass

An intensity high-pass filter reduces the effects of uneven lighting in particle identification for cross-correlation. High-pass filters are useful for suppressing low frequency information caused by uneven illumination while preserving high frequency information surrounding particles [114].

3.2.3.3. Intensity Capping

Intensity capping limits the greyscale intensity threshold and assists in normalizing particle brightness, preventing bias in correlation signal to bright particles and bright spots caused by uneven lighting [118].

3.2.3.4. Mean Background Subtraction

Background elimination removes background noise that contributes error during cross-correlation, particularly from internal reflections in the flow channel of the flow phantom. This is accomplished via calculating the mean image and subtracting it from each input image, which significantly reduces the intensity of stationary features common to each image [113].

3.2.3.5. Smoothing in Postprocessing

Data smoothing is an effective method for noise reduction [114,119]. A least squares method of data smoothing called the 'Smoothn' algorithm can be applied in postprocessing, and is used to increase the quality and accuracy of velocity estimation [114,119].

3.2.4. PIV Setup

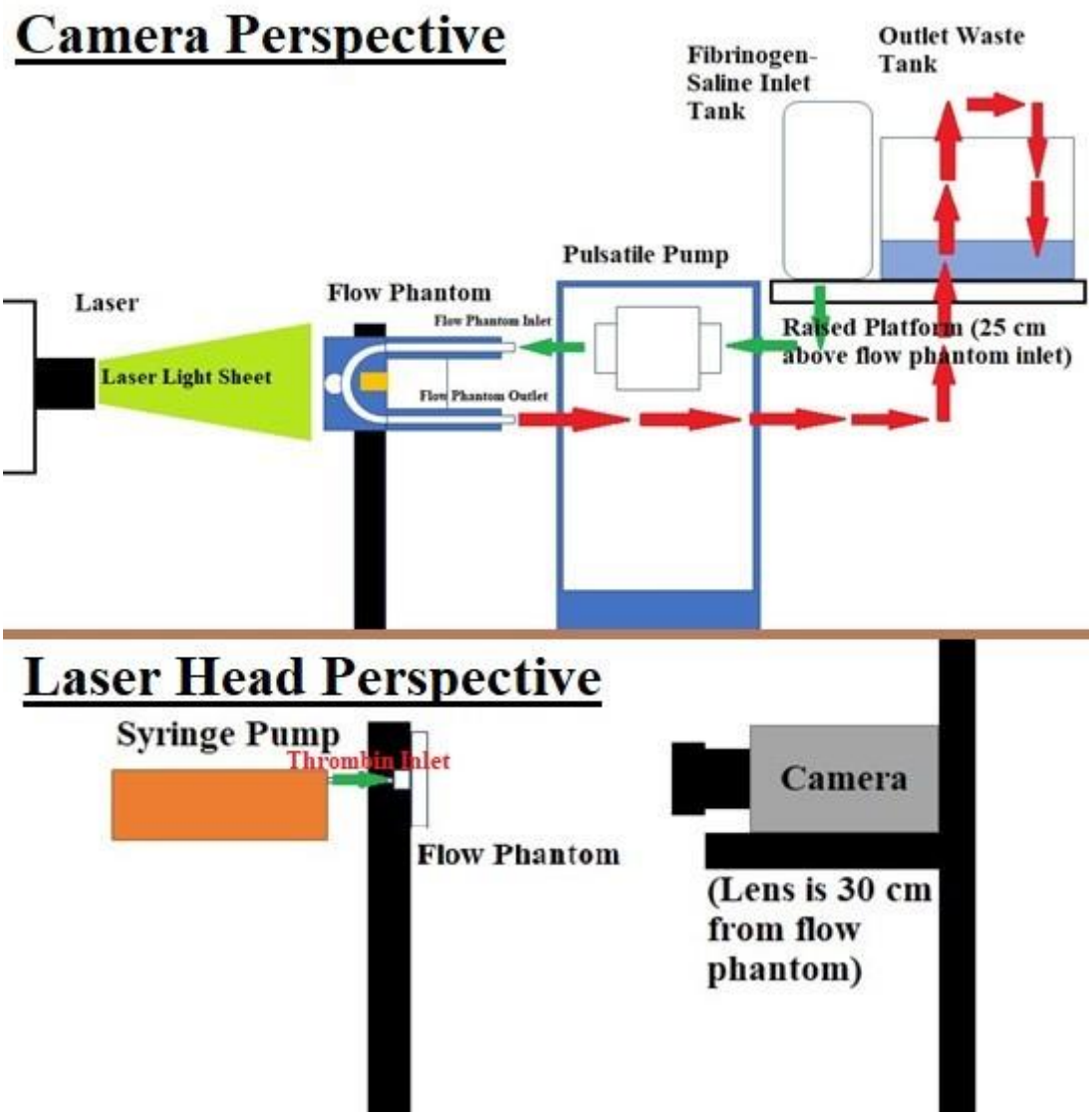

Figure 4: Physical PIV configuration relative to camera perspective (top), and laser head perspective (bottom)

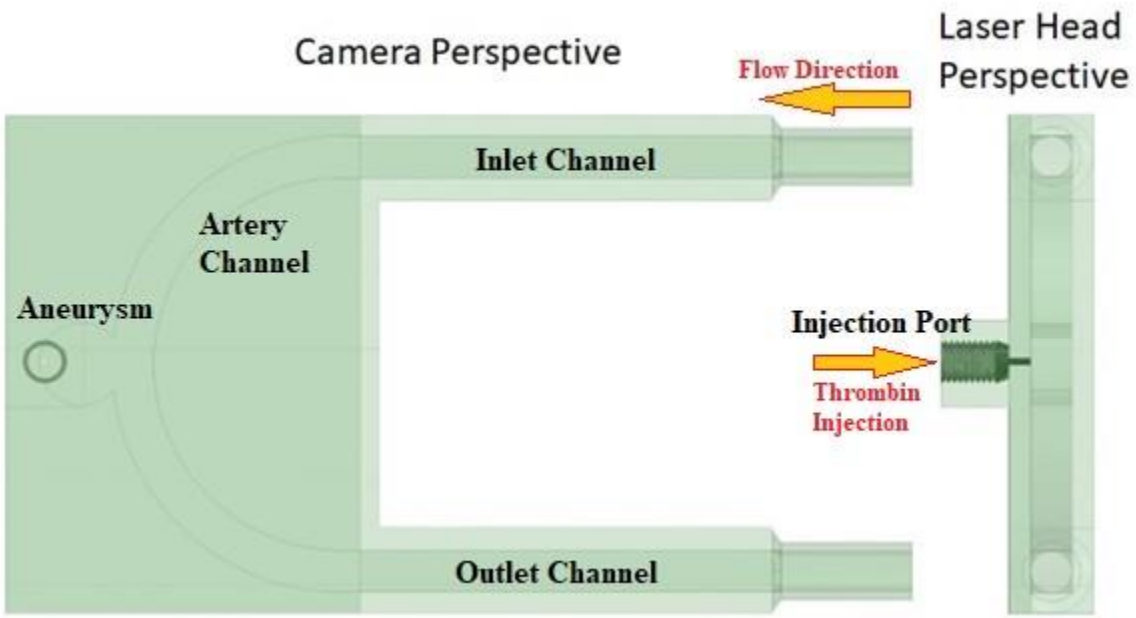

Figure 5: Flow phantom relative to camera perspective (left) and laser head perspective (right)

The detailed physical orientation of the PIV experiment setup is shown in Figure 4, and the accompanying orientation of the PIV flow phantom is shown in Figure 5. As shown in Figure 2, the top of the aneurysm is oriented towards the laser sheet so that the particles in the aneurysm are illuminated with as little interference as possible. As shown in Figure 4 (top), a reservoir is oriented directly above the pump, and the pump is connected with as short of a feed as possible to the flow phantom, which is fixed at a height roughly level with the feed from the pump. The exit tube flows to an exit tank roughly at the same height as the inlet tank to prevent the flow from being affected gravitationally. The length of tube from the inlet tank to the outlet tank is made as short as possible to efficiently fill the system with fibrinogen solution. As shown in Figure 4 (bottom), the camera is held from a length of 30cm which is optimal for the focal length of the lens applied, described in section 3.2.4.4.

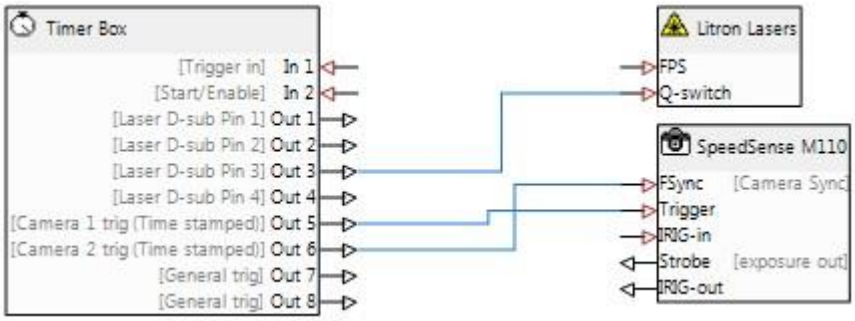

Figure 6: DynamicStudio timer box configuration

The DynamicStudio PIV platform is used to synchronize the laser with the camera. The timer box configuration shown in Figure 6 is applied to accomplish this.

3.2.4.1. Harvard Apparatus Pulsatile Pump

A Harvard apparatus pulsatile pump is applied to provide a pulsatile flow pattern through the PIV flow phantom. The pump is set to provide 38 $\pm$ 1 strokes/min at 15 ml per stroke for an average flow velocity of 30 cm/s into the flow phantom, which is reasonably close to flow rates measured in intracranial arteries [120].

3.2.4.2. Seeding Particles

The seeding particles applied are Dantec Dynamics borosilicate glass hollow glass sphere (HGS) particles that have a mean diameter of 20 µm and a density of 1.1 g/cm^3.

3.2.4.3. Litron LDY300-PIV Lasers

The PIV experiments use Litron LDY300-PIV series DPSS Nd:YLF lasers. This system consists of two independently pulsed Nd:YLF DPSS laser resonators that produce an infrared laser light at 1053 nm, which are then converted to 527 nm green light beams via a harmonic generation assembly, and then exit through a single port of the laser head. For this experiment, only a low pulse frequency is necessary, so only one laser resonator is active to produce a pulse frequency of 0.5 kHz and a pulse duration of 12 µs. 50% of the maximum lasers power is applied for optimal laser light brightness.

3.2.4.4. SpeedSense Miro 110 PIV Camera

Camera Specifications	Units
Resolution (horizontal x vertical)	1280 x 800 pixels
Pixel size (horizontal x vertical	10 µm
Minimum Exposure time	2 µs
Image frequency (frame rate)	1600 fps
Memory	3 GB

Table 3: SpeedSense Miro 110 PIV Camera

A SpeedSense Miro 110 PIV camera is used for image capture in the PIV experiment. The relevant specifications for this camera model can be seen in Table 3 and exceed the requirements for the PIV experiment being performed, which does not require such a high frame rate and resolution, nor very low exposure times enabled by the shutter speed.

Camera Settings	Units
Image Pair Capture Frequency	20 Hz (20 image pairs / s)
Time Step	2000 µs
Exposure Time	3000 µs
Image Area	512 x 512 pixels

Table 4: Camera Settings for PIV experiment

The camera settings applied for the PIV experiment are shown in Table 4. An image pair capture frequency of 20 Hz is applied in combination with the image area of 512 x 512 pixels to compensate for memory limitations of the camera while still capturing a sufficient number of images for analysis of the flow area in question. The time step and exposure time optimize particle brightness and minimize blur.

3.2.4.4.1. Nikon 105mm F2.8 G VR Macro Lens

The lens applied on the Speedsense Miro 110 PIV Camera is a Nikon 105mm F2.8 G VR Macro Lens. This lens is applied due to its short focal length of 105 mm, which allows for closeup images on the flow phantom; ensuring maximum resolution on regions of interest.

3.2.5. Equations for Flow Results Comparison

Evaluation of flow is accomplished in part by the calculation of Reynolds Re, Womersley α, and Dean De numbers as conventionally defined for standard square channel geometries. These values are standard across flow experiments, as each operating fluid theoretically has identical density and viscosity.

4. Flow Experiments

This chapter details experimental design, results, and discussion specific to each flow experiment performed. These flow experiments are analyzed using a PIV framework and include an analysis of flow within the flow phantom shown in Figure 1. The experimental design and results for two experiments are presented in sections 4.1-4.3 and include a water-gelatin flow experiment and a thrombin-fibrinogen flow experiment, where the latter experiment is addressed across multiple sections (4.2-4.3).

The water-gelatin flow experiment measures flow of room temperature water through the flow phantom shown in Figure 1 before and after injection of gelatin into the aneurysm. This experiment

is performed once and is used as a preliminary test to determine the feasibility of flow analysis and clot-identification for the thrombin-fibrinogen flow experiment.

The thrombin-fibrinogen flow experiment measures the flow of a fibrinogen-saline solution through the flow phantom shown in Figure 1. A thrombin-saline solution is injected into the aneurysm, and the interaction between fibrinogen and thrombin generates fibrin, which forms a fibrin mesh once a sufficient concentration of fibrin is accumulated. The thrombin-fibrinogen flow experiment is conducted twice and each is evaluated across two cases (once per) in sections 4.2 and 4.3, due to a difference in experimental design and results analysis pre- and post-clotting.

Finally, a discussion of the two experiments results is presented in section 4.4, where a comparison to results from similar studies is made.

4.1. Water-Gelatin Flow Experiment

The water-gelatin flow experiment is a preliminary test aimed at determining whether a separate material such as a clot could be identified independently of the surrounding flow field and vice-versa. In this case, water is used instead of a fibrinogen-saline mixture, and household kitchen gelatin is used instead of thrombin. The water and gelatin do not react with one another like fibrinogen and thrombin do when they create a fibrin clot. However, gelatin is visually and behaviorally distinct from water, similarly to a fibrin clot within a fibrinogen-saline solution as seen in previous thrombin-fibrinogen flow experiments [73,75]. It is therefore able to act as a rudimentary trial material for determining the efficacy of clot and valid vector identification for the subsequent fibrinogen-thrombin flow experiments as well as help to streamline any methodology before moving onto the actual material which is very expensive.

4.1.1. Experimental Design

4.1.1.1. Materials, Physical Setup, and Procedure

The experiment operates as described in section 3.2.4 of the broad PIV methodology described in chapter 3.2, where room-temperature tap water is used as the working fluid. Once water has filled the system shown in Figure 4, and circulated for 30 seconds by the pulsatile pump described in section 3.2.4.1, a syringe pump releases 0.2 ml of gelatin mixture over 1s via the injection port shown in Figure 4 (bottom).

To create the gelatin-mixture for the gelatin-injection, 10 grams of 120 bloom strength household flavorless gelatin are added to 60 ml of hot water and allowed to cool for 30 minutes before the experiment is performed. This allows the gelatin to reach a consistency where it has not solidified and

can still flow at relatively low shear-rates, which is qualitatively tested by adjusting the orientation of its mixing-container and observing its change in position.

Camera Settings	Units
Image Pair Capture Frequency	30 Hz (30 image pairs / s)
Time Step	1500 µs
Exposure Time	2000 µs
Image Area	1280 x 800 pixels

Table 5: Camera Settings for water-gelatin experiment

The camera is positioned 60 cm away from the flow phantom for this experiment to capture flow within both the parent artery and the aneurysm, and uses the settings shown in Table 5. This is done in part to measure the pulsatile waveform for use in the validation simulation discussed in upcoming chapter 5.

4.1.1.2. Image Pre-Processing and FFT Settings

Image Pre-Processing Settings	Units
CLAHE window size	64 pixels
Intensity High-Pass kernel size	15 pixels
Wiener Denoise Filter and Gaussian Low Pass window size	2 pixels
Mean Intensity Background Subtraction	Enabled

Table 6: Image pre-processing for the water-gelatin experiment

The relevant image pre-processing techniques described in section 3.2.3 are applied for the images derived in this experiment, and the values applied for each technique can be found in Table 6.

FFT Window Deformation Settings	Interrogation Area	Step Size
Pass 1	128 pixels	64 pixels
Pass 2	64 pixels	32 pixels
Pass 3	32 pixels	16 pixels
Pass 4	16 pixels	8 pixels
Sub-pixel estimator	2x3 Gauss	
Sub-pixel estimator auto-correlation	Disabled	
Correlation robustness	Extreme	

Table 7: FFT Window Deformation Settings for the water-gelatin experiment

The image pre-processing setting's values are based on recommended default settings in PIVlab and the FFT pass window sizes shown in Table 7. The CLAHE window size is equivalent to the pass 1 step-

size and pass 2 interrogation area, such that each interrogation area for the 2nd pass is optimized independently. This value is unaltered from the default value provided in PIVlab to optimize intensities for accurate particle identification for high and mean flow rates. The intensity high-pass kernel size is set to 15 pixels to suppress background noise. The Wiener denoise filter and Gaussian low pass window size of 2 pixels are selected to further eliminate background noise and are based on image resolution with consideration that the lowest particle displacement is 2 pixels, and a higher window size may cause loss of particle displacement information. Mean intensity background subtraction is applied to remove background noise that is consistent across all images.

The FFT pass window sizes are selected based on the maximum and minimum particle displacements, which are 8 pixels and 2 pixels respectively, as well as particle count. Particle count informs the 1st and 2nd interrogation areas, which are necessary once gelatin is injected, since the intensity of the gelatin can interfere with the detection of surrounding and enveloped particles and can therefore interfere with accurate displacement detection. The maximum particle displacement is no greater than ¼ of the 3rd interrogation area, and the minimum particle displacement is no greater than ¼ of the final interrogation area.

2D Gauss subpixel estimation is selected for increased accuracy when motion blur is present, with auto-correlation disabled to reduce detection of invalid vectors from background noise caused by the gelatin injection [113]. The highest and most computationally expensive setting for correlation robustness quality in PIVlab is selected to ensure further accuracy.

4.1.1.3. Image Calibration and Post-Processing

Image Calibration Settings	Units
Reference length [px]	729.95 pixels
Real distance of reference length [mm]	76 mm
Time Step	1.5 ms
Pixel to distance conversion	1 pixel = 1.04115e-4 m
Pixel/frame to velocity conversion	1 pixel/timestep = 0.06941 m/s

Table 8: Image calibration settings for water-gealtin experiment

The image calibration settings applied to determine the velocity values for vectors derived from the FFT cross-correlation are shown in Table 8. These are derived from the characteristic length of 76 mm of the top side of the flow phantom shown in Figure 3, which is measured to be 729.95 pixels in length for the PIV derived images. When the pixel to distance conversion is divided by the time step between image pairs of 1.5 ms, the pixel/timestep of each vector for an image pair can be converted to velocity, where 1 pixel/frame is equivalent to 0.06941 m/s.

Image-Based Vector Validation Settings	Units
Bright Object Filter Threshold	0.46471

Table 9: Image-based vector validation settings for water-gelatin experiment

Due to the high correlation robustness algorithm applied, and the use of data-smoothing in the derivation of spatial parameters, velocity-based postprocessing is not applied. Image-based vector validation is used, however, specifically to filter out vectors derived from above the intensity threshold shown in Table 9, since this value is associated with areas of flow that include large fragments of gelatin.

4.1.1.4. Gelatin identification

To adequately assess the validity and/or cause of localized flow effects after a gelatin injection, it is critical to identify the location of nearby gelatin fragments. Large gelatin fragments can be easily identified visually, but smaller fragments are not as easily identified and may affect the surrounding flow area. Fragments of gelatin in a flow area are identified using a preprocessing technique that specifically includes mean background subtraction and intensity capping. This method helps to capture not only the gelatin intersecting with the laser light sheet, which is usually visible without image-processing, but also gelatin in the far field, which may affect the trajectory of nearby particles even if they are not acting on the same plane perpendicular from the camera, shown in Figure 5. The locations of gelatin fragments are shown as regions of bright white in subsequent “gelatin identification” results presented in section 4.1.4.1.

4.1.2. Pulsatile Inlet Velocity Waveform

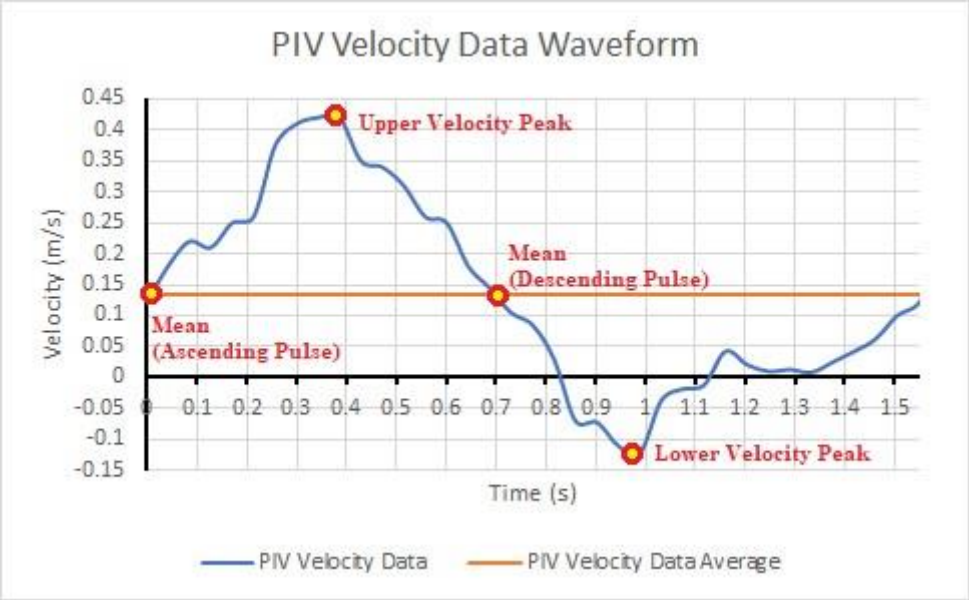

Figure 7: Waveform of PIV inlet velocity data indicating waveform features with yellow dots

Figure 7 demonstrates a single velocity waveform derived from flow exiting the inlet channel, and indicates waveform features in a pulse that will be referenced throughout the flow experiment results analysis. The indicated waveform features of the inlet velocity Fourier transform are specifically the mean flow as the pulse ascends towards the upper velocity peak (left), the upper velocity peak (middle-left), the mean flow as the pulse descends towards the lower velocity peak (middle-right), and the lower velocity peak (right).

The PIV velocity data waveform shown in blue in Figure 7 is derived within the PIV flow phantom from the average of velocity measurements across a line probe spanning the width of the artery channel (6.35 mm) just downstream of the inlet channel shown in Figure 5 (left). The line probe measures flow across 7 interpolated points. Velocities of points interpolated at the walls are discarded, leaving a remainder of 5 velocities which are averaged using the following equation:

$$\bar{v} = \frac{1}{5}\sum_{i=1}^{5} v_i \tag{44}$$

Where:

$\bar{v}$ average velocity

v_i individual sample velocity

4.1.3. Pre-Injection Flow Results

The flow results of water prior to gelatin-injection are presented and analyzed in this section to demonstrate a baseline for comparison of flow results for the post-gelatin injection water-gelatin experiment results in upcoming section 4.1.4, as well as flow results for the thrombin-fibrinogen flow experiment in upcoming sections 4.2-4.3.

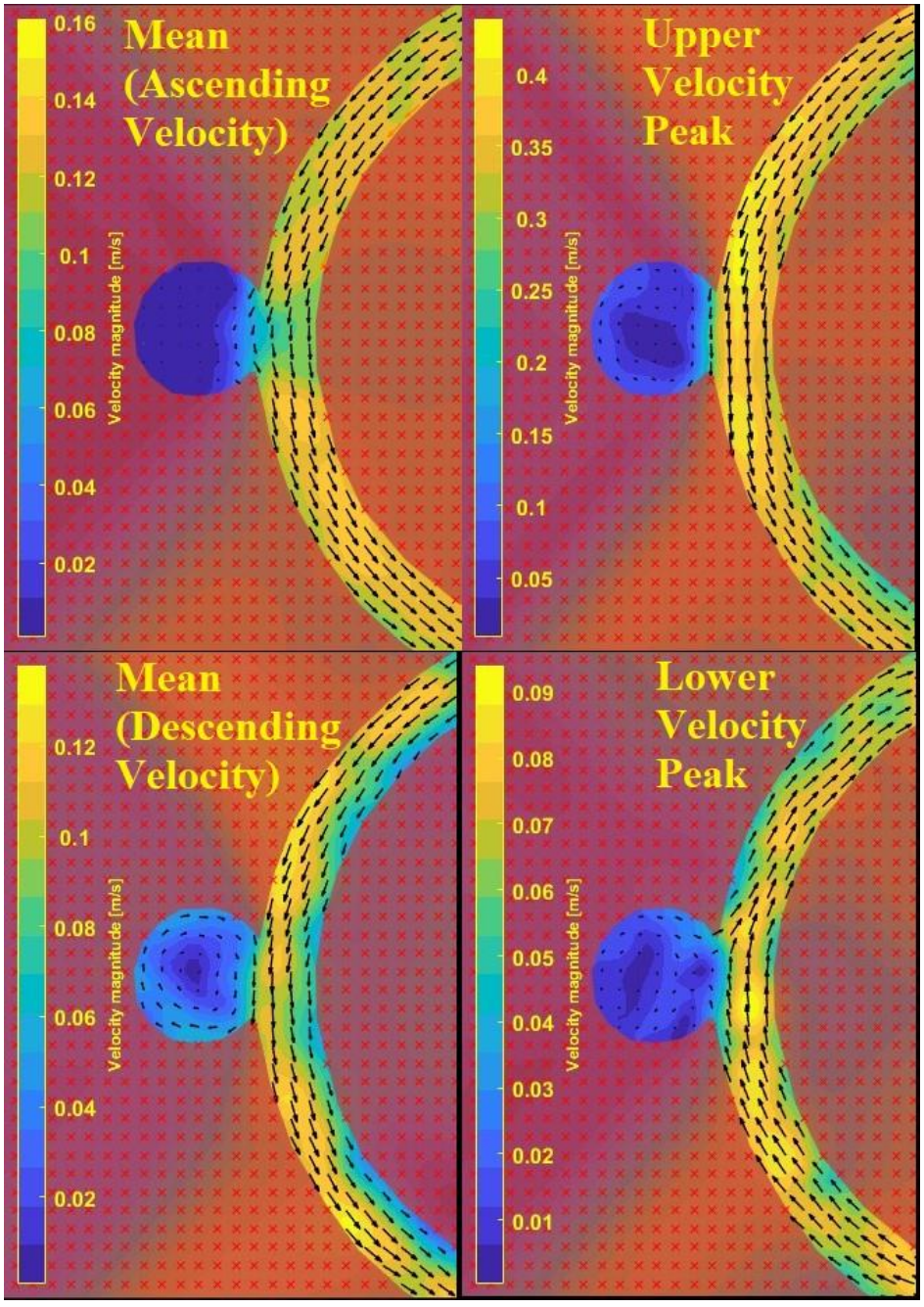

Figure 8: Water-gelatin experiment pre-injection arterial flow behavior at different times throughout a pulse wavelength shown in Figure 7; mean pulsatile flow velocity ascending towards upper velocity peak (top left), pulsatile flow upper velocity peak (top right), mean pulsatile flow velocity descending towards lower velocity peak (bottom left), pulsatile flow lower velocity peak (bottom right).

The arterial flow behavior of water in the water-gelatin experiment is seen in Figure 8, which presents flow at different stages of a pulse wavelength referenced in Figure 7. The flow within the artery during the upper velocity peak and the mean of the ascending pulse, shown in the top right and left of Figure 8 respectively, is well distributed throughout the entire artery. The exception is the neck of the aneurysm in the case of the mean, due to the relatively high velocity fluid from the artery being diverted into the relatively slow recirculating fluid within the aneurysm. Flow is less well distributed during the mean of the descending pulse and the lower velocity peak, where the former demonstrates higher velocity flow on one side of the artery than the other by a factor of two, which is possibly due to an imbalance of momentum as the velocity in the artery drops. The latter, by contrast, demonstrates pockets of low velocity flow near high velocity flow regions likely due to rapid and uneven change in direction of flow.

Womersley number α is 12.39, De ranges from 10 at the lower velocity peak and 50 at the upper velocity peak and Re ranges from 500 to 2900, where transitional flow is reached only around the upper velocity peak for around 0.3s per pulse. Womersley number α suggests that flow is dominated by the inertial effects by comparison to the viscosity of the fluid. Both α and De numbers suggest that there are secondary flows present in flow, though the results shown in Figure 8 do not indicate that these secondary flows are identifiable on the viewing plane outside of skewing high velocity flow towards the outer wall of the artery channel of the flow phantom.

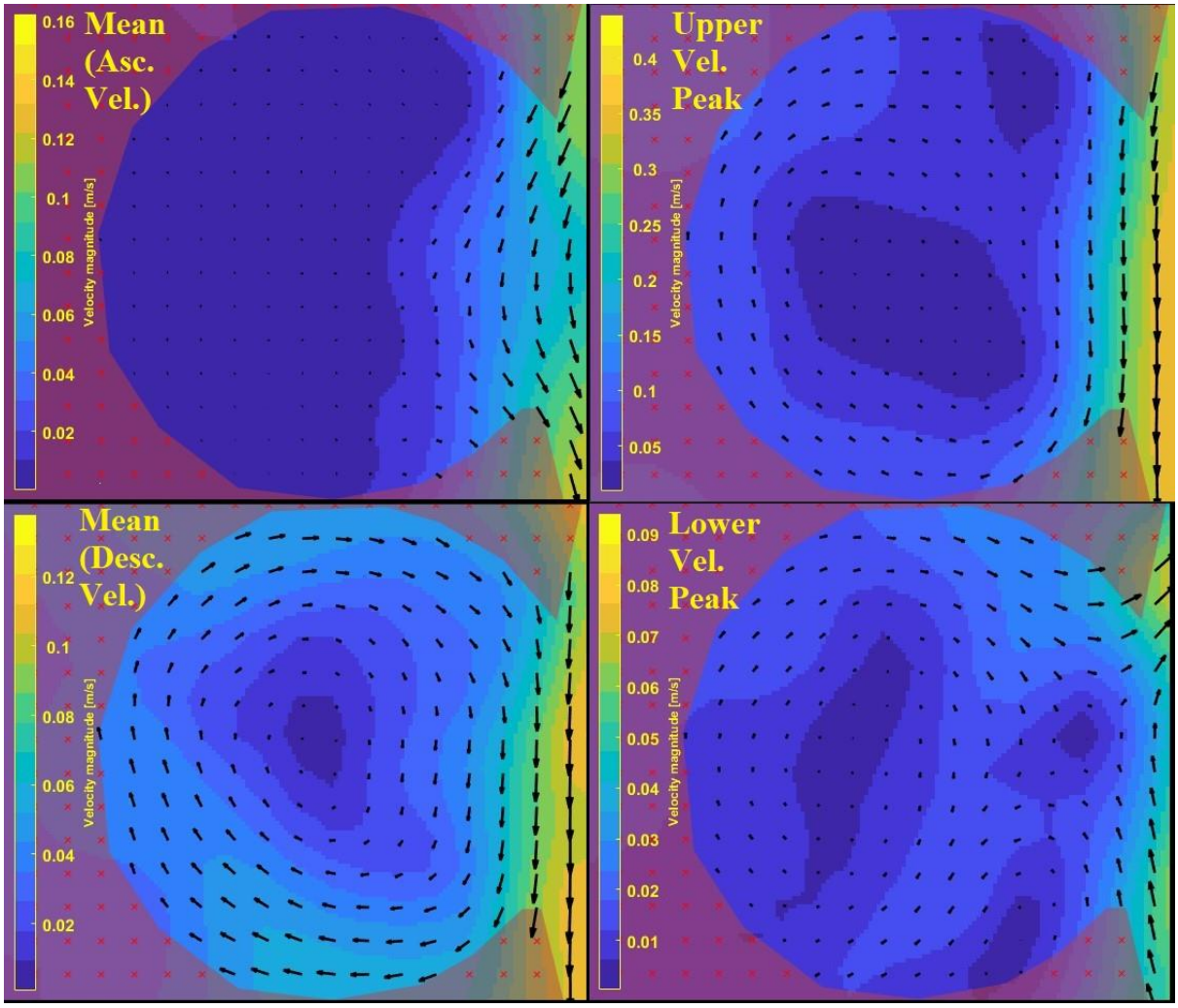

Figure 9: Water-gelatin experiment pre-injection aneurysmal flow behavior at different times throughout a pulse wavelength shown in Figure 7; mean pulsatile flow velocity ascending towards upper velocity peak (top left), pulsatile flow upper velocity peak (top right), mean pulsatile flow velocity descending towards lower velocity peak (bottom left), pulsatile flow lower velocity peak (bottom right).

The aneurysmal flow behavior of water in the water-gelatin experiment is shown in Figure 9, which presents flow at different stages of a pulse wavelength similar to Figure 8. Flow within the aneurysm is lowest during the ascending mean, shown in the upper left of Figure 9, when the pulse is increasing towards the upper velocity peak. High velocity flow from the aneurysm is diverted downstream as it reaches the neck of the aneurysm. This interaction triggers a higher rate of flow along the walls of the aneurysm by the time the upper velocity peak is reached, as shown in the top right of Figure 9. As the pulse decreases towards the descending mean, shown in the bottom left of Figure 9, the high recirculatory flow within the aneurysm becomes well distributed around the center of the aneurysm. This recirculatory behavior appears to be mostly eliminated by the time the lower velocity peak is reached, as show in the bottom right of Figure 9, coinciding with the change in flow direction within the artery.

4.1.4. Post-Injection Flow Results

4.1.4.1. Gelatin Location Identification

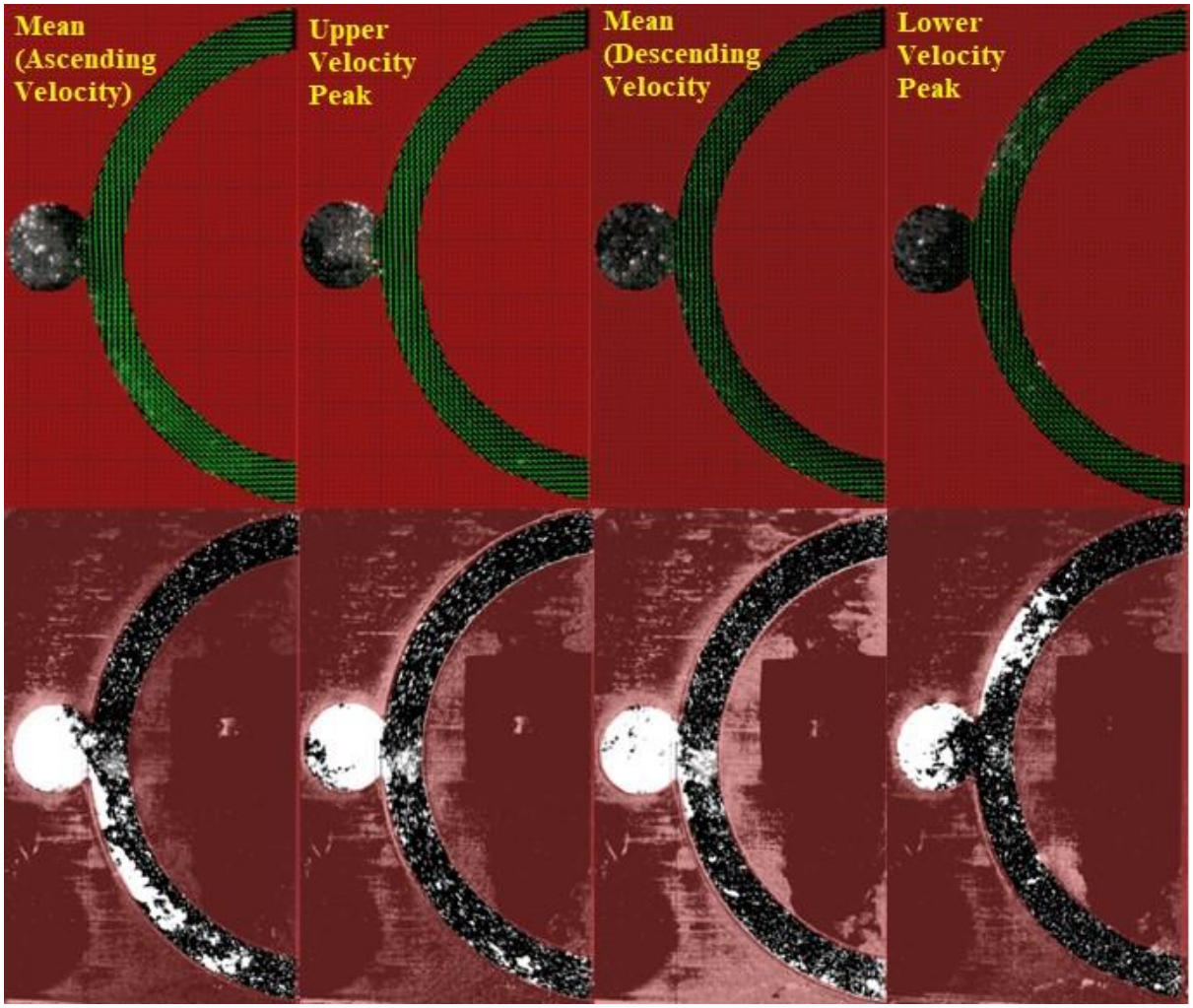

Figure 10: Gelatin identification (bottom) and corresponding vector maps (top) at different times throughout a pulse wavelength shown in Figure 7; mean pulsatile flow velocity ascending towards upper velocity peak (left), pulsatile flow upper velocity peak (middle left), mean pulsatile flow velocity descending towards lower velocity peak (middle right), pulsatile flow lower velocity peak (right).

The results of the gelatin identification preprocessing method described in section 4.1.1.4 are shown in Figure 10. The corresponding gelatin-identification images (bottom) are mapped relative to corresponding pre-processed vector diagrams at different stages of a pulse (top), starting with the mean flow of an ascending pulse waveform 0.87s after thrombin injection. The upper row of images shows the locations of the highest concentrations of gelatin in the laser field and demonstrate that vectors of nearby particles can be captured so long as they are not engulfed by large fragments of gelatin. The bottom row illuminates all areas with gelatin concentration of equal intensity and demonstrates that some vector capture from particle displacement is occurring even in areas with gelatin present in the view plane.

4.1.4.2. Flow Field Results and Quality Assessment

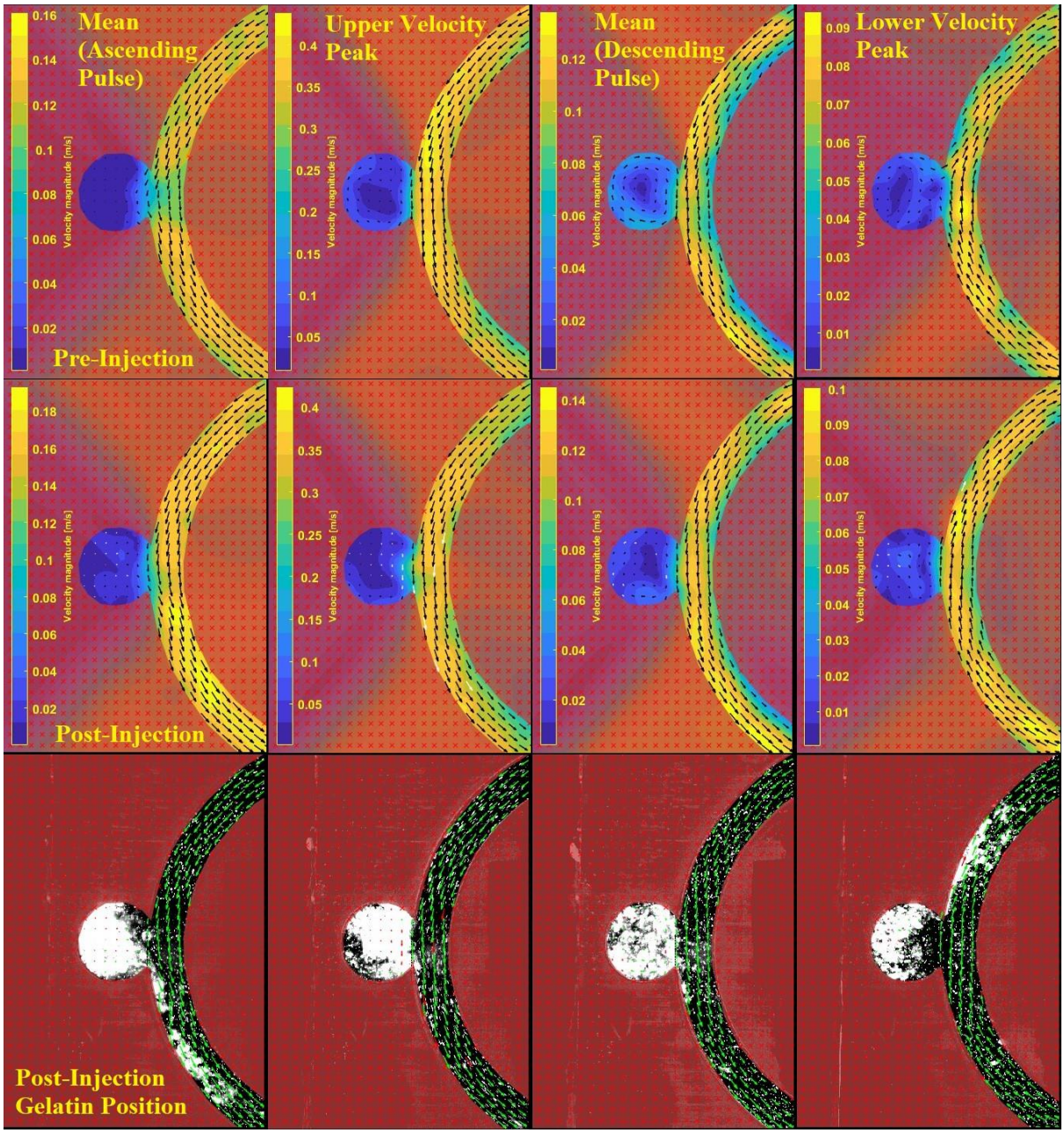

Figure 11: Water-gelatin experiment pre-injection arterial flow behavior (top) comparison with post-injection aneurysmal flow behavior (middle) with images of relative gelatin position (bottom) at different times throughout a pulse wavelength shown in Figure 7; mean pulsatile flow velocity ascending towards upper velocity peak (left), pulsatile flow upper velocity peak (center left), mean pulsatile flow velocity descending towards lower velocity peak (center right), pulsatile flow lower velocity peak (right).

A comparison of arterial flow behavior of water before and after the gelatin-injection in the water-gelatin experiment is seen in Figure 11. This presents flow at different stages of a pulse wavelength shown in Figure 7. Except for minor velocity magnitude differences, the flow behavior in the artery with gelatin present, as seen in Figure 11 (middle and bottom) is nearly identical to flow behavior

without gelatin present (top). This is possibly due to the thixotropic properties of partially set gelatin where apparent viscosity decreases with increased shear stress over time, allowing it to demonstrate higher viscosity within the low flow environment within the aneurysm and lower viscosity within the periodically high shear environment of the artery [121]. Otherwise it is possible that gelatin in water takes on localized non-Newtonian behavior due to it having some characteristics of a suspension, due to gelatin fragments behaving as semi-solid particles in water, and some characteristics of a colloid, due to the mixture of water with the large collagen proteins of which the partially-set gelatin (relevantly, a colloidal gel) is composed [122,123]. The derivation of material properties for gelatin is however a broad field of study, and without rheological measurements for the gelatin applied specifically to this experiment, only broad speculations can be made on the topic of its behavior in flow [123].

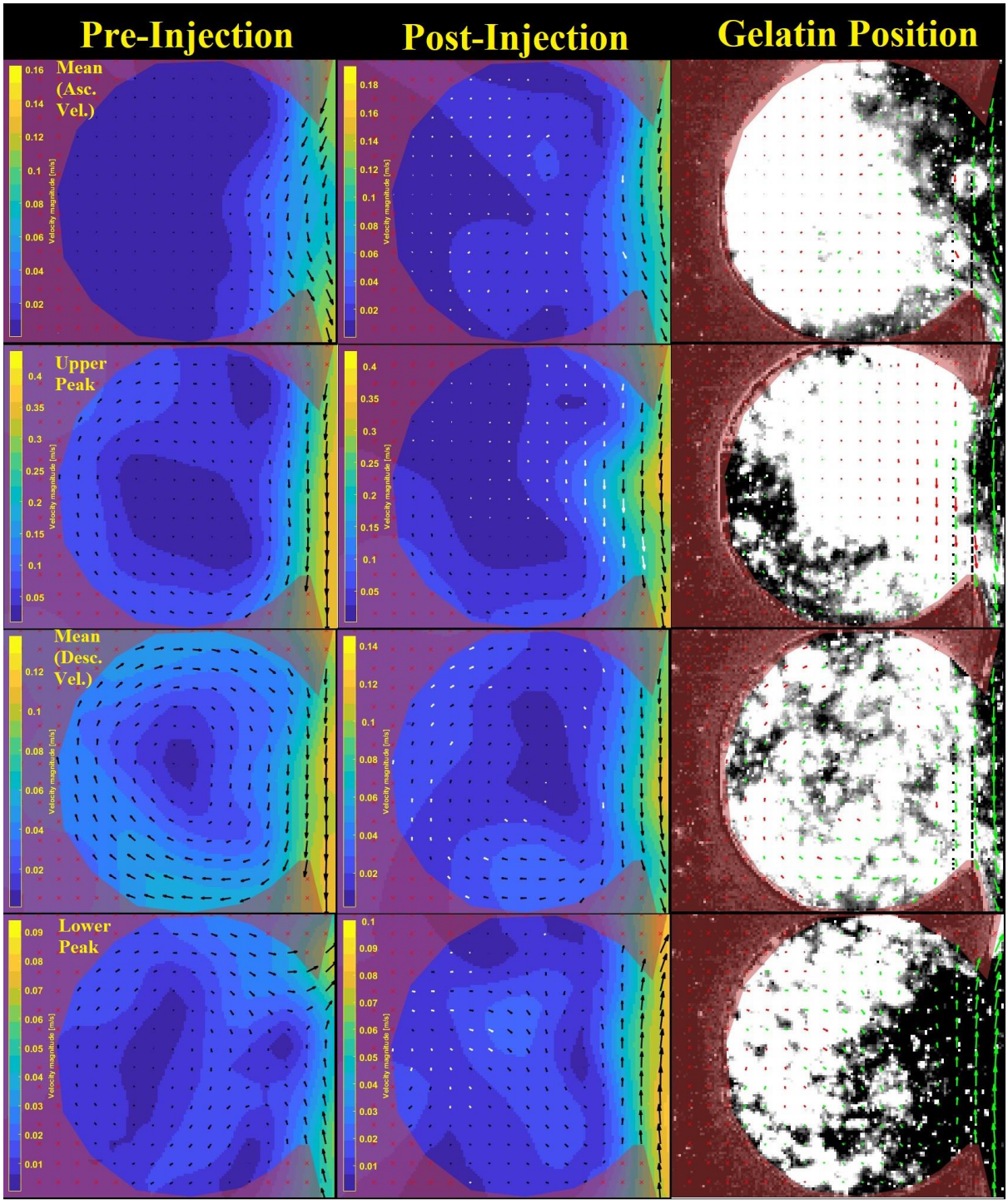

Figure 12: Water-gelatin experiment pre-injection aneurysmal flow behavior (left) comparison with post-injection aneurysmal flow behavior (middle) with images of relative gelatin position (right) at different times throughout a pulse wavelength shown in Figure 7; mean pulsatile flow velocity ascending towards upper velocity peak (top), pulsatile flow upper velocity peak (upper middle), mean pulsatile flow velocity descending towards lower velocity peak (lower middle), pulsatile flow lower velocity peak (bottom).

The aneurysmal flow behavior in the presence of gelatin is shown in Figure 12 (middle and right) and is presented with the corresponding flow behavior prior to the gelatin injection (left), at different stages in the pulsatile wavelength. Notably, because data-smoothing is applied for the derivation of

spatial parameters, vector interpolation is forced on areas that lack vectors. In the context of this experiment, this means that vectors that are discarded, either due to lack of robust correlation or image-based validation brightness filtering, are assigned vectors interpolated from the surrounding vectors. Vectors assigned this way appear in white in Figure 12, and their directions and magnitudes are less accurate. Consequently, the direction and magnitudes of white vectors shown in Figure 12 should be given less weight, and should rather be considered an indicator for high gelatin concentration in areas that they occupy.

Taking this factor into account, the valid vectors for the water-gelatin experiment with gelatin present, shown in Figure 12 (center), bear a strong resemblance to the vectors derived prior to the gelatin-injection shown in Figure 12 (left), apart from the flow behavior at the lower velocity peak (bottom). At the ascending mean velocity, shown in Figure 12 (upper middle), flow is similarly low within the aneurysm both pre- and post-injection. Both the upper velocity peak and descending mean velocity, shown in Figure 12 (upper middle & lower middle), demonstrate that the velocity at the bottom of the aneurysm is similar in profile between pre- and post-injection results, though a little lower in magnitude for the post-injection results, perhaps due to differences in viscosity between water and gelatin which can significantly exceed the viscosity of water based on concentration and application [8,124]. The lower velocity peak shown in Figure 12 (bottom), by contrast, demonstrates significantly different profiles between the pre- and post-injection results. Referencing the location of the concentrated gelatin fragments in Figure 10 (right), it is possible that this discrepancy is also due to differences in viscosity between the water and gelatin, which appears to have been squeezed into the top left of the aneurysm.

Overall, for flow fields where gelatin is present, Figure 10 demonstrates that areas including gelatin can be identified using preprocessing techniques. Figure 12 demonstrates that using the PIVlab settings described in section 4.1.1 enables identification of areas with large gelatin fragments and derivation of valid vectors surrounding these areas, even when particles in these areas are immersed in smaller fragments of gelatin.

This experimental outcome indicates that clot capture in PIV for the thrombin-fibrinogen flow experiment is feasible under similar conditions.

4.2. Thrombin-Fibrinogen Flow Experiment (Pre-Clot)

The thrombin-fibrinogen flow experiments utilize the same reagents and concentrations for the pre- and post-clot PIV image gathering. However, the presence (or lack thereof) of a clot makes a significant difference in the PIV analysis method required to adequately capture flow, where a FFT method is sufficient to capture flow before the clot has been formed, and an ensemble correlation method

tailored for this experiment is required once a clot has developed. As such, the thrombin-fibrinogen flow experiment is analyzed across two sections, where this section discusses methods and results of the thrombin-fibrinogen experiment prior to clotting.

4.2.1. Experiment-Specific Framework & PIV Settings

4.2.1.1. Materials, Physical Setup, and Procedure

Fluid Concentrations	Units
Fibrinogen-Saline Solution (0.9% NaCl)	0.25 mg / ml
Thrombin-Saline Solution (0.9% NaCl)	1 mg / ml

Table 10: Fluid concentrations for thrombin-fibrinogen experiment

The primary operating fluid for the thrombin-fibrinogen experiment is fibrinogen combined with 4l of 0.9% NaCl saline solution to make a concentration of 0.25 mg / ml shown in Table 10. The syringe is filled with thrombin combined with saline solution to make a concentration of 1 mg/ml and is attached to the syringe pump. Afterwards, the fibrinogen-saline inlet tank shown in Figure 4 is filled with 1.34 liters of the fibrinogen-saline solution, which is then seeded with density-neutral microparticles and briefly pumped into the system before each experiment to ensure that the flow phantom is filled entirely with fibrinogen-saline solution and no bubbles are present. Once the laser is switched on, the pump is activated again using the settings detailed in section 3.2.4.1. Following the first pulse, image acquisition is started, followed immediately by the syringe pump, which injects 1 ml of thrombin-saline solution into the aneurysm over 5 seconds. Image acquisition lasts for 3 minutes.

Camera Settings	Units
Image Pair Capture Frequency	20 Hz (20 image pairs / s)
Time Step	1700 µs
Exposure Time	3000 µs
Image Area	512 x 512 pixels

Table 11: Camera Settings for thrombin-fibrinogen experiment

The camera is positioned 30 cm away from the flow phantom for this experiment to maximize flow resolution within the aneurysm, and uses the settings shown in Table 11, where the time step and exposure time are optimized to capture particle transport with sufficient brightness and minimal blurring. The image area is optimized to capture clotting effects and camera memory usage.

4.2.1.2. Image Pre-Processing and FFT Settings

Image Pre-Processing Settings	Units
CLAHE window size	64 pixels
Intensity Capping	Enabled
Wiener Denoise Filter and Gaussian Low Pass window size	3 pixels
Mean Intensity Background Subtraction	Enabled

Table 12: Image pre-processing for thrombin-fibrinogen experiment

Select image preprocessing techniques described in section 3.2.3 are applied for the images derived in this experiment, and the values applied for each technique can be found in Table 12.

FFT Window Deformation Settings	Interrogation Area	Step Size
Pass 1	128 pixels	64 pixels
Pass 2	64 pixels	32 pixels
Pass 3	32 pixels	16 pixels
Sub-pixel estimator	2x3 point Gauss	
Auto-Correlation	Disabled	
Correlation robustness quality	Extreme	

Table 13: FFT Window Deformation Settings for fibrinogen-thrombin experiment

The image pre-processing setting's values have been selected in part based upon recommended default settings in PIVlab and the FFT pass window sizes shown in Table 13. The CLAHE window size is equivalent to the pass 1 step-size and pass 2 interrogation area, such that each interrogation area for the 2nd pass is optimized independently. This value is unaltered from the default value provided in PIVlab to optimize intensities for accurate particle identification for high flow rates. The Wiener denoise filter and Gaussian low pass window size of 3 pixels is selected to eliminate background noise and is based upon image resolution. Mean intensity background subtraction is applied to remove background noise that is consistent across all images, and intensity capping is enabled to assign the same intensity to all flow field particles.

The FFT pass window sizes shown in Table 13 are selected based primarily upon the maximum particle displacement and particle count. The large displacements that occur at high flow rates, coupled with the interference of the fibrin clots that form on particle seeds prior to thrombin injection necessitates the use of the interrogation area of 128 pixels for pass 1. The subsequent pass 2 and pass 3

interrogation areas of 64 and 32 pixels, respectively, are selected to capture finer flow features, particularly at low flow rates.

2x3 Gauss subpixel estimation is selected, with auto-correlation disabled to reduce detection of invalid vectors from background noise caused by clotting [113]. The highest and most computationally expensive setting for correlation robustness quality in PIVlab is selected to ensure further accuracy.

4.2.1.3. Image Calibration

Image Calibration Settings	Units
Reference length [px]	422.74 pixels
Real distance of reference length [mm]	12.8 mm
Time Step	1.7 ms
Pixel to distance conversion	1 pixel = 3e-5 m
Pixel/frame to velocity conversion	1 pixel/frame = 0.01815 m/s

Table 14: Image calibration settings for thrombin-fibrinogen experiment

The image calibration settings applied to determine the velocity values for vectors derived from the FFT cross-correlation are shown in Table 14 and are derived from the 12.8 mm diameter of the aneurysm of the flow phantom shown in Figure 3, which is measured to be 422.74 pixels in length for the PIV derived images. When the pixel to distance conversion is divided by the time step between image pairs of 1.7 ms, the pixel/frame of each vector for an image pair can be converted to velocity, where 1 pixel/frame is equivalent to 0.01815 m/s.

4.2.2. Pre-Clot Flow Analysis

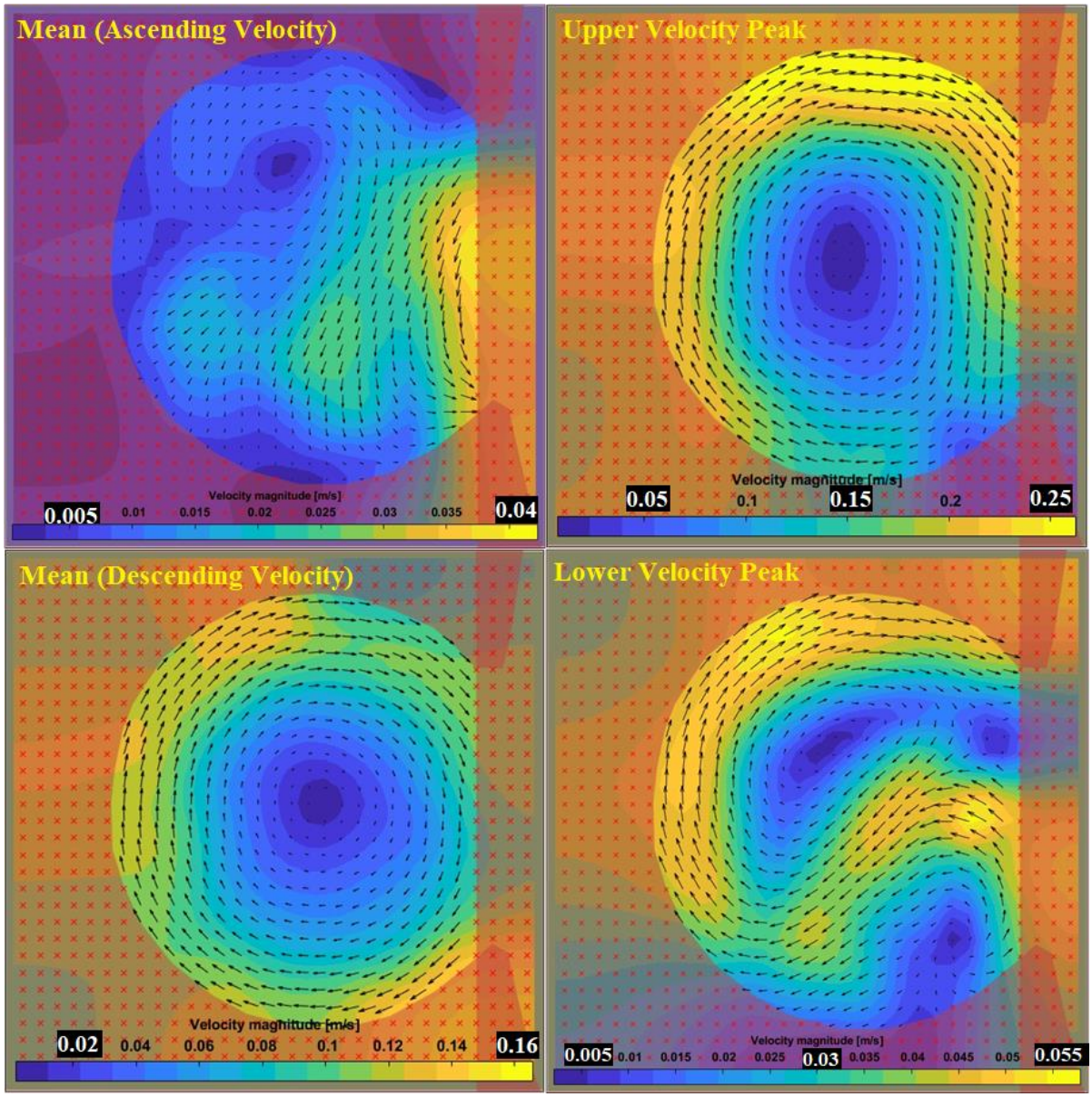

Figure 13: Thrombin-fibrinogen experiment pre-clot aneurysmal pulsatile flow behavior at different times throughout a pulse wavelength shown in Figure 7; mean pulsatile flow velocity ascending towards upper velocity peak (top left), pulsatile flow upper velocity peak (top right), mean pulsatile flow velocity descending towards lower velocity peak (bottom left), pulsatile flow lower velocity peak (bottom right).

The flow behavior within the aneurysm at different times during a pulsatile wavelength for the thrombin-fibrinogen flow experiment prior to the formation of a detectable clot is shown in Figure 13, specifically at the upper and lower velocity peaks as well as the mean velocities between these two peaks. Flow within the aneurysm is lowest during the ascending mean velocity, shown in Figure 13 (top left), and the lower pulsatile velocity peak also shown in Figure 13 (bottom right). This flow

behavior is similar to that seen in Figure 9 for the water-gelatin flow experiment described in section 4.1, where both cases demonstrate similar flow distributions and magnitudes for corresponding flow behaviors.

The flow distribution of the upper velocity peak and descending mean velocity, shown in Figure 13 (top right & bottom left), is well distributed along most of the aneurysmal wall, where the highest flow of the upper velocity peak is distributed towards the top and left side of the aneurysm with comparatively low flow at the bottom of the aneurysm, and the highest flow of the mean is distributed towards the bottom and right side of the aneurysm, with comparatively low flow at the top of the aneurysm. The magnitudes of corresponding flow behaviors in the water-gelatin experiment, shown in Figure 9, are significantly lower in magnitude, indicating a difference in viscous behavior between the operating fluids of the two experiments.

Flow in the channel is not measured for the thrombin-fibrinogen experiments, however the fluid properties of thrombin-saline solution are considered virtually identical to that of water with consideration towards Archimedes principle as it relates to the mass of reagents within the solution. It is therefore assumed that α, Re, and De are identical to that described in section 4.1.3. for the pre-injection water-gelatin experiment.

4.3. Thrombin-Fibrinogen Flow Experiment (Clot Capture)

This section describes the post-clot fibrinogen-thrombin experiment procedure, ensemble correlation methodology, and an analysis of flow vectors derived from the PIV images taken during clot formation.

4.3.1. Procedure

Clot capture for the thrombin-fibrinogen flow experiment involves identical materials, physical setup, procedure, preprocessing, and postprocessing to the same pre-clot experiment with the exception that thrombin-saline solution is injected into the system twice at the amounts described in section 4.2.1.1, where the first injection takes place approximately 2 minutes prior to the activation of the camera and laser, and the second injection takes place just after the activation of the camera and laser. The pump is activated for a short period of time during the first injection at a high pulse frequency to remove bubbles from the system after the injection.

4.3.2. Ensemble Correlation Methodology and Settings

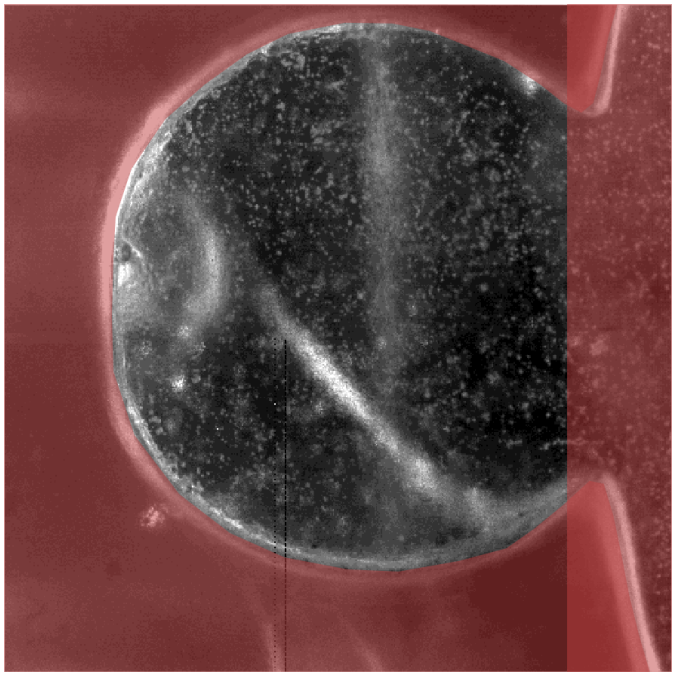

Figure 14: Raw PIV image for thrombin-fibrinogen flow experiment with strand-like clot attached to the bottom of the aneurysm

Figure 14 shows the resulting fibrin clot which is bound to the bottom surface of the flow phantom aneurysm. Fibrin is a surfactant, and through adsorption are able to quickly bind to foreign surfaces [125]. The FFT method employed for pre-clot images is insufficient for capturing flow once a clot has been formed due to the interference that clotting against the channel walls has on particle detection. Instead, an ensemble correlation method is employed to analyze flow behaviors at select times in the duration of the flow pulse to provide a more robust understanding of flow at different stages of a pulse. This is enabled in part by the nature of fibrin formation in this experiment, where the clot takes the form of a long strand shown in Figure 14. This strand shifts in position based on the surrounding flow and thereby has diminished impact on the surrounding flow features by comparison to a stationary clot.

An ensemble correlation method is applied to sets of 10 image pairs for each recorded time in a pulse to ensure that a complete flow field is captured. Using the pump settings described in section 3.2.4.1, the wavelength of each pulse is 1.55s. Accounting for this when considering the applied image pair capture frequency described in Table 11 means that the flow for each wavelength is captured across 31 images. Therefore, an ensemble correlation was performed for 31 sets of 10 image pairs to capture the average flow for each 0.05s of the 1.55s pulsatile wavelength. This is possible due to the dynamic

position of the clot, which is strand-like in nature as shown in Figure 14. Window deformation settings are otherwise identical to that applied for the FFT correlation applied to pre-clot images as detailed in Table 13.

4.3.3. Clot and Flow Analysis

4.3.3.1. Exploring the Effects of Periodic Movement of Clot on Valid Vector Detection

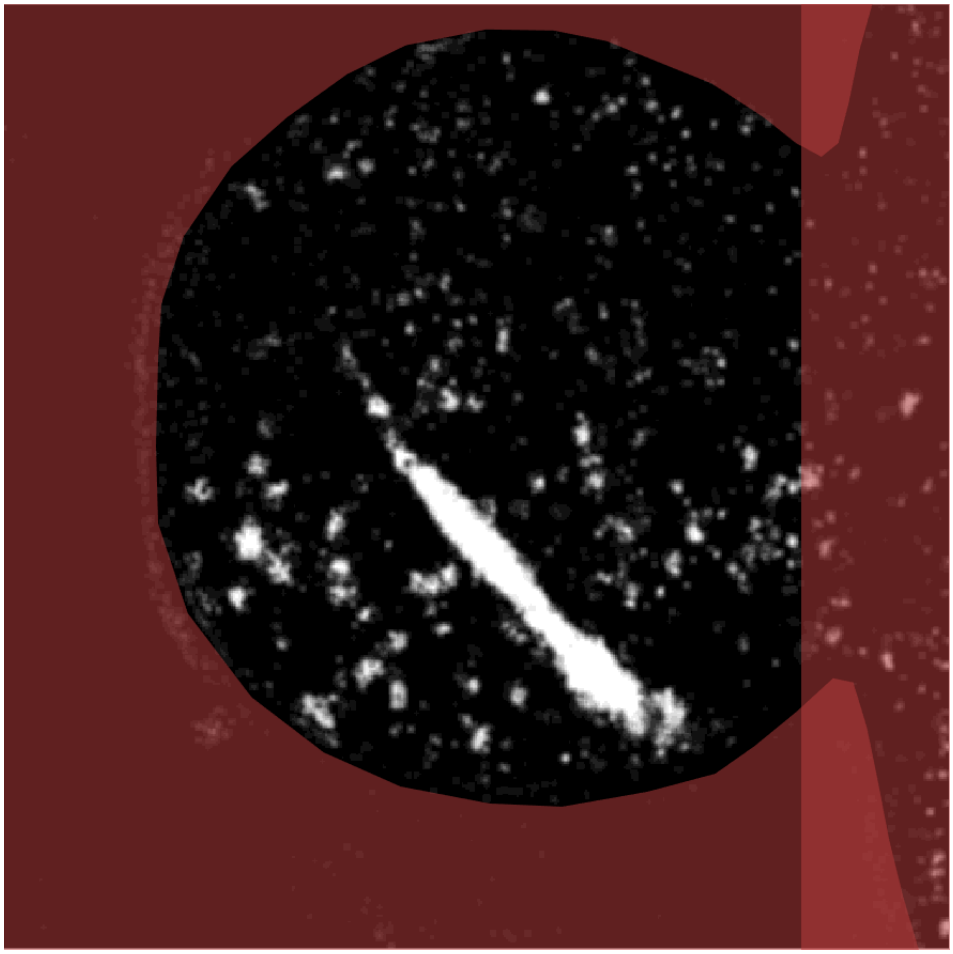

Figure 15: Pre-processed PIV image for thrombin-fibrinogen flow experiment with strand-like clot attached to the bottom of the aneurysm

Owing to the formed clot appearing as a high-intensity non-stationary object that has the potential to interfere with the calculation of valid vectors for nearby particle displacements, and that no feasible pre-processing methods exist that can suitably reduce the intensity of this structure relative to surrounding particles, an analysis of its impact on the derived flow vector maps is necessary. To accomplish this, the images belonging to each ensemble correlation are analyzed with and without the inclusion of a mask placed over the fibrin clot where it intersects with the laser sheet. For the masked case, this is determined after preprocessing for each individual image pair by qualitatively identifying bright areas in the shape of the fibrin strand clot, like that shown in Figure 15, and masking

it. This is repeated for each image pair of an ensemble, where the clot mask for each image pair as part of the same ensemble is aggregated together, and the sum aggregate clot mask is then applied to all image pairs prior to performing the ensemble correlation analysis.

4.3.3.2. *Mid-Clot Vector Flow Field Results and Analysis Including the Effects of Strand-Like Clot on Valid Vector Detection*

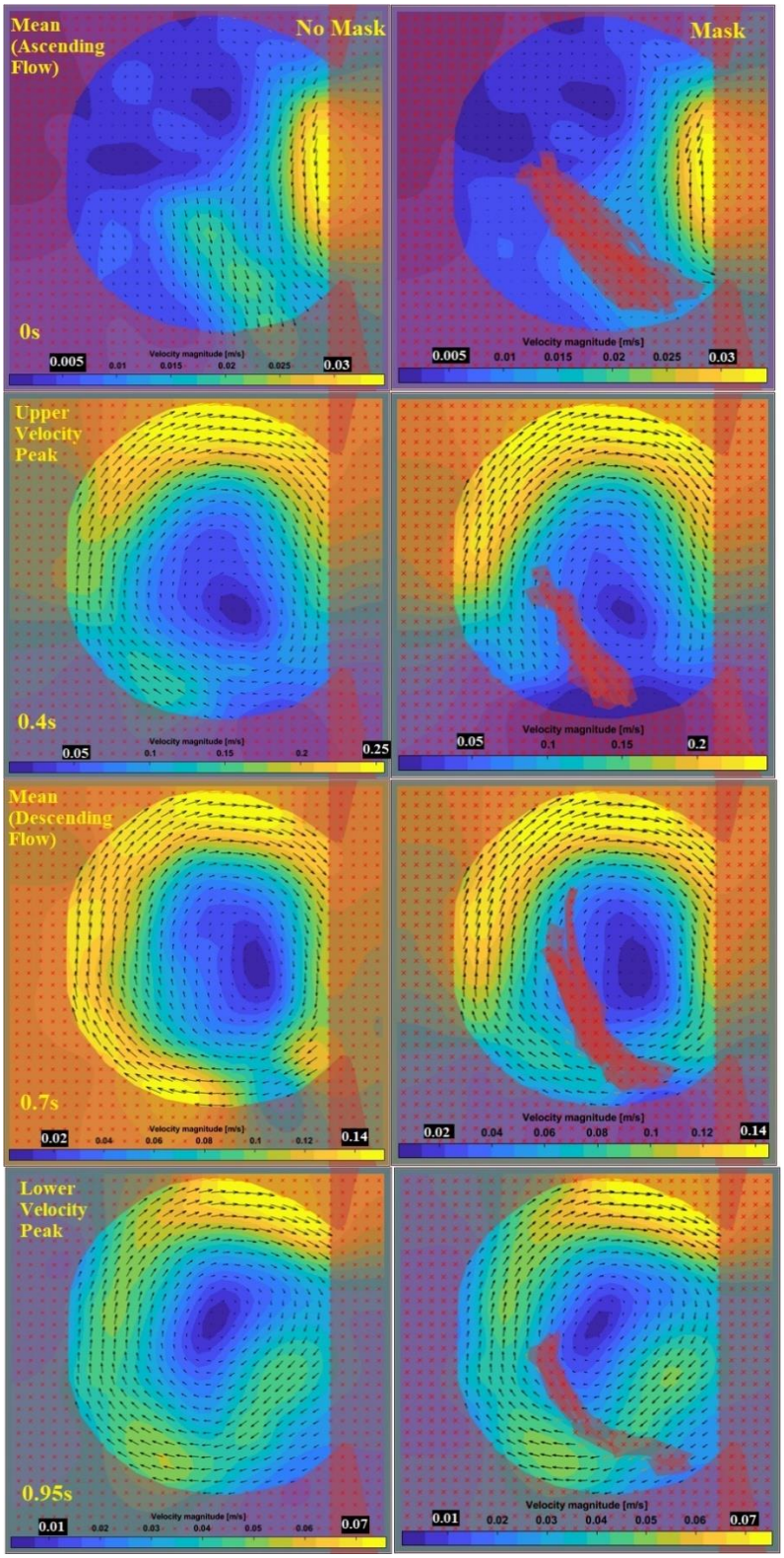

Figure 16: Fibrinogen-thrombin experiment post-clot ensemble correlation results excluding (left) and including (right) clot masking at different times throughout a pulse wavelength shown in Figure 7; mean pulsatile flow velocity ascending towards upper velocity peak (top), pulsatile flow upper velocity peak (upper middle), mean pulsatile flow velocity descending towards lower velocity peak (lower middle), pulsatile flow lower velocity peak (bottom).

Figure 16 demonstrates a comparison of the derived post-clot flow field of the thrombin-fibrinogen flow comparison with and without the inclusion of the clot masking method described in section 4.3.3.1. The flow velocity magnitudes and flow distribution of the masked and unmasked flow fields bear strong resemblance to one another with some exceptions. The masking of the clot appears to eliminate the derivation of nearby flow vectors for the upper velocity peak (upper-middle) and descending mean flow (lower-middle) as seen in Figure 16, where flow in the bottom of the aneurysm is significantly lower when a mask is present. At the ascending mean flow (top), downward flow vectors of approximately 0.02 m/s are eliminated in the masked case specifically in the location of the fibrin strand, indicating that vectors in this location are mapped by the cross-correlation algorithm based upon the intensity of the fibrin strand. The vectors in the unmasked case (left) indicate that during the ascending mean pulsatile flow (top), the fibrin strand is being pulled downwards.

The unmasked case vector maps (left) may be valid with consideration towards the change in position of the clot between the ascending mean (top) and upper velocity peak (upper-middle) with reference to the general location of the clot indicated by the masked regions (right) in Figure 16, where the average position of the clot shifts downwards by the upper velocity peak. With consideration that an ‘extreme’ robustness correlation is applied as described in section 3.2.2, wherein the cross-correlation algorithm repeats five times per frame analysis with slightly shifted interrogation windows each time, and eliminates any vector that is not produced in all five frame analyses; it is plausible that the cross-correlation algorithm is correctly identifying the movement of the strand-like fibrin clot [113,117].

Looking at the rest of the pulse (left upper-middle, …, bottom) for the unmasked case in Figure 16, this rationale potentially provides an explanation for the areas at the bottom of the aneurysm wall that have very low velocity regions relative to surrounding high velocity vectors. With reference to the masked case (right), these low flow areas correspond with the location of the strand-like fibrin clot. This indicates that the ‘extreme’ robustness algorithm either eliminates vectors in these regions due the presence of the fibrin clot, or these regions are demonstrating low velocity because they are representative of the movement of the fibrin clot. Cross-referencing this rationale with the fact that vectors farther away from the aneurysm wall in the unmasked case (left upper-middle, …, bottom) are representative of surrounding flow patterns even if they are located in regions that are occupied by the clot as indicated by the masked case (right), it is possible that the unmasked case vectors are representative of the movement of the strand-like clot.

4.3.3.3. Pre- and Post-Clot Flow Comparison

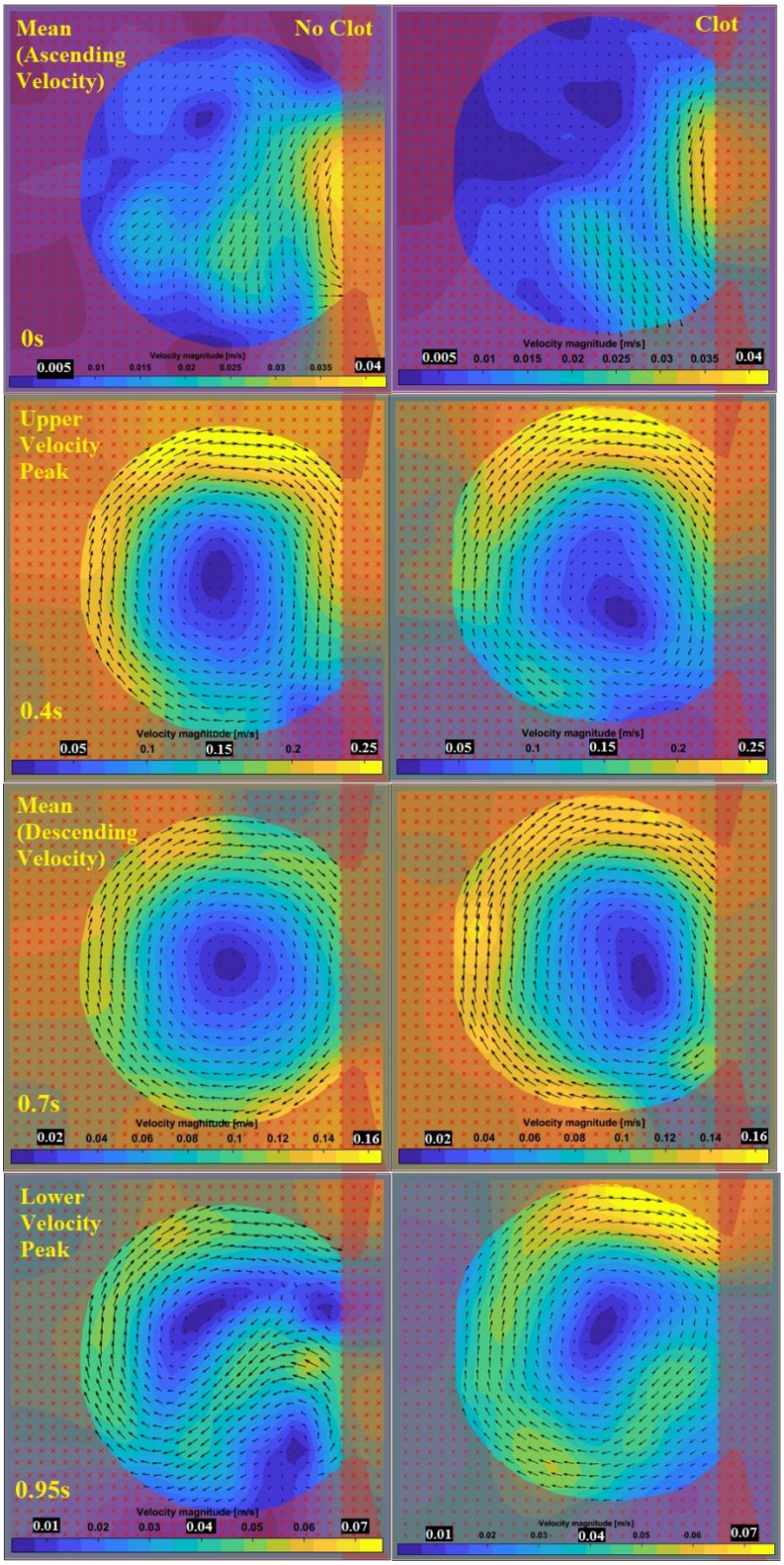

Figure 17: Fibrinogen-thrombin experiment pre-clot FFT results (left) and post-clot ensemble correlation results (right) at different times throughout a pulse wavelength shown in Figure 7; mean pulsatile flow velocity ascending towards upper velocity peak (top), pulsatile flow upper velocity peak (upper middle), mean pulsatile flow velocity descending towards lower velocity peak (lower middle), pulsatile flow lower velocity peak (bottom).

When further cross-referencing the derived flow-field of the unmasked post-clot case with the flow field derived prior to clot formation using FFT window deformation analysis as shown in Figure 17, it is apparent that the flow field derived with the presence of the fibrin clot strongly resembles the flow field prior to clot formation with small exceptions; all of which are attributable to the presence of the fibrin clot strand. These exceptions, shown on the right of Figure 17, include the bottom of the aneurysm at 0.4-0.95s, where there is a pocket of low flow at the location of fibrin-strand clot attachment to the aneurysm, the center of recirculation at 0.4-0.95s that is shifted slightly to the right and downwards, and at the lower velocity peak which lacks the second recirculation zone at the bottom of the aneurysm nearby the location of fibrin-strand clot attachment to the aneurysm.

Broadly, the flow magnitudes and distribution at different stages of the pulse wavelength are nearly the same in both cases, indicating that the fibrin-clot strand at this stage of clotting has minimal effect on the flow field. The ensemble correlation methodology applied for post-clot flow analysis demonstrates effectiveness in capturing flow despite high levels of background noise caused by fibrin formation on the flow channel faces.

Cross-referencing the comparison of the pre-and post-clot flow fields shown in Figure 17 with the comparison of post-clot flow-fields with and without clot masking shown in Figure 16, clot-masking removes vectors that otherwise agree with the pre-clot flow field, which is particularly prevalent at the upper velocity peak and mean velocity of the descending pulse.

When further considering in that the flow vectors derived at the location of the fibrin clot at the ascending mean flow in Figure 16 are of similar magnitude to similarly positioned vectors in the corresponding pre-clot case shown in Figure 17, there is indication that the vectors derived from the intensity of the fibrin strand clot are capturing its average movement.

4.4. Comparison of Thrombin-Fibrinogen Flow Experiment Results and to Flow Experiments in Literature

The framework of the fibrinogen-thrombin flow experiments described and analyzed in this section is built on work from Hume & Tshimanga et al., where flow within an idealized cerebral aneurysm vessel is analyzed using PIV to validate a pulsatile model of direct thrombosis in cerebral aneurysms, and the clotting flow experiments designed by Jimoh-Taiwo et al. and Ngoepe et al., that qualitatively measure clot formation using similar reagents in a straight channel under pulsatile conditions and an idealized cerebral aneurysm vessel under steady flow conditions, respectively [71,73,75]. These experiments are designed as validation tools, but individually do not accommodate the analysis of fibrin formation under physiological flow conditions simultaneously to measurement of the flow field.

The thrombin-fibrinogen PIV-based flow experiment, by comparison to these experiments, combines flow visualization and clotting into a single flow experiment with physiological flow conditions, such that it can be used to simultaneously validate clot formation and flow for the CFD thrombosis model for each individual timestep, which each directly correspond to a PIV image pair taken at an identical time. This has resulted in a novel and comprehensive validation method for macroscopic clotting in a flowing environment built upon the in-vitro flow experiments by Ngoepe et al., Hume & Tshimanga et al., and Jimoh Taiwo et al. [71,73,75].

The fibrinogen-thrombin experiment presented in sections 4.2-4.3 combines many of the features of the experiments described in addition to that of Gester et al. and Clauser et al., and further allows the measurement of flow simultaneously to clot development. The clot grown in the fibrinogen-thrombin experiment, however, differs greatly in structure from the clots grown in these prior flow studies, wherein the clots are relatively stationary and concentrated, as compared to the strand-like fibrin clot formed in this study which changes position subject to local flow conditions as shown in Figure 16 [68,72,73,75].

Studies by Campbell et al. and Gersch et al. address the strong influence of flow effects on the structure of fibrin formation, demonstrating that fibrin fibers align in the direction of flow, and that this alignment increases dramatically with increase in shear [126,127]. Fibrin is also well documented as having non-linear elasticity and high extensibility. A fibrin clot can extend 2.5-3.3 times their original length before rupturing [128–132]. A variety of factors likely contribute to this discrepancy [126,131]. These include the use of a pulsatile waveform with relatively high periodic velocities and the comparatively lower concentration of fibrinogen in saline than in other studies [126]. High periodic velocities associated with physiological flow patterns have been associated with loss of thrombin concentration within the aneurysm according to Hume & Tshimanga et al., and the flow velocities applied by the pulse in this study are significantly higher than similar in-vitro flow studies apart from Clauser et al. and Gersch et al., wherein a physiologically representative clot was not formed [68,71–73,75]. Coupled with the relative sparseness of fibrinogen in saline by comparison to studies Jimoh-Taiwo et al. and Ngoepe et al., the tendency of thick fibrin strands to form in parallel under higher flow conditions according to Campbell et al., and the high elasticity and extensibility of fibrin as a polymer, the difference in clot development from similar studies is logically explicable [68,71–73,75,126,128–132]. Further, the *in vitro* experiment of high-shear thrombi-formation by van Rooij et al. demonstrates ‘mountains-and-valleys-like’ platelet aggregates for under high shear, which appear as strand-like aggregates outward from the vessel walls, perhaps indicating similar behavior [133].

There are, however, many limitations for the thrombin-fibrinogen experiment as a validation tool for computational models of thrombosis. Despite the application of physiological materials, the idealized nature of the experiment means it is only crudely representative of physiological flow and clotting therein. Furthermore, due to the necessity of a square channel to circumvent refractive-index-matching between the PIV fluid and the flow phantom, analysis of flow in more complicated patient-derived arterial vessels is not possible for the thrombin-fibrinogen experiment in its current form.

From an operational perspective there are many limitations as well, including seeding particles vulnerable to fibrin aggregation, fibrin formation against the vessel wall obscuring particles within the channel, limited fibrinogen concentration in the operating fluid, the necessity of a square channel to limit light refraction, a PIV setup that is not optimized to operate for long periods of time to capture the entire clot formation, and internal light refraction caused by the introduction of a clot within the flow field. These limitations were difficult to account for ahead of this study. Outside of inference from some medical studies of clots, there are few similar flow experiment studies that can be referenced for guidance.

However, since the operational limitations have been made apparent with the results of the fibrinogen-thrombin flow experiment, they should be relatively trivial to correct for future studies and recommendations for such changes are as follows:

- To prevent embolization of seeding particles during the experiment, either switch seeding particles to a material option that does not promote fibrin aggregation, or only mix fibrinogen-saline solution with particles immediately before conducting the experiment.
- Develop a method to distribute seeding particles more effectively in the fibrinogen-saline solution, since they tend to float.
- Coat channel surfaces perpendicular to the camera with either an anti-adhesive surface or serum albumin to prevent clots and biofilms from forming over them that may prevent accurate capture of flow.
- Increase fibrinogen content of fibrinogen-saline solution to be more consistent with blood to induce faster and more significant fibrin generation upon contact with injected thrombin within the aneurysm.
- Change the location of the injection port of flow phantom because unintended light scattering illuminates it and causes background noise that interferes with particle detection during PIV analysis. This might be achieved by orienting the injection port to the top of the aneurysm, although this was attempted for this study, and reorientation of the flow phantom sideways relative to the laser head resulted in uneven lighting within the artery channel, potentially

caused by compounding light-refraction from the laser lightsheet, which can pass through up to four solid-liquid interfaces within the flow phantom in this configuration.

- Change camera resolution to ideally capture flow in the artery as well as the aneurysm, which was not possible for this experiment due to memory limitations.
- Should it be feasible to acquire 5l of human plasma, consider using human-plasma derived PIV-Fluid in place of the fibrinogen-saline solution for even more physiologically representative flow and clotting behavior such as that developed in work by Clauser et al. [72].
- Consider switch to bovine model to simplify acquisition of large volumes of plasma and blood-derived reagents

4.5. Conclusion and Data Quantities

The PIV-based thrombin-fibrinogen clotting flow experiment approach builds and innovates upon previous in-vitro flow experiments and provides a novel and comprehensive validation method for macroscopic clotting in a flowing environment. By integrating flow visualization with clotting under a physiological flow profile, this setup allows for validation of clot formation and flow for the CFD thrombosis model at each individual timestep, which correspond directly to PIV image pairs.

This experiment results in a strand-like fibrin clot that changes position with local flow conditions, contrasting with the relatively stationary and concentrated clots observed in previous studies. This result appears to agree with the results of microscopic studies measuring fibrin fiber alignment under high shear, which indicates that high flow rates may have a significant effect upon fibrin clot macrostructure as well. Given the lack of similar macrovascular clotting experiments and macroscale fibrin clot structure studies, this highlights an area that may benefit from further research.

While the idealized nature of this experiment leaves it only crudely representative of an in-vivo environment, its reductionist design allows for validation of flow and acute thrombosis clot development predicted by the presented thrombosis model that cannot be achieved by other existing experiments. With refinement to the PIV-based thrombin-fibrinogen clotting flow experiment design, this formula presents a comprehensive validation method for direct thrombosis models that is a crucial stepping-stone to achieving their application in clinical environments as sorely needed patient intervention planning tools.

Flow Behavior and location	Pre-Injection	Post-Injection
Water-Gelatin Experiment Max Velocity		
Arterial Mean (Ascending) Velocity	0.16 m/s	0.19 m/s
Arterial Upper Velocity Peak	0.45 m/s	0.425 m/s
Arterial Mean (Descending) Velocity	0.14 m/s	0.14 m/s
Arterial Lower Velocity Peak	0.09 m/s	0.1 m/s
Aneurysmal Mean (Ascending) Velocity	0.09 m/s	0.09 m/s
Aneurysmal Upper Velocity Peak	0.25 m/s	0.275 m/s
Aneurysmal Mean (Descending) Velocity	0.07 m/s	0.09 m/s
Aneurysmal Lower Velocity Peak	0.045 m/s	0.055 m/s
Thrombin-Fibrinogen Experiment Max Velocity		
Aneurysmal Mean (Ascending) Velocity	0.04 m/s	0.035 m/s
Aneurysmal Upper Velocity Peak	0.25 m/s	0.25 m/s
Aneurysmal Mean (Descending) Velocity	0.16 m/s	0.15 m/s
Aneurysmal Lower Velocity Peak	0.0575 m/s	0.075 m/s
Thrombin-Fibrinogen Clot Subtraction Max Velocity		
Aneurysmal Mean (Ascending) Velocity	0.035 m/s	
Aneurysmal Upper Velocity Peak	0.25 m/s	
Aneurysmal Mean (Descending) Velocity	0.14 m/s	
Aneurysmal Lower Velocity Peak	0.075 m/s	

Dimensionless Quantities Common Across Experiments				
α = 12.39	Mean (Asc)	Upper Peak	Mean (Desc)	Lower Peak
De	19.1	53.74	16.71	10.75
Re	1016	2857.5	889	571.5

Table 15: Data quantities for PIV-based flow experiments

5. Validation Simulation

This chapter addresses the methods, results, and discussion specific to the experimental validation of the computational thrombosis model of cerebral aneurysms via a validation simulation that mimics the flow field, flow properties and clotting reagents within the fibrinogen-thrombin flow experiment discussed in chapter 4.

Specifically, this chapter includes:

1. The methodology of the validation simulation.
2. A comparison of computational flow results with no-slip and free-slip wall boundary conditions to the results of the pre-clot fibrinogen-thrombin experiment detailed in section 4.2.
3. A comparison of computational clot results to the results of the post-clot fibrinogen-thrombin experiment detailed in section 4.3.
4. A comparison of the computational results to similar models in literature.

5.1. Validation Simulation Specific Methodology

The computational framework specific to the validation simulation is presented. This expands on the computational framework described in chapter 3.1. This specifically includes relevant features of the idealized PIV aneurysm geometry and mesh, the specific boundary conditions applied to the validation simulation, and a discussion of wall boundary theory that includes and provides necessary context for a grid independence study.

5.1.1. Idealized PIV Aneurysm Geometry

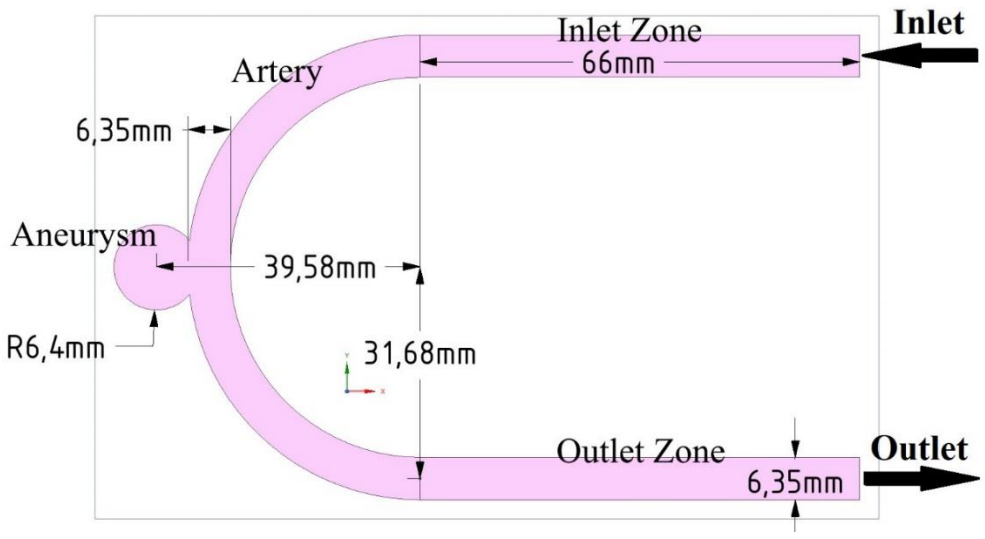

Figure 18: Front view of PIV flow phantom channel dimensions and features

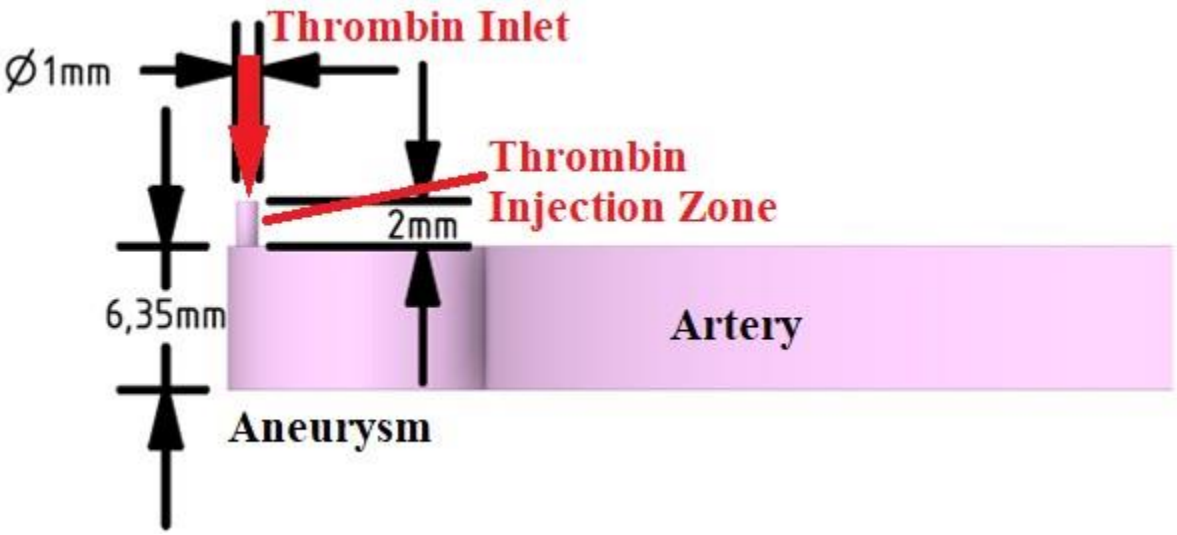

Figure 19: Side view PIV flow phantom channel dimensions (inclusive of thrombin injection zone)

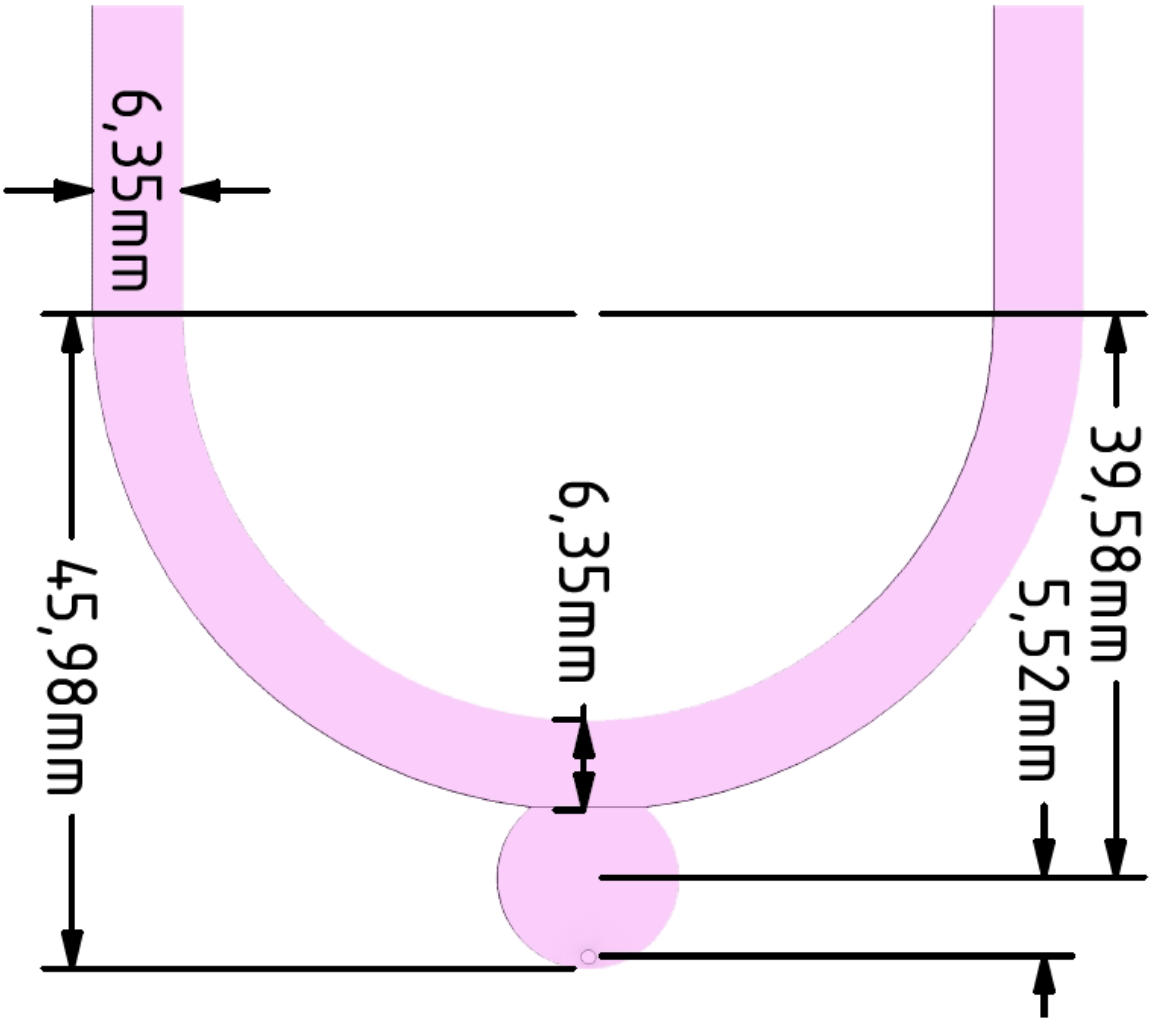

Figure 20: Rear view PIV flow phantom channel dimensions (inclusive of relative position of injection port)

A 3D simulation geometry with the flow phantom's dimensions is used for the validation simulation and is illustrated in Figure 18-Figure 20. This mimics the flow boundaries of the thrombin-fibrinogen flow experiment, described in sections 4.2-4.3. The geometry consists of four fluid zones, including the inlet zone, outlet zone and artery shown in Figure 18, and thrombin injection zone shown in Figure 19-Figure 20. As shown in Figure 18, an inlet boundary condition is set at the inlet zone and an outlet boundary condition is set at the outlet zone. As shown in Figure 19, an inlet boundary condition is set at the thrombin injection zone. The aneurysm shown in Figure 18-Figure 20 is part of the artery fluid zone. Fluid properties are consistent across these four fluid boundaries, with the exception of the Michaelis-Menten model and porosity-based clotting model described in sections 3.1.4-3.1.5 which only activate in the artery and aneurysm in order to reduce the potential of convergence errors from clots forming nearby inlet and outlet flow boundaries as described previously in section 3.1.6.

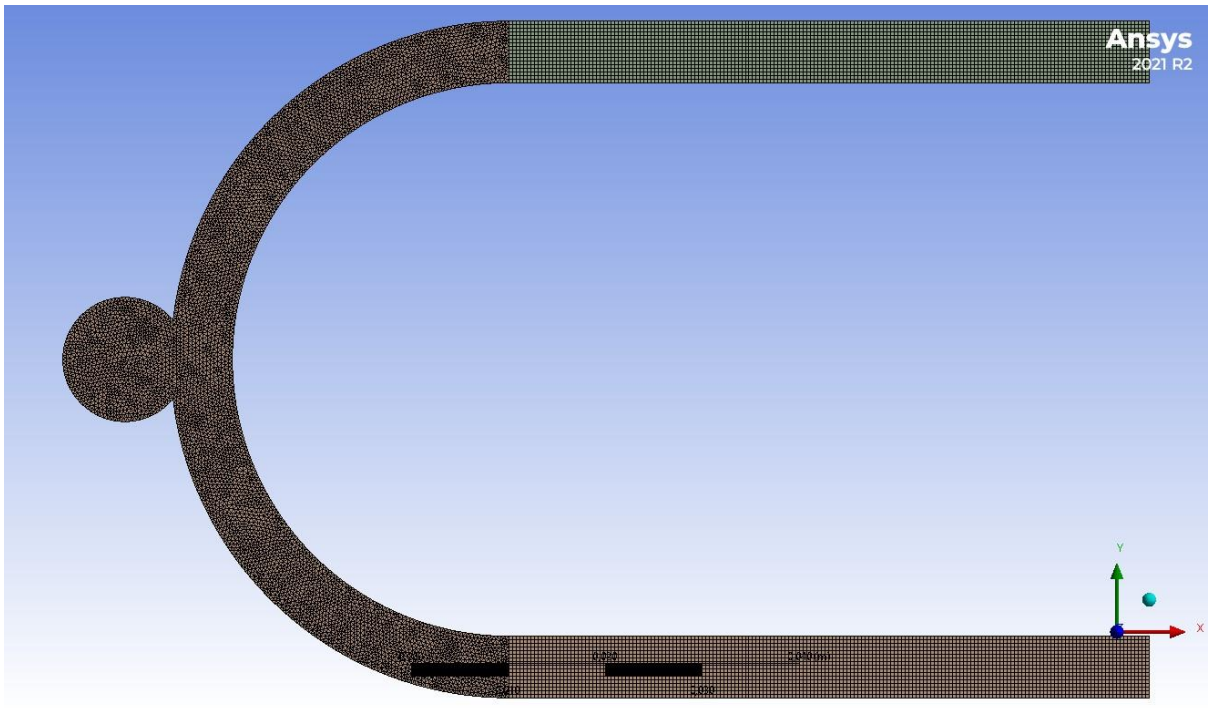

Figure 21: Front view of PIV simulation mesh

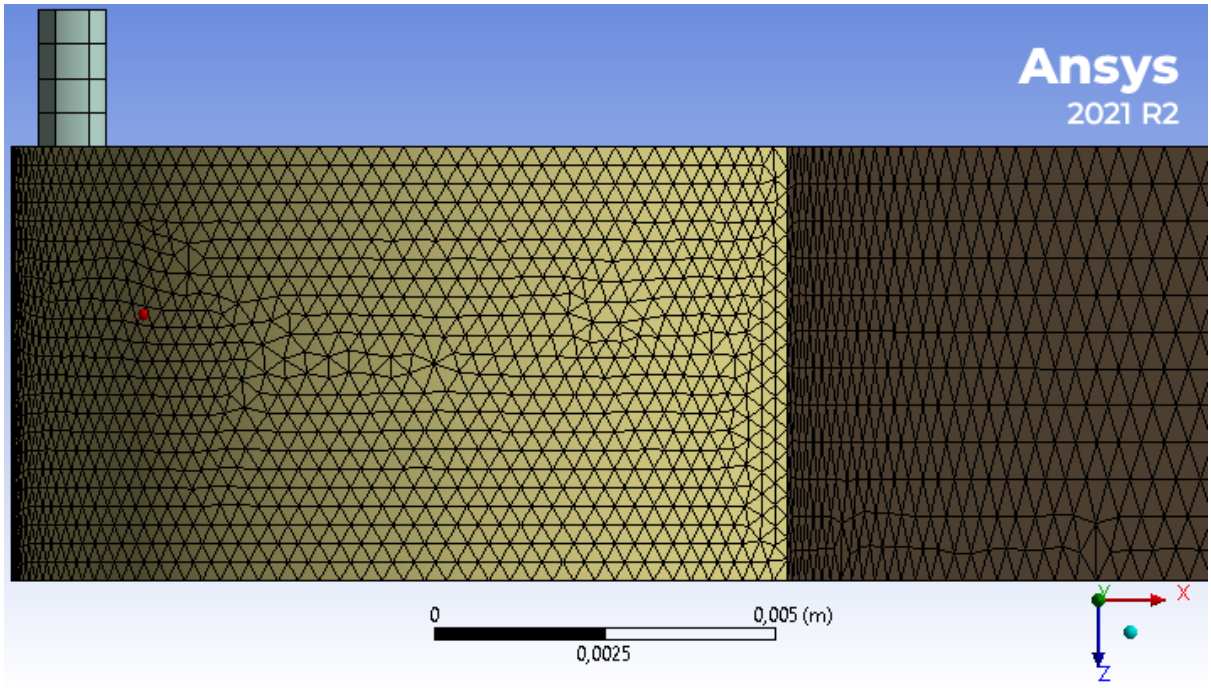

Figure 22: Side view of PIV simulation mesh

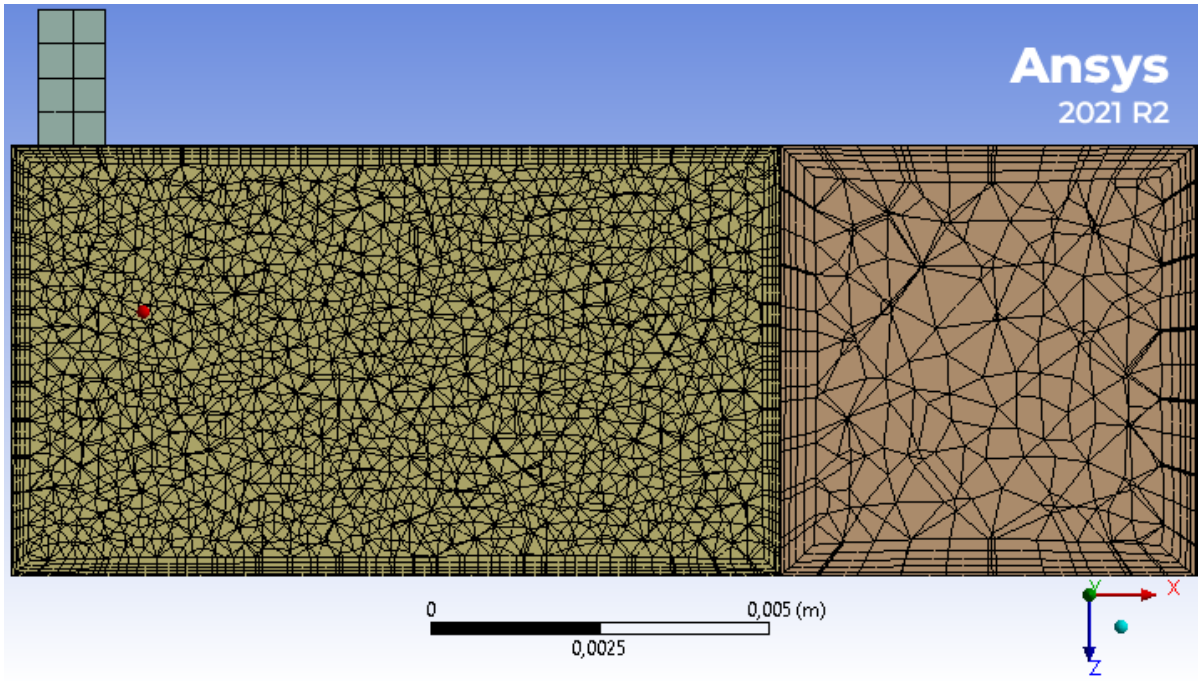

Figure 23: PIV simulation mesh inflation layers

The mesh shown in Figure 21 and Figure 22 is tailored to be computationally efficient in the inlet zone, outlet zone and thrombin injection zone, and to provide higher resolution results in the aneurysm and artery. As such the thrombin inlet zone, inlet zone and outlet zone are composed of quadrilaterals, shown in Figure 22, and the rest of the flow field is composed of tetrahedrons. An inflation layer of 5 cells shown in Figure 23 is added to the walls of the inlet zone, outlet zone, artery and aneurysm shown

in Figure 18 to reduce skewness in the geometry and enhance the user-defined scalar residual robustness within the ANSYS Fluent framework. This inflation layer uses a smooth transition algorithm based on the global element size producing a total boundary layer of approximately 0.0006 m in the artery zone and 0.0003 in the aneurysm.

	Orthogonal Quality	Skewness
Minimum	0.30053	2.6533e-4
Maximum	0.99999	0.69947
Average	0.80909	0.21296
Standard Deviation	0.10771	0.11073

Table 16: Quality metrics for PIV simulation mesh

This results in a mesh with a sum of 507857 elements and 1309359 nodes as shown in Figure 21, where the orthogonal quality and skewness metrics can be viewed on Table 16.

Details of the grid-independence study used to arrive at this mesh is provided later in section 5.1.3.2.

5.1.2. Boundary Conditions

The boundary conditions specific to the validation experiment are detailed in this section. These broadly include velocity inlet and pressure outlet pulsatile flow functions derived from velocity-data of the water-gelatin experiment of the chapter 4 flow experiments shown in Figure 7, the thrombin inlet whose location is shown in Figure 19, and the wall boundary conditions applied at all solid surfaces for which there is an accompanying discussion of theory and details for the grid independence study.

5.1.2.1. PIV-Derived Velocity Inlet and Pressure Outlet Pulsatile Flow Functions

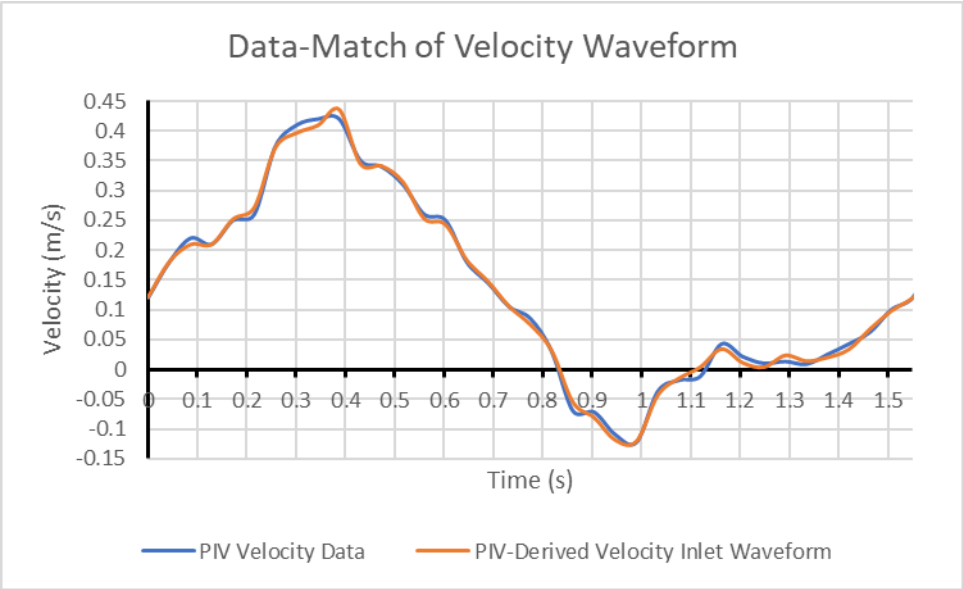

Figure 24: PIV velocity data (blue) and PIV-derived velocity inlet waveform (orange)

$$v(t) = a_1\sin(b_1 t + c_1) + a_2\sin(b_2 t + c_2) + \cdots a_8\sin(b_8 t + c_8) \quad (45)$$

Sinusoid number	a	b	c
1	0.2333	2.389	0.02324
2	0.2313	4.666	0.3514
3	0.02571	10.5	-4.156
4	0.03799	15.7	2.37
5	0.01468	24.65	0.1259
6	0.00766	60.47	-2.211
7	0.01389	57.46	-1.898
8	0.01076	47.23	2.526

Table 17: Constants for PIV-derived velocity inlet waveform function equation (45)

The PIV-derived velocity inlet waveform shown in orange in Figure 24 is derived at the inlet of the PIV flow phantom from velocity-data of the water-gelatin experiment of the chapter 4 flow experiments shown in Figure 7. The sum of sines fit was accomplished using the Matlab Curve Fitting Toolbox version 3.5.12., and the resulting PIV-derived velocity inlet waveform function is described using equation (45) and corresponding Table 17.

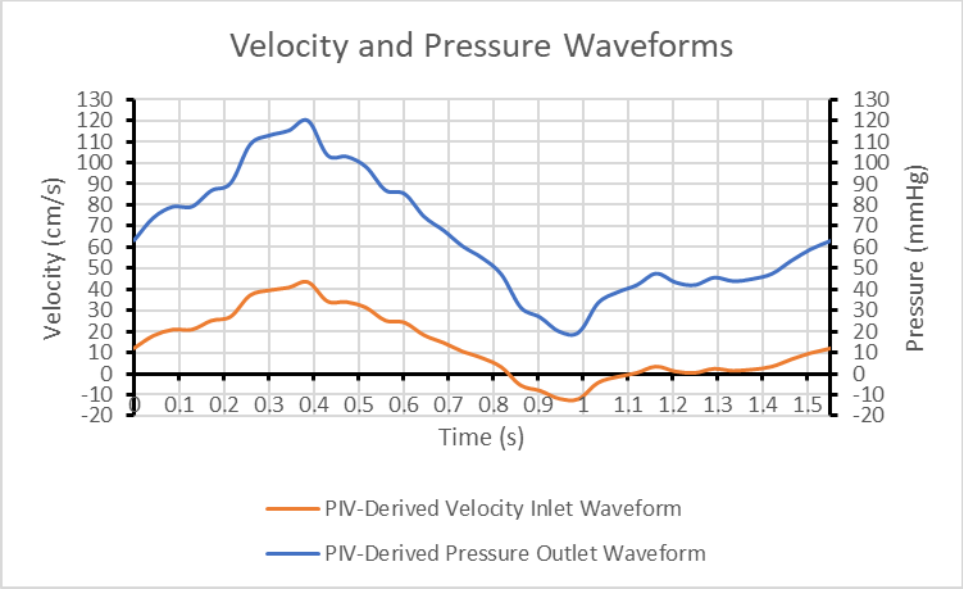

Figure 25: PIV-derived velocity inlet waveform (orange) and PIV-derived pressure outlet waveform (blue)

Importantly however, although the PIV-velocity data produces a repeating waveform, the PIV-derived velocity inlet waveform function shown in (45) does not, and rather only captures a single wavelength of the PIV-velocity data. As such the function is altered to repeat after every 1.55s for use in a UDF (user-defined function) to define the PIV simulation velocity inlet as shown in equations (46) and (48) below:

$$v(t) = a_1\sin(b_1(t-1.55n)+c_1) + a_2\sin(b_2(t-1.55n)+c_2) + \cdots a_8\sin(b_8(t-1.55n)+c_8) \quad (46)$$

$$P(t) = (24000(a_1\sin(b_1(t-1.55n)+c_1) + a_2\sin(b_2(t-1.55n)+c_2) + \cdots a_8\sin(b_8(t-1.55n)+c_8)) + 5500)(7.5\times10^{-3}) \quad (47)$$

Where:

$$n = \lfloor t \rfloor - 1.55 \quad (48)$$

Pressure is not measured for any of the experiments however the inlet and outlet functions, shown in Figure 35 for the patient-specific aneurysm simulation in upcoming chapter 6, demonstrate that the applied in-vivo pressure waveforms demonstrate a nearly identical periodicity and sinusoidal structure to corresponding velocity waveforms. With this consideration, the PIV simulation pressure outlet function shown in equation (47) is derived from a further alteration of equation (46) by increasing the scale and shifting the mean to create a similar function in scale to that derived from patient-data shown in Figure 35 for the patient-specific aneurysm geometries discussed in section 6.1.2.1.

The velocity flow profile is otherwise defined as plug flow at inlet, and the extended inlet zone is applied to parabolically distribute ahead of the artery zone, shown in Figure 18.

5.1.2.1.1. Reference Features of Velocity Inlet Waveform

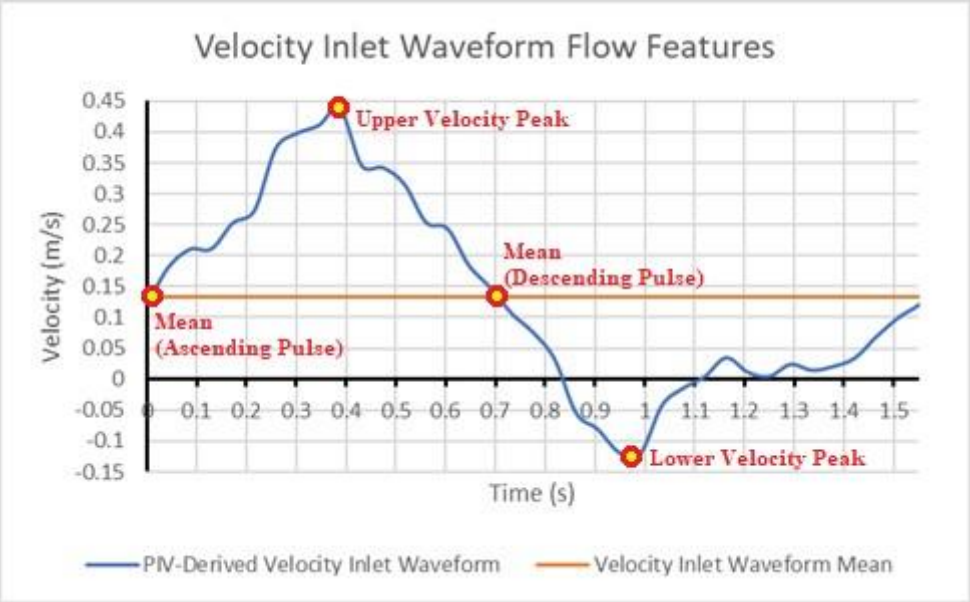

Figure 26: Waveform of PIV-derived velocity inlet waveform indicating waveform features with yellow dots

Figure 26 indicates waveform features in a pulse that will be referenced throughout the PIV-validation simulation results analysis. The indicated waveform features of the inlet velocity Fourier transform are specifically the mean flow as the pulse ascends towards the upper velocity peak (left), the upper velocity peak (middle-left), the mean flow as the pulse descends towards the lower velocity peak (middle-right), and the lower velocity peak (right).

5.1.2.1.2. Fibrinogen at the Velocity Inlet Boundary

The velocity inlet described broadly in section 3.1.6.3 is designed to represent the flow of 0.25 mg/ml concentration fibrinogen in saline solution described in section 4.2.1.1 of the thrombin-fibrinogen flow experiment. As such the velocity inlet continuously outputs a fixed user-defined scalar boundary value of 7.41 nMol of fibrinogen, such that a fixed scalar value of 7.41 nMol of fibrinogen is always present in the flow field prior to biochemical interactions.

5.1.2.2. Thrombin Inlet

The thrombin inlet is designed to represent the thrombin injection of 0.1 ml of 1 mg/ml concentration thrombin in saline solution described in section 4.2.1.1 of the thrombin-fibrinogen flow experiment. As such the thrombin velocity inlet has a steady velocity of 0.025 m/s and outputs a user-defined scalar boundary value of 0.524 nMol/s of thrombin for 5 seconds once as described in the pre-clot thrombin-

fibrinogen flow experiment in section 4.2.1.1, and twice as described in the thrombin-fibrinogen flow experiment for clot capture in section 4.3.1.

5.1.2.3. Porosity Clotting Threshold

The porosity clotting model is adjusted based on the clotting times in the PIV experiment, where the concentrations of thrombin and fibrinogen described in section 4.2.1.1 produce fibrin structures shortly after the first thrombin injection and produce a full clot in roughly 2 minutes in the clot-capture thrombin-fibrinogen flow experiment as described in section 4.3.1. As such, a porosity value of 0.75 and permeability of 1e12 m^{-1} is reached when a fibrin concentration of 1.25 nMol is reached, which is achieved slightly under 10s in the clotting PIV-validation simulation as described later in section 5.3.1.

5.1.3. No-Slip and Free-Slip Wall Boundary Conditions

The majority of CFD thrombosis models apply a no-slip wall boundary condition [55,57,64,71,75,134]. There has long been evidence, however, that a partial-slip wall boundary is more appropriate for representing some of the non-Newtonian flow behavior of blood [100,135]. While the effects of the non-Newtonian characteristics of blood are usually considered negligible in arterial flow modeling with exception to flow through very small vessels such as arterioles, there are a growing number of models demonstrating that these non-Newtonian effects are significant even in large vessels with predominantly high shear rates [83].

The modelling of a partial-slip wall boundary function for macro-vessels is outside the scope of the presented thrombosis model, however due to its allowance of near-wall flow, a free-slip wall boundary theoretically provides a better approximation to this behavior than a no-slip wall boundary. Therefore, a comparison of flow results between wall boundaries with free-slip and no-slip conditions to the flow results of thrombin-fibrinogen pre-clot flow experiment shown in section 4.2.2 is applied to determine the extent to which a partial-slip wall boundary may be relevant, and whether it is better approximated by a free-slip or no-slip wall boundary condition.

5.1.3.1. Free-Slip vs No-Slip Theory

A no-slip boundary condition at a wall causes fluid to stick to it and match its velocity, if any, where the specified shear boundary condition at a wall allows you to specify the directional components of shear stress.

For a no-slip wall boundary condition in a laminar flow case, shear stress on the fluid at the wall is determined by the normal velocity gradient at the wall shown in equation (49).

$$\tau_{wall} = \mu \frac{dv}{dn} \tag{49}$$

Where μ is dynamic viscosity and $\frac{dv}{dn}$ is the velocity gradient [136].

Holding dynamic viscosity μ constant, specifying a shear τ_{wall} to zero sets the velocity gradient $\frac{dv}{dn}$ to 0 as well, which eliminates the velocity gradient altogether.

5.1.3.2. Grid Independence Study

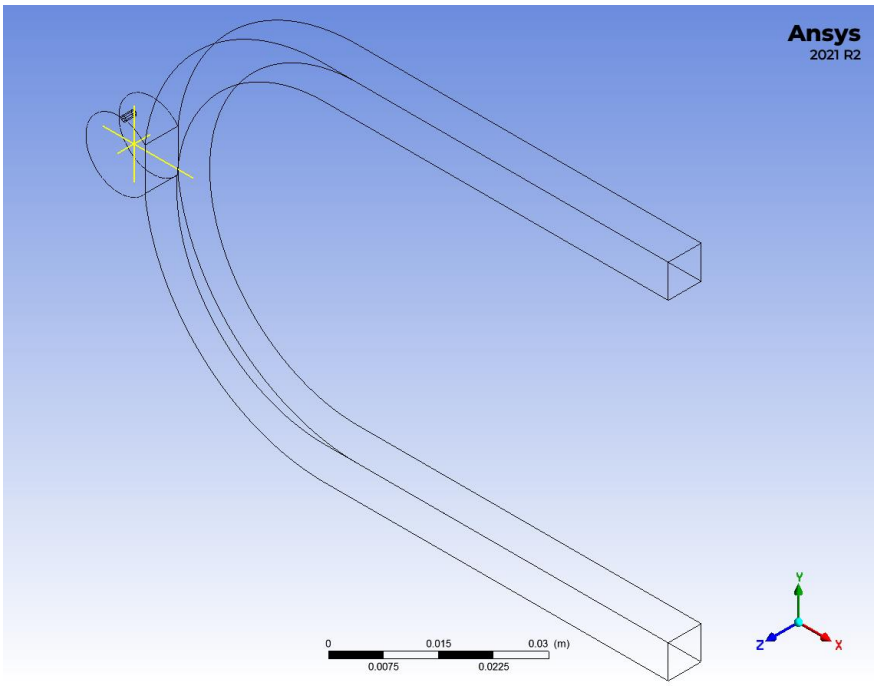

Figure 27: Idealized-PIV Flow Geometry

Elements	Wall Condition	Average (mm/s)			Maximum (mm/s)		
		X	Y	Z	X	Y	Z
527,133	NS	25.7879	11.1729	5.91543	240.763	35.7266	7.65218
(Baseline)	ZS	36.7498	23.8064	10.0096	161.671	62.1783	12.2116
55,657	NS	30.7328	12.1966	5.46411	211.69	50.0761	6.91521
	ZS	44.868	32.9134	3.48265	161.063	80.7226	4.0747
98,637	NS	29.8763	12.838	5.53014	214.836	48.5532	7.03183
	ZS	42.8024	31.2326	3.5314	161.45	77.2224	3.95331
1,024,379	NS	24.6126	11.3296	7.18399	237.902	31.9238	9.65115
	ZS	39.4962	26.471	4.68757	162.563	75.4565	4.92174

Table 18: Grid independence study of both no-slip and free-slip CFD flow phantom geometry cases comparing average, maximum, and minimum velocity magnitudes within the aneurysm along the X, Y, and Z axes.

Elements	Wall Condition	Average			Maximum		
		X	Y	Z	X	Y	Z
527,133 (Baseline)	NS	0%	0%	0%	0%	0%	0%
	ZS	0%	0%	0%	0%	0%	0%
55,657	NS	-19.18%	-9.16%	7.63%	12.08%	-40.16%	9.63%
	ZS	-22.09%	-38.25%	65.21%	0.38%	-29.82%	66.63%
98,637	NS	-15.85%	-14.90%	6.51%	10.77%	-35.90%	8.11%
	ZS	-16.47%	-31.19%	64.72%	0.14%	-24.20%	67.63%
1,024,379	NS	4.56%	-1.40%	-21.44%	1.19%	10.64%	-26.12%
	ZS	-7.47%	-11.19%	53.17%	--0.55%	-21.36%	59.70%

Table 19: Grid independence study average deviation from grid baseline for both no-slip and free-slip CFD flow phantom geometry cases for average, and maximum velocity magnitudes within the aneurysm along the X, Y, and Z axes.

To arrive at the mesh shown in Figure 21-Figure 22, a grid independence study is performed using a steady velocity inlet boundary of 0.23 m/s, a pressure outlet boundary of 11000 Pa. A transient solver with a timestep size of 0.01s and 1000 time-steps is applied using the solver settings described in section 3.1.2 without the addition of the UDS' and related functions. The thrombin inlet boundary is set at 0 m/s, as it is not critical to capture high resolution flow effects from this inlet.

To reduce mesh size and retain sufficient accuracy, the simulation is repeated for coarser meshes, and subsequent probe values are compared to previously measured probe values of the maximum cell/node mesh.

To accomplish this, three probes are employed within the center of the aneurysm across the x, y, and z axis respectively, as shown in Figure 27. The maximum and average velocity across these probes is measured and compared as shown in Table 18. Average and maximum velocity are chosen as metrics for grid independence to reflect the influence of grid size on velocity distribution within the flow field. Because of considerations towards multiple wall boundary conditions, discussed in detail in section 5.1.3, the grid independence study is performed for different meshes with both free-slip and no-slip wall boundary conditions. Table 19 shows the average deviation of each mesh size from a baseline grid of roughly 500,000 elements, which is selected due to the relatively low deviation it has from the 1,000,000-element mesh in the x and y directions when considering velocity average. The x and y directions are considered the most important due to the z-axis being perpendicular to the direction of flow throughout the entire aneurysm. The velocity average standard deviation of the 1,000,000-element mesh is 4.56% and -1.4% in the x and y direction for the no-slip case, and -7.47% and -11.19% in the x and y direction for the free-slip case.

5.2. Validation Simulation Flow Results Comparison to Flow Experiments

This section describes the validation simulation pre-clot flow procedure and results, and compares the flow results to the PIV-derived flow results of the thrombin-fibrinogen experiment discussed in section 4.2.2, followed by the water-gelatin experiment discussed in section 4.1.3.

Following this general analysis, distinctions in flow behavior observed between the in-vitro experiments as well as the wall-boundary-specific flow results of the simulation are cross-referenced with the agreement of each flow experiment with the simulation dependent upon the wall-boundary applied, and a discussion of this phenomenon relative to existing literature is presented.

5.2.1. Validation Simulation Pre-Clot Flow Procedure

Velocity Inlet	Thrombin-Injection Inlet	Time
Pulsatile velocity equation (46)	0.025 m/s	0-5s
Pulsatile velocity equation (46)	0 m/s	5-120s

Table 20: PIV-validation simulation pre-clot flow inlet boundaries' order of operations; velocity inlet (left), thrombin-injection inlet (middle), relative simulation time (right)

To compare the validation simulation flow results to the flow results of the pre-clot thrombin-fibrinogen flow experiment discussed in section 4.2.2, the validation simulation applies a similar procedure as described in section 4.2.1.1, and as shown in Table 20.

5.2.2. PIV-Validation Simulation Flow Results Comparison to Thrombin-Fibrinogen Flow Experiment Results (Pre-Clot)

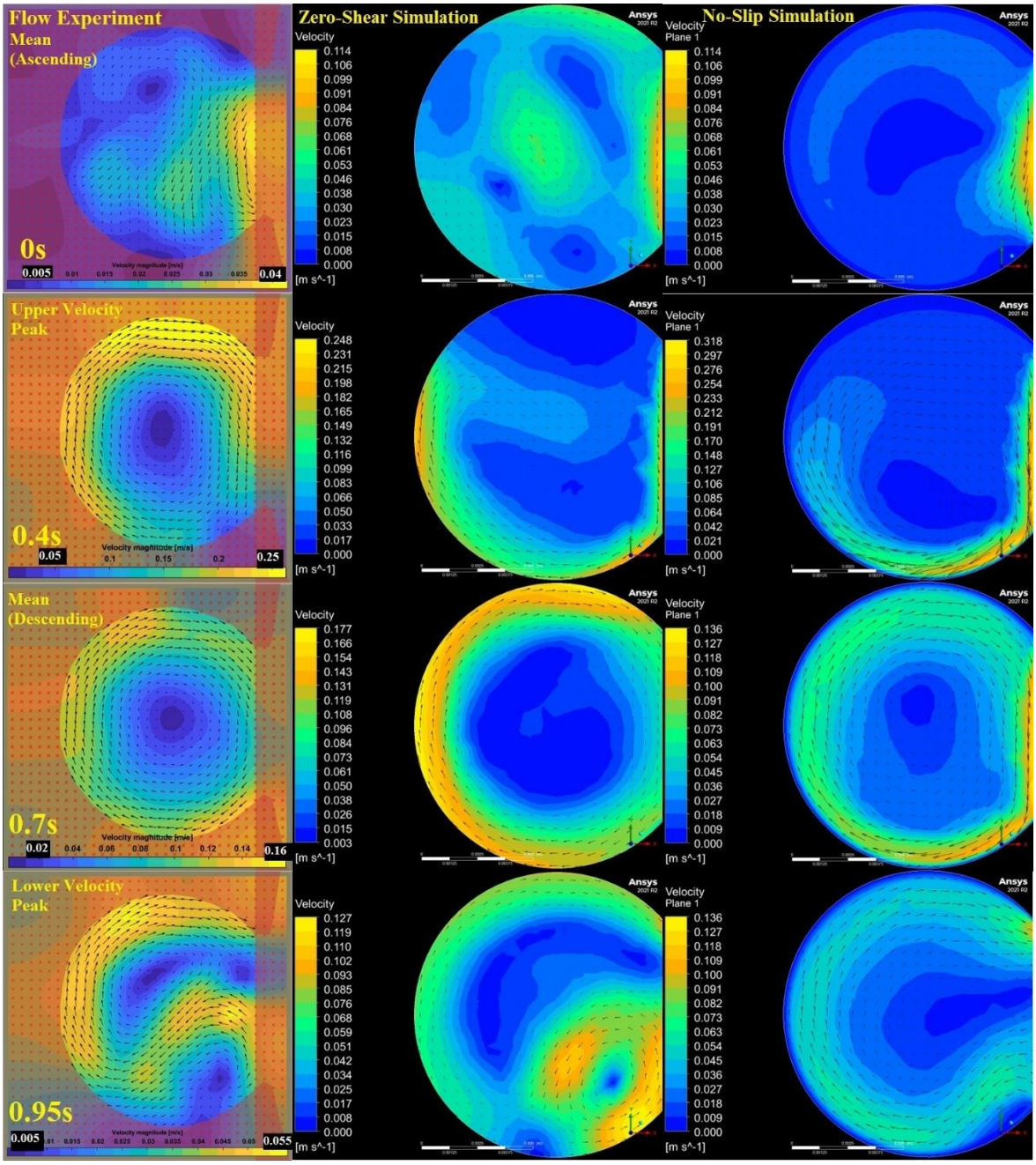

Figure 28: Flow comparison between thrombin-fibrinogen flow experiment (pre-clot) results (left) described in section 4.1.3 and PIV-validation simulation with free-slip (middle) and no-slip (right) wall boundary conditions at different times throughout a pulse wavelength shown in Figure 26; mean pulsatile flow velocity ascending towards upper velocity peak (top), pulsatile flow upper velocity peak (upper middle), mean pulsatile flow velocity descending towards lower velocity peak (lower middle), pulsatile flow lower velocity peak (bottom).

Figure 28 illustrates the comparison of flow patterns between the pre-clot thrombin-fibrinogen flow experiment results described in section 4.1.3, and the validation simulation with free-slip and no-slip wall boundaries at different times relative to the PIV-derived velocity inlet waveform shown in Figure 25.

The validation simulation free-slip case shown in Figure 28 (middle) generally has significant recirculation within the aneurysm and high velocity flow at the aneurysm wall. The CFD no-slip case (right) by comparison generally has relatively low velocity within the aneurysm apart from the bottom of the aneurysm near where it connects with the artery.

In Figure 28, the no-slip case (right) bears similar vector distribution to the pre-clot thrombin-fibrinogen flow experiment (left) at t=0s (top), t=0.7s (lower-middle) and t=0.95s (bottom), but is not representative of the experiment flow magnitude except during periods of relatively low flow within the aneurysm at t=0s and t=0.95s. The validation simulation free-slip case shown in Figure 28 (middle) also bears similar vector distribution to the pre-clot thrombin-fibrinogen flow experiment (left) at t=0s (top), t=0.7s (lower-middle) and t=0.95s (bottom), and is representative of the experiment flow magnitude at t=0.4s (upper-middle), t=0.7s and t=0.95s, with notable exception of the recirculation zone at t=0.95s which is roughly twice the magnitude as seen in the flow experiment.

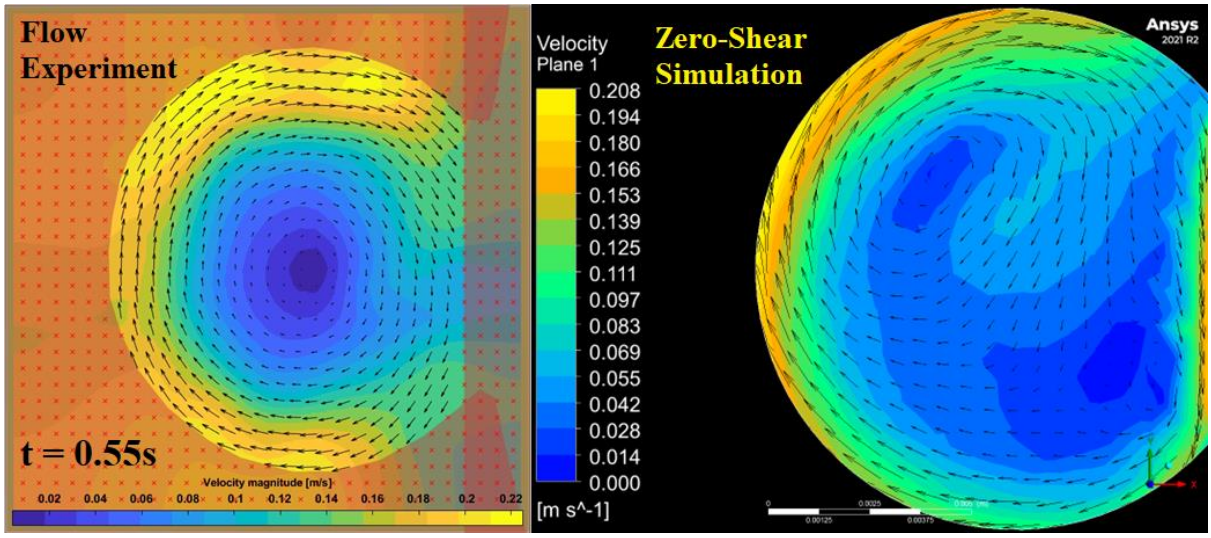

Figure 29: Flow comparison between thrombin-fibrinogen flow experiment (pre-clot) flow field (left) described in section 4.1.3 and PIV-validation simulation result with free-slip wall boundary condition (right) between the ascending mean velocity and upper velocity peak of the pulse wavelength shown in Figure 25 at t = 0.55s.

Overall, Figure 28 demonstrates that the free-slip case has qualitatively better vector agreement with the flow experiment results than the no-slip case at all times except t=0s (top), as well as better velocity magnitude agreement with the flow experiment at t=0.4s (upper-middle) and t=0.7s (lower-middle) than the no-slip case, where velocity magnitude agreement with the flow experiment at t=0.95s (bottom) is only slightly worse in the free-slip case due to the presence of the recirculation zone. Both computational cases, however, differ from the flow experiment in terms of flow distribution at t=0.4s. This appears to be due to flow in the thrombin-fibrinogen flow experiment quickly distributing across the walls of the aneurysm at t=0.4s, although the free-slip computational case distributes flow in a similar way closely afterwards at t=0.55s as shown in Figure 29.

In Figure 28, the difference between the results of the validation flow simulation with the no-slip and free-slip wall boundary conditions, and the reason that the free-slip case more closely resembles thrombin-fibrinogen flow results, is due to the no-slip wall boundary condition that causes high velocity flow along the aneurysm wall to disperse into significantly lower velocity flow towards the top of the aneurysm as can be seen at t = 0.7s (lower middle). This is likely caused by a dampening effect on flow near the wall boundary as a consequence of the velocity gradient described in equation (49), either indicating an over-estimate in wall shear-stress or slip behavior of the fibrinogen-saline solution described in section 4.2.1.1.

5.2.3. PIV-Validation No-Slip Wall Boundary Simulation Flow Results Comparison to Gelatin-Injection Flow Experiment Results (Pre-Injection)

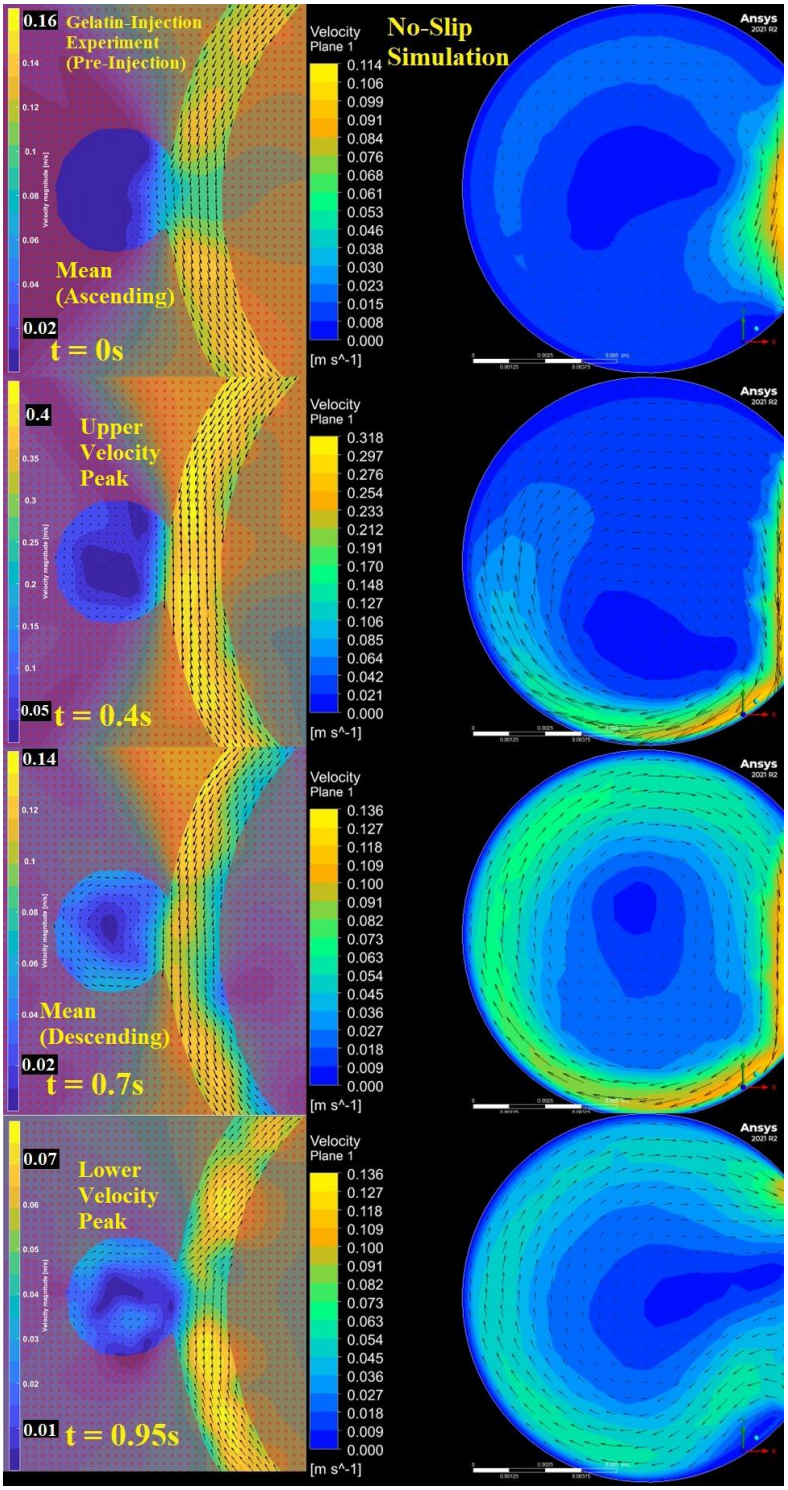

Figure 30: Flow comparison between gelatin-injection flow experiment (pre-injection) results (left) described in section 4.1.3 and PIV-validation simulation with a no-slip wall boundary condition (right) at different times throughout a pulse wavelength shown in Figure 26; mean pulsatile flow velocity ascending towards upper velocity peak (top), pulsatile flow upper velocity peak (upper middle), mean pulsatile flow velocity descending towards lower velocity peak (lower middle), pulsatile flow lower velocity peak (bottom).

Figure 30 provides a similar comparison of simulation to experimental results as Figure 28, and comparing both flow magnitude and direction of vectors for the no-slip simulation (right) by comparison to the flow-field derived for Newtonian tap water prior to gelatin-injection (left) in Figure 30, there is a high amount of agreement between the computational and experimental results, where flow magnitude and distribution is nearly the same across the entire pulse wavelength as shown in t=0-0.95s (top-bottom).

When considering the agreement of results in the flow comparison in Figure 30 of the PIV-validation simulation results with the no-slip boundary (right) to the flow results of tap water prior to gelatin-injection in the gelatin-injection experiment described in section 4.1.3 (left), and the lack of fit of the no-slip boundary simulation results to the fibrinogen-thrombin flow experiment by comparison to the free-slip boundary simulation discussed in 5.2.2, this is potentially an indication of non-Newtonian behavior by the fibrinogen-saline solution.

5.2.4. Comparison between PIV-Validation Simulation Flow Results with free-slip and No-Slip Wall Conditions

As discussed in section 5.2.2, Figure 28 demonstrates that the validation flow simulation with a free-slip wall boundary condition yields results that are representative of the pre-clot thrombin-fibrinogen flow experiment over the course of the entire pulse of the PIV-derived velocity inlet waveform shown in Figure 25. The validation flow simulation with a free-slip wall boundary condition is furthermore significantly more representative of the pre-clot thrombin-fibrinogen flow experiment results than with a no-slip wall boundary condition, which fails to capture high velocity flow features throughout the majority of a pulse wavelength.

As discussed in section 5.2.3, Figure 30 demonstrates that the validation simulation with a no-slip condition succeeds in capturing the magnitude and flow features of the gelatin-injection experiment prior to gelatin injection.

Given that the difference between the experimental framework of thrombin-fibrinogen flow experiment and the gelatin-injection flow experiment is primarily the operating fluid, which is fibrinogen-saline solution (section 4.2.1.1) and room temperature water (section 4.1.1.1) respectively, these experiments are potentially better represented by different wall boundary conditions due to the presence or lack thereof of fibrinogen.

Fibrinogen has been suggested to be a significant contributor to yield stress and thixotropic properties of blood, and has been proposed as the main contributor to the viscoelastic features of blood plasma [137,138]. Blood plasma has demonstrated exponential shear-thinning behavior by contrast to Newtonian fluids as shown by Brust et al. [139,140].

When comparing the pre-clot flow results of the thrombin-fibrinogen experiment in Figure 28 to the pre-injection flow results of the gelatin-injection experiment in Figure 30, the velocity distribution within the aneurysm differs significantly between the two experiments at t=0.4s during the upper pulsatile velocity peak and mean (descending) pulsatile velocity at t=0.7s, where much higher flow rates are observed throughout the aneurysm in the thrombin-fibrinogen flow experiment; a difference that may be accounted for by non-Newtonian behavior of fibrinogen-saline solution, as opposed to the Newtonian behavior of tap-water.

The lack of a velocity gradient at the aneurysm wall due to the free-slip wall boundary condition prevents the flow dampening effect caused by the no-slip wall boundary as discussed in section 5.2.2. Due to this, the free-slip wall boundary condition appears to allow the fluid to artificially emulate shear-thinning behavior at high velocities, but since the fluid is still fundamentally defined as Newtonian, the flow magnitude is similarly high across the low velocity periods within the aneurysm, as shown in Figure 28 at 0s and 0.95s.

In previous work by Hume & Tshimanga et al., differences in results between the PIV experiment and the computational validation simulation are speculated to be due to the no-slip condition applied at the walls of the simulation, which create an easily identifiable zero-velocity region along the walls that causes a more even distribution of flow through the artery than is seen in the PIV experiment which distributes high velocity flow more on one side of a curved channel than the other [71]. This phenomenon is not directly identified in other PIV-validated studies, though zero-velocity regions at the walls are readily identifiable in simulations and may be similarly responsible for mismatched flow distribution [68,69,141]. This zero-velocity region can be identified in the no-slip validation simulation shown in Figure 30, although it is less pronounced due to the inflation layers applied for the mesh described in section 5.1. Overall, this indicates that even without other considerations, the velocity-gradient of the no-slip condition can have an outsized effect on flow distribution that can be unrepresentative of PIV experiment results if not appropriately accounted for. However, it is important to consider that the presence (or there lack of) of slip is difficult to directly capture in PIV due to limitations of resolution, since adequate distribution of particles to capture flow in the near-wall region is nontrivial, and cross-correlation windows and flow averaging algorithms can include part of the wall in addition to particle capture [142].

It can be concluded that the fibrinogen-saline solution described in section 4.2.1.1 of the thrombin-fibrinogen pre-clot experiment did not exhibit the same behavior as a well understood Newtonian fluid under identical flow conditions (see Figure 9-Figure 13), and that simulations assuming a Newtonian fluid with a free-slip wall boundary condition represent this flow behavior significantly

more accurately than with a no-slip boundary condition as shown in Figure 29. The simulation with the no-slip boundary condition furthermore replicates the Newtonian flow behavior of tap-water in the pre-injection gelatin-injection experiment as shown in Figure 30. This seems to indicate the presence of non-Newtonian slip and shear-thinning features consistent with literature, though further studies similar to that by Brust et al. are required to verify such properties [139].

The presence of macrovascular slip is not considered for most existing cardiovascular models. With consideration towards the results presented in this section though the following considerations should be made regarding this seeming contradiction:

1. It is unclear whether slip manifests outside of clotting conditions, and specifically the presence of fibrin.
2. The full-slip wall condition is an approximation made for this study, and a partial-slip wall model will likely more realistically captures the flow behavior of the thrombin-fibrinogen PIV experiment
3. The fibrinogen-saline solution is not analogous to full blood. Though extrapolating from fibrinogen-saline solution's similarities to blood plasma, and blood plasma being the transport medium for blood cells, some measure of slip is potentially present for full blood in macrovascular environments.
4. Cardiovascular models that apply a no-slip condition may also be valid with a partial-slip condition, since mechanistically the features of near-wall flow such as vortices and wall shear stress are present for both cases [94]

5.3. Validation Simulation Clot Results Comparison to Thrombin-Fibrinogen Flow Experiment Clotting Outcome

5.3.1. Validation Simulation Post-Clot Flow Procedure

Velocity Inlet	Thrombin-Injection Inlet	Time
0 m/s	0.0625 m/s	0-2s
0 m/s	0 m/s	2-10s
Pulsatile velocity equation (46)	0 m/s	10-15s
0 m/s	0 m/s	15-120s
Pulsatile velocity equation (46)	0.025 m/s	120-125s
Pulsatile velocity equation (46)	0 m/s	125-300s

Table 21: PIV-validation simulation post-clot flow inlet boundaries' order of operations; velocity inlet (left), thrombin-injection inlet (middle), relative simulation time (right)

To compare the validation simulation clot results to the clot results of the clot capture thrombin-fibrinogen flow experiment discussed in section 4.3.3, the validation simulation applies a similar procedure as described in section 4.3.1 and shown in Table 21.

5.3.2. PIV-Validation Simulation Clotting Results Comparison to Thrombin-Fibrinogen Flow Experiment (Post-Clot)

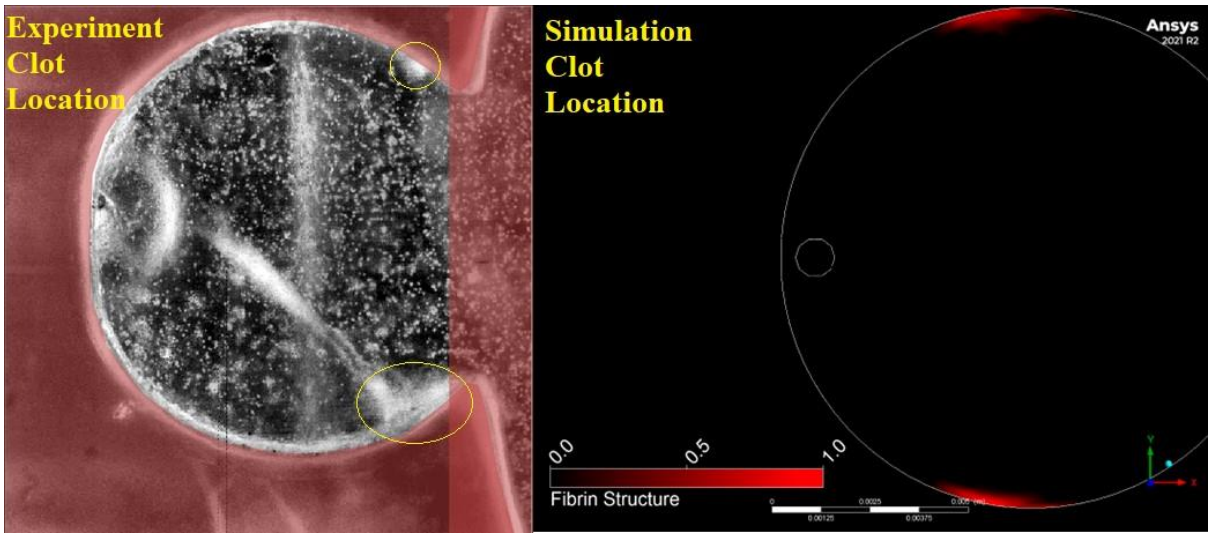

Figure 31: Clot comparison between thrombin-fibrinogen flow experiment circled in yellow (left) and Validation simulation highlighted in red (right)

Figure 31 compares the location of clot formation between the thrombin-fibrinogen flow experiment and the PIV-validation simulation. In both cases, a clot begins to form on both the top and the bottom of the aneurysm shortly after the first thrombin injection and continues to develop marginally over 2 minutes, where in the flow experiment the clots form closer to the neck of the aneurysm than the simulation. The most notable difference between the two cases is the formation of the fibrin strand in the flow experiment, which is not capable of being reproduced in ANSYS Fluent.

5.3.3. PIV-Validation Simulation Flow Results Comparison to Thrombin-Fibrinogen Flow Experiment (Post-Clot)

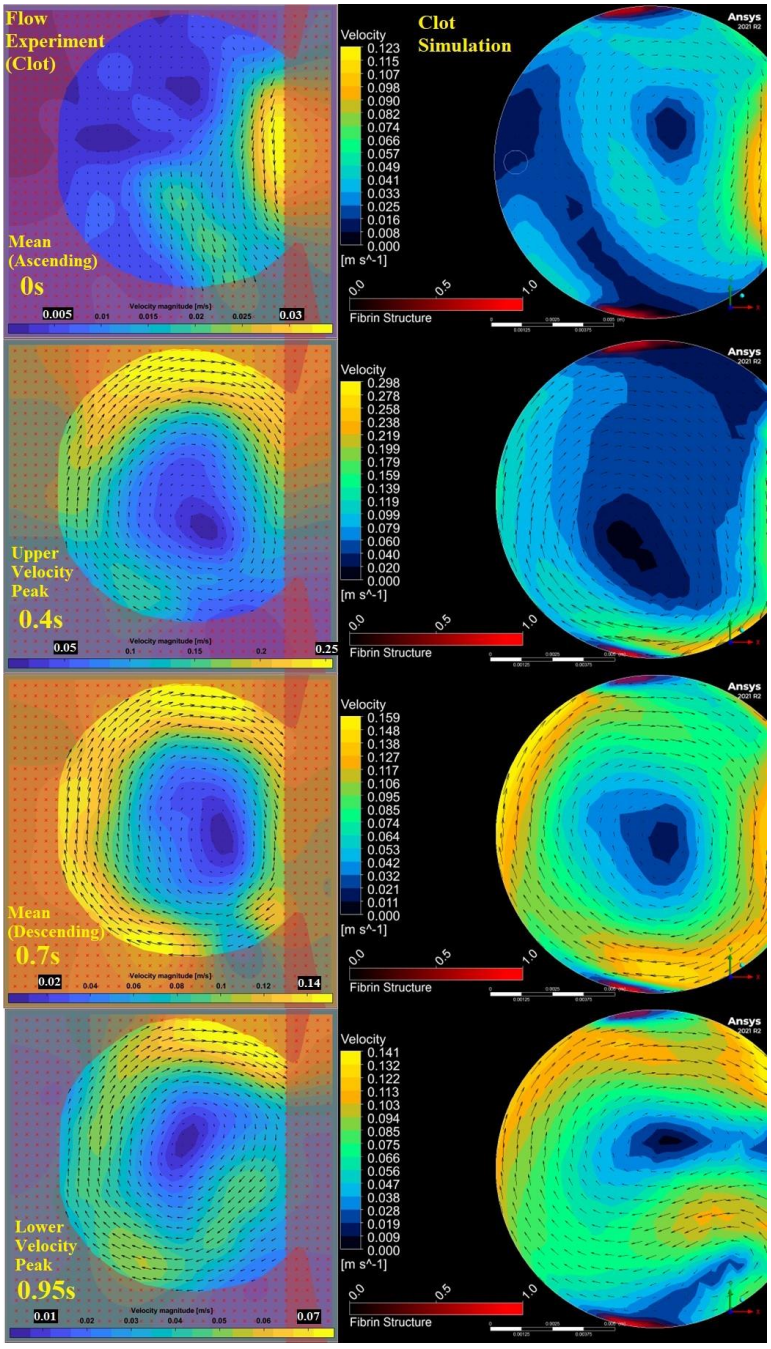

Figure 32: Flow comparison between thrombin-fibrinogen flow experiment post-clot results (left) described in section 4.1.3 (see Figure 16 for clot position) and PIV-validation simulation with free-slip wall boundary conditions inclusive of clot location (red) at different times throughout a pulse wavelength shown in Figure 26; mean pulsatile flow velocity ascending towards upper velocity peak (top), pulsatile flow upper velocity peak (upper middle), mean pulsatile flow velocity descending towards lower velocity peak (lower middle), pulsatile flow lower velocity peak (bottom).

Figure 32 demonstrates a comparison between the flow patterns between the post-clot thrombin-fibrinogen flow experiment results described in section 4.1.3, and the clotting validation simulation with free-slip at different times relative to the PIV-derived velocity inlet waveform shown in Figure 25.

Similarly to the free-slip case comparison to the pre-clot thrombin-fibrinogen experiment discussed in section 5.2.2, the validation simulation free-slip clotting case shown in Figure 32 bears similar vector distribution to the post-clot thrombin-fibrinogen flow experiment at t=0s (top), t=0.7s (lower-middle) and t=0.95s (bottom), and is representative of the experiment flow magnitude at t=0.4s (upper-middle), and t=0.7s (lower-middle). Deviation from the flow experiment vector distribution occurs at 0.4s and 0.7s due to the difference in clot position between the flow experiment and the computational case, where at 0.4s the clot provides a buffer against high velocity flow against the aneurysm wall when compared to the free-slip simulation flow results at the same time in Figure 28. Other deviations occur at 0.7s where the clot at the top of the aneurysm also buffers flow when compared to the free-slip simulation flow results at the same time in Figure 28. Similarly, in the thrombin-fibrinogen post-clot experiment flow results shown in Figure 32, at 0.4s (upper-middle) and 0.7s (lower-middle) flow at the top of the aneurysm decreases after passing through the clot that has formed there shown in Figure 31. To a lesser degree, this also occurs along the aneurysm wall at the bottom of the aneurysm in the post-clot experiment at 0.4s and 0.7s as shown in Figure 32.

Otherwise, the simulation flow behavior at t=0.95s is roughly twice the magnitude as seen in the flow experiment in the clotting case, and as in section 5.2.2 the clotting simulation differs from the post-clot flow experiment in terms of flow distribution at t=0.4s, which again appears to be due to a delay in flow distribution across the walls of the aneurysm at t=0.4s in the computational case.

5.4. Post-Clot Validation Simulation Comparison to Experimentally Validated Clotting Models in Literature

The clotting outcome of the validation simulation as discussed in section 5.3.2 is representative of the clotting outcome of the thrombin-fibrinogen flow experiment apart from the formation of a fibrin strand seen in Figure 31. This complex structure requires fluid-structure-interface modelling to be accounted for and is therefore not capable of being addressed by the current model framework. It furthermore appears, to the best of the authors knowledge, not to have been accounted for by any other clotting model to date. This is perhaps in part due to it being an unusual clotting outcome with reference to similar flow experiments for validation of computational thrombosis models, though these are few in number and there is a lot of variability in experimental clotting outcomes in general [65,73,75,131].

The computational model of thrombosis used in the validation simulation is built upon work by Jimoh-Taiwo et al. and Ngoepe et al. [73,75]. Jimoh-Taiwo et al.'s own validation simulation demonstrates good agreement with the corresponding flow experiment clot [75]. The clotting flow model by Ngoepe et al. produces similarly shaped clots to Jimoh-Taiwo et al. Considering this, as well as the agreement of the locations of validation simulation clots to the thrombin-fibrinogen experiment clots in this

study, there is sufficient evidence to suggest that the clot prediction by the thrombosis model applied in this study demonstrates a level of accuracy.

Other studies apply a variety of methods for experimental validation of computational results [64,65,68,71,75,87,143,144]. Of these studies only a few use flow visualization methods [65,68,71,75]. Fewer models still are validated via both flow visualization and clotting outcomes [65,68,75], and virtually none include the simultaneous measurement of flow and clot growth, nor validation via flow visualization and clotting outcomes both under realistic pulsatile blood flow patterns.

There is furthermore a lack of macroscopic computational thrombosis models and corresponding validation experiments that directly account for the clot formation observed in the thrombin-fibrinogen flow experiment, where most models either form a large thrombus as seen in work by Gester et al., Sarrami-Foroushani et al. and Ou et al. [64,65,68], or small clots similar to that observed in the simulation clot results in Figure 31 as seen in work by Blum et al. for a rotary blood pump driving similarly high flow rates to the thrombin-fibrinogen experiment [145]. These models all consider platelets as a component of clotting, which the model presented in this study eschews due to a variety of factors.

This study applies a thrombin generation curve (derived from work by Wagenvoord, Hemker & Kremers) at the aneurysm wall for the patient-specific thrombosis simulations discussed in upcoming section 6.1.2.3, which presents a computationally efficient method to account for the complex network of biochemical interactions leading to the activation of thrombin [63,71]. Given thrombin's central role in clotting, being responsible for both the conversion of fibrinogen to fibrin and platelet activation, it is a meaningful surrogate for both fibrin and platelet activity [146]. Furthermore, given that fibrin is the primary contributor to clot structure, and the potentially chronic use of anti-platelet medication following flow diverter treatment which inhibit binding of fibrinogen to platelets and thereby inhibit platelet aggregation, the role of platelets are deprioritized relative to the role of fibrin for the consideration of clot structure in the presented model [147,148].

The inclusion of platelets in the thrombin-fibrinogen flow experiment like in the experiment by Clauser et al. could potentially result in a more clump-like clot as seen in work by Gester et al. and Sarrami-Foroushani et al., which in turn could potentially match the PIV-validation clotting results shown in Figure 31 more closely [65,68,72]. The inclusion of platelets in the flow-experiment, however, would necessitate testing for a broader biochemical model inclusive of platelet interactions, which may be addressed in future studies. Inclusion of a power-law model and partial-slip wall boundary to capture the non-Newtonian behavior of fibrinogen-saline solution discussed in section 5.2.3 may also further the accuracy of clot prediction of the validation simulation.

The model described in this thesis combines flow visualization and clotting into a single flow experiment, such that it can be used to simultaneously validate clot formation and flow for the CFD thrombosis model at each individual timestep, which directly corresponds to a PIV image pair taken at an identical time.

This presents a novel proof-of-concept for macroscopic clotting in a flowing environment built upon the in-vitro flow experiment by Ngoepe et al., that validates a thrombosis model built upon work by Hume & Tshimanga et al. and Jimoh Taiwo et al. [71,73,75].

5.5. Conclusion and Data Quantities

The study presents a novel approach to simultaneously validate computationally simulated flow and clot formation from a single experiment, resulting in a novel proof-of-concept for macroscopic clotting in a flowing environment that validates a thrombosis model.

The exploration of wall boundaries in this study highlight differences between the flow of water and fibrinogen-saline solution, despite being subject to identical pulsatile flow conditions. The PIV-validation flow simulation with a free-slip wall boundary condition closely matches the thrombin-fibrinogen flow experiment results, unlike the no-slip condition, which fails to capture high-velocity flow features within the aneurysm. The no-slip condition otherwise successfully replicates the pre-injection gelatin-injection experiment results.

Given the well-understood Newtonian properties of water applied as the gelatin-injection flow experiment operating fluid, the fibrinogen-saline solution of the thrombin-fibrinogen experiment by comparison appears to demonstrate non-Newtonian behavior. This non-Newtonian behavior is emulated by the free-slip wall condition, indicating that both non-Newtonian flow and corresponding slip wall modelling are important inclusions for modelling macrovascular flows under clotting conditions when extrapolating the importance of fibrinogen to the material properties of blood plasma.

The free-slip condition applied in this study is otherwise an idealized approximation that likely overestimates shear-thinning effects of the fibrinogen-saline solution, and viscometric quantification of this fluid paired with a partial-slip wall model will likely result in a closer match between experimental and computational results. Slip in macrovascular environments is poorly understood, and as of current partial-slip models are included only for microvascular and stenosed cases, highlighting an area for future vascular flow modelling research.

The PIV-validation simulation with a free-slip wall boundary condition closely represents the thrombin-fibrinogen flow experiment's clotting outcome, except for the complex fibrin strand

formation. Fluid-structure-interface modelling is necessary to account for this kind of structure, which this framework is incapable of addressing. The thrombosis model shows good agreement with similar preceding studies, and is novelly validated such that direct comparison of the velocity distribution and corresponding clot development under a physiologically realistic pulsatile flow profile can be made to experimental results for any 0.05s interval of the simulation (e.g. 0.05s, 0.1s, 0.15s,…).

Overall, this validation framework presents a promising tool for evaluating computational direct thrombosis models and the validity or limitations of assumptions and simplifications applied therein such that they may yield more accurate results on a patient-specific basis.

Flow Behavior and location	Pre-Injection	Post-Injection
Water-Gelatin Experiment Max Velocity		
Arterial Mean (Ascending) Velocity	0.16 m/s	0.19 m/s
Arterial Upper Velocity Peak	0.45 m/s	0.425 m/s
Arterial Mean (Descending) Velocity	0.14 m/s	0.14 m/s
Arterial Lower Velocity Peak	0.09 m/s	0.1 m/s
Aneurysmal Mean (Ascending) Velocity	0.09 m/s	0.09 m/s
Aneurysmal Upper Velocity Peak	0.25 m/s	0.275 m/s
Aneurysmal Mean (Descending) Velocity	0.07 m/s	0.09 m/s
Aneurysmal Lower Velocity Peak	0.045 m/s	0.055 m/s
Thrombin-Fibrinogen Experiment Max Velocity		
Aneurysmal Mean (Ascending) Velocity	0.04 m/s	0.035 m/s
Aneurysmal Upper Velocity Peak	0.25 m/s	0.25 m/s
Aneurysmal Mean (Descending) Velocity	0.16 m/s	0.15 m/s
Aneurysmal Lower Velocity Peak	0.0575 m/s	0.075 m/s
Free-Slip PIV Validation Simulation Max Velocity		
Aneurysmal Mean (Ascending) Velocity	0.114 m/s	0.123 m/s
Aneurysmal Upper Velocity Peak	0.25 m/s	0.298 m/s
Aneurysmal Mean (Descending) Velocity	0.18 m/s	0.16 m/s
Aneurysmal Lower Velocity Peak	0.13 m/s	0.141 m/s
No-Slip PIV Validation Simulation Max Velocity		
Aneurysmal Mean (Ascending) Velocity	0.114 m/s	
Aneurysmal Upper Velocity Peak	0.318 m/s	
Aneurysmal Mean (Descending) Velocity	0.14 m/s	
Aneurysmal Lower Velocity Peak	0.07 m/s	

Dimensionless Quantities Common Across Simulations and Experiments				
α = 12.39	Mean (Asc)	Upper Peak	Mean (Desc)	Lower Peak
De	19.1	53.74	16.71	10.75
Re	1016	2857.5	889	571.5

Table 22: Data quantities for PIV-based flow experiments and PIV-validation simulations

6. Patient Specific Aneurysm Simulation

In this chapter, the computational framework of the thrombosis model of cerebral aneurysms described in the section 3.1 CFD methodology is applied to three patient-derived aneurysm flow geometries to compare aneurysm clotting outcomes with and without the inclusion of a flow diverter stent.

The methodology of the patient specific aneurysm simulation as it differs or expands upon the section 3.1 CFD methodology is discussed in section 6.1, followed by a presentation and analysis of results in section 6.2.

This chapter is concluded by a discussion in section 6.3, where the sum of results and analysis is compared with in vivo clotting outcomes and comparable direct thrombosis and clotting computational models in literature.

6.1. Patient Specific Aneurysm Simulation Methodology

This section details the patient specific aneurysm simulation methodology as it differs or expands upon the broad CFD methodology described in section 3.1. Section 6.1.1 presents the patient-specific aneurysm and corresponding flow diverter geometries and indicates relevant boundary and fluid zone locations. Section 6.1.2 provides details for the in vivo data derived pulsatile velocity inlet and pressure outlet boundary functions, the free-slip wall boundary selected based upon literature and results in section 5.2.4 of the chapter 5 validation simulation, and the aneurysm wall scalar function responsible for thrombin-release. Finally, section 6.1.3 describes the meshing methodology and provides metrics for grid element quality and quantity for the stented and unstented case for each patient-derived geometry.

6.1.1. Patient-Specific Aneurysm Geometries

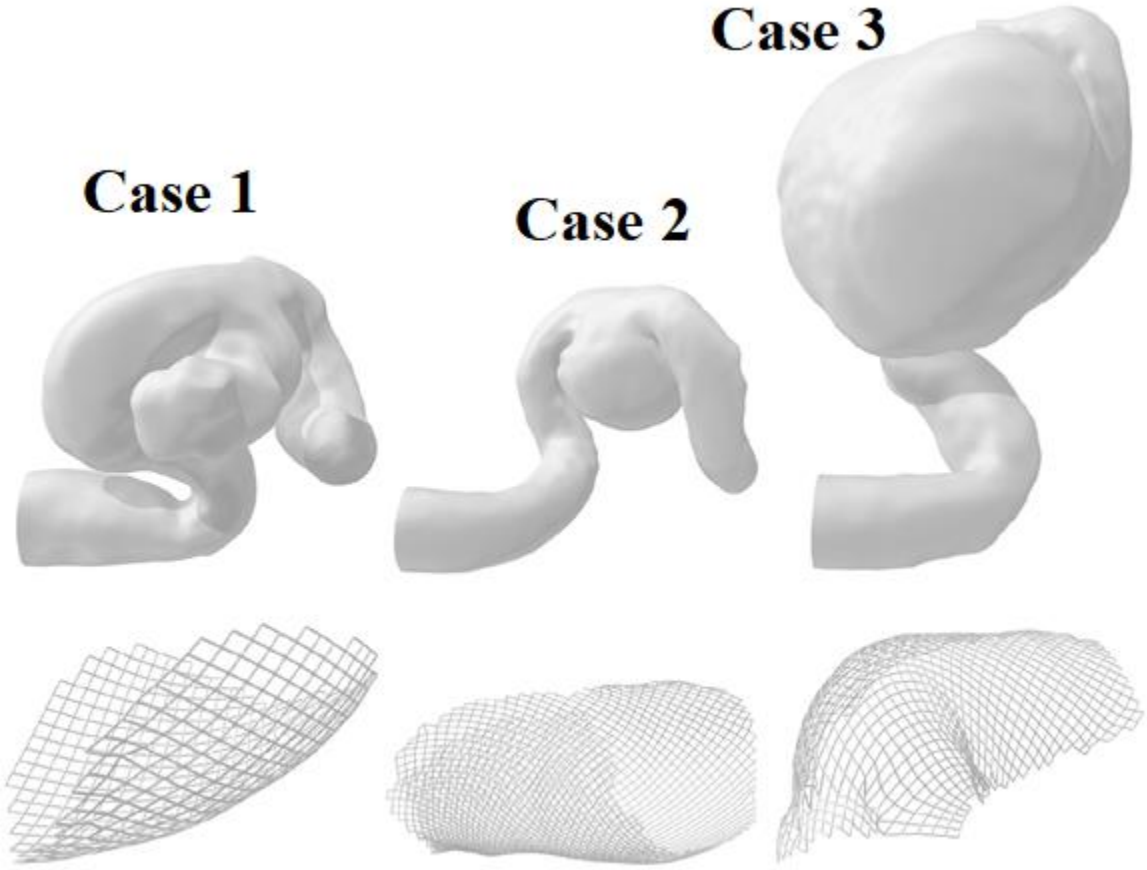

Figure 33: Patient-specific aneurysms and corresponding flow diverters

The patient-derived aneurysm geometries and accompanying stents are shown in Figure 33. Flow and clotting results for each patient-derived aneurysm are computed for flow volumes with and without the inclusion of a flow diverter stent, where for the stented cases the flow diverter geometries shown in Figure 33 (bottom) are subtracted from the corresponding patient-specific aneurysm volumes (top). This totals six simulations; one for each stented, and each unstented volume, of each patient-specific aneurysm geometry.

Outside of what is discussed in section 6.1, the flow boundary conditions and solver settings for each flow volume shown in Figure 33 with and without the inclusion of its accompanying flow diverter are defined as described in the section 3.1 CFD methodology.

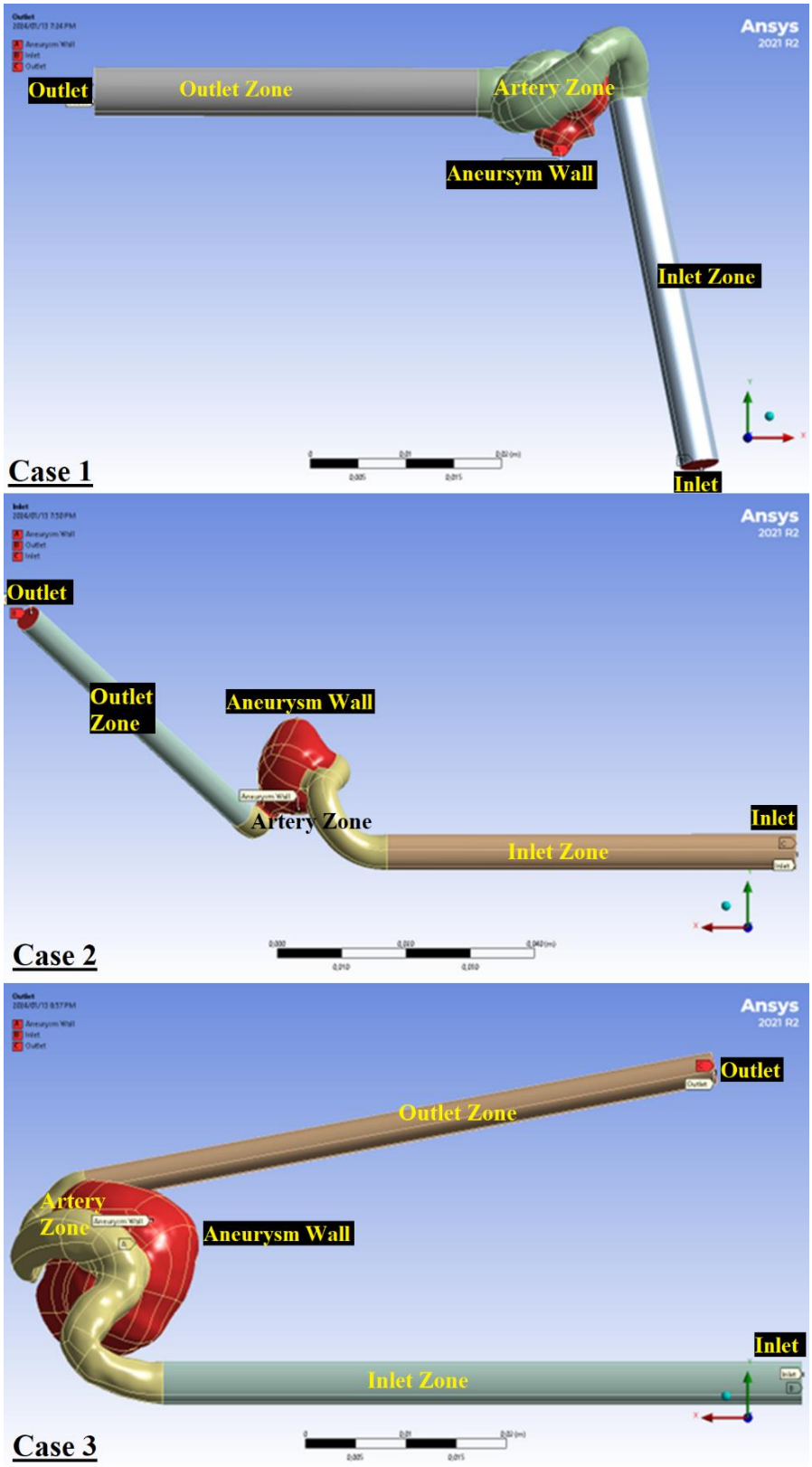

Figure 34: Location of fluid zones, inlet/outlet boundaries, and aneurysm wall boundaries for each patient-specific aneurysm case geometry for both stented and unstented cases

As shown in Figure 34, each geometry consists of 3 fluid zones including the inlet zone, outlet zone, and artery zone. The inlet and outlet zones are included to allow flow to fully develop from the inlet and to prevent clotting near the inlet and outlet boundaries. This is accomplished by excluding the porosity-based clotting model described in section 3.1.5 from the inlet zone and outlet zone.

The artery zone is the fluid zone of interest and as such the porosity-based clotting model operates normally in this volume. The aneurysm wall for each case shown in Figure 34 is responsible for thrombin expression, which is accomplished through the aneurysm wall thrombin-release function described further in subsequent section 6.1.2.3.

6.1.2. Boundary Conditions

6.1.2.1. In-Vivo Data-Derived Pulsatile Flow Velocity Inlet and Pressure Outlet Functions

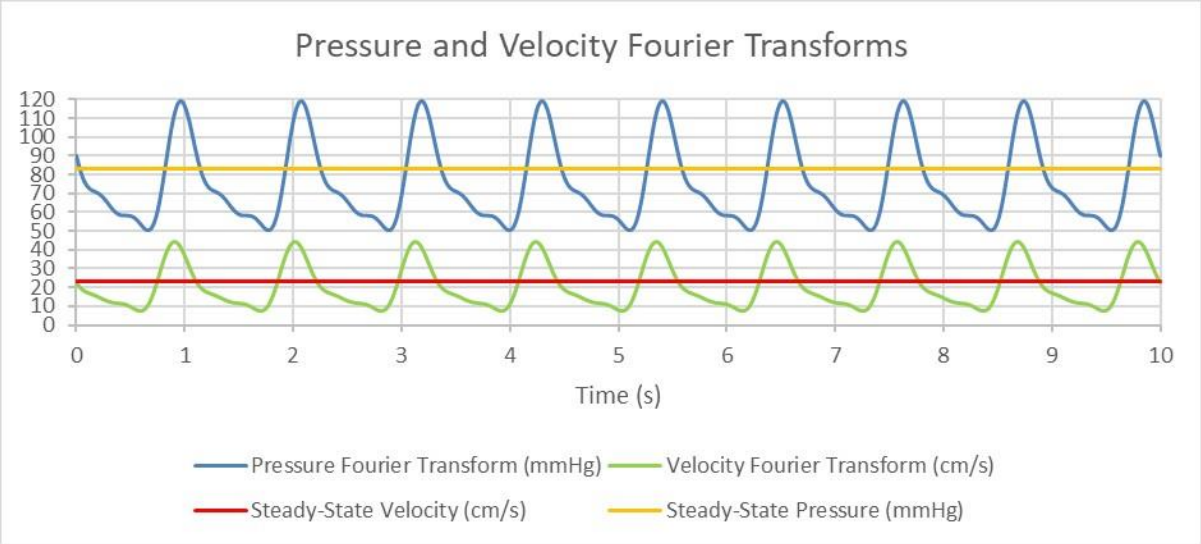

Figure 35: Pressure outlet and velocity inlet Fourier transforms

Pressure Fourier Transform:

$$P(t) = -30.44 * \sin(2\pi(0.89)t - 13.19) + 2.96 * \sin(2\pi(-1.93)t + 0.5) + 1.39 * \sin(2\pi(15.86)t - 2.01) + 75.07 \quad (50)$$

Velocity Fourier Transform:

$$U(t) = -15.49 * \sin(2\pi(0.89)t - 12.84) + 9.42 * \sin(2\pi(-1.78)t - 1.61) + 0.27 * \sin(2\pi(18.44)t - 1.44) + 19.59 \quad (51)$$

The Fourier transforms shown in equations (50)-(51) and plotted in Figure 35 are derived from Ferns et al. for a thrombin transport computational study by Hume & Tshimanga et al., and are applied as the velocity inlet and pressure outlet boundary functions across each case geometry shown in Figure 34 [71,120].

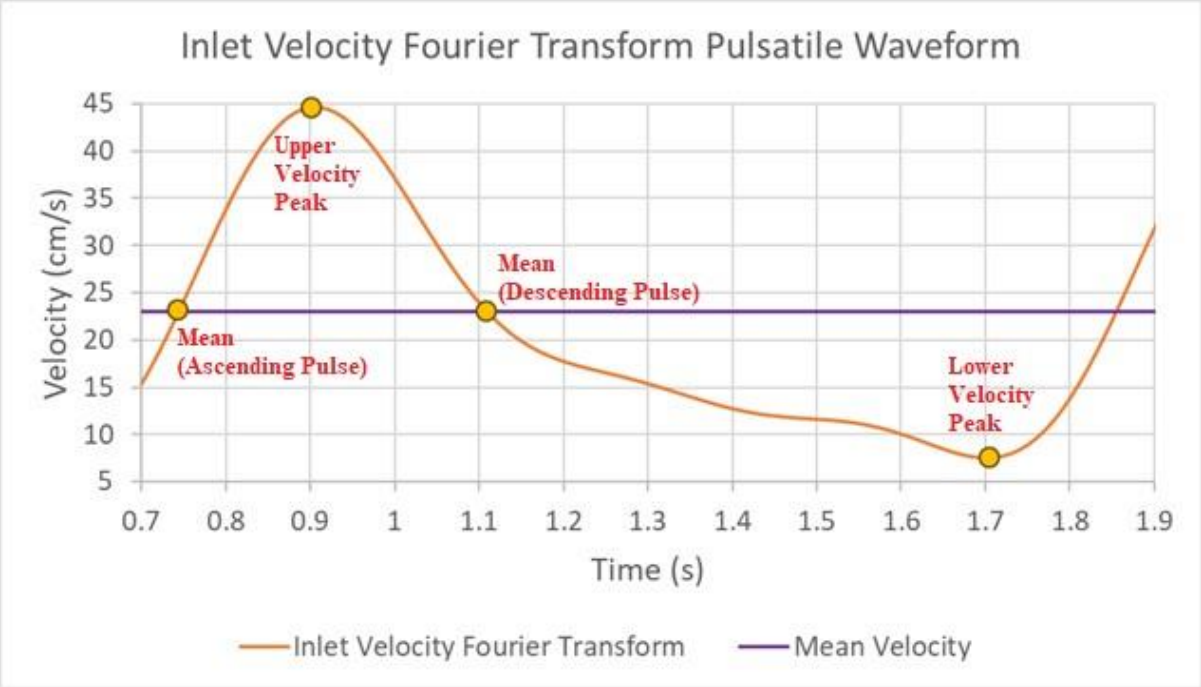

Figure 36: Waveform of inlet velocity Fourier transform indicating waveform features with yellow dots

Figure 36 demonstrates a single pulse waveform of the inlet velocity Fourier transform initially shown in Figure 35 and described by equation (51), and indicates waveform features in a pulse that will be referenced throughout the upcoming patient specific aneurysm results analysis in section 6.2. The indicated waveform features of the inlet velocity Fourier transform are specifically the mean flow as the pulse ascends towards the upper velocity peak (left), the upper velocity peak (middle-left), the mean flow as the pulse descends towards the lower velocity peak (middle-right), and the lower velocity peak (right).

6.1.2.1.1. Fibrinogen at the Velocity Inlet Boundary

A UDS defined at the velocity inlet distributes a value of 7000 nMol of fibrinogen across the flow field for each timestep. This value is derived from work by Ou et al. [64].

6.1.2.2. Free-slip Wall Boundary

The wall boundaries across all three fluid zones for each case geometry shown in Figure 34 are defined as having zero shear stress based upon the reasoning presented in sections 5.1.3 of the validation simulation, cross referenced with the discussion of results and their comparison to relevant literature in section 5.2.4.

6.1.2.3. Aneurysm Wall Thrombin Release Function

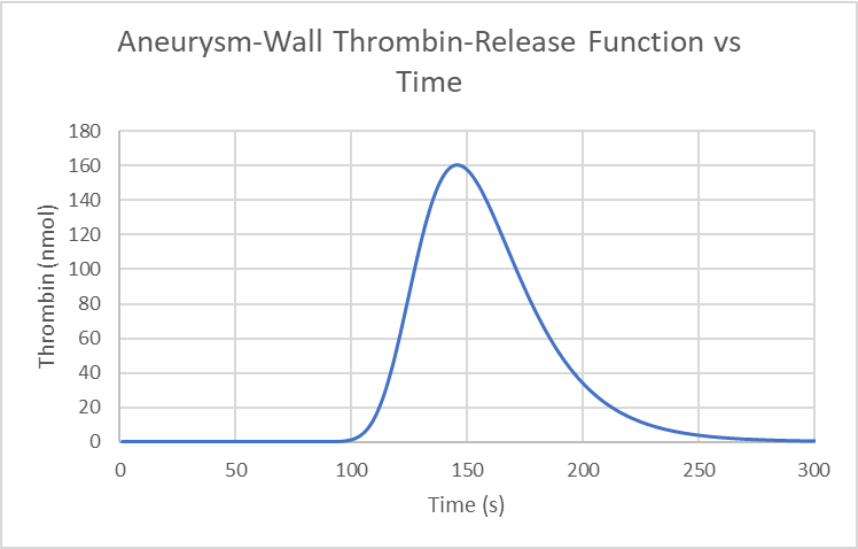

Figure 37: Aneurysm wall thrombin release function vs time

To account for the expression of thrombin from the aneurysm wall, a thrombin release function, shown plotted against time in Figure 37, is applied at the aneurysm wall of each case shown in Figure 34. The variable thrombin release model is derived from a thrombin generation curve fitting function developed by Wagenvoord, Hemker & Kremers, and is applied in a thrombin transport computational study by Hume & Tshimanga et al. [63,71]. This model is derived from thrombin generation curves derived from a stagnant assay. Thrombin generation may not necessarily behave the same way under flow *in vivo*, but the strength of this model has a clearly defined simple formula and limited variables that may be feasibly extracted from samples for individual patients [63]. This function's value represents the damaged tissue of aneurysm and assists in activating clotting in combination with the Michaelis-Menten model described in section 3.1.4 of the CFD methodology.

The function is as follows:

$$F(t) = \frac{(2.73)(\pi)^2}{\varepsilon} e^{-2.73(t-\tau)e^{-\left(\frac{\pi}{\varepsilon}\right)e^{-2.73(t-\tau)}}} \quad (52)$$

Where:

π Peak Thrombin Generation Value (nMol)

ε Total Thrombin Generation (nMol.min)

τ Time to peak (min)

Where the values of π, ε, and τ are 160 nM, 800 nMol.min and 3.02 min, respectively, and result in the curve shown in Figure 37.

The concentration of thrombin released is represented in part by a user-defined scalar (UDS) and the value is effected by the aneurysm wall thrombin release function changing the UDS diffusion near the aneurysm wall [107].

The aneurysm wall function relates to the diffusion value in the following way:

$$F(t) = \Gamma_k \frac{\partial \phi_k}{\partial x_i} \cdot \vec{n} \tag{53}$$

Where:

ϕ_k	Arbitrary Scalar
Γ_k	Diffusion coefficient
$\vec{n}$	Vector normal to the surface

See section 3.1.2.8 of the CFD methodology for the overall UDS equation for the simulation.

6.1.2.4. Porosity Clotting Threshold

The porosity clotting model operates as described in section 3.1.5 of the CFD methodology, such that a porosity value of 0.75 and a permeability of 1e12 m^{-1} is reached when fibrin concentration exceeds 600 nMol, provided prerequisite flow conditions are met.

6.1.3. Patient-Specific Aneurysm Geometry Meshes

The initial mesh for each unstented and stented case is created using ANSYS Mesher. The inlet/outlet zones shown in Figure 34 are composed of hexahedral cells to ensure numerical stability of cells surrounding the inlet/outlet boundaries, and the artery zones are composed of tetrahedral cells to capture the highly complex geometry of the patient-specific geometries; particularly in the stented cases for which fine elements are required for the wall boundary surrounding the subtracted stent. To produce meshes of similar global scale for each stented/unstented geometry comparison, the global element size specific to each stented case mesh is applied to each corresponding unstented case mesh.

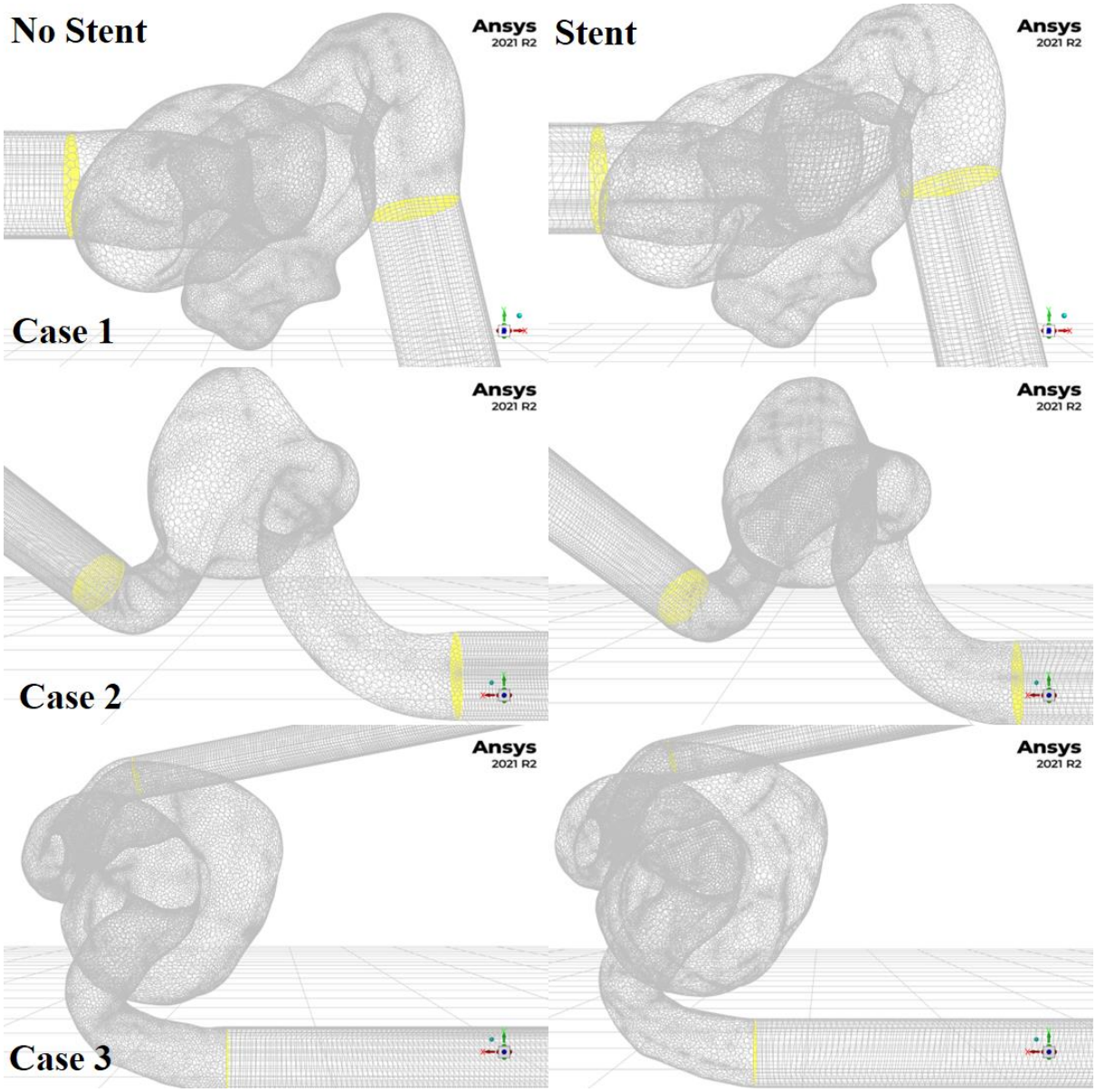

Figure 38: Surface mesh for each patient-specific aneurysm case with and without a flow diverter installed

After being imported to ANSYS FLUENT, the tetrahedral mesh of the artery zone is converted to a polyhedral mesh for each stented and unstented patient case, as shown in Figure 38. In accordance with findings by Sosnowski et al., the conversion to a polyhedral mesh from a tetrahedral mesh significantly improves the convergence of the stented cases by improving the quality of approximation of cell gradients and reducing numerical diffusion of cells surrounding a subtracted stent [149].

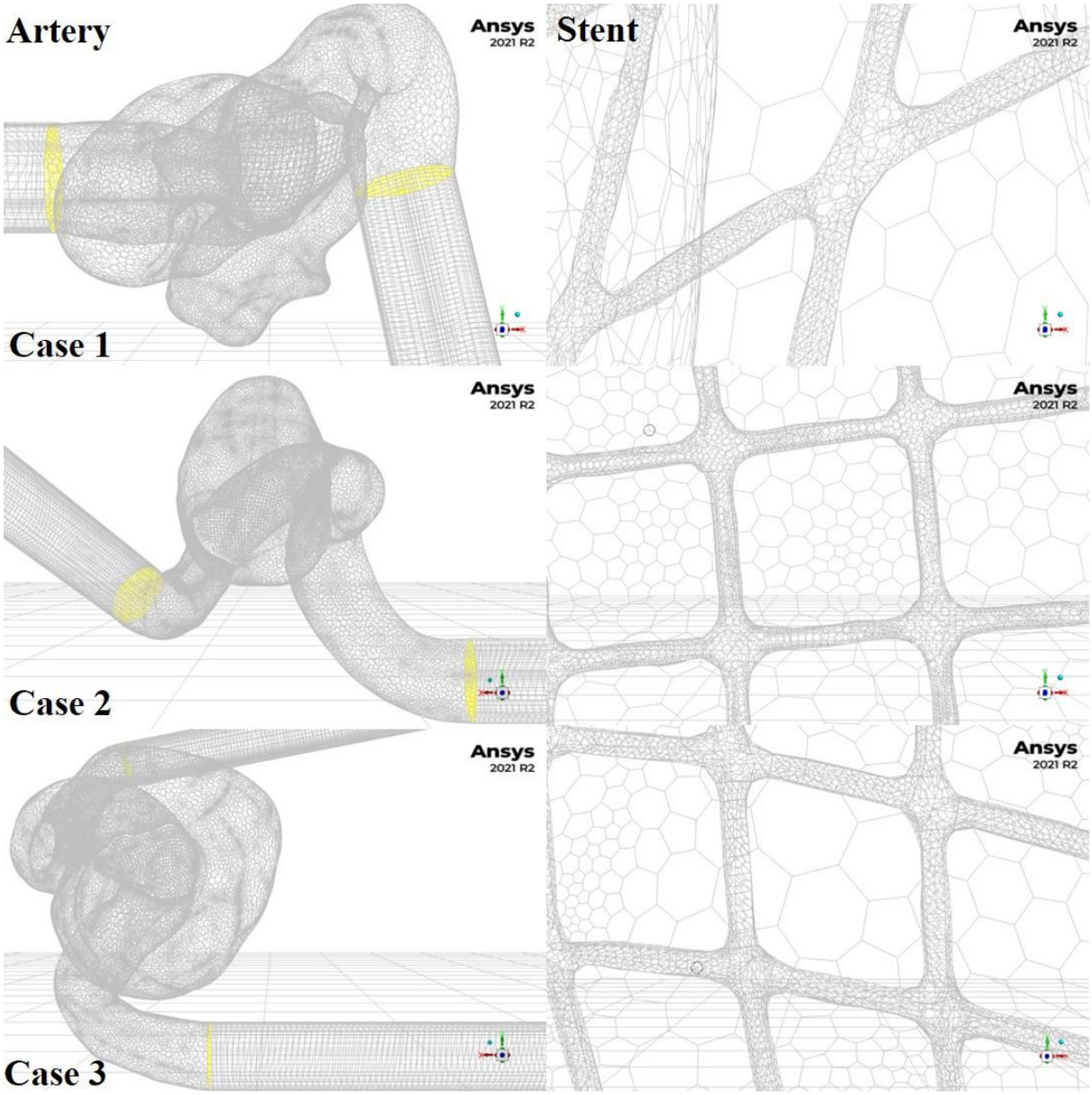

Figure 39: Surface mesh of subtracted flow diverter volume for each stented patient-specific aneurysm case

Furthermore, the conversion to a polyhedral mesh increases the cell size of cells surrounding the stent wall boundary shown in Figure 39, and consequently significantly decreases the cell count of the stented cases, which in turn significantly decreases the otherwise prohibitive computational cost of the stented case simulations. The polyhedral mesh is not necessary for the unstented cases, though is still applied to make the mesh of the unstented cases as analogous to the corresponding stented cases as possible for adequate comparison of flow and clot results.

Case	Stent Presence	Cells	Nodes	Minimum Orthogonal Quality
Case 1	Unstented	307,658	1,330,823	0.231596
	Stented	2,041,788	6,653,958	0.0830319
Case 2	Unstented	173,377	984,366	0.0243124
	Stented	12,153,868	52,619,937	0.0105560
Case 3	Unstented	294,945	1,097,626	0.160887
	Stented	1,781,822	5,616,422	0.120884

Table 23: Polyhedral mesh quantity of cells and nodes, and minimum orthogonal quality for each case with and without the inclusion of a stent

The broad statistics of the polyhedral mesh for each case is shown in Table 23, where the number of cells and nodes indicate the complexity of the mesh, and minimum orthogonal quality indicates the quality for each mesh. Each mesh produces a convergent and stable solution across 300s with timesteps of 0.005s for each stented and unstented case.

6.2. Results

In this section the clotting and flow results for each patient-specific aneurysm case with and without a flow-diverter present are analyzed at different stages of clotting; when a stable clot initially develops, the middle of clot development, and soon after a clot fully develops. The clotting UDS described in section 3.1.4 and 3.1.5 of the CFD methodology reaches a value of 1 when a stable clot is formed via the porosity-based clotting model described in equations (34) and (35) as determined by the formation of sufficient fibrin UDS concentration via the Michaelis-Menten formulation described in equation (33). A volume report indicates the maximum value of the clot UDS in the artery zone for each timestep, and is thus used to determine the beginning of clot development. Full development of a stable clot is determined qualitatively when the formation of a clot UDS reaches a steady state until the end of the simulation, which can be reasonably assumed not to occur by 200s due to the significant reduction in thrombin expression by this time in the aneurysm wall thrombin release function shown in Figure 37. The middle of clot development is identified as being roughly halfway between the initial development of a stable clot and the full clot development.

For each case, three figures are used to demonstrate each stage of clot development, wherein flow and clotting within the artery zone shown in Figure 34 are demonstrated across each stage of a pulse wavelength shown in Figure 36, including the mean flow of an ascending pulse (top), the upper velocity peak (upper-middle), the mean of a descending pulse (lower middle), and the lower velocity peak (bottom). Velocity is demonstrated via a streamline, and clot presence is indicated in red by a contour, which is applied to the wall boundaries of the artery zone (transparent red), as well as a plane intersecting the aneurysm to demonstrate a cross-section of the clot (solid red).

6.2.1. Case 1

6.2.1.1. Initial Clot

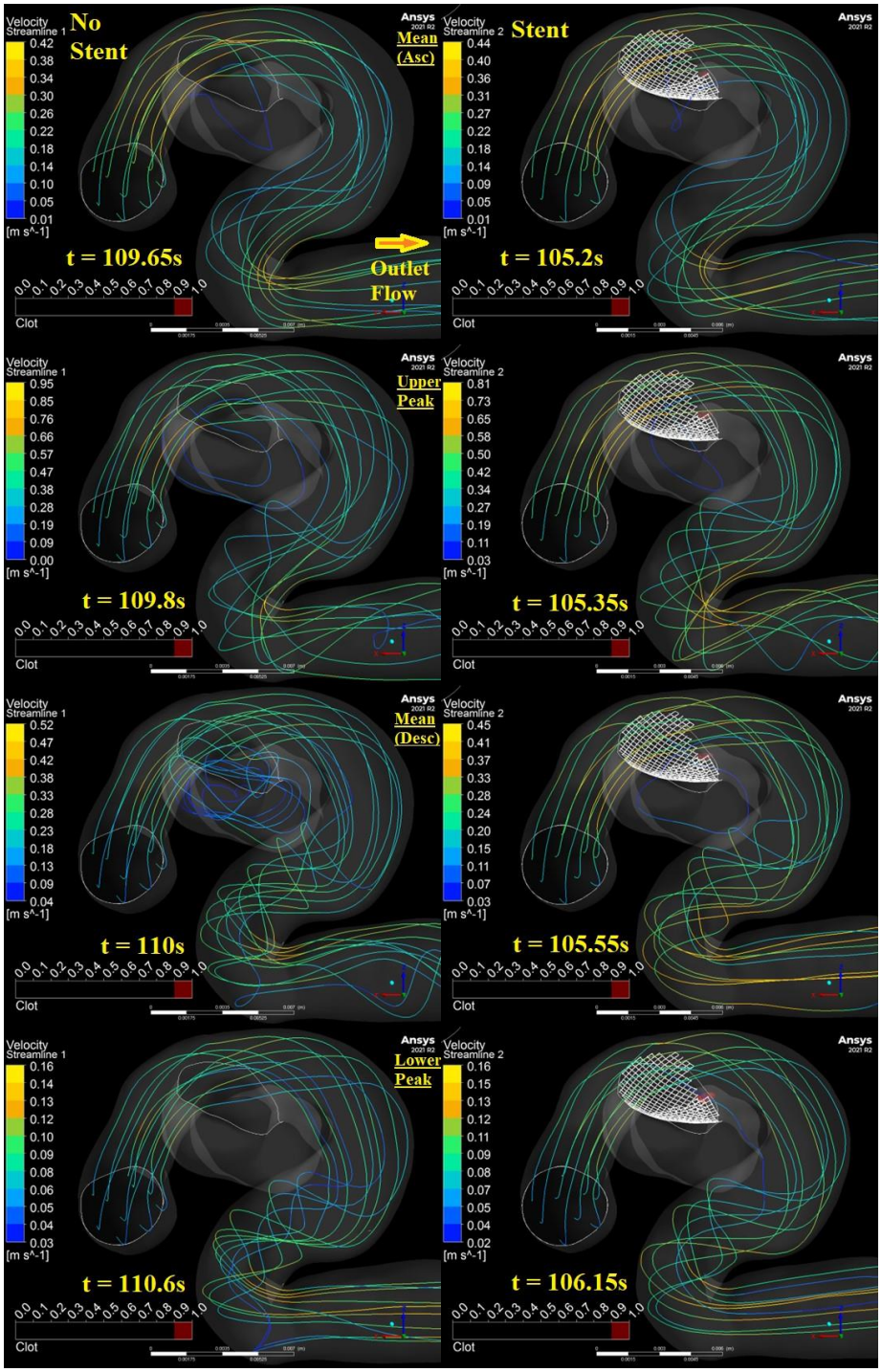

Figure 40: Velocity and initial clot comparison between patient geometry 1 without a stent (left) and with a stent (right) at different times throughout a pulse wavelength shown in Figure 36; mean pulsatile flow velocity ascending towards upper velocity peak (top), pulsatile flow upper velocity peak (upper middle), mean pulsatile flow velocity descending towards lower velocity peak (lower middle), pulsatile flow lower velocity peak (bottom). Direction of flow is demonstrated relative to the outward flow boundary by an arrow (top left).

A comparison between the stented and unstented case of patient geometry 1 during initial clot formation is shown in Figure 40, and is interpreted as described in the introductory paragraphs of results section 6.2.

Flow between the two cases is very similar in both magnitude and location of streamlines, except during the mean descending velocity (lower-middle), where the stent of the stented case appears to prevent much of the flow into the aneurysm by comparison to the unstented case, for which there is relatively high velocity recirculation within the aneurysm. Maximum flow magnitudes in both cases are otherwise much higher than the corresponding inlet Fourier transform velocity shown in Figure 36, though these high velocities appear to be localized to certain areas of the flow volume, particularly at the inner curves of the parent artery near where fluid enters and leaves the artery zone, corresponding with local narrowing of the parent artery.

Notably, the high velocity flow along the streamline at the inner curve of the parent artery just downstream of the inlet zone drops in magnitude significantly as it passes by the aneurysm neck in unstented case. The corresponding streamlines in the stented case, by contrast, maintain a high velocity magnitude as they pass by the stent at all demonstrated times in Figure 40, indicating the flow diverter geometry successfully directs flow away from the aneurysm opening for this patient-derived aneurysm case.

Otherwise, the median velocity of streamlines indicated by the legends in Figure 40 for a particular time is roughly analogous to the corresponding inlet Fourier transform velocity shown in Figure 36.

The stented case begins clotting roughly 4s earlier than the unstented case and produces a small but visible clot at the aneurysm wall just downstream of the stent.

6.2.1.2. Mid-Development Clot

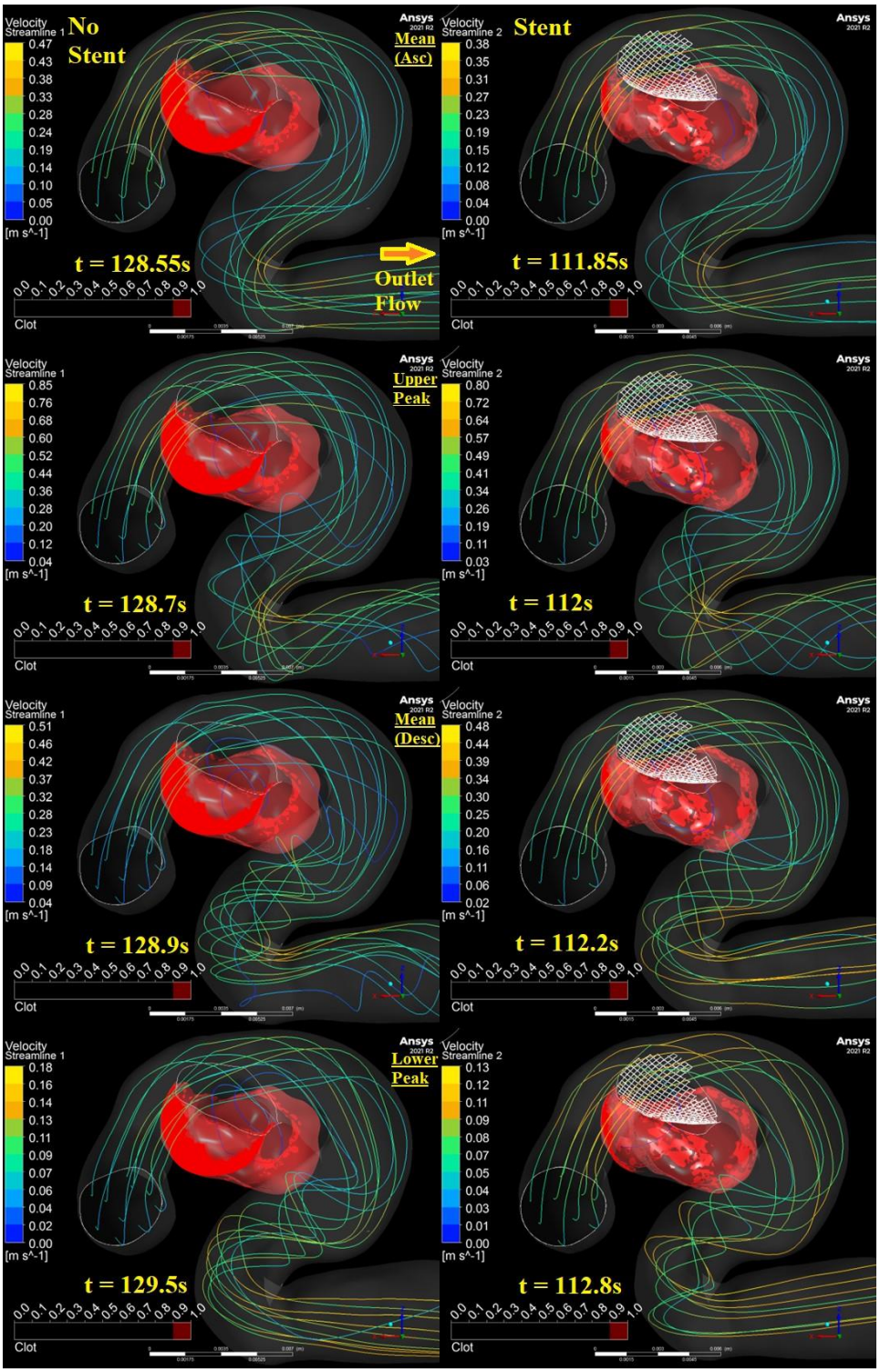

Figure 41: Velocity and mid-development clot comparison between patient geometry 2 without a stent (left) and with a stent (right) at different times throughout a pulse wavelength shown in Figure 36; mean pulsatile flow velocity ascending towards upper velocity peak (top), pulsatile flow upper velocity peak (upper middle), mean pulsatile flow velocity descending towards lower velocity peak (lower middle), pulsatile flow lower velocity peak (bottom). Direction of flow is demonstrated relative to the outward flow boundary by an arrow (top left).

A comparison between the stented and unstented case of patient geometry 1 during the middle of clot development is shown in Figure 41, and is interpreted as described in the introductory paragraphs of results section 6.2.

Observations made for flow during initial clot development shown in Figure 40 remain valid for flow during the middle of clot development shown in Figure 41, except for the flow streamlines within the aneurysm of the unstented case, which by the middle of clot development demonstrate significantly lower recirculation velocity across all stages of the pulse due to the growing presence of porous clot (red).

As shown in Figure 41, the clot during the middle of clot development is more advanced in the unstented case than the stented case for the times shown. This is due to the significantly slower rate of clot propagation in the unstented case than the stented case, which produces a fully developed clot by 117s. In both cases the clot grows outwards from the aneurysm wall, and reduces the effective flow volume in the aneurysm as evidenced by the change in location of streamlines during mean descending flow (lower-middle) from along the aneurysm wall at the initial formation of a stable clot shown in Figure 40 to circulating around the middle of the aneurysm and away from formed clot (red) during the middle of clot development shown in Figure 41.

6.2.1.3. Fully Developed Clot

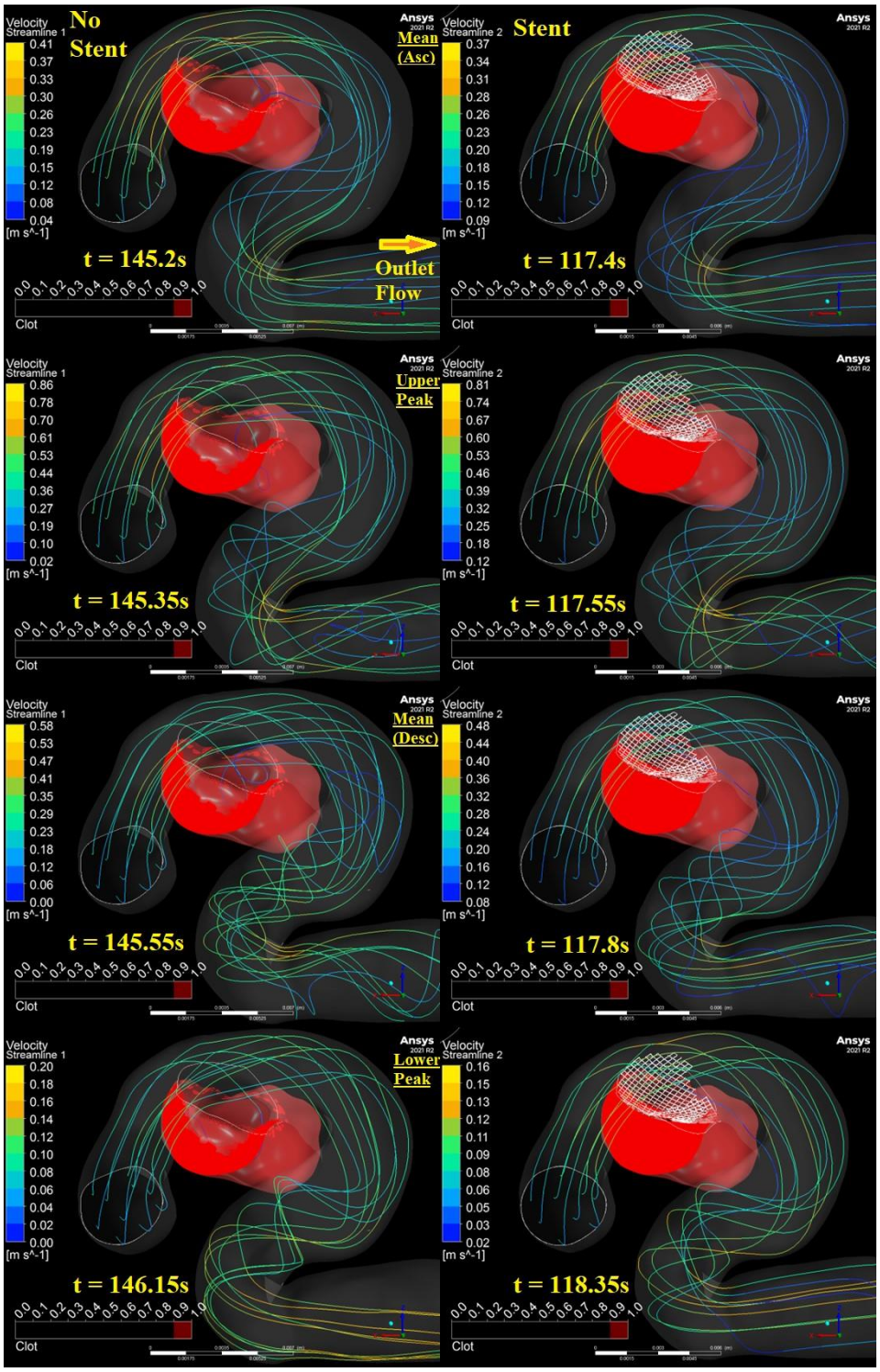

Figure 42: Velocity and fully developed clot comparison between patient geometry 1 without a stent (left) and with a stent (right) at different times throughout a pulse wavelength shown in Figure 36; mean pulsatile flow velocity ascending towards upper velocity peak (top), pulsatile flow upper velocity peak (upper middle), mean pulsatile flow velocity descending towards lower velocity peak (lower middle), pulsatile flow lower velocity peak (bottom). Direction of flow is demonstrated relative to the outward flow boundary by an arrow (top left).

A comparison between the stented and unstented case of patient geometry 1 just after full clot development is shown in Figure 42, , and is interpreted as described in the introductory paragraphs of results section 6.2.

As shown in Figure 42, the fully developed clot in the stented case completely occludes the aneurysm. The fully developed clot in the unstented case, by comparison, leaves a residual volume in the aneurysm, through which velocity streamlines continue to travel.

These results indicate that the flow diverter is successful in redirecting flow away from the aneurysm, such that sufficiently low shear rates can be achieved within the aneurysm to fully occlude. Although shear rates within the aneurysm are periodically low enough for a clot to develop without a flow diverter as in the unstented case, high rates of flow enter the aneurysm and create periodically high shear rates and rapid flow patterns that eject clotting reagents into the parent artery, resulting in an environment unsuitable for sustained clot formation during thrombosis.

6.2.2. Case 2

6.2.2.1. Initial Clot

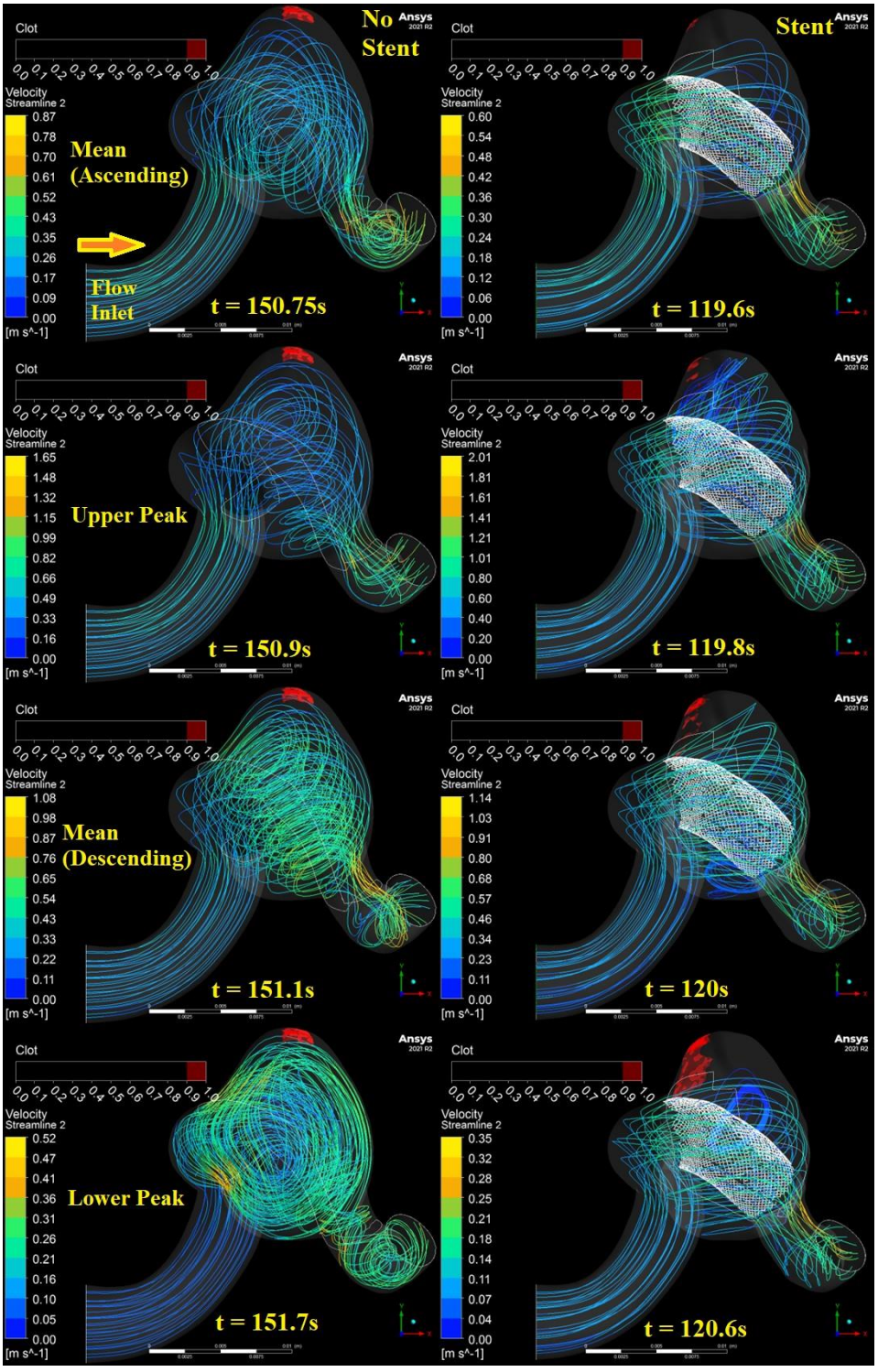

Figure 43: Velocity and initial clot comparison between patient geometry 1 without a stent (left) and with a stent (right) at different times throughout a pulse wavelength shown in Figure 36; mean pulsatile flow velocity ascending towards upper velocity peak (top), pulsatile flow upper velocity peak (upper middle), mean pulsatile flow velocity descending towards lower velocity peak (lower middle), pulsatile flow lower velocity peak (bottom). Direction of flow is demonstrated relative to the incoming flow boundary by an arrow (top left).

A comparison between the stented and unstented case of patient geometry 2 during initial clot formation is shown in Figure 43, and is interpreted as described in the introductory paragraphs of results section 6.2.

Flow magnitudes between the two cases are similar at corresponding times of the pulse, but there is significantly more recirculation and higher magnitude flow within the aneurysm for the unstented case than the stented case across all stages of a pulse. This is evidenced by the vortex-like structure created by the flow streamlines within the aneurysm of the unstented case. This difference is reflected by the time-gap for initial clot formation between the two cases, where the stented case begins producing a stable clot roughly 30s earlier than the unstented case, which only produces a stable clot at roughly 150s, just after peak thrombin expression by the aneurysm wall shown in Figure 37. The difference in flow patterns within the aneurysm also affects the location of clot development for each case, where in the unstented case clot growth begins at the very top portion of the aneurysm, and in the stented case clot growth begins at the side of the aneurysm closest to the incoming flow from the parent artery.

Maximum flow magnitudes in both cases are otherwise much higher than the corresponding inlet Fourier transform velocity shown in Figure 36, though these high velocities appear to be localized to certain areas of the artery, particularly at the inner curves of the parent artery ahead of the outlet zone potentially corresponding with local narrowing of the artery. Otherwise, the median velocity of streamlines indicated by the legends in Figure 43 are roughly analogous to corresponding inlet Fourier transform velocity shown in Figure 36.

6.2.2.2. Mid-Development Clot

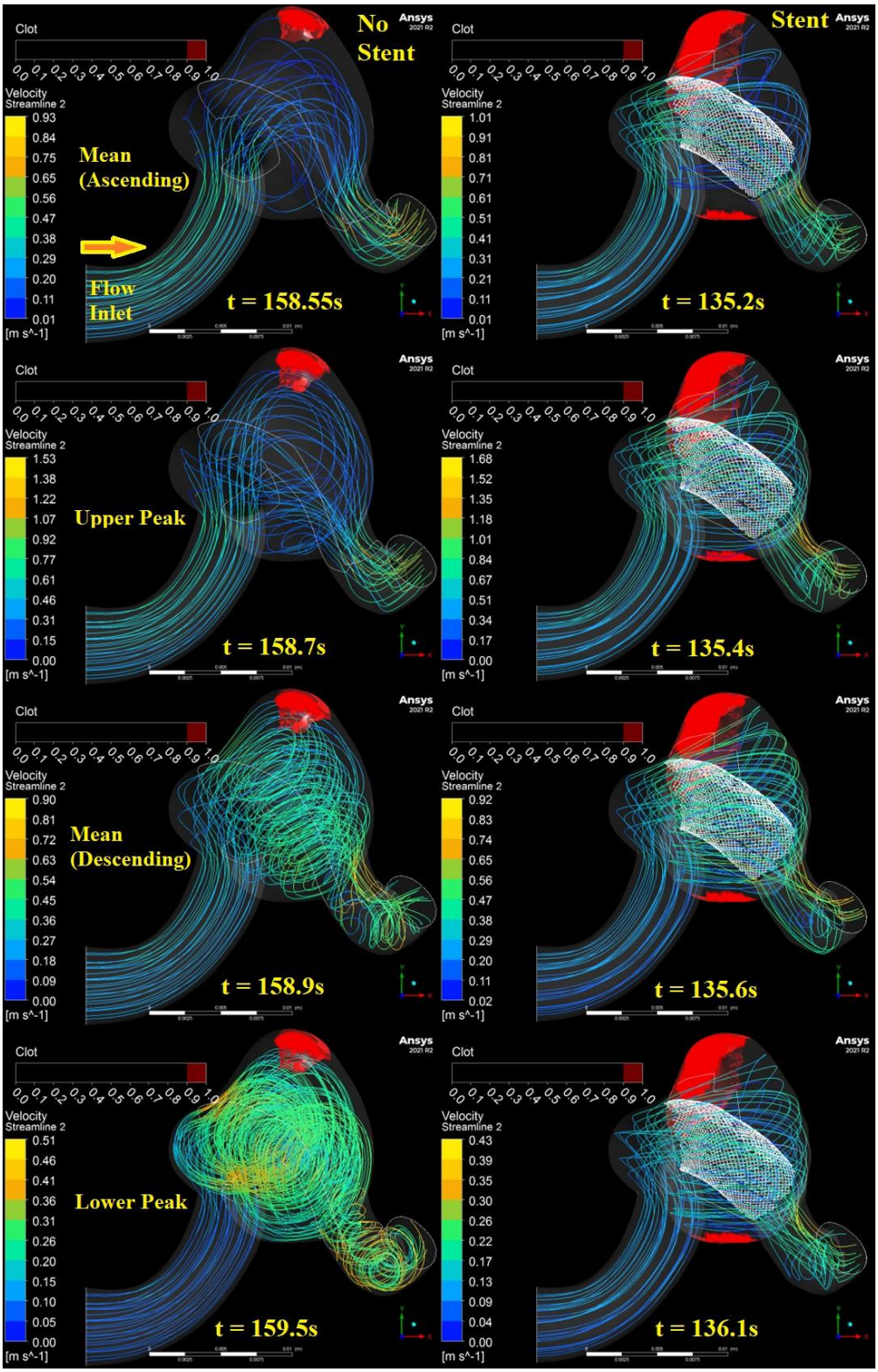

Figure 44: Velocity and mid-development clot comparison between patient geometry 2 without a stent (left) and with a stent (right) at different times throughout a pulse wavelength shown in Figure 36; mean pulsatile flow velocity ascending towards upper velocity peak (top), pulsatile flow upper velocity peak (upper middle), mean pulsatile flow velocity descending towards lower velocity peak (lower middle), pulsatile flow lower velocity peak (bottom). Direction of flow is demonstrated relative to the incoming flow boundary by an arrow (top left).

A comparison between the stented and unstented case of patient geometry 2 during the middle of clot development is shown in Figure 44, and is interpreted as described in the introductory paragraphs of results section 6.2.

Observations made for flow during initial clot development shown in Figure 43 remain consistent for flow during the middle of clot development shown in Figure 44, which appears to have a large effect on clot development for both cases. Specifically, clot propagation since the initial formation of stable clot in Figure 43 is marginal for the unstented case relative to the size of the aneurysm as shown in Figure 44. This is true to a lesser extent for the stented case, in which a large enough clot has formed at the top of the aneurysm to slightly alter flow trajectory within the aneurysm, and a separate clot has formed tightly against the bottom wall of the aneurysm.

6.2.2.3. Fully Developed Clot

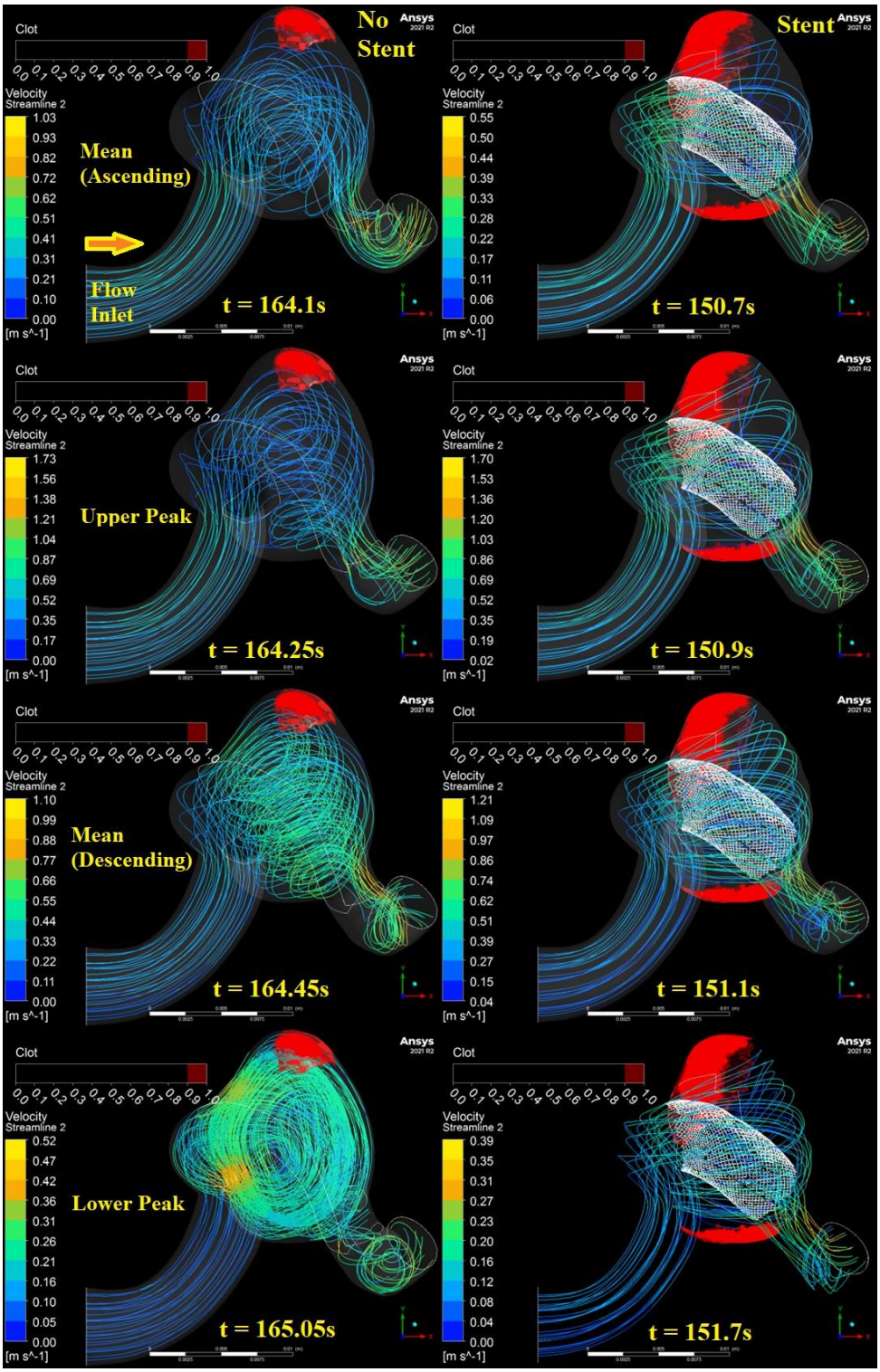

Figure 45: Velocity and fully developed clot comparison between patient geometry 2 without a stent (left) and with a stent (right) at different times throughout a pulse wavelength shown in Figure 36; mean pulsatile flow velocity ascending towards upper velocity peak (top), pulsatile flow upper velocity peak (upper middle), mean pulsatile flow velocity descending towards lower velocity peak (lower middle), pulsatile flow lower velocity peak (bottom). Direction of flow is demonstrated relative to the incoming flow boundary by an arrow (top left).

A comparison between the stented and unstented case of patient geometry 2 just after full clot development is shown in Figure 45, and is interpreted as described in the introductory paragraphs of results section 6.2.

As shown in Figure 45, the flow diverter is unsuccessful in sufficiently redirecting flow away from the aneurysm wall to allow for significant occlusion of the aneurysm. As such, the fully developed clot in both the stented and unstented case leaves an enormous residual aneurysm that qualitatively is not significantly smaller than the original aneurysm.

Although shear rates within the aneurysm are periodically low enough for a clot to develop in portions of the aneurysm, the high rates of flow entering the aneurysm create periodically high shear rates and rapid flow patterns that eject clotting reagents into the parent artery, resulting in an environment unsuitable for sustained clot formation in either case.

A different flow diverter or perhaps different placement of the same flow diverter shown in Figure 33 may be more successful in creating such an environment under the prescribed inlet flow velocity shown in Figure 36, though it is important to consider that the prescribed inlet and outlet boundary conditions are not specific to the patient from which the aneurysm geometry was derived, and may create more overpronounced or even subdued flow conditions within the aneurysm than is present in vivo.

6.2.3. Case 3

6.2.3.1. Initial Clot

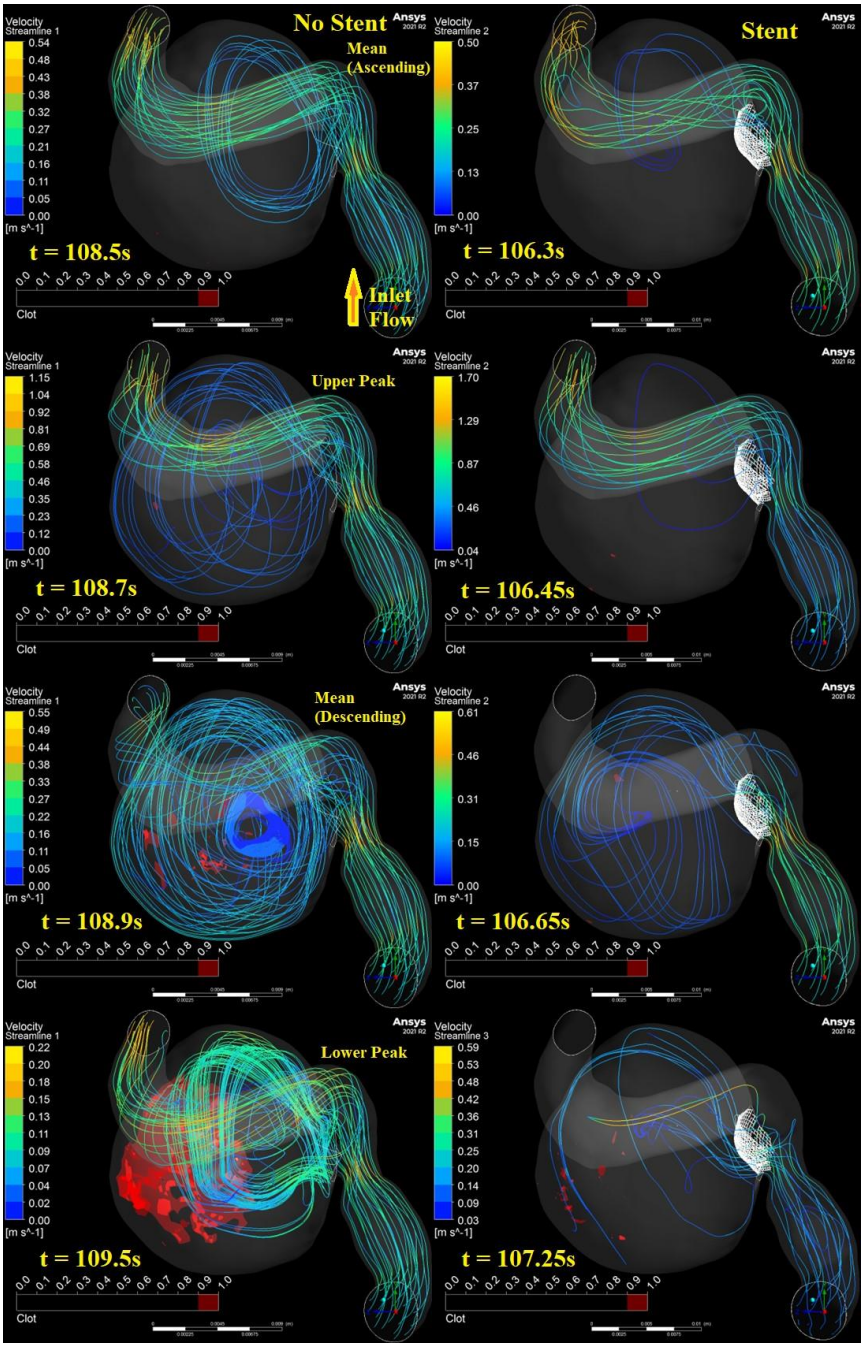

Figure 46: Velocity and initial clot comparison between patient geometry 3 without a stent (left) and with a stent (right) at different times throughout a pulse wavelength shown in Figure 36; mean pulsatile flow velocity ascending towards upper velocity peak (top), pulsatile flow upper velocity peak (upper middle), mean pulsatile flow velocity descending towards lower velocity peak (lower middle), pulsatile flow lower velocity peak (bottom). Direction of flow is demonstrated relative to the incoming flow boundary by an arrow (top left).

A comparison between the stented and unstented case of patient geometry 3 during initial clot formation is shown in Figure 46, and is interpreted as described in the introductory paragraphs of results section 6.2.

Flow between the two cases is similar, though the unstented case demonstrates significantly higher flow rates within the aneurysm than the stented case at corresponding stages of a pulse, and the maximum velocity magnitude of the stented case is significantly higher than the unstented case at the upper velocity peak and the lower velocity peak, though this may potentially be attributed to a slight mismatch in timesteps corresponding to a pulse stage as indicated by Figure 36 due to the 0.05s timestep data file save intervals for both simulations. The stented case also demonstrates streamlines that end within the aneurysm during the mean descending pulse and lower velocity peak, as opposed to the unstented case which demonstrates streamlines entering the aneurysm and circulating back out into the parent artery. Otherwise, high velocity sections of the velocity streamlines occur at the narrowing of the artery ahead of the aneurysm and towards the artery ahead of the outlet zone shown in Figure 34.

Maximum flow magnitudes in both cases are much higher than the corresponding inlet Fourier transform velocity shown in Figure 36, potentially corresponding with narrowing of the artery ahead of the aneurysm.

Otherwise, median velocity of the streamlines is roughly analogous to corresponding inlet Fourier transform velocity shown in Figure 36 across most of a pulse save for the upper velocity peak for both cases.

The stented case begins clotting roughly 2s earlier than the unstented case, though the clot propagates at a faster rate in the unstented case as shown in Figure 46, where at the lower velocity peak the unstented case produces a larger clotted area along the aneurysm wall than the stented case.

6.2.3.2. Mid-Development Clot

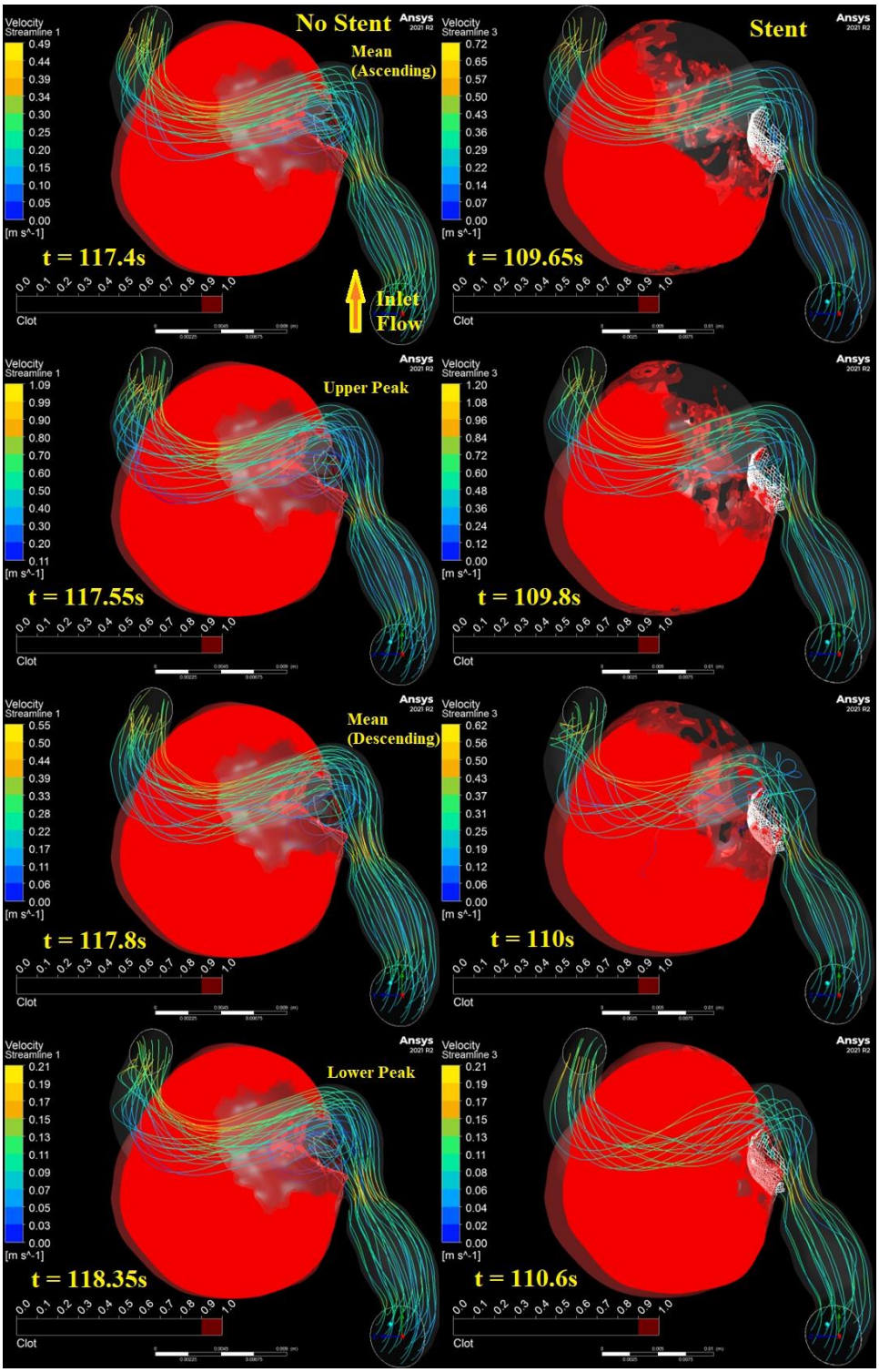

Figure 47: Velocity and mid-development clot comparison between patient geometry 3 without a stent (left) and with a stent (right) at different times throughout a pulse wavelength shown in Figure 36; mean pulsatile flow velocity ascending towards upper velocity peak (top), pulsatile flow upper velocity peak (upper middle), mean pulsatile flow velocity descending towards lower velocity peak (lower middle), pulsatile flow lower velocity peak (bottom). Direction of flow is demonstrated relative to the incoming flow boundary by an arrow (top left).

A comparison between the stented and unstented case of patient geometry 3 during the middle of clot development is shown in Figure 47, and is interpreted as described in the introductory paragraphs of results section 6.2.

Observations made for flow during initial clot development shown in Figure 46 remain mostly valid for flow during the middle of clot development shown in Figure 47. However, at the middle of clot development circulation from the artery into the aneurysm narrows with the growth of the clot in the unstented case, and is reduced significantly in the stented case, evidenced by the lack of flow streamlines into the aneurysm. Maximum velocity magnitudes also become more comparable between the two cases at corresponding stages of a pulse shown in Figure 36, and maximum velocity within the aneurysm consistently occurs at the narrowing of the artery ahead of the aneurysm and the inner bending wall of the artery ahead of the outlet zone.

Clot development for the stented case progresses significantly faster than the unstented case, where in the stented case the aneurysm occludes rapidly over the course of the pulse as shown in Figure 47, and by comparison the unstented case does not grow significantly over a pulse 7s ahead of the stented case due to the high velocity flow entering the aneurysm from the parent artery.

6.2.3.3. Fully Developed Clot

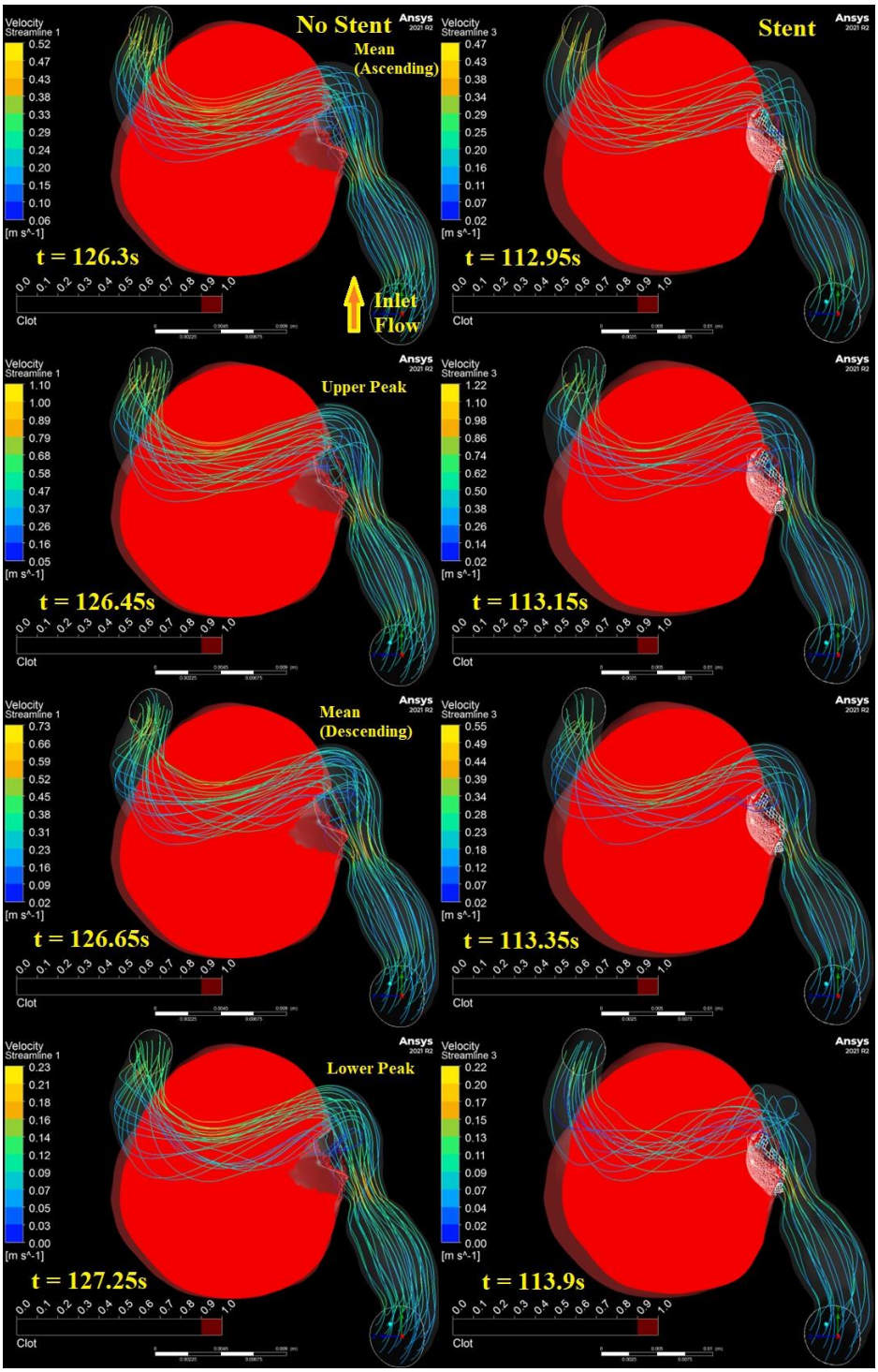

Figure 48: Velocity and fully developed clot comparison between patient geometry 3 without a stent (left) and with a stent (right) at different times throughout a pulse wavelength shown in Figure 36; mean pulsatile flow velocity ascending towards upper velocity peak (top), pulsatile flow upper velocity peak (upper middle), mean pulsatile flow velocity descending towards lower velocity peak (lower middle), pulsatile flow lower velocity peak (bottom). Direction of flow is demonstrated relative to the incoming flow boundary by an arrow (top left).

A comparison between the stented and unstented case of patient geometry 3 just after full clot development is shown in Figure 48, and is interpreted as described in the introductory paragraphs of results section 6.2.

As shown in Figure 48, the fully developed clot in the stented case completely occludes the aneurysm. The fully developed clot in the unstented case, by comparison, creates a residual neck.

These results indicate that the flow diverter is successful in redirecting flow away from the aneurysm, such that sufficiently low shear rates can be achieved within the aneurysm to fully occlude.

Due to the size and position of the aneurysm, flow rates within the aneurysm are periodically low enough for a large clot to form that nearly fully occludes the aneurysm without a stent. However, as the clot approaches the parent artery it becomes subject to much higher flow rates, which significantly increase the shear rate, and carry clotting reagents downstream the parent vessel.

6.3. Discussion of Results and Comparison to Literature

The computational model of direct thrombosis in cerebral aneurysms compared to the novel PIV-based *in vitro* clotting flow experiment produces a clotting outcome within individual patient-derived aneurysm geometries with and without the inclusion of a flow diverter to determine the efficacy of flow diverter placement in full occlusion of anatomically accurate aneurysms. Figure 42 demonstrates that the clotting outcome produced by the thrombosis model in the case 1 aneurysm leaves a residual aneurysm absent of a flow altering device (left), and a fully occluded aneurysm with the placement of a flow diverter (right). In the case 3 aneurysm shown in Figure 48, flow diverter placement similarly results in full occlusion of the giant aneurysm (right), as opposed to the residual neck left in the aneurysm without surgical intervention (left). By contrast, the clotting outcome produced by the thrombosis model for the case 2 aneurysm shown in Figure 45 results in a large residual aneurysm regardless of whether a flow diverter is installed.

Spontaneous thrombosis, although rare, has been reported to occur in saccular aneurysms such as the patient geometries case 1 and case 3 shown in Figure 33 [150]. Spontaneous full thrombosis of giant saccular aneurysms such as in the case 3 patient geometry seen in Figure 42 (left) is also well documented [150,151]. Full occlusion of the aneurysm with no residual volume is the intended outcome of flow diverter placement in an artery, and as such the fully occluded aneurysms for the stented cases of patient geometries case 1 and case 3 shown in Figure 42 and Figure 48, respectively, are outcomes that can be reasonably assumed to occur.

Fusiform aneurysms such as the case 2 patient geometry shown in Figure 33 are not trivial to treat, and according to a retrospective analysis of pipe embolization devices by Griffin et al. may require

multiple flow diverters and endovascular coiling to reach a favorable aneurysm occlusion rate, which was not achieved in roughly a quarter of cases [152]. With this insight, the lack of clot formation despite the presence of a flow diverter in the case 2 patient geometry shown in Figure 45 (right) is a realistic outcome, if not a favorable one, that may still be overcome with the inclusion of endovascular coiling or a second flow diverter.

The thrombosis model of cerebral aneurysms presented in this research applies a free-slip or zero-shear boundary condition at all the wall boundaries, a departure from nearly every computational model for predicting clot development to date, which almost universally apply no-slip boundary conditions to artery walls in the case of finite-volume-method CFD simulations [55,57,64,71,75,134]. There has long been evidence, however, that a partial-slip wall boundary is more appropriate for representing some of the non-Newtonian flow behavior of blood [100,135]. While the effects of the non-Newtonian characteristics of blood are usually considered negligible in arterial flow modeling with exception to flow through small vessels, there are a growing number of models demonstrating that these non-Newtonian effects are significant even in large vessels with predominantly high shear rates [83].

While the modelling and inclusion of a partial-slip wall boundary function is outside the scope of the presented thrombosis model, the results of the validation simulation presented in Figure 28-Figure 29 of section 5.2.2 clearly demonstrate better alignment to the flow results of the PIV-based thrombin-fibrinogen experiment with free-slip wall boundaries as opposed to no-slip wall boundaries, despite the fibrinogen-saline solution being modelled with Newtonian fluid properties as demonstrated in the validation simulation specific methodology detailed in section 5.1.

Given that the fibrinogen-saline solution for the PIV-based thrombin-fibrinogen experiment described in section 4.2.1.1 is a colloid similar to blood plasma but lacking other macromolecules, that blood plasma demonstrates non-Newtonian viscoelastic properties and shear-thinning, and there is reasonable evidence that the elastic properties of fibrinogen are potentially the most significant contributor to non-Newtonian shear-thinning in blood plasma; fibrinogen-saline solution appears to have some analog to blood plasma for flow modeling [137,139,140]. Therefore there are grounds to assume that a partial-slip wall boundary may also be applicable to blood plasma, and given that blood plasma is the fluid in which red blood cells are suspended there is a possibility that partial-slip wall boundary is significant to model flow in thrombosis models for full blood. By this thread of reasoning, the fibrinogen-saline solution has some analog to blood with respect to wall boundary exploration. As such, the free-slip wall boundary is favored over the no-slip wall boundary as the mathematical

simplification of the more physiologically accurate but unparameterized partial-slip condition to determine clotting outcomes for the patient-specific aneurysm case geometries.

This, however, introduces complications when comparing clotting outcomes to aneurysm clotting models that use wall shear stress as a determinant or marker for locations of clot development, since in the case of a free-slip wall boundary, wall shear stress is zero. This unfortunately allows only for speculative comparison of clotting outcomes using this metric, which is of questionable value. Although in the model by Rayz et al., the cross-sectional plane demonstrating increased flow residence times with the ink scalar method for patient 3 shown in their figure 6 demonstrates good agreement with the clotting outcomes of the fusiform aneurysm of the case 2 patient aneurysm geometry shown in Figure 45 of the model presented here [153].

Otherwise, several models demonstrate similar flow behavior to the patient geometry cases. The non-Newtonian pulsatile flow model by Yang et al. demonstrates the decrease of flow within the aneurysm with the increase of coiling porosity, which shows agreement with the gradual decrease in flow within the aneurysm of patient geometries 1 and 3 shown across Figure 40-Figure 43 and Figure 46-Figure 48 due to the porosity > 0.75 in the aneurysm (not visible) [154]. The MRI and corresponding CFD streamlines for cerebral arteries in work by Cebral et al. demonstrate similar velocity magnitude at peak systole to the upper velocity peaks across all patient geometries presented in this chapter and shown in Figure 40-Figure 48 where areas of highest velocity correlate with narrowing of blood vessels for both models [82].

There is some analog between the flow streamline distribution of the patient geometry cases shown in Figure 40-Figure 43, and Figure 46 (right) to the flow streamlines presented by Ou et al. in patient geometries with stents modeled as porous media, despite their use of a steady flow inlet and no-slip wall boundaries [141].

Only two computational models of thrombosis in cerebral aneurysm studies exist that employ similar biochemical models, and apply the model to realistic aneurysms with and without flow diverters [57,65,67]. Of these models, only Sarrami et al. features flow and clot validation [65,68].

The model presented in this thesis is partially built upon the model by Ngoepe et al., and departs from their framework with pulsatile inlet/outlet and free-slip wall boundaries, and a reduced biochemical model built upon work by Jimoh-Taiwo et al. [57,75]. The clotting outcomes generated by Ngoepe et al. in both stented and unstented cases of the ICA giant aneurysm shown in their figure 4 appear more conservative than clotting outcomes for the patient geometry case 3 shown in Figure 48. This discrepancy is potentially due to a variety of factors. When considering flow in isolation, the steady

flow boundaries applied by Ngoepe et al., which have been demonstrated to significantly impact protein transport, do not account for periodically shifting shear rates which for their model impacts the expression of tissue factor [57]. Otherwise the model presented in this thesis simplifies and bypasses many biochemical mechanisms that otherwise would limit clot growth, potentially contributing to an overestimate in clotting by comparison to Ngoepe et al. [57].

The model by Sarrami et al. features *in vitro* flow and clot validation by an experiment presented by Gester et al. [65,68]. Sarrami et al. has applied this model to patient-specific geometries to predict flow-diversion success rates [67]. The validation experiment by Gester et al. differs from the novel PIV-based thrombin-fibrinogen clotting flow experiment insofar as clotting and flow are not measured simultaneously, as discussed in sections 4.4 and 5.4. The computational model of direct thrombosis in cerebral aneurysms presented in this thesis also differs from the model by Sarrami et al. insofar as it features a reduced biochemical model inclusive of only three proteins, and includes a biomechanical representation of clotting which is not considered by Sarrami et al. [65]. Their model is applied to four giant saccular aneurysms, and their stented geometry clotting predictions align well with the clotting outcome of the stented case 3 patient geometry simulation for a giant aneurysm shown in Figure 48 [67]. Sarrami et al. reports, however, that their model produces no clot for their unstented cases, a departure from the results of the unstented case 3 patient geometry clotting outcome shown in Figure 48. This difference may be accounted for by either, the difference in biochemical approach by Sarrami et al. which includes a wall shear stress threshold for tissue factor expression as opposed to the direct expression of thrombin from the aneurysm wall in our model, or for the inclusion of biomechanical consideration of clot development in our model, which significantly alters the flow field within the aneurysm as shown in both the patient geometry case 1 and 3 in Figure 40-Figure 42 and Figure 46-Figure 48. Crucially, however, both results are plausible, as full occlusion of giant saccular aneurysms independent of invasive treatment is well documented in cases of acute thrombosis [150,151].

Ultimately, the computational model of direct thrombosis in cerebral aneurysms validated by a novel PIV-based *in vitro* thrombin-fibrinogen clotting flow experiment demonstrates reasonable clotting outcomes. There are relatively few models with which it can be adequately compared to, however, and further validation of assumptions against macroscale *in vitro* flow experiments employing biological blood-derived fluids and against patient-specific clotting outcomes in-vivo are required.

6.4. Conclusion and Data Quantities

The study presents a comparison of patient-specific clotting outcomes of three cases with and without diverters for a validated model of direct thrombosis of cerebral aneurysms.

The computational thrombosis model shows that aneurysms can be fully occluded with the placement of a flow diverter, as seen in case 1 and case 3. Without a flow diverter, residual aneurysms remain. Spontaneous thrombosis can occur in saccular aneurysms, and the occlusion observed in case 3 is consistent with documented outcomes for giant saccular aneurysms. In case 2, the model predicts a large residual aneurysm regardless of flow diverter placement, reflecting the complexity of treating fusiform aneurysms, which often require additional interventions like endovascular coiling.

The model uses a free-slip wall boundary condition as a simplification of a theoretically more physiologically accurate but thus far unparameterized macrovascular partial-slip condition. The application of free-slip at the wall boundary contrasts with most models that use no-slip boundaries. This is done to align the model with the non-Newtonian flow behavior observed in the PIV-based thrombin-fibrinogen experiment, which are assumed to be relevant to whole blood based upon fibrinogen's theorized primary contribution to the non-Newtonian properties of blood plasma.

Overall, the computational model of direct thrombosis in cerebral aneurysms, validated by a novel PIV-based in vitro clotting flow experiment, produces reasonable clotting outcomes by comparison to literature. There are relatively few models with which it can be adequately compared to however, and further validation of assumptions by comparison to macroscale in vitro and in vivo clotting outcomes is required.

Max Velocity		Mean (Asc)	Upper Peak	Mean (Desc)	Lower Peak
Patient 1 (Initial)	No Stent	0.42 m/s	0.95 m/s	0.52 m/s	0.16 m/s
	Stent	0.44 m/s	0.81 m/s	0.45 m/s	0.16 m/s
Patient 1 (Mid)	No Stent	0.47 m/s	0.85 m/s	0.51 m/s	0.18 m/s
	Stent	0.38 m/s	0.8 m/s	0.48 m/s	0.13 m/s
Patient 1 (Full)	No Stent	0.41 m/s	0.86 m/s	0.58 m/s	0.2 m/s
	Stent	0.37 m/s	0.81 m/s	0.48 m/s	0.16 m/s
Patient 2 (Initial)	No Stent	0.87 m/s	1.65 m/s	1.08 m/s	0.52 m/s
	Stent	0.6 m/s	2.01 m/s	1.14 m/s	0.35 m/s
Patient 2 (Mid)	No Stent	0.93 m/s	1.53 m/s	0.9 m/s	0.51 m/s
	Stent	1.01 m/s	1.68 m/s	0.92 m/s	0.43 m/s
Patient 2 (Full)	No Stent	1.03 m/s	1.73 m/s	1.1 m/s	0.52 m/s
	Stent	0.55 m/s	1.7 m/s	1.21 m/s	0.39 m/s
Patient 3 (Initial)	No Stent	0.54 m/s	1.15 m/s	0.55 m/s	0.22 m/s
	Stent	0.5 m/s	1.7 m/s	0.61 m/s	0.59 m/s
Patient 3 (Mid)	No Stent	0.49 m/s	1.09 m/s	0.55 m/s	0.21 m/s
	Stent	0.72 m/s	1.2 m/s	0.62 m/s	0.21 m/s
Patient 3 (Full)	No Stent	0.52 m/s	1.1 m/s	0.73 m/s	0.23 m/s
	Stent	0.47 m/s	1.22 m/s	0.55 m/s	0.22 m/s

Time		Initial Clot	Mid Clot	Full Clot
Patient 1	No Stent	109.65s	128.55s	145.2s
	Stent	105.2s	111.85s	117.4s
Patient 2	No Stent	150.75s	158.55s	164.1s
	Stent	119.6s	135.2s	150.7s
Patient 3	No Stent	108.5s	117.4s	126.3s
	Stent	106.3s	109.65s	112.95s

Table 24: Data quantities for patient-specific aneurysm simulation results

7. Research Conclusions

In this thesis, three studies are presented with the combined aim of creating a directly and comprehensively validated direct model of thrombosis in cerebral aneurysms. The first of these studies presents the results of a PIV-based idealized cerebral aneurysm thrombin-fibrinogen *in vitro* flow experiment which captures flow fields of fibrinogen-saline solution under physiological flow conditions simultaneously to fibrin clot growth induced by the addition of a controlled injection of thrombin-saline solution. The second study presents a direct model of thrombosis in cerebral aneurysms using a porosity-based clotting model based on a reduced Michaelis-Menten formulation, and models the parameters of the PIV-based *in vitro* flow clotting experiment for validation with an accompanying exploration of wall boundaries. The third and final study considers the direct model of thrombosis in cerebral aneurysms validated in the second study with consideration towards a clinical context, and applies it to patient-specific cases with and without endovascular flow diverter treatment to predict reasonably expectable thrombosis clotting outcomes. The novelty of this thesis is a framework wherein a pulsatile-flow direct thrombosis fibrin clot-model that predicts plausible clotting outcomes in patient-specific cerebral aneurysm cases with and without flow diverter treatment is directly validated by a novel PIV-based idealized cerebral aneurysm thrombin-fibrinogen *in vitro* flow experiment which is capable of simultaneous measurement of clot and flow field development under physiologically realistic flow.

In achieving this aim, the objectives of this research to perform a PIV-based *in vitro* clotting flow experiment to directly validate a computational model of thrombosis in cerebral aneurysms for predicting reasonable clotting outcomes of flow-diverter treatment in patient-specific cases are met. In so doing, these studies highlight a series of unexpected but explicable outcomes with cross-reference to literature.

The thrombin-fibrinogen *in vitro* flow experiment produces a strand-like fibrin clot that does not appear to be replicated in comparable macroscale *in vitro* flow studies. These studies are few however, and the outcome aligns with the variability in shape of fibrin clots in microscale studies, particularly as they relate to local shear rates and the elastic and extensible properties of fibrin clots. The thrombin-fibrinogen experiment further demonstrates significantly higher flow magnitudes and recirculation than a prototype water-gelatin flow experiment that uses identical flow patterns and geometry.

The flow field produced by the validation simulation of the direct thrombosis model demonstrates agreement with the flow results of the thrombin-fibrinogen experiment when applying free-slip wall boundaries and demonstrates agreement with the flow results of the water-gelatin experiment when

applying no-slip wall boundaries. Using free-slip wall boundaries, the validation simulation also produces similarly sized and located fibrin formations against the aneurysm wall as the thrombin-fibrinogen *in vitro* flow experiment, though it lacks the fluid-structure-interaction framework required to model the strand-like fibrin clot.

The patient-specific aneurysm simulations of the validated direct thrombosis model are able to predict reasonably expected clotting outcomes with and without the presence of flow diverters within the aneurysm using free-slip wall boundaries, a departure from virtually every other comparable direct thrombosis model. Flow diversion treatment reliably reduces shear rates within the aneurysm for each patient-specific case, and the benefit of patient-specific modelling is highlighted with the poor clotting outcome observed for the case 2 fusiform aneurysm despite endovascular flow diversion treatment.

The cross reference of these studies with literature indicates discrepancies in the validity of the commonly held Newtonian assumption for *in vitro* macroscale flows which may have relevance both in terms of fluid properties and wall boundaries, as well as the notable and potentially important effects of periodically high flow rates on fibrin clot macrostructure and morphology. There are few other similar studies for macroscale vessels, and with further consideration towards the in-part exploratory nature of the studies performed and the single sample-size they present, further exploration of macroscale in-vitro flow studies of blood and blood-derived fluids is required.

The studies comprising this thesis have several other limitations to consider. Due to the inherent requirements for PIV, coupled with the justified ethical framework preventing a single donor from providing a sufficiently large sample of human blood and plasma, the thrombin-fibrinogen experiments account only for a reduced order coagulation composed of fibrinogen and thrombin that is not fully representative of physiological clotting. Furthermore, the rheological properties of the fibrinogen-saline solution are not measured and are therefore not well understood in the context of validating a direct thrombosis model. This is reflected in the direct thrombosis model with the use of a free-slip wall boundary rather than a more physiologically realistic partial-slip wall, for which to the best of the authors knowledge there are no existing models for macroscale vessels, and for this reason was considered outside the scope of this thesis. Otherwise, the use of a reduced-order Michaelis-Menten formulation leads to a significantly accelerated rate of clotting to that in vivo, such that clotting outcomes may be over-predicted owing to the lack of regulatory biochemistry.

Regardless, this thesis presents a framework that combines direct fibrin clot growth with a pulsatile flow field both computationally and experimentally, such that a direct comparison of flow and clotting between computational and experimental results may be made at any and all points upon a directly corresponding timescale. With further refinement to the experimental framework, this thesis

demonstrates a comprehensive validation method that gives direct thrombosis models renewed potential to quantitatively address questions in need of answer to eventually make the transition to direct clinical applications.

BIBLIOGRAPHY

1. Lawton, M.T.; Quiones-Hinojosa, A.; Chang, E.F.; Yu, T. Thrombotic Intracranial Aneurysms: Classification Scheme and Management Strategies in 68 Patients. *Neurosurgery* **2005**, *56*, 441–454, doi:10.1227/01.NEU.0000153927.70897.A2.

2. Brisman, J.L.; Song, J.K.; Newell, D.W. Cerebral aneurysms. *N. Engl. J. Med.* **2006**, *355*, 928–939, doi:10.1056/NEJMra052760.

3. Becske, T.; Kallmes, D.F.; Saatci, I.; McDougall, C.G.; Szikora, I.; Lanzino, G.; Moran, C.J.; Woo, H.H.; Lopes, D.K.; Berez, A.L.; et al. Pipeline for uncoilable or failed aneurysms: results from a multicenter clinical trial. *Radiology* **2013**, *267*, 858–868, doi:10.1148/radiol.13120099.

4. Algra, A.M.; Greving, J.P.; De Winkel, J.; Kurtelius, A.; Laban, K.; Verbaan, D.; Van Den Berg, R.; Vandertop, W.; Lindgren, A.; Krings, T.; et al. Development of the SAFETEA Scores for Predicting Risks of Complications of Preventive Endovascular or Microneurosurgical Intracranial Aneurysm Occlusion. *Neurology* **2022**, *99*, E1725–E1737, doi:10.1212/WNL.0000000000200978.

5. Kotowski, M.; Naggara, O.; Darsaut, T.E.; Nolet, S.; Gevry, G.; Kouznetsov, E.; Raymond, J. Safety and occlusion rates of surgical treatment of unruptured intracranial aneurysms: a systematic review and meta-analysis of the literature from 1990 to 2011. *J. Neurol. Neurosurg. Psychiatry* **2013**, *84*, 42–48, doi:10.1136/jnnp-2011-302068.

6. Naggara, O.N.; Lecler, A.; Oppenheim, C.; Meder, J.-F.; Raymond, J. Endovascular treatment of intracranial unruptured aneurysms: a systematic review of the literature on safety with emphasis on subgroup analyses. *Radiology* **2012**, *263*, 828–835, doi:10.1148/radiol.12112114.

7. Nieuwkamp, D.J.; Setz, L.E.; Algra, A.; Linn, F.H.H.; de Rooij, N.K.; Rinkel, G.J.E. Changes in case fatality of aneurysmal subarachnoid haemorrhage over time, according to age, sex, and region: a meta-analysis. *Lancet. Neurol.* **2009**, *8*, 635–642, doi:10.1016/S1474-4422(09)70126-7.

8. Yunoki, S.; Sugimoto, K.; Ohyabu, Y.; Ida, H.; Hiraoka, Y. Accurate and precise viscosity measurements of gelatin solutions using a rotational rheometer. *Food Sci. Technol. Res.* **2019**, *25*, 217–226, doi:10.3136/fstr.25.217.

9. Vlak, M.H.; Algra, A.; Brandenburg, R.; Rinkel, G.J. Prevalence of unruptured intracranial aneurysms, with emphasis on sex, age, comorbidity, country, and time period: a systematic review and meta-analysis. *Lancet. Neurol.* **2011**, *10*, 626–636, doi:10.1016/S1474-4422(11)70109-0.

10. Williams, L.N.; Brown, R.D. Management of unruptured intracranial aneurysms. *Neurol. Clin. Pract.* **2013**, *3*, 99–108, doi:10.1212/CPJ.0b013e31828d9f6b.

11. Thompson, B.G.; Brown, R.D.; Amin-Hanjani, S.; Broderick, J.P.; Cockroft, K.M.; Connolly, E.S.; Duckwiler, G.R.; Harris, C.C.; Howard, V.J.; Johnston, S.C.C. la.; et al. *Guidelines for the Management of Patients With Unruptured Intracranial Aneurysms: A Guideline for Healthcare Professionals From the American Heart Association/American Stroke Association*; 2015; Vol. 46; ISBN 0000000000000.

12. Etminan, N.; Rinkel, G.J. Unruptured intracranial aneurysms: development, rupture and preventive management. *Nat. Rev. Neurol.* **2016**, *12*, 699–713, doi:10.1038/nrneurol.2016.150.

13. van Gijn, J.; Kerr, R.S.; Rinkel, G.J.E. Subarachnoid haemorrhage. *Lancet (London, England)* **2007**, *369*, 306–318, doi:10.1016/S0140-6736(07)60153-6.

14. Toussaint, L.G.; Friedman, J.A.; Wijdicks, E.F.M.; Piepgras, D.G.; Pichelmann, M.A.; McIver, J.I.; McClelland, R.L.; Nichols, D.A.; Meyer, F.B.; Atkinson, J.L.D. Survival of cardiac arrest after aneurysmal subarachnoid hemorrhage. *Neurosurgery* **2005**, *57*, 25–31, doi:10.1227/01.NEU.0000163086.23124.70.

15. Mocco, J.; Brown, R.D.; Torner, J.C.; Capuano, A.W.; Fargen, K.M.; || M.; Raghavan, M.L.; Piepgras, D.G.; Meissner, I.; Huston, J. Aneurysm Morphology and Prediction of Rupture: An International Study of Unruptured Intracranial Aneurysms Analysis. *Neurosurgery* **2017**, doi:10.1093/neuros/nyx226.

16. Griessenauer, C.J.; Ogilvy, C.S.; Foreman, P.M.; Chua, M.H.; Harrigan, M.R.; He, L.; Fusco, M.R.; Mocco, J.D.; Stapleton, C.J.; Patel, A.B.; et al. Pipeline Embolization Device for Small Intracranial Aneurysms: Evaluation of Safety and Efficacy in a Multicenter Cohort. *Neurosurgery* **2017**, *80*.

17. Becske, T.; Brinjikji, W.; Potts, M.B.; Kallmes, D.F.; Shapiro, M.; Moran, C.J.; Levy, E.I.; McDougall, C.G.; Szikora, I.; Lanzino, G.; et al. Long-Term clinical and angiographic outcomes following pipeline embolization device treatment of complex internal carotid artery aneurysms: Five-year results of the pipeline for uncoilable or failed aneurysms trial. *Neurosurgery* **2017**, *80*, 40–48, doi:10.1093/neuros/nyw014.

18. Limbucci, N.; Leone, G.; Renieri, L.; Nappini, S.; Cagnazzo, F.; Laiso, A.; Muto, M.; Mangiafico, S. Expanding Indications for Flow Diverters: Distal Aneurysms, Bifurcation Aneurysms, Small Aneurysms, Previously Coiled Aneurysms and Clipped Aneurysms, and Carotid Cavernous Fistulas. *Neurosurgery* **2020**, *86*, S85–S94, doi:10.1093/neuros/nyz334.

19. Eller, T.W. MRI demonstration of clot in a small unruptured aneurysm causing stroke. Case report. *J. Neurosurg.* **1986**, *65*, 411–2, doi:10.3171/jns.1986.65.3.0411.

20. Ishikawa, T.; Nakayama, N.; Yoshimoto, T.; Aoki, T.; Terasaka, S.; Nomura, M.; Takahashi, A.; Kuroda, S.; Iwasaki, Y. How does spontaneous hemostasis occur in ruptured cerebral aneurysms? Preliminary investigation on 247 clipping surgeries. *Surg. Neurol.* **2006**, *66*, 269–75; discussion 275-6, doi:10.1016/j.surneu.2006.03.030.

21. Calviere, L.; Viguier, A.; Da Silva, N.A.; Cognard, C.; Larrue, V. Unruptured intracranial aneurysm as a cause of cerebral ischemia. *Clin. Neurol. Neurosurg.* **2011**, *113*, 28–33, doi:10.1016/j.clineuro.2010.08.016.

22. Frösen, J.; Tulamo, R.; Paetau, A.; Laaksamo, E.; Korja, M.; Laakso, A.; Niemelä, M.; Hernesniemi, J. Saccular intracranial aneurysm: pathology and mechanisms. *Acta Neuropathol.* **2012**, *123*, 773–786, doi:10.1007/s00401-011-0939-3.

23. Ngoepe, M.N.; Frangi, A.F.; Byrne, J. V.; Ventikos, Y. Thrombosis in cerebral aneurysms and the computational modeling thereof: A review. *Front. Physiol.* **2018**, *9*, 1–22, doi:10.3389/fphys.2018.00306.

24. SAKARIASSEN, K.S.; BOLHUIS, P.A.; SIXMA, J.J. Human blood platelet adhesion to artery subendothelium is mediated by factor VIII–Von Willebrand factor bound to the subendothelium. *Nature* **1979**, *279*, 636–638, doi:10.1038/279636a0.

25. Stel, H. V; Sakariassen, K.S.; de Groot, P.G.; van Mourik, J.A.; Sixma, J.J. Von Willebrand factor in the vessel wall mediates platelet adherence. *Blood* **1985**, *65*, 85–90.

26. Humphrey, J.D.; Canham, P.B. Structure , Mechanical Properties , and Mechanics of

Intracranial Saccular Aneurysms. *J. Elast.* **2000**, *61*, 49–81.

27. Sutherland, G.R.; King, M.E.; Peerless, S.J.; Vezina, W.C.; Brown, G.W.; Chamberlain, M.J. Platelet interaction within giant intracranial aneurysms. *J. Neurosurg.* **1982**, *56*, 53–61, doi:10.3171/jns.1982.56.1.0053.

28. Goldsmith, H.L.; Karino, T. Interactions of human blood cells with the vascular endothelium. *Ann. N. Y. Acad. Sci.* **1987**, *516*, 468–483, doi:10.1111/j.1749-6632.1987.tb33067.x.

29. Kuwahara, M.; Sugimoto, M.; Tsuji, S.; Matsui, H.; Mizuno, T.; Miyata, S.; Yoshioka, A. Platelet shape changes and adhesion under high shear flow. *Arterioscler. Thromb. Vasc. Biol.* **2002**, *22*, 329–334, doi:10.1161/hq0202.104122.

30. Falati, S.; Gross, P.; Merrill-Skoloff, G.; Furie, B.C.; Furie, B. Real-time in vivo imaging of platelets, tissue factor and fibrin during arterial thrombus formation in the mouse. *Nat. Med.* **2002**, *8*, 1175–1181, doi:10.1038/nm782.

31. Hoffman, M. A cell-based model of coagulation and the role of factor VIIa. *Blood Rev.* **2003**, *17 Suppl 1*, S1-5, doi:10.1016/s0268-960x(03)90000-2.

32. Furie, B.; Furie, B.C. Thrombus formation in vivo. *J. Clin. Invest.* **2005**, *115*, 3355–3362, doi:10.1172/JCI26987.

33. Orfeo, T.; Butenas, S.; Brummel-Ziedins, K.E.; Mann, K.G. The tissue factor requirement in blood coagulation. *J. Biol. Chem.* **2005**, *280*, 42887–96, doi:10.1074/jbc.M505506200.

34. Brinkman, H.J.; Mertens, K.; Holthuis, J.; Zwart-Huinink, L.A.; Grijm, K.; van Mourik, J.A. The activation of human blood coagulation factor X on the surface of endothelial cells: a comparison with various vascular cells, platelets and monocytes. *Br. J. Haematol.* **1994**, *87*, 332–342, doi:10.1111/j.1365-2141.1994.tb04918.x.

35. Rosing, J.; van Rijn, J.L.; Bevers, E.M.; van Dieijen, G.; Comfurius, P.; Zwaal, R.F. The role of activated human platelets in prothrombin and factor X activation. *Blood* **1985**, *65*, 319–332.

36. Davie, E.W.; Ratnoff, O.D. Waterfall Sequence for Intrinsic Blood Clotting. *Science (80-.).* **1964**, *145*, 1310–1312, doi:10.1126/science.145.3638.1310.

37. MACFARLANE, R.G. An Enzyme Cascade in the Blood Clotting Mechanism, and its Function as a Biochemical Amplifier. *Nature* **1964**, *202*, 498–499, doi:10.1038/202498a0.

38. Furie, B.; Furie, B.C. Molecular and cellular biology of blood coagulation. *N. Engl. J. Med.* **1992**, *326*, 800–806, doi:10.1056/NEJM199203193261205.

39. Hoffman, M. Remodeling the blood coagulation cascade. *J. Thromb. Thrombolysis* **2003**, *16*, 17–20, doi:10.1023/B:THRO.0000014588.95061.28.

40. Scanarini, M.; Mingrino, S.; Giordano, R.; Baroni, A. Histological and ultrastructural study of intracranial saccular aneurysmal wall. *Acta Neurochir. (Wien).* **1978**, *43*, 171–82.

41. Bugge, T.H.; Xiao, Q.; Kombrinck, K.W.; Flick, M.J.; Holmbäck, K.; Danton, M.J.; Colbert, M.C.; Witte, D.P.; Fujikawa, K.; Davie, E.W.; et al. Fatal embryonic bleeding events in mice lacking tissue factor, the cell-associated initiator of blood coagulation. *Proc. Natl. Acad. Sci. U. S. A.* **1996**, *93*, 6258–6263, doi:10.1073/pnas.93.13.6258.

42. Carmeliet, P.; Mackman, N.; Moons, L.; Luther, T.; Gressens, P.; Van Vlaenderen, I.; Demunck, H.; Kasper, M.; Breier, G.; Evrard, P.; et al. Role of tissue factor in embryonic blood vessel development. *Nature* **1996**, *383*, 73–75, doi:10.1038/383073a0.

43. Toomey, J.R.; Kratzer, K.E.; Lasky, N.M.; Stanton, J.J.; Broze, G.J.J. Targeted disruption of the murine tissue factor gene results in embryonic lethality. *Blood* **1996**, *88*, 1583–1587.

44. Hoffman, M.; Whinna, H.C.; Monroe, D.M. Circulating tissue factor accumulates in thrombi, but not in hemostatic plugs. *J. Thromb. Haemost.* 2006, *4*, 2092–2093.

45. Furie, B.; Furie, B.C. Mechanisms of thrombus formation. *N. Engl. J. Med.* **2008**, *359*, 938–949, doi:10.1056/NEJMra0801082.

46. Morel, O.; Jesel, L.; Freyssinet, J.-M.; Toti, F. Cellular mechanisms underlying the formation of circulating microparticles. *Arterioscler. Thromb. Vasc. Biol.* **2011**, *31*, 15–26, doi:10.1161/ATVBAHA.109.200956.

47. Giesen, P.L.; Rauch, U.; Bohrmann, B.; Kling, D.; Roqué, M.; Fallon, J.T.; Badimon, J.J.; Himber, J.; Riederer, M.A.; Nemerson, Y. Blood-borne tissue factor: another view of thrombosis. *Proc. Natl. Acad. Sci. U. S. A.* **1999**, *96*, 2311–5.

48. Hathcock, J.J.; Nemerson, Y. Platelet deposition inhibits tissue factor activity: in vitro clots are impermeable to factor Xa. *Blood* **2004**, *104*, 123–7, doi:10.1182/blood-2003-12-4352.

49. Morel, O.; Toti, F.; Hugel, B.; Bakouboula, B.; Camoin-Jau, L.; Dignat-George, F.; Freyssinet, J.-M. Procoagulant microparticles: disrupting the vascular homeostasis equation? *Arterioscler. Thromb. Vasc. Biol.* **2006**, *26*, 2594–2604, doi:10.1161/01.ATV.0000246775.14471.26.

50. Butenas, S.; Orfeo, T.; Mann, K.G. Tissue factor in coagulation: Which? Where? When? *Arterioscler. Thromb. Vasc. Biol.* **2009**, *29*, 1989–1996, doi:10.1161/ATVBAHA.108.177402.

51. Mann, K.G. Adding the vessel wall to Virchow's triad. *J. Thromb. Haemost.* **2006**, *4*, 58–59, doi:10.1111/j.1538-7836.2005.01738.x.

52. Okorie, U.M.; Denney, W.S.; Chatterjee, M.S.; Neeves, K.B.; Diamond, S.L. Determination of surface tissue factor thresholds that trigger coagulation at venous and arterial shear rates: amplification of 100 fM circulating tissue factor requires flow. *Blood* **2008**, *111*, 3507–3513, doi:10.1182/blood-2007-08-106229.

53. Peach, T.W.; Ngoepe, M.; Spranger, K.; Ventikos, Y. Personalizing flow-diverter intervention for cerebral aneurysms : from computational hemodynamics to biochemical modeling. *Int. J. Numer. Methods Biomed. Eng.* **2014**, 1–21, doi:10.1002/cnm.

54. Einav, S. Dynamics of Blood Flow and Platelet Transport in Pathological Vessels. *Ann.N.Y.Acad.Sci.* **2004**, *1015*, 351–366.

55. Rayz, V.L.; Boussel, L.; Lawton, M.T.; Acevedo-Bolton, G.; Ge, L.; Young, W.L.; Higashida, R.T.; Saloner, D. Numerical modeling of the flow in intracranial aneurysms: prediction of regions prone to thrombus formation. *Ann. Biomed. Eng.* **2008**, *36*, 1793–804, doi:10.1007/s10439-008-9561-5.

56. Di Achille, P.; Tellides, G.; Figueroa, C.A.; Humphrey, J.D. A haemodynamic predictor of intraluminal thrombus formation in abdominal aortic aneurysms. *Proc. R. Soc. London A Math. Phys. Eng. Sci.* **2014**, *470*.

57. Ngoepe, M.N.; Ventikos, Y. Computational modelling of clot development in patient-specific cerebral aneurysm cases. *J. Thromb. Haemost.* **2016**, *14*, 262–272, doi:10.1111/jth.13220.

58. Ngoepe, M.N.; Frangi, A.F.; Byrne, J. V.; Ventikos, Y. Thrombosis in cerebral aneurysms and the computational modeling thereof: A review. *Front. Physiol.* 2018, *9*.

59. Bedekar, A.S.; Pant, K.; Ventikos, Y.; Sundaram, S. A computational model combining vascular

biology and haemodynamics for thrombosis prediction in anatomically accurate cerebral aneurysms. *Food Bioprod. Process.* **2005**, *83*, 118–126, doi:10.1205/fbp.05020.

60. Sorensen, E.N.; Burgreen, G.W.; Wagner, W.R.; Antaki, J.F. Computational simulation of platelet deposition and activation: I. Model development and properties. *Ann. Biomed. Eng.* **1999**, *27*, 436–448, doi:10.1114/1.200.

61. Ouared, R.; Chopard, B.; Stahl, B.; Rüfenacht, D.A.; Yilmaz, H.; Courbebaisse, G. Thrombosis modeling in intracranial aneurysms: a lattice Boltzmann numerical algorithm. *Comput. Phys. Commun.* **2008**, *179*, 128–131, doi:10.1016/j.cpc.2008.01.021.

62. Hockin, M.F.; Jones, K.C.; Everse, S.J.; Mann, K.G. A model for the stoichiometric regulation of blood coagulation. *J. Biol. Chem.* **2002**, *277*, 18322–18333, doi:10.1074/jbc.M201173200.

63. Kremers, R.M.W.; de Laat, B.; Wagenvoord, R.J.; Hemker, H.C. Computational modelling of clot development in patient-specific cerebral aneurysm cases: rebuttal. *J. Thromb. Haemost.* 2017, *15*, 399.

64. Ou, C.; Huang, W.; Yuen, M.M.F. A computational model based on fibrin accumulation for the prediction of stasis thrombosis following flow-diverting treatment in cerebral aneurysms. *Med. Biol. Eng. Comput.* **2017**, *55*, 89–99, doi:10.1007/s11517-016-1501-1.

65. Sarrami-Foroushani, A.; Lassila, T.; Hejazi, S.M.; Nagaraja, S.; Bacon, A.; Frangi, A.F. A computational model for prediction of clot platelet content in flow-diverted intracranial aneurysms. *J. Biomech.* **2019**, *91*, 7–13, doi:10.1016/j.jbiomech.2019.04.045.

66. Gester, K.; Lu, I.; Bu, M. In Vitro Evaluation of Intra-Aneurysmal , Flow-Diverter-Induced. **2016**.

67. Sarrami-Foroushani, A.; Lassila, T.; MacRaild, M.; Asquith, J.; Roes, K.C.B.; Byrne, J. V.; Frangi, A.F. In-silico trial of intracranial flow diverters replicates and expands insights from conventional clinical trials. *Nat. Commun.* **2021**, *12*, 1–12, doi:10.1038/s41467-021-23998-w.

68. Gester, K.; Lu, I.; Bu, M. In Vitro Evaluation of Intra-Aneurysmal , Flow-Diverter-Induced. *Am. J. Neuroradiol.* **2016**, *37*, 490–496, doi:10.3174/ajnr.A4555.

69. Mulder, G.; Bogaerds, A.C.B.; Rongen, P.; Vosse, F.N. On automated analysis of flow patterns in cerebral aneurysms based on vortex identification. *J. Eng. Math.* **2009**, *64*, 391–401, doi:10.1007/s10665-009-9270-6.

70. Adrian, R.J.; Westerweel, J. *Particle Image Velocimetry*; Cambridge Aerospace Series; Cambridge University Press, 2011; ISBN 9780521440080.

71. Hume, S.; Tshimanga, J.M.I.; Geoghegan, P.; Malan, A.G.; Ho, W.H.; Ngoepe, M.N. Effect of Pulsatility on the Transport of Thrombin in an Idealized Cerebral Aneurysm Geometry. *Symmetry (Basel).* **2022**, *14*, 1–18, doi:10.3390/sym14010133.

72. Clauser, J.; Knieps, M.S.; Büsen, M.; Ding, A.; Schmitz-Rode, T.; Steinseifer, U.; Arens, J.; Cattaneo, G. A Novel Plasma-Based Fluid for Particle Image Velocimetry (PIV): In-Vitro Feasibility Study of Flow Diverter Effects in Aneurysm Model. *Ann. Biomed. Eng.* **2018**, *46*, 841–848, doi:10.1007/s10439-018-2002-1.

73. Ngoepe, M.N.; Pretorius, E.; Tshimanga, I.J.; Shaikh, Z.; Ventikos, Y.; Ho, W.H. Thrombin–Fibrinogen In Vitro Flow Model of Thrombus Growth in Cerebral Aneurysms. *TH Open* **2021**, *05*, e155–e162, doi:10.1055/s-0041-1728790.

74. Ho, W.H.; Tshimanga, I.J.; Ngoepe, M.N.; Jermy, M.C.; Geoghegan, P.H. Evaluation of a Desktop 3D Printed Rigid Refractive-Indexed-Matched Flow Phantom for PIV Measurements

on Cerebral Aneurysms. *Cardiovasc. Eng. Technol.* **2019**, 24–28, doi:10.1007/s13239-019-00444-z.

75. Jimoh-Taiwo, Q.; Haffejee, R.; Ngoepe, M. a Mechano-Chemical Computational Model of Deep Vein Thrombosis. **2021**, *10*, 1–145, doi:10.3389/fphy.2022.886193.

76. Rana, K.; Neeves, K.B. Blood flow and mass transfer regulation of coagulation. *Blood Rev.* **2016**, *30*, 357–368, doi:10.1016/j.blre.2016.04.004.

77. Corbett, S.C.; Ajdari, A.; Coskun, A.U.; Nayeb-Hashemi, H. Effect of pulsatile blood flow on thrombosis potential with a step wall transition. *ASAIO J.* **2010**, *56*, 290–295, doi:10.1097/MAT.0b013e3181db2476.

78. Society, M.; Presents, T.; Staff, C.S.; February, R.; Staff, C.; February, R.; Staff, C.S. Downloaded from https://royalsocietypublishing.org/ on 22 January 2024 Downloaded from https://royalsocietypublishing.org/ on 22 January 2024. **1876**.

79. Day, M.A. The no-slip condition of fluid dynamics. *Erkenntnis* **1990**, *33*, 285–296, doi:10.1007/BF00717588.

80. Kulcsár, Z.; Augsburger, L.; Reymond, P.; Pereira, V.M.; Hirsch, S.; Mallik, A.S.; Millar, J.; Wetzel, S.G.; Wanke, I.; Rüfenacht, D.A. Flow diversion treatment: Intra-aneurismal blood flow velocity and WSS reduction are parameters to predict aneurysm thrombosis. *Acta Neurochir. (Wien).* **2012**, *154*, 1827–1834, doi:10.1007/s00701-012-1482-2.

81. Bazilevs, Y.; Hsu, M.C.; Zhang, Y.; Wang, W.; Kvamsdal, T.; Hentschel, S.; Isaksen, J.G. Computational vascular fluid-structure interaction: Methodology and application to cerebral aneurysms. *Biomech. Model. Mechanobiol.* **2010**, *9*, 481–498, doi:10.1007/s10237-010-0189-7.

82. Cebral, J.R.; Putman, C.M.; Alley, M.T.; Hope, T.; Bammer, R.; Calamante, F. Hemodynamics in normal cerebral arteries: Qualitative comparison of 4D phase-contrast magnetic resonance and image-based computational fluid dynamics. *J. Eng. Math.* **2009**, *64*, 367–378, doi:10.1007/s10665-009-9266-2.

83. Apostolidis, A.J.; Moyer, A.P.; Beris, A.N. Non-Newtonian effects in simulations of coronary arterial blood flow. *J. Nonnewton. Fluid Mech.* **2016**, *233*, 155–165, doi:10.1016/j.jnnfm.2016.03.008.

84. Cavazzuti, M.; Atherton, M.A.; Collins, M.W.; Barozzi, G.S. Non-Newtonian and flow pulsatility effects in simulation models of a stented intracranial aneurysm. *Proc. Inst. Mech. Eng. Part H J. Eng. Med.* **2011**, *225*, 597–609, doi:10.1177/09544119JEIM894.

85. Tu, C.; Deville, M.; Dheur, L.; Vanderschuren, L. Finite element simulation of pulsatile flow through arterial stenosis. *J. Biomech.* **1992**, *25*, 1141–1152, doi:10.1016/0021-9290(92)90070-h.

86. Zhu, Y.; Granick, S. Limits of the Hydrodynamic No-Slip Boundary Condition. *Phys. Rev. Lett.* **2002**, *88*, 4, doi:10.1103/PhysRevLett.88.106102.

87. Taylor, J.O.; Meyer, R.S.; Deutsch, S.; Manning, K.B. Development of a computational model for macroscopic predictions of device-induced thrombosis. *Biomech. Model. Mechanobiol.* **2016**, *15*, 1713–1731, doi:10.1007/s10237-016-0793-2.

88. Li, Y.; Amili, O.; Moen, S.; Van de Moortele, P.F.; Grande, A.; Jagadeesan, B.; Coletti, F. Flow residence time in intracranial aneurysms evaluated by in vitro 4D flow MRI. *J. Biomech.* **2022**, *141*, 111211, doi:10.1016/j.jbiomech.2022.111211.

89. Reza, M.M.S.; Arzani, A. A critical comparison of different residence time measures in aneurysms. *J. Biomech.* **2019**, *88*, 122–129, doi:10.1016/j.jbiomech.2019.03.028.

90. Johnston, B.M.; Johnston, P.R.; Corney, S.; Kilpatrick, D. Non-Newtonian blood flow in human right coronary arteries: Transient simulations. *J. Biomech.* **2006**, *39*, 1116–1128, doi:10.1016/j.jbiomech.2005.01.034.

91. Morales, H.G.; Larrabide, I.; Geers, A.J.; Aguilar, M.L.; Frangi, A.F. Newtonian and non-Newtonian blood flow in coiled cerebral aneurysms. *J. Biomech.* **2013**, *46*, 2158–2164, doi:10.1016/j.jbiomech.2013.06.034.

92. Bernsdorf, J.; Wang, D. Non-Newtonian blood flow simulation in cerebral aneurysms. *Comput. Math. with Appl.* **2009**, *58*, 1024–1029, doi:10.1016/j.camwa.2009.02.019.

93. Ardakani, V.G.; Tu, X.; Gambaruto, A.M.; Velho, I.; Tiago, J.; Sequeira, A.; Pereira, R. Near-wall flow in cerebral aneurysms. *Fluids* **2019**, *4*, 1–27, doi:10.3390/fluids4020089.

94. Mazzi, V.; Gallo, D.; Calò, K.; Steinman, D.A.; Morbiducci, U. Linking wall shear stress and vorticity topologies: Toward a unified theory of cardiovascular flow disturbances. *Phys. Fluids* **2024**, *36*, 0–2, doi:10.1063/5.0209003.

95. Ngwenya, T.; Grundlingh, D.; Ngoepe, M.N. Influence of vortical structures on fibrin clot formation in cerebral aneurysms: A two-dimensional computational study. *J. Biomech.* **2024**, *165*, 111994, doi:10.1016/j.jbiomech.2024.111994.

96. Gomez-Sousa, H.; Rubinos-Lopez, O.; Martinez-Lorenzo, J.A. Hematologic characterization and 3D imaging of red blood cells using a Compressive Nano-antenna and ML-FMA modeling. *2016 10th Eur. Conf. Antennas Propagation, EuCAP 2016* **2016**, doi:10.1109/EuCAP.2016.7481922.

97. Easthope, P.L.; Brooks, D.E. A comparison of rheological constitutive functions for whole human blood. *Biorheology* **1980**, *17*, 235–247.

98. Chien, S.; Usami, S.; Dellenback, R.J.; Gregersen, M.I. Shear-dependent deformation of erythrocytes in rheology of human blood. *Am. J. Physiol.* **1970**, *219*, 136–142, doi:10.1152/ajplegacy.1970.219.1.136.

99. Thurston, G.B. Viscoelasticity of human blood. *Biophys. J.* **1972**, *12*, 1205–1217, doi:10.1016/S0006-3495(72)86156-3.

100. Nubar, Y. Blood Flow, Slip, and Viscometry. *Biophys. J.* **1973**, *13*, 405–406, doi:10.1016/S0006-3495(73)85995-8.

101. Zhu, Y.; Granick, S. Rate-Dependent Slip of Newtonian Liquid at Smooth Surfaces. *Phys. Rev. Lett.* **2001**, *87*, 1–4, doi:10.1103/PhysRevLett.87.096105.

102. Long, Q.; Xu, X.Y.; Ramnarine, K. V; Hoskins, P. Numerical investigation of physiologically realistic pulsatile flow through arterial stenosis. *J. Biomech.* **2001**, *34*, 1229–1242, doi:10.1016/s0021-9290(01)00100-2.

103. Sinha, A.; Shit, G.C.; Kundu, P.K. Slip Effects on Pulsatile Flow of Blood through a Stenosed Arterial Segment under Periodic Body Acceleration. *ISRN Biomed. Eng.* **2013**, *2013*, 1–10, doi:10.1155/2013/925876.

104. MISRA, J.C.; SHIT, G.C. ROLE OF SLIP VELOCITY IN BLOOD FLOW THROUGH STENOSED ARTERIES: A NON-NEWTONIAN MODEL. *J. Mech. Med. Biol.* **2007**, *07*, 337–353, doi:10.1142/S0219519407002303.

105. Nandal, J.; Kumari, S.; Rathee, R. The Effect of Slip Velocity on Unsteady Peristalsis MHD Blood Flow through a Constricted Artery Experiencing Body Acceleration. *Int. J. Appl. Mech. Eng.* **2019**, *24*, 645–659, doi:10.2478/ijame-2019-0040.

106. Eldesoky, I.M.I. Unsteady MHD pulsatile blood flow through porous medium in stenotic channel with slip at permeable walls subjected to time dependent velocity (injection/suction). *Walailak J. Sci. Technol.* **2014**, *11*, 901–922, doi:10.21608/icmep.2014.29736.

107. Ansys Fluent Theory Guide Ansys Fluent Theory Guide. *ANSYS Inc., USA* **2021**, *15317*, 724–746.

108. Pretorius, E.; Mbotwe, S.; Bester, J.; Robinson, C.J.; Kell, D.B. Acute induction of anomalous and amyloidogenic blood clotting by molecular amplification of highly substoichiometric levels of bacterial lipopolysaccharide. *J. R. Soc. Interface* **2016**, *13*, doi:10.1098/rsif.2016.0539.

109. Mishra, H.; Philip, J. Importance of Refractive Index Matching of Fluids for PIV and PLIF Measurements in Buoyant Jets BT - Proceedings of 16th Asian Congress of Fluid Mechanics.; Venkatakrishnan, L., Majumdar, S., Subramanian, G., Bhat, G.S., Dasgupta, R., Arakeri, J., Eds.; Springer Singapore: Singapore, 2021; pp. 277–284.

110. Yu, C.H.; Matsumoto, K.; Shida, S.; Kim, D.J.; Ohta, M. A steady flow analsys on a cerebral aneurysm model with several stents for new stent design using PIV. *J. Mech. Sci. Technol.* **2012**, *26*, 1333–1340, doi:10.1007/s12206-012-0322-x.

111. Ho, W.H.; Tshimanga, I.J.; Ngoepe, M.N.; Jermy, M.C.; Geoghegan, P.H. Evaluation of a Desktop 3D Printed Rigid Refractive-Indexed-Matched Flow Phantom for PIV Measurements on Cerebral Aneurysms. *Cardiovasc. Eng. Technol.* **2020**, *11*, 14–23, doi:10.1007/s13239-019-00444-z.

112. Parlea, L.; Fahrig, R.; Holdsworth, D.W.; Lownie, S.P. An analysis of the geometry of saccular intracranial aneurysms. *Am. J. Neuroradiol.* **1999**, *20*, 1079–1089.

113. Thielicke, W.; Sonntag, R. Particle Image Velocimetry for MATLAB: Accuracy and enhanced algorithms in PIVlab. *J. Open Res. Softw.* **2021**, *9*, 1–14, doi:10.5334/JORS.334.

114. Thielicke, W.; Stamhuis, E.J. PIVlab – Towards User-friendly, Affordable and Accurate Digital Particle Image Velocimetry in MATLAB. *J. Open Res. Softw.* **2014**, *2*, doi:10.5334/jors.bl.

115. Thielicke, W. *The flapping flight of birds: analysis and application. University of Groningen, Groningen, the Netherlands*; 2014; ISBN 9789036772419.

116. H Huang; D Dabiri; M Gharib On errors of digital particle image velocimetry. *Meas. Sci. Technol.* **1997**, *8*, 1427, doi:10.1088/0957-0233/8/12/007.

117. Hart, D.P. PIV Error Correction BT - Laser Techniques Applied to Fluid Mechanics.; Adrian, R.J., Durão, D.F.G., Durst, F., Heitor, M. V, Maeda, M., Whitelaw, J.H., Eds.; Springer Berlin Heidelberg: Berlin, Heidelberg, 2000; pp. 19–35.

118. Shavit, U.; Lowe, R.J.; Steinbuck, J. V Intensity Capping: a simple method to improve cross-correlation PIV results. *Exp. Fluids* **2007**, *42*, 225–240, doi:10.1007/s00348-006-0233-7.

119. Garcia, D. CIHR Author Manuscript A fast all-in-one method for automated post-processing of PIV data. **2014**, *50*, 1247–1259, doi:10.1007/s00348-010-0985-y.A.

120. Ferns, S.P.; Schneiders, J.J.; Siebes, M.; Van Den Berg, R.; Van Bavel, E.T.; Majoie, C.B. Intracranial blood-flow velocity and pressure measurements using an intra-arterial dual-

sensor guidewire. *Am. J. Neuroradiol.* **2010**, *31*, 324–326, doi:10.3174/ajnr.A1718.

121. Tropea, C.; Yarin, A.; Foss, J. *Springer Handbook of Experimental Fluid Mechanics*; 2007; ISBN 9783540251415.

122. Krieger, I.M.; Dougherty, T.J. A Mechanism for Non-Newtonian Flow in Suspensions of Rigid Spheres. *Trans. Soc. Rheol.* **1959**, *3*, 137–152, doi:10.1122/1.548848.

123. Zaccarelli, E. Colloidal gels: Equilibrium and non-equilibrium routes. *J. Phys. Condens. Matter* **2007**, *19*, doi:10.1088/0953-8984/19/32/323101.

124. Sancakli, A.; Basaran, B.; Arican, F.; Polat, O. Effects of bovine gelatin viscosity on gelatin-based edible film mechanical, physical and morphological properties. *SN Appl. Sci.* **2021**, *3*, 1–11, doi:10.1007/s42452-020-04076-0.

125. Horbett, T.A. Fibrinogen adsorption to biomaterials. *Physiol. Behav.* **2017**, *176*, 139–148, doi:10.1002/jbm.a.36460.Fibrinogen.

126. Campbell, R.A.; Aleman, M.M.; Gray, L.D.; Falvo, M.R.; Wolberg, A.S. Flow profoundly influences fibrin network structure: Implications for fibrin formation and clot stability in haemostasis. *Thromb. Haemost.* **2010**, *104*, 1281–1284, doi:10.1160/TH10-07-0442.

127. Gersh, K.C.; Edmondson, K.E.; Weisel, J.W. Flow rate and fibrin fiber alignment. *J. Thromb. Haemost.* **2010**, *8*, 2826, doi:10.1111/J.1538-7836.2010.04118.X.

128. Liu, W.; Jawerth, L.M.; Sparks, E.A.; Falvo, M.R.; Hantgan, R.R.; Superfine, R.; Lord, S.T.; Guthold, M. Fibrin fibers have extraordinary extensibility and elasticity. *Science (80-.).* **2006**, *313*, 634, doi:10.1126/science.1127317.

129. Guthold, M.; Liu, W.; Sparks, E.A.; Jawerth, L.M.; Peng, L.; Falvo, M.; Superfine, R.; Hantgan, R.R.; Lord, S.T. A Comparison of the Mechanical and Structural Properties of Fibrin Fibers with Other Protein Fibers. *Cell Biochem. Biophys. 2007 493* **2007**, *49*, 165–181, doi:10.1007/S12013-007-9001-4.

130. Liu, W.; Carlisle, C.R.; Sparks, E.A.; Guthold, M. The mechanical properties of single fibrin fibers. *J. Thromb. Haemost.* **2010**, *8*, 1030–1036, doi:10.1111/J.1538-7836.2010.03745.X.

131. Weisel, J.W.; Litvinov, R.I. Fibrin Formation, Structure and Properties., doi:10.1007/978-3-319-49674-0_13.

132. Brown, A.E.X.; Litvinov, R.I.; Discher, D.E.; Purohit, P.K.; Weisel, J.W. Multiscale mechanics of fibrin polymer: Gel stretching with protein unfolding and loss of water. *Science (80-.).* **2009**, *325*, 741–744, doi:10.1126/SCIENCE.1172484/SUPPL_FILE/BROWN.SOM.PDF.

133. van Rooij, B.J.M.; Závodszky, G.; Hoekstra, A.G.; Ku, D.N. Biorheology of occlusive thrombi formation under high shear: in vitro growth and shrinkage. *Sci. Rep.* **2020**, *10*, 1–11, doi:10.1038/s41598-020-74518-7.

134. De Sousa, D.R.; Vallecilla, C.; Chodzynski, K.; Jerez, R.C.; Malaspinas, O.; Eker, O.F.; Ouared, R.; Vanhamme, L.; Legrand, A.; Chopard, B.; et al. Determination of a shear rate threshold for thrombus formation in intracranial aneurysms. *J. Neurointerv. Surg.* **2016**, *8*, 853–858, doi:10.1136/neurintsurg-2015-011737.

135. Brunn, P. The velocity slip of polar fluids. *Rheol. Acta* **1975**, *14*, 1039–1054, doi:10.1007/BF01515899.

136. Canonsburg, T.D. ANSYS FLUENT User ' s Guide. *Knowl. Creat. Diffus. Util.* **2012**, *15317*, 724–746.

137. MERRILL, E.W.; COKELET, G.C.; BRITTEN, A.; WELLS, R.E. Non-Newtonian Rheology of Human Blood--Effect of Fibrinogen Deduced By “Subtraction”. *Circ. Res.* **1963**, *13*, 48–55, doi:10.1161/01.RES.13.1.48.

138. Giannokostas, K.; Moschopoulos, P.; Varchanis, S.; Dimakopoulos, Y.; Tsamopoulos, J. Advanced constitutive modeling of the thixotropic elasto-visco-plastic behavior of blood: Description of the model and rheological predictions. *Materials (Basel).* **2020**, *13*, doi:10.3390/ma13184184.

139. Brust, M.; Schaefer, C.; Doerr, R.; Pan, L.; Garcia, M.; Arratia, P.E.; Wagner, C. Rheology of human blood plasma: Viscoelastic versus Newtonian behavior. *Phys. Rev. Lett.* **2013**, *110*, 6–10, doi:10.1103/PhysRevLett.110.078305.

140. Varchanis, S.; Dimakopoulos, Y.; Wagner, C.; Tsamopoulos, J. How viscoelastic is human blood plasma? *Soft Matter* **2018**, *14*, 4238–4251, doi:10.1039/c8sm00061a.

141. Ou, C.; Hou, X.; Duan, C.Z.; Zhang, X.; Chong, W.; Qian, Y. Flow diverter modeled as heterogeneous and anisotropic porous medium: Simulation, experimental validation and case analysis. *J. Biomech.* **2021**, *123*, 110525, doi:10.1016/j.jbiomech.2021.110525.

142. Nguyen, T.D.; Wells, J.C.; Nguyen, C.V. Velocity measurement of near-wall flow over inclined and curved boundaries by extended interfacial particle image velocimetry. *Flow Meas. Instrum.* **2012**, *23*, 33–39, doi:10.1016/j.flowmeasinst.2011.12.006.

143. Rezaeimoghaddam, M.; van de Vosse, F.N. Continuum modeling of thrombus formation and growth under different shear rates. *J. Biomech.* **2022**, *132*, 110915, doi:10.1016/j.jbiomech.2021.110915.

144. Goodman, P.D.; Barlow, E.T.; Crapo, P.M.; Mohammad, S.F.; Solen, K.A. Computational model of device-induced thrombosis and thromboembolism. *Ann. Biomed. Eng.* **2005**, *33*, 780–797, doi:10.1007/s10439-005-2951-z.

145. Blum, C.; Groß-Hardt, S.; Steinseifer, U.; Neidlin, M. An Accelerated Thrombosis Model for Computational Fluid Dynamics Simulations in Rotary Blood Pumps. *Cardiovasc. Eng. Technol.* **2022**, *13*, 638–649, doi:10.1007/s13239-021-00606-y.

146. Narayanan, S. Multifunctional roles of thrombin. *Ann. Clin. Lab. Sci.* **1999**, *29*, 275–280.

147. La Corte, A.L.C.; Philippou, H.; Ariëns, R.A.S. Chapter 3 - Role of Fibrin Structure in Thrombosis and Vascular Disease. In *Protein Structure and Diseases*; Donev, R.B.T.-A. in P.C. and S.B., Ed.; Academic Press, 2011; Vol. 83, pp. 75–127 ISBN 1876-1623.

148. Born, G.; Patrono, C. Antiplatelet drugs. *Br. J. Pharmacol.* **2006**, *147*, 241–251, doi:10.1038/sj.bjp.0706401.

149. Sosnowski, M.; Krzywanski, J.; Grabowska, K.; Gnatowska, R. Polyhedral meshing in numerical analysis of conjugate heat transfer. *EPJ Web Conf.* **2018**, *180*, 4–9, doi:10.1051/epjconf/201817002096.

150. Vandenbulcke, A.; Messerer, M.; Starnoni, D.; Puccinelli, F.; Daniel, R.T.; Cossu, G. Complete spontaneous thrombosis in unruptured non-giant intracranial aneurysms: A case report and systematic review. *Clin. Neurol. Neurosurg.* **2021**, *200*, 106319, doi:10.1016/j.clineuro.2020.106319.

151. Whittle, I.R.; Williams, D.B.; Halmagyi, G.M.; Besser, M. Spontaneous thrombosis of a giant intracranial aneurysm and ipsilateral internal carotid artery. Case report. *J. Neurosurg.* **1982**, *56*, 287–289, doi:10.3171/jns.1982.56.2.0287.

152. Griffin, A.; Lerner, E.; Zuchowski, A.; Zomorodi, A.; Gonzalez, L.F.; Hauck, E.F. Flow diversion of fusiform intracranial aneurysms. *Neurosurg. Rev.* **2021**, *44*, 1471–1478, doi:10.1007/s10143-020-01332-0.

153. Rayz, V.L.; Boussel, L.; Ge, L.; Leach, J.R.; Martin, A.J.; Lawton, M.T.; McCulloch, C.; Saloner, D. Flow residence time and regions of intraluminal thrombus deposition in intracranial aneurysms. *Ann. Biomed. Eng.* **2010**, *38*, 3058–3069, doi:10.1007/s10439-010-0065-8.

154. Yang, R.; Yang, L.; Ghane, G. Computational and statistical analyses of blood hemodynamic inside cerebral aneurysms for treatment evaluation of endovascular coiling. *Sci. Rep.* **2023**, *13*, 1–13, doi:10.1038/s41598-023-47867-2.

APPENDICES

Appendix A

Patient-Specific Artery and Flow Diverter Geometry Processing Methodology

Processing complex nonuniform geometries that have numerous fine features to successfully produce a convergent mesh within the Ansys framework is nontrivial. As such, this appendix section presents a step-by-step process for how this is accomplished for this study.

In general, this involves processing a patient-specific flow diverter geometry sufficiently such that it may be subtracted from the interior of its corresponding patient geometry. In order to achieve this, it must not intersect with the wall of the patient geometry, and must have sufficient distance from the walls of the patient-specific geometry such that a sufficient number of cells may be meshed between interior and exterior wall boundaries.

STL files for each patient-specific case are applied in ANSYS SpaceClaim, and must be converted to a ANSYS-specific CAD format for use within the ANSYS framework. Direct conversion of these files to ANSYS CAD geometries results in geometries with more than 5 million faces before meshing. Combined with the lack of support for parallel processing in SpaceClaim, this direct approach is infeasible. As such, steps must be taken to significantly reduce the number of faces on each geometry in their native STL format such that they may be 'skinned' by a ANSYS geometry surface, which functions similarly to a shrink-wrap.

Because of the complexity of the flow-diverter geometry in particular, significant processing and repair of the skinned surface must occur prior to its subtraction from the patient-specific artery. The stent geometry rarely closes to form a volume after skinning, so surfaces must be manually created and aligned, since ensuring that surface edges of a geometry align to each other without folding is critical to mesh the geometry without error.

The broad methods for processing patient-specific artery STL's into ANSYS CAD geometries is detailed first, followed by processing methods for patient-specific flow diverter STL's; which includes conversion to CAD geometries and implementation into patient-specific artery CAD geometries. Specific challenges arise in processing each case, and due to some qualitative methods, errors that prevent the completion of a step in this guide should be expected. To limit duplicate efforts, it is advised to save a new file for each step of each process, should resources to do so be available.

Patient-Specific Artery Processing

1. Open STL in SpaceClaim

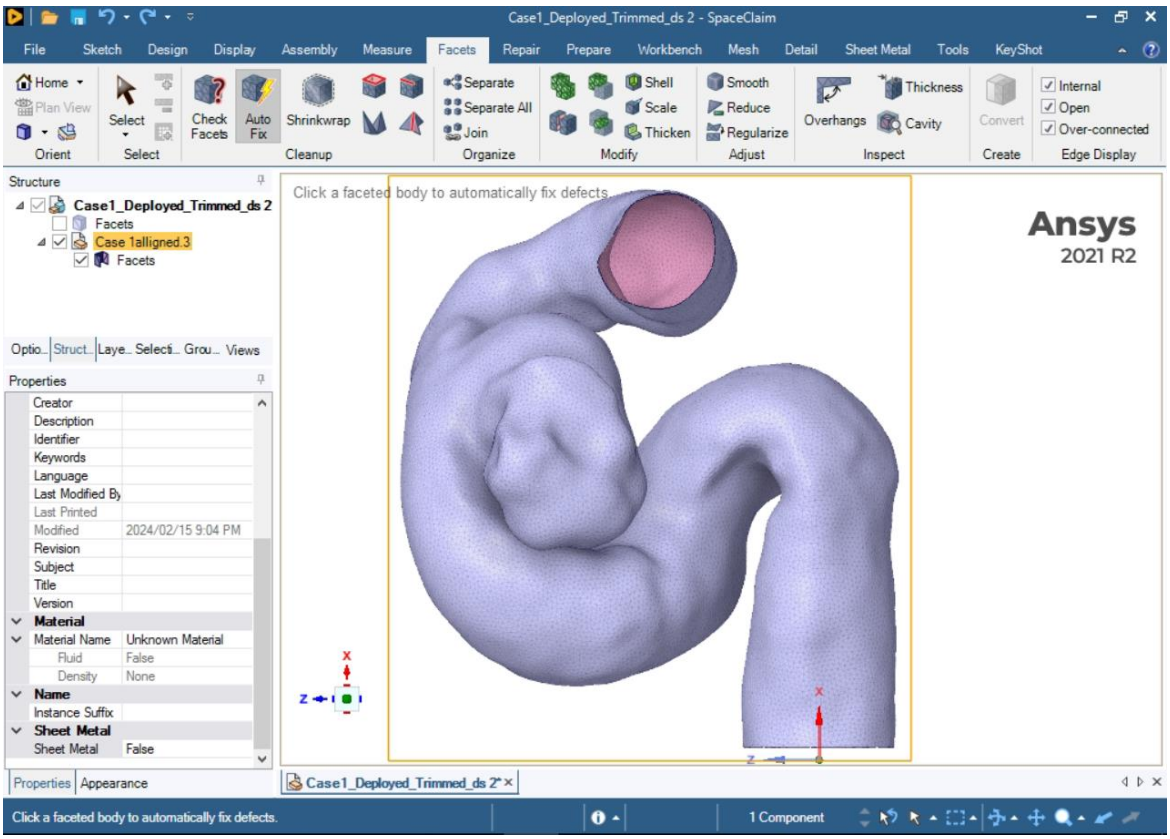

2. Autofix STL

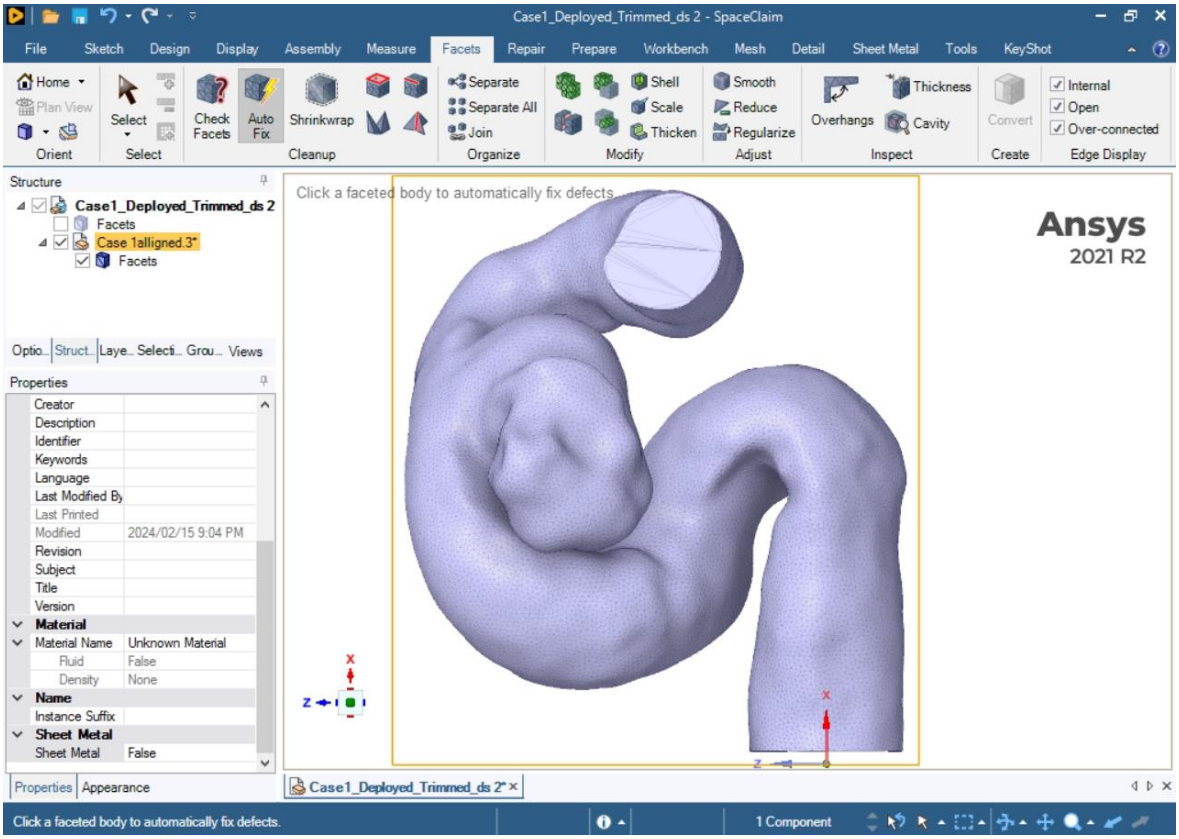

3. Place planes at inlet and outlet faces

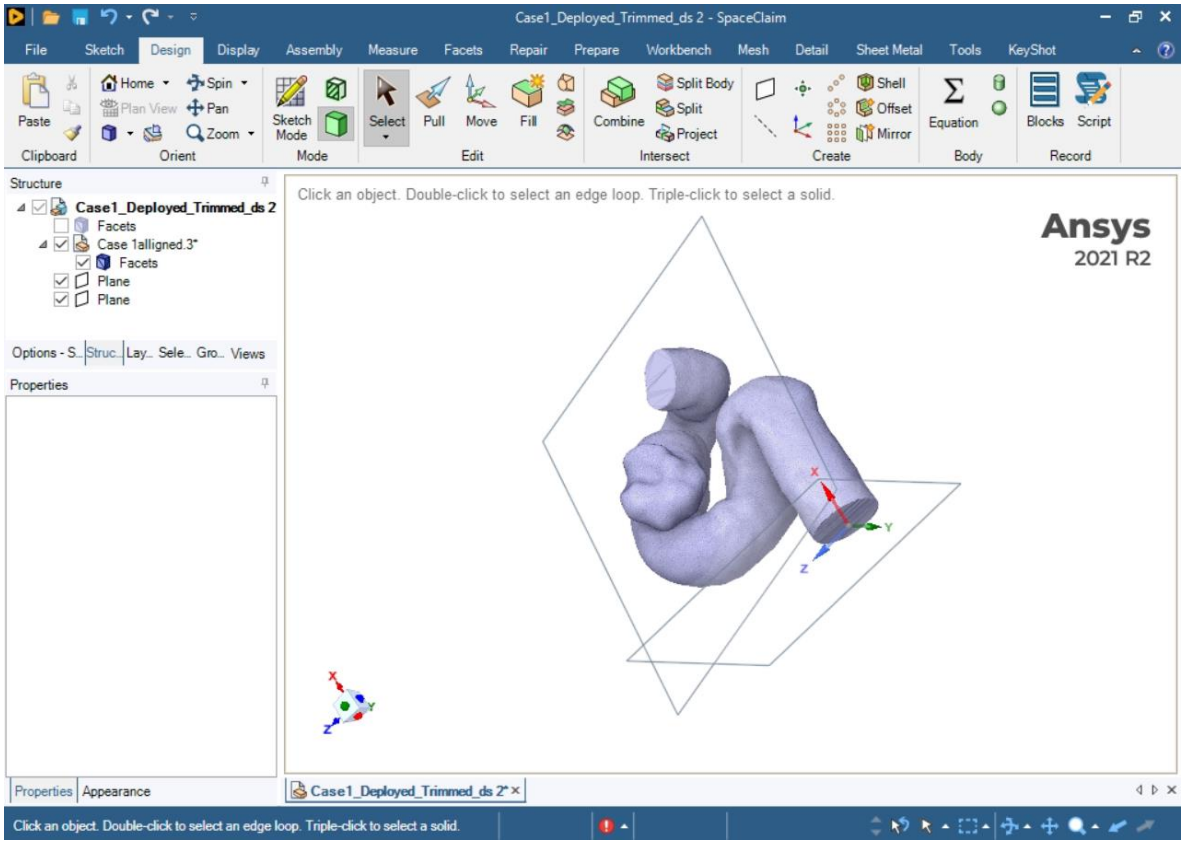

4. Smooth Facets -> Fix Sharps

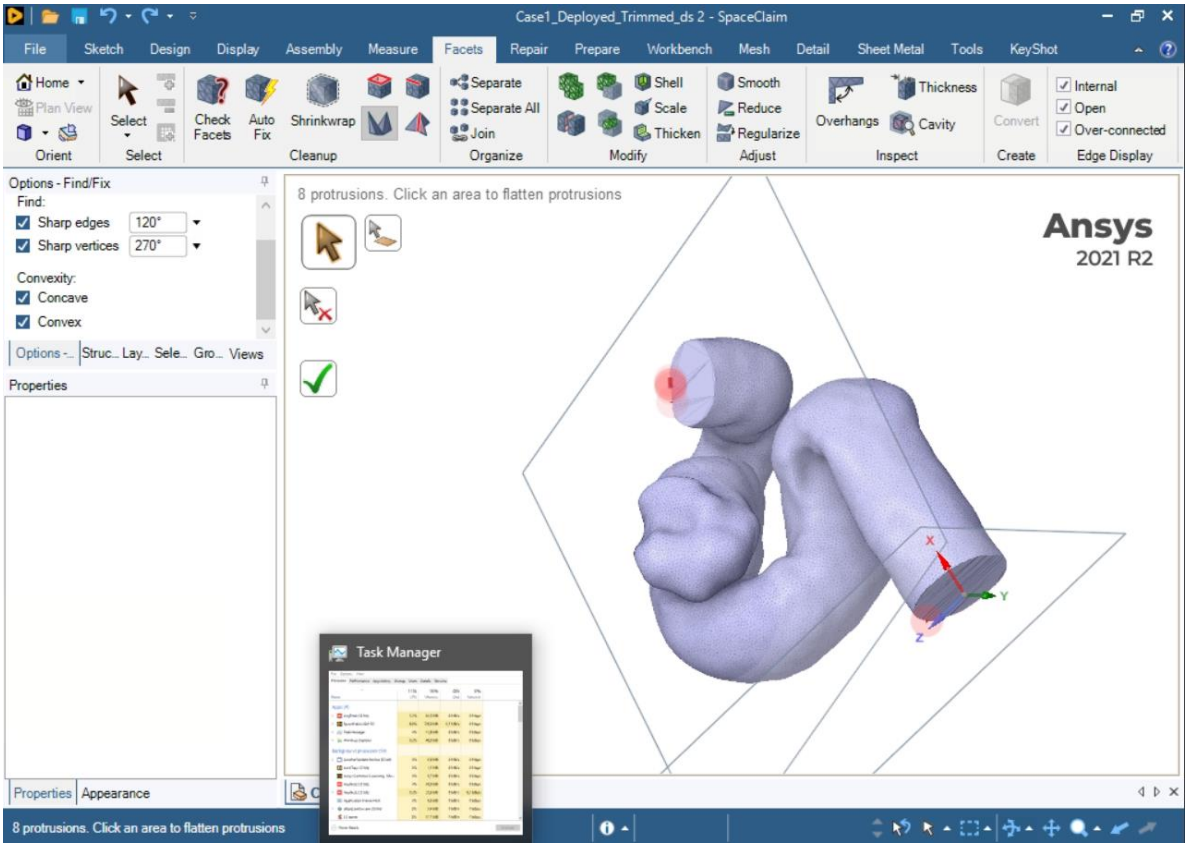

5. Apply Auto skin tool to STL (this forms a 2D CAD surface)

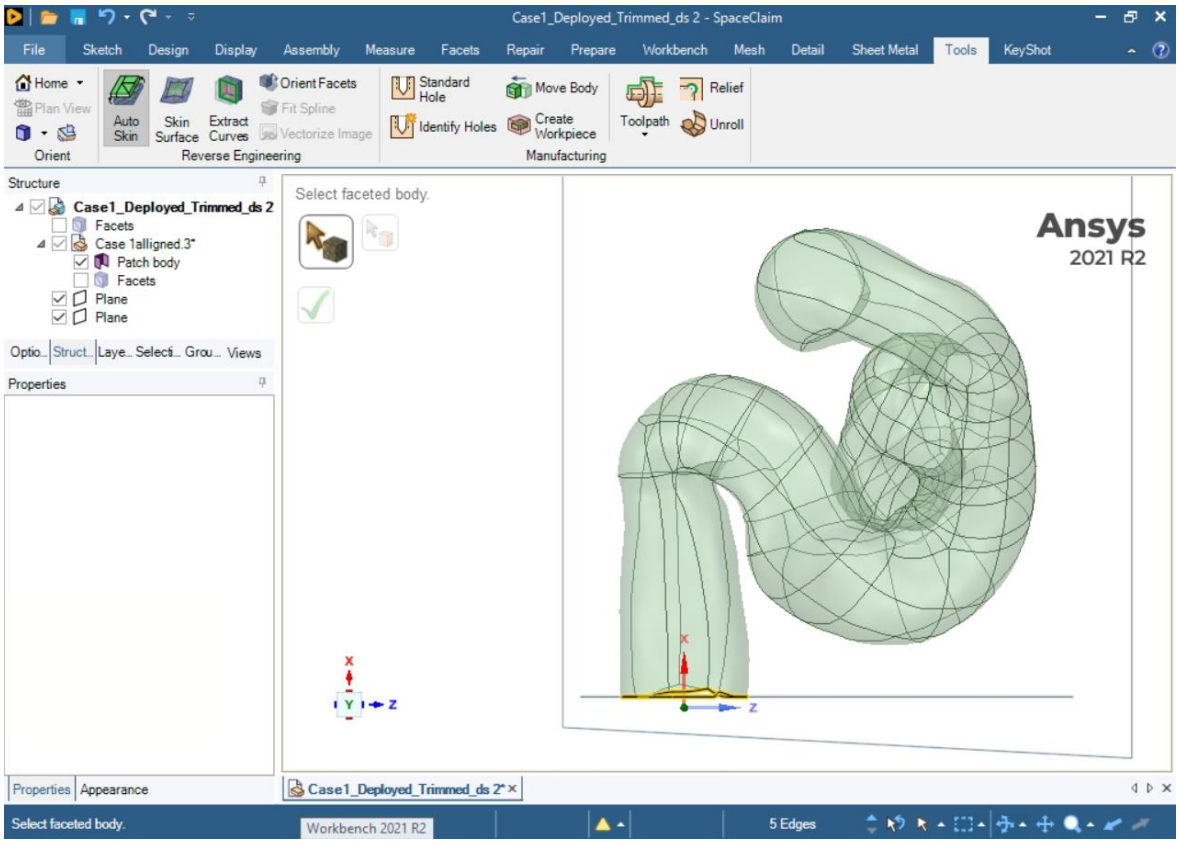

6. Shift planes from step 1 up the axis of the corresponding inlet/outlet-> split CAD body using planes as cutters

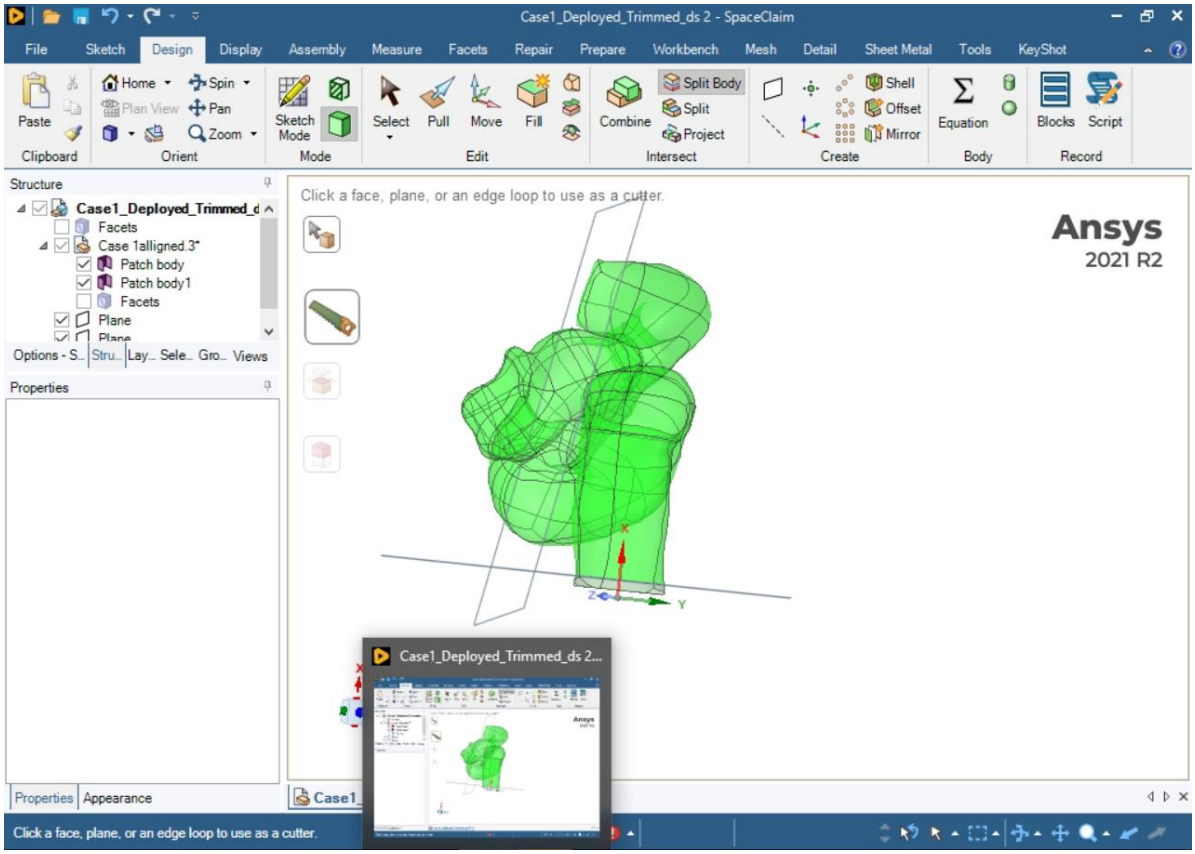

7. Delete ‘caps’ at either end of the geometry -> merge remaining parts

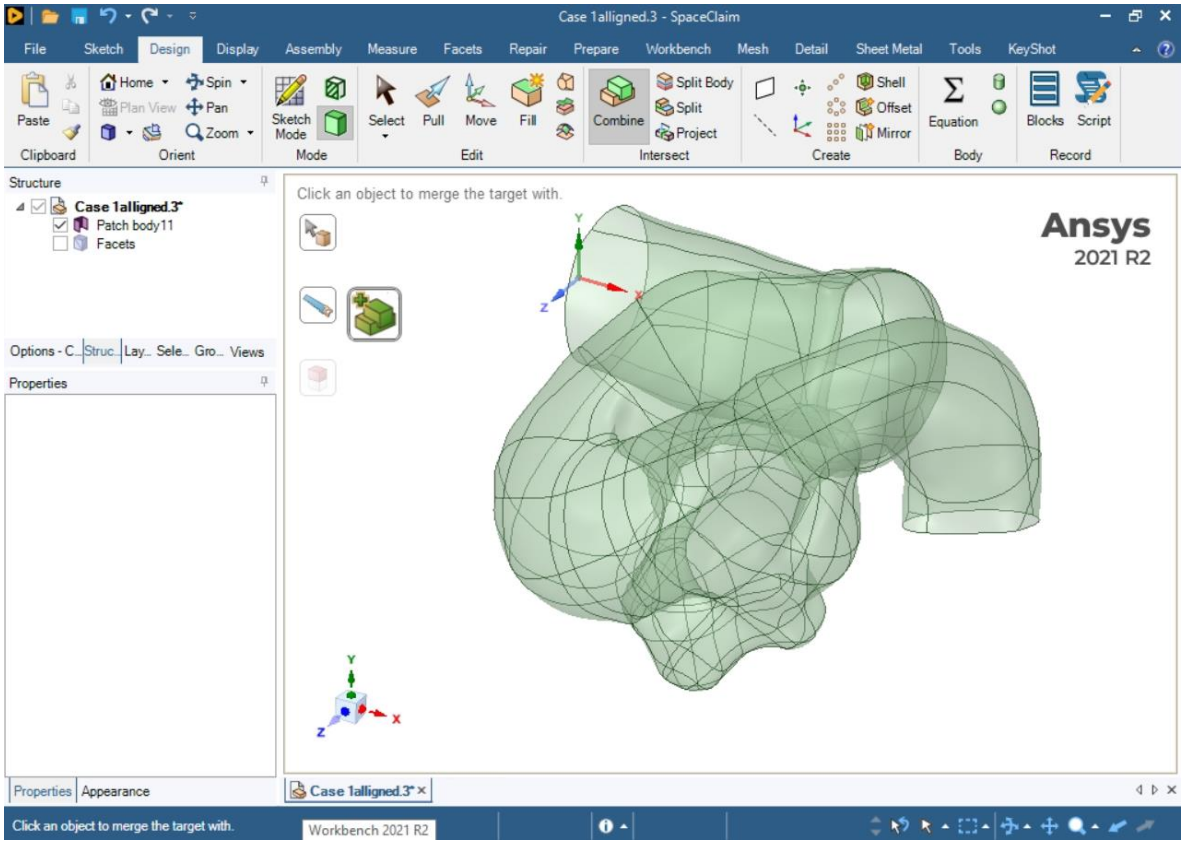

8. Repair missing faces

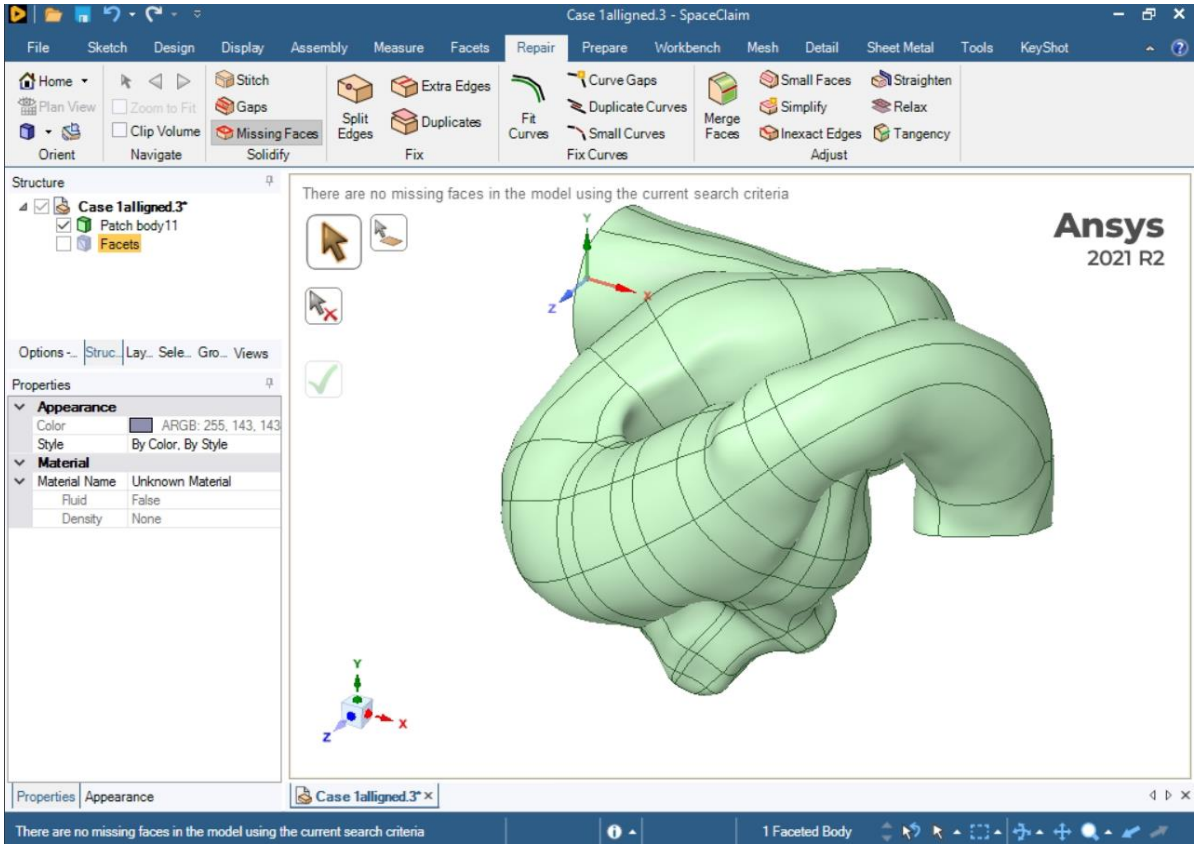

9. Pull inlet and outlet surfaces to desired length -> split CAD body using planes as cutters such that extensions are separate volumes. Remerge primary artery geometry as needed.

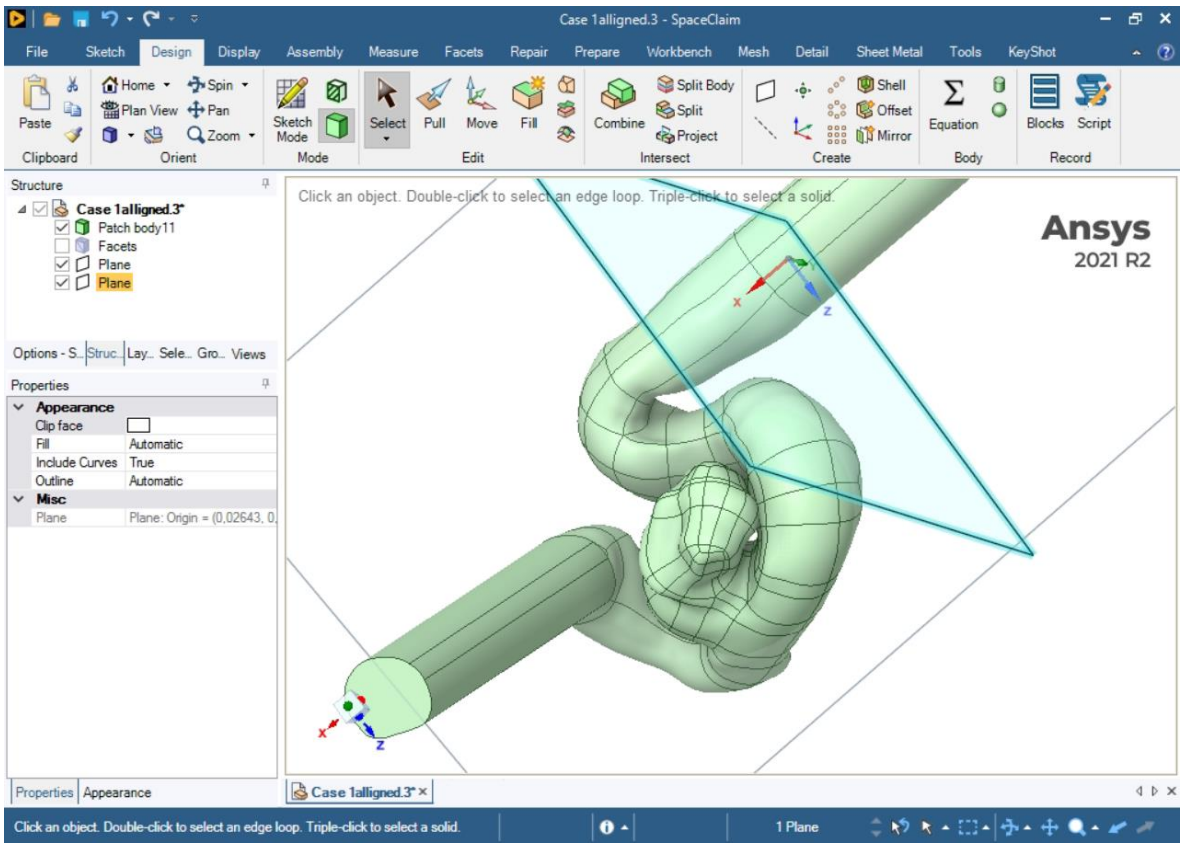

Flow Diverter Processing

1. Open STL in SpaceClaim -> autofix
2. Regularize – Max edge length 0.1 mm Curvature Dependent

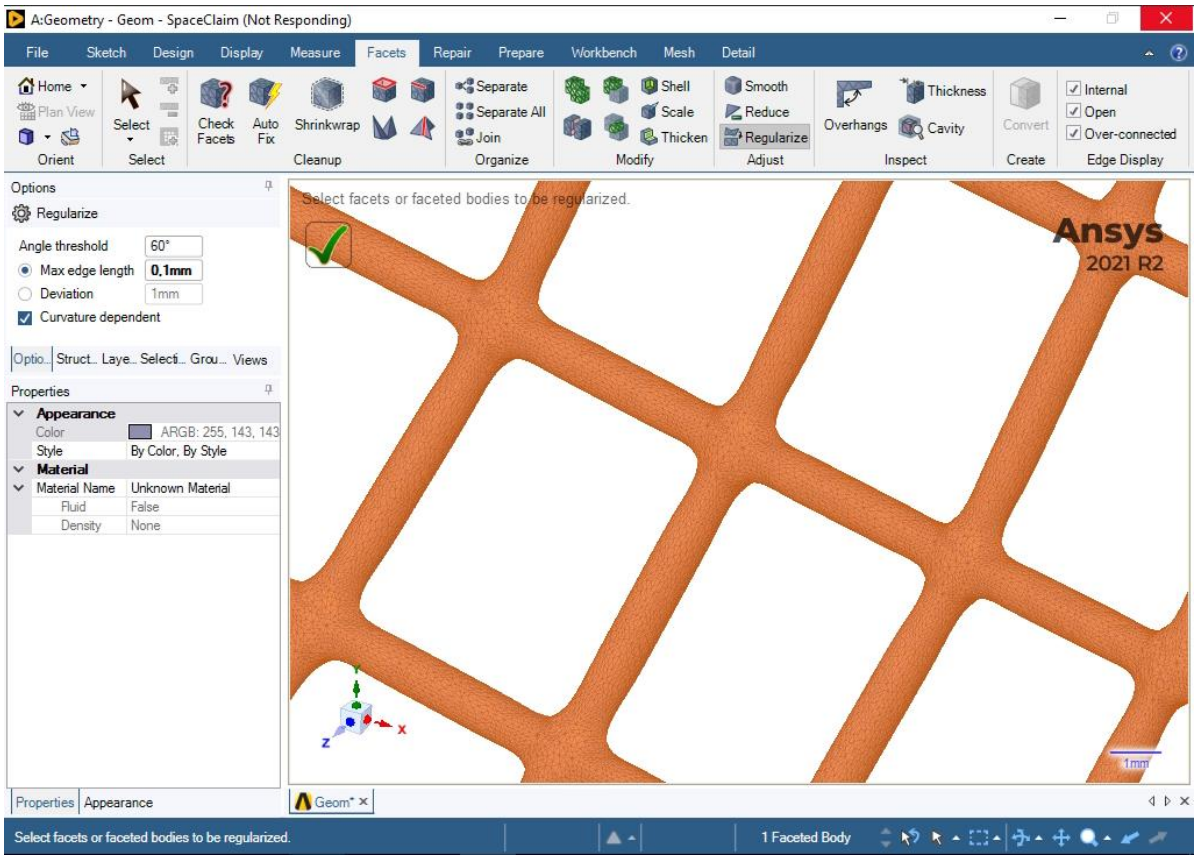

3. Fix Sharps (repeat until no sharps are left)-> Reduce Facets (95%)

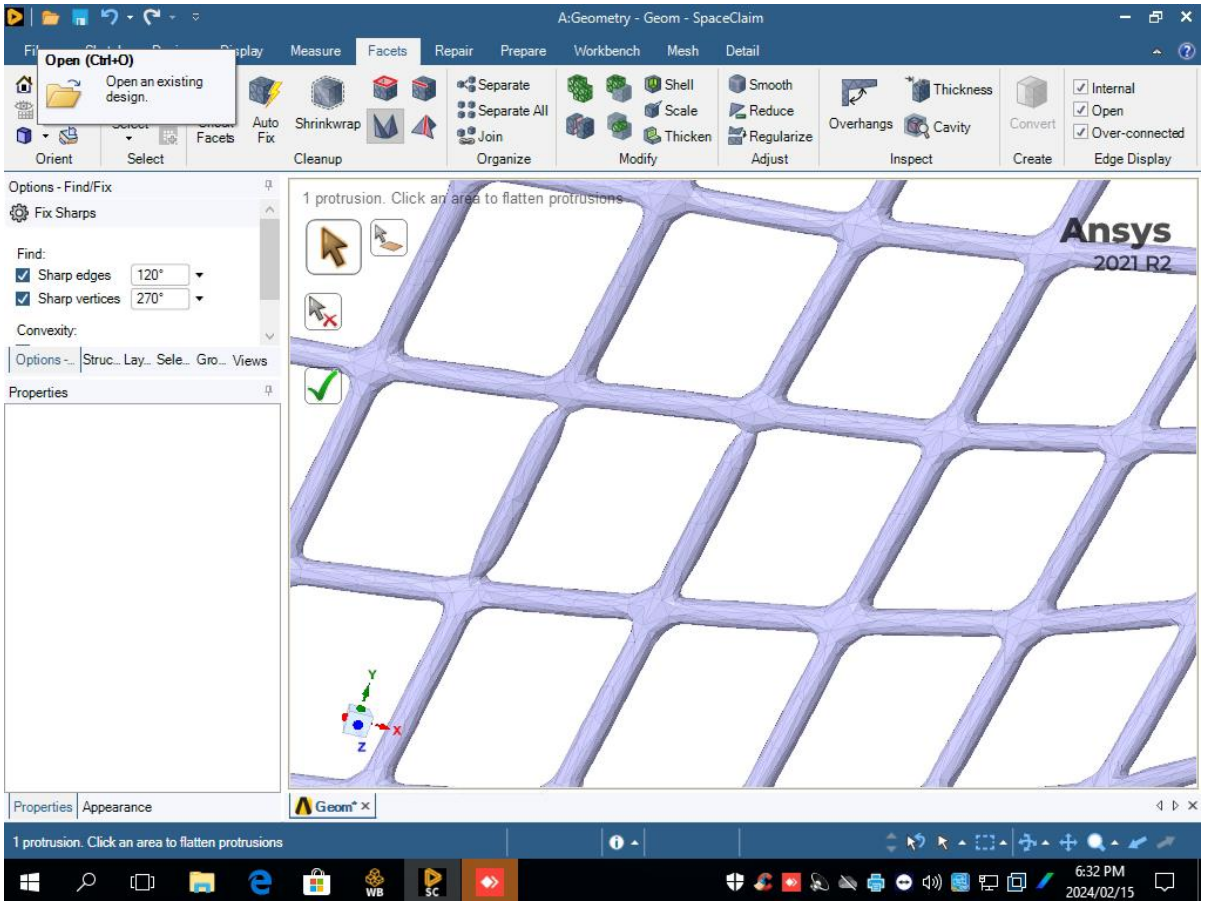

4. Autofix->Fix sharps (it may be necessary to select triangles by hand and delete manually, if so continue to perform this step until there are no sharp edges left)
5. Add corresponding artery geometry to the same SpaceClaim file as an assembly part

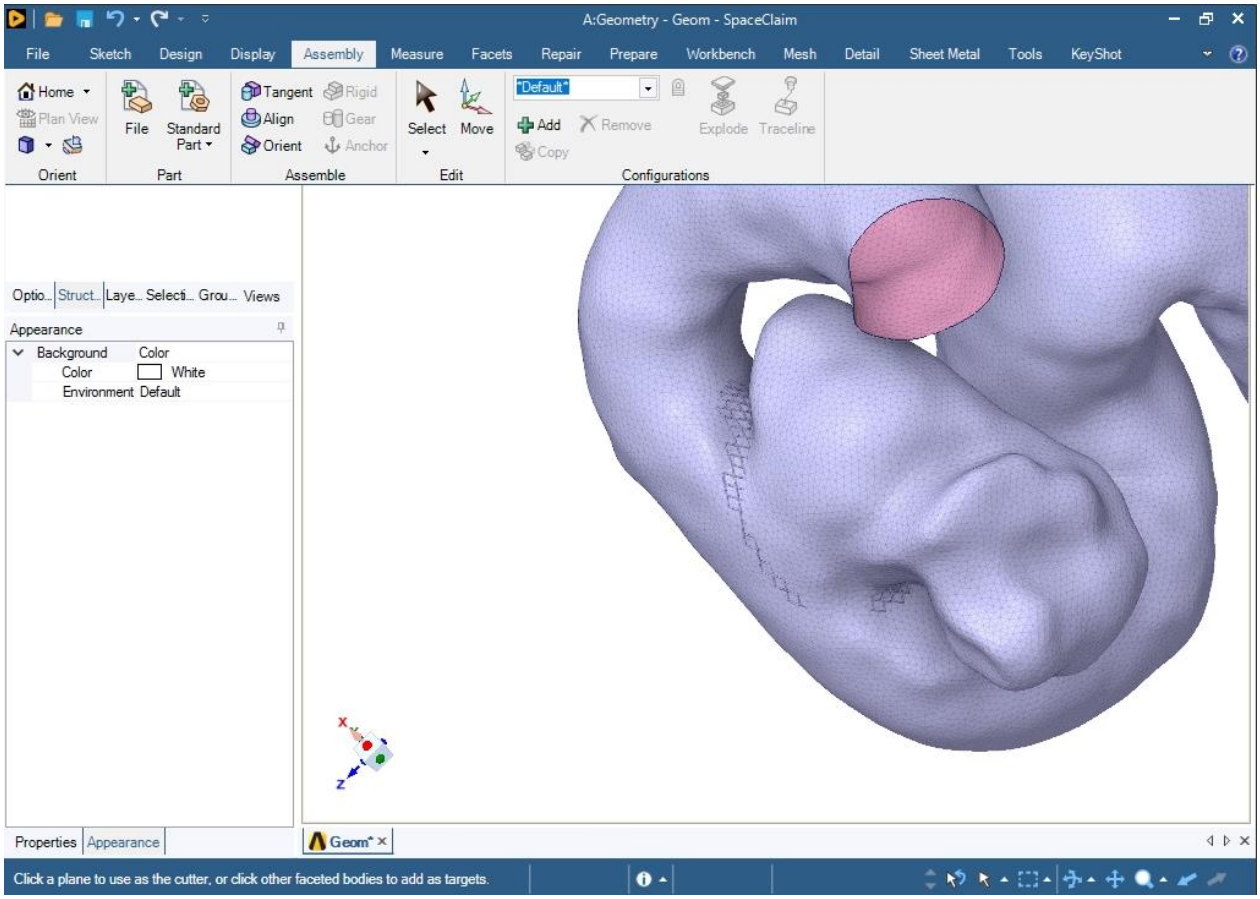

6. Cut flow diverter STL using artery STL as a 2D cutting plane

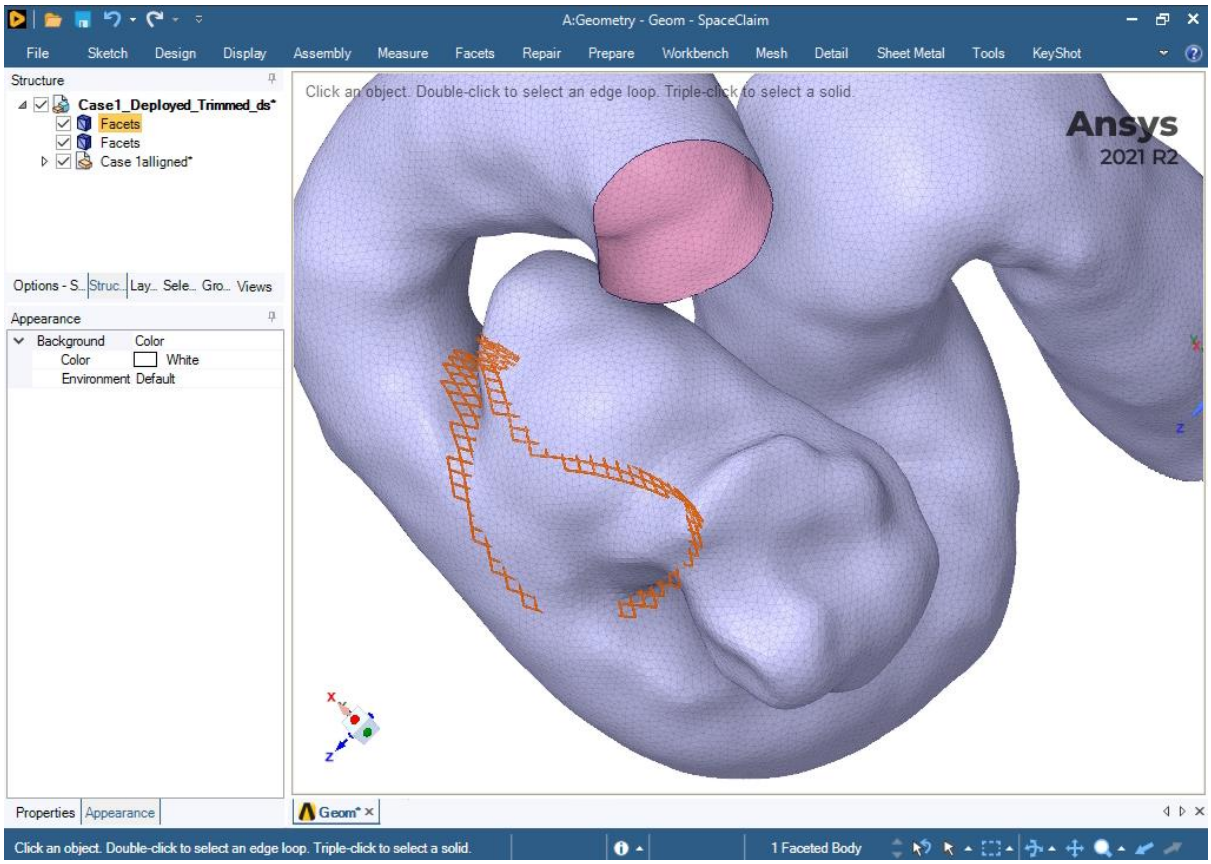

7. Separate all bodies of the flow diverter

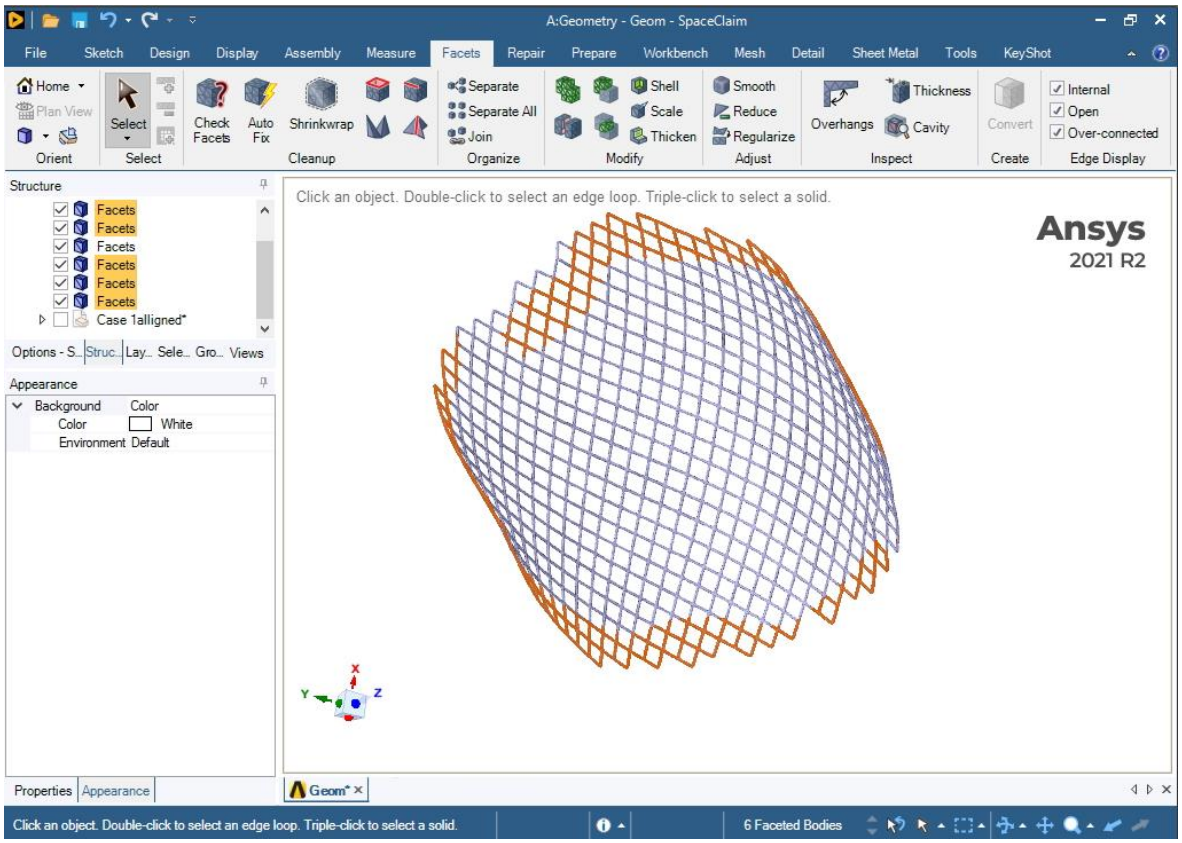

8. Delete all flow diverter bodies falling on the outside of the artery geometry

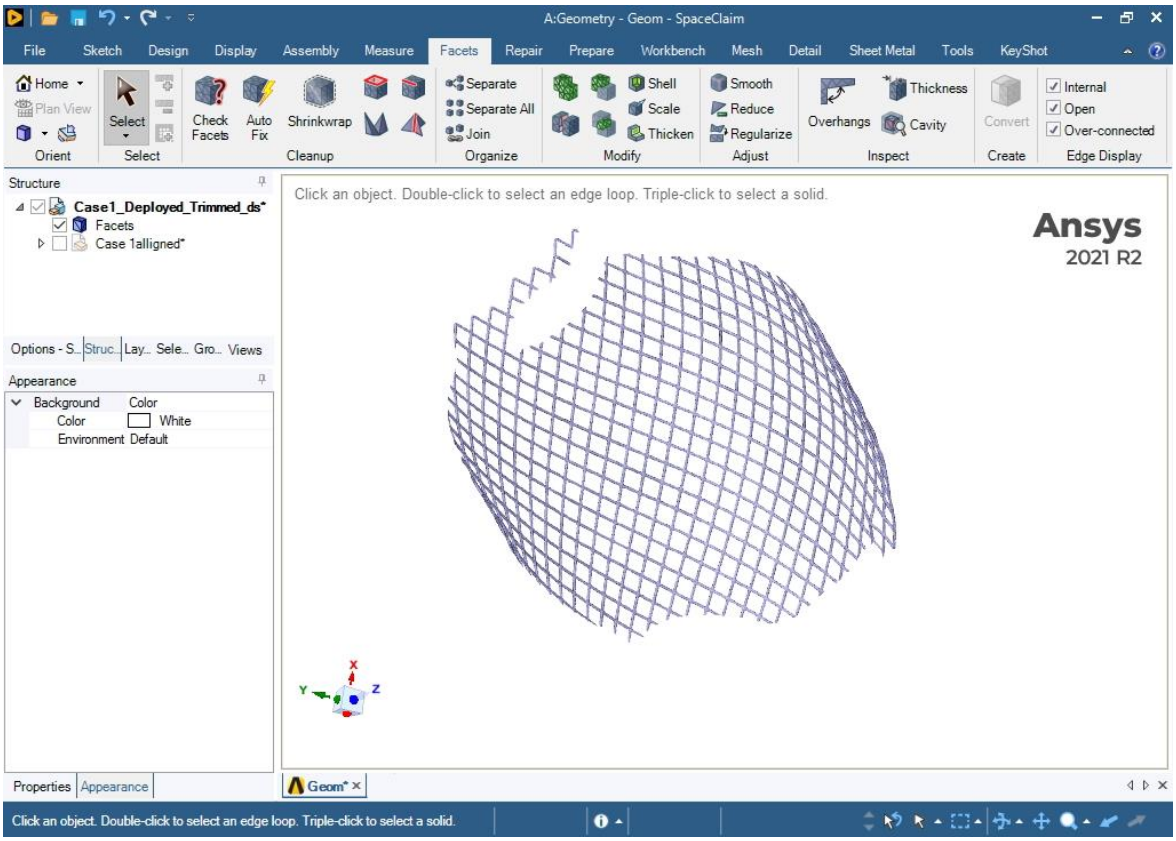

9. Delete between 1-2 lengths of wire mesh around the entire stent, ensuring there are no protruding wire segments of the stent geometry. This is done to ensure that the remaining geometry is sufficiently far away from the artery wall of the patient geometry. Note that it is not critical to delete leftover facets separated from the primary geometry.

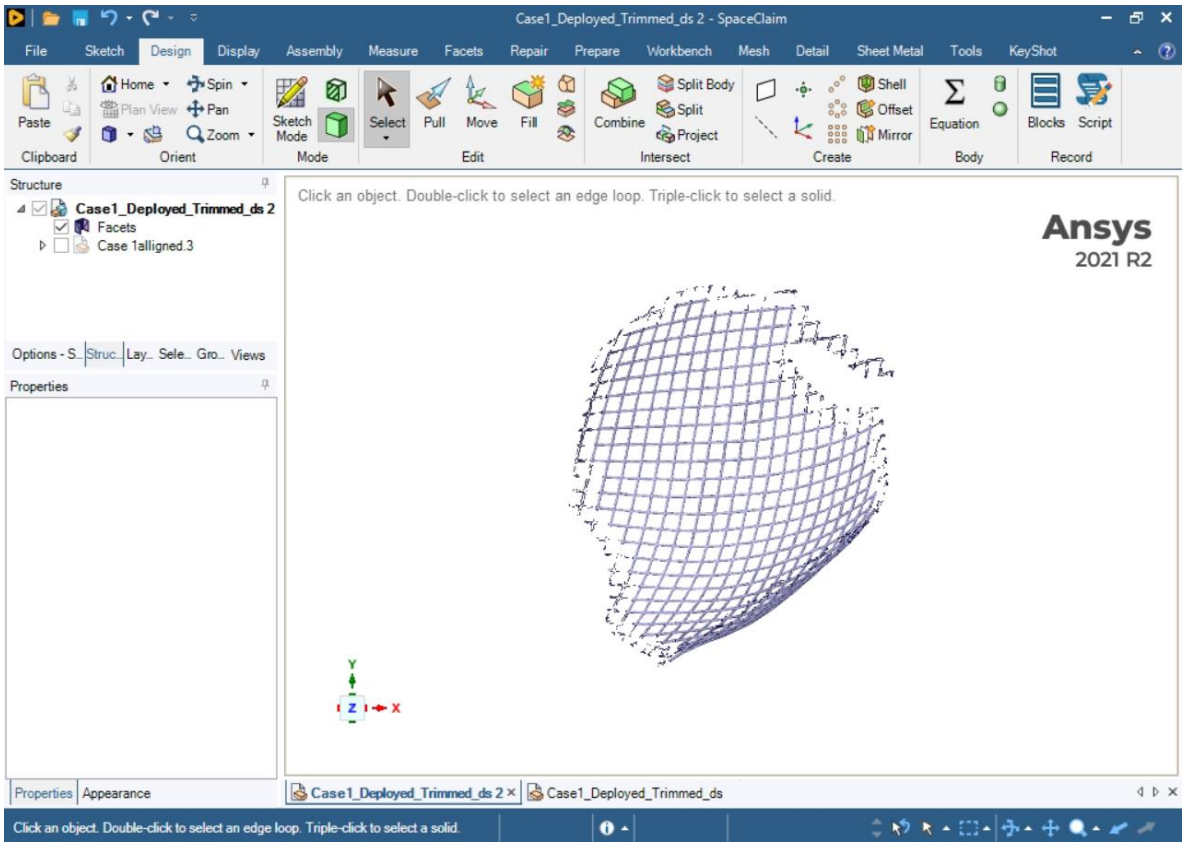

10. Separate facet bodies -> delete facets outside the region of interest

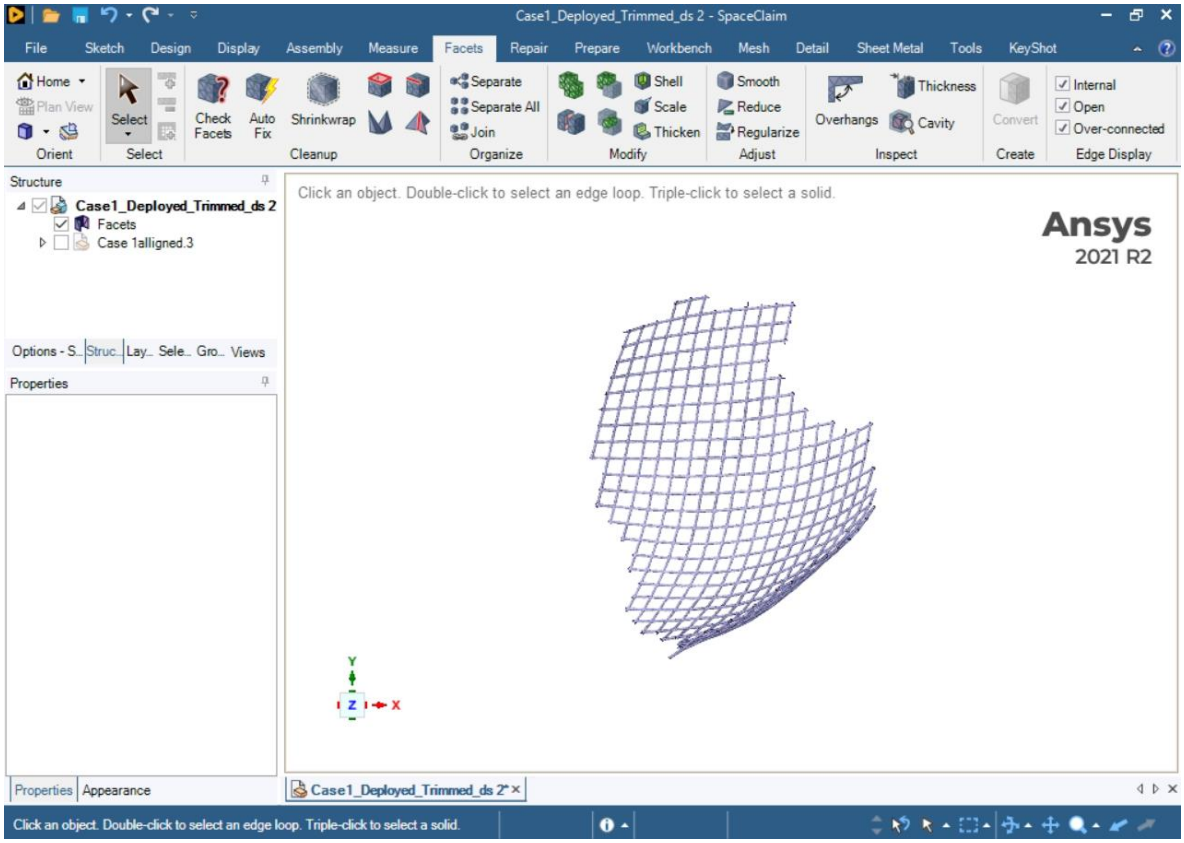

11. Auto fix -> fix sharps. This must be repeated several times until all protrusions have been flattened. Some protrusions may need to be eliminated manually by selecting faces and deleting them.

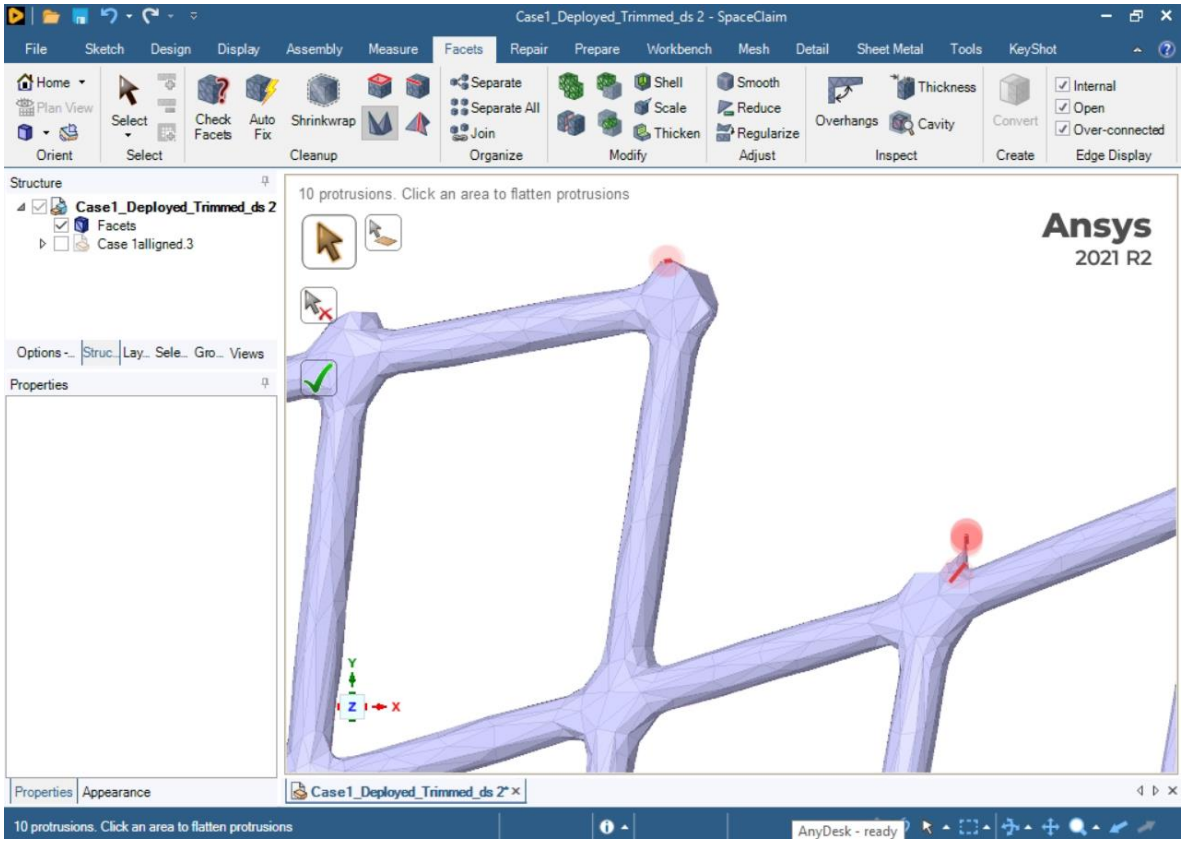

12. Regularize Facets -> Smooth Facets -> fix sharps. Max edge length for regularization must be very fine. Performing this step well is critical for the expedience of the next step

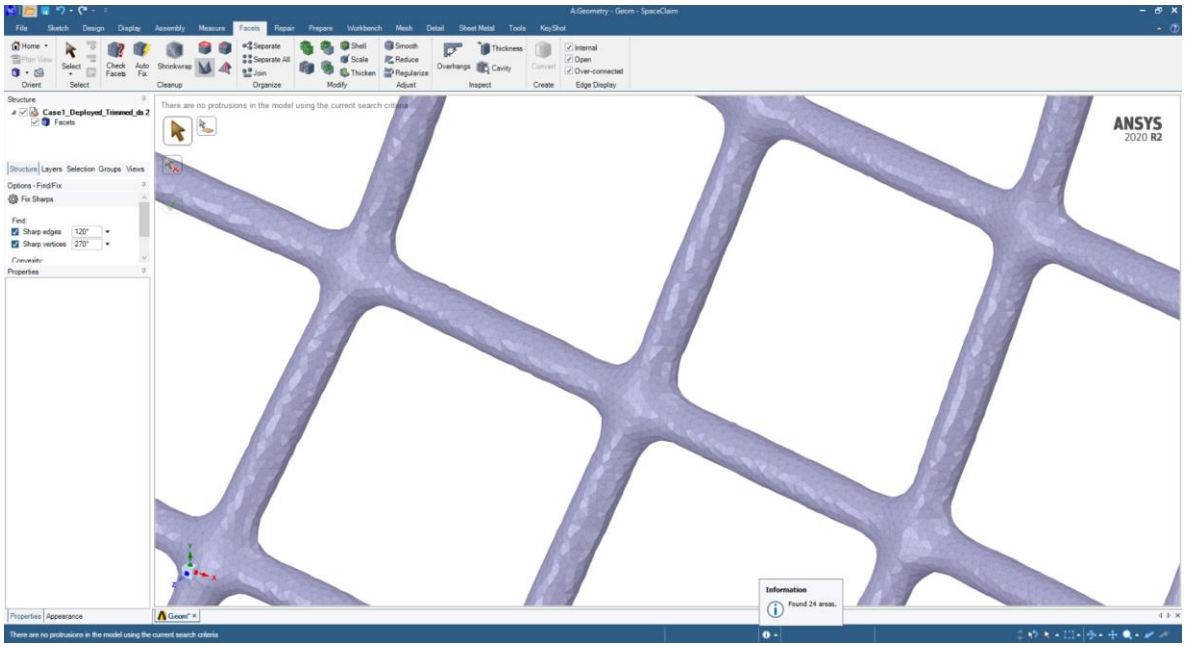

13. Apply Auto skin tool to remaining flow diverter STL (this forms a 2D CAD surface)

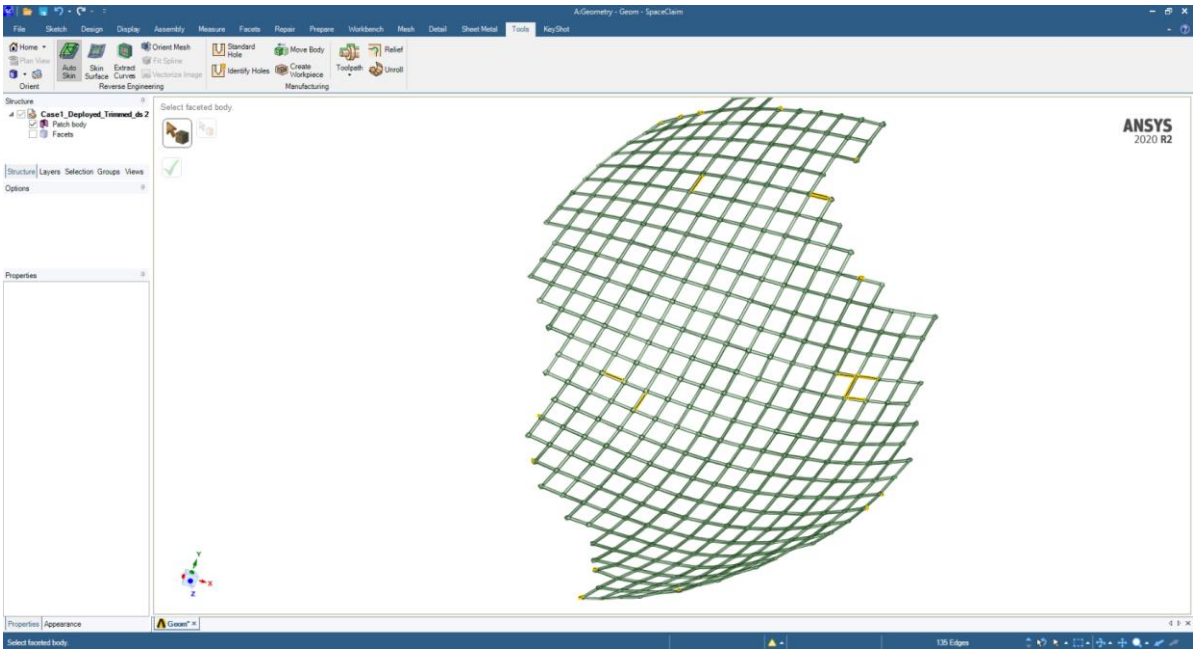

14. Repair missing faces. The automatic face repair tool may not detect very small missing faces unless the tolerance is tightened. The tool will also likely not repair every face due to some poor surfaces created during the auto skin. A face blending tool can be applied to create some of these missing faces. In cases where this is not feasible, problematic faces may be deleted, although this may leave a gap in the stent. When this step is complete, the 2D CAD surface will close to form a 3d Object.

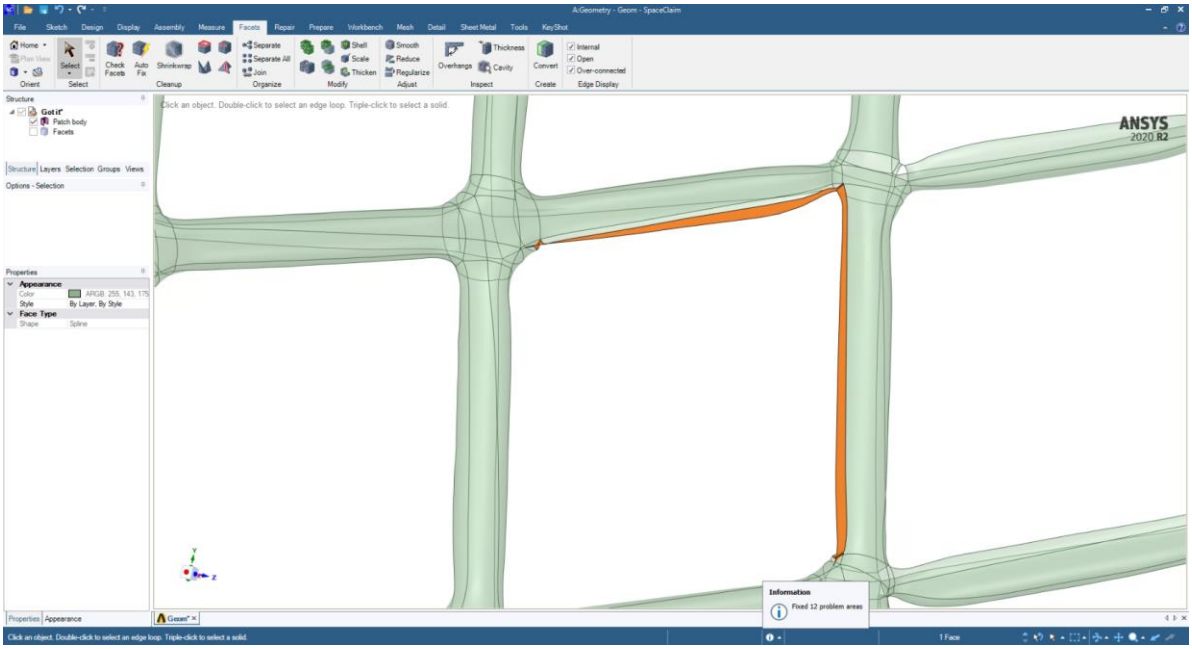
ANSYS
2020 R2
Information
Fixed 12 problem areas

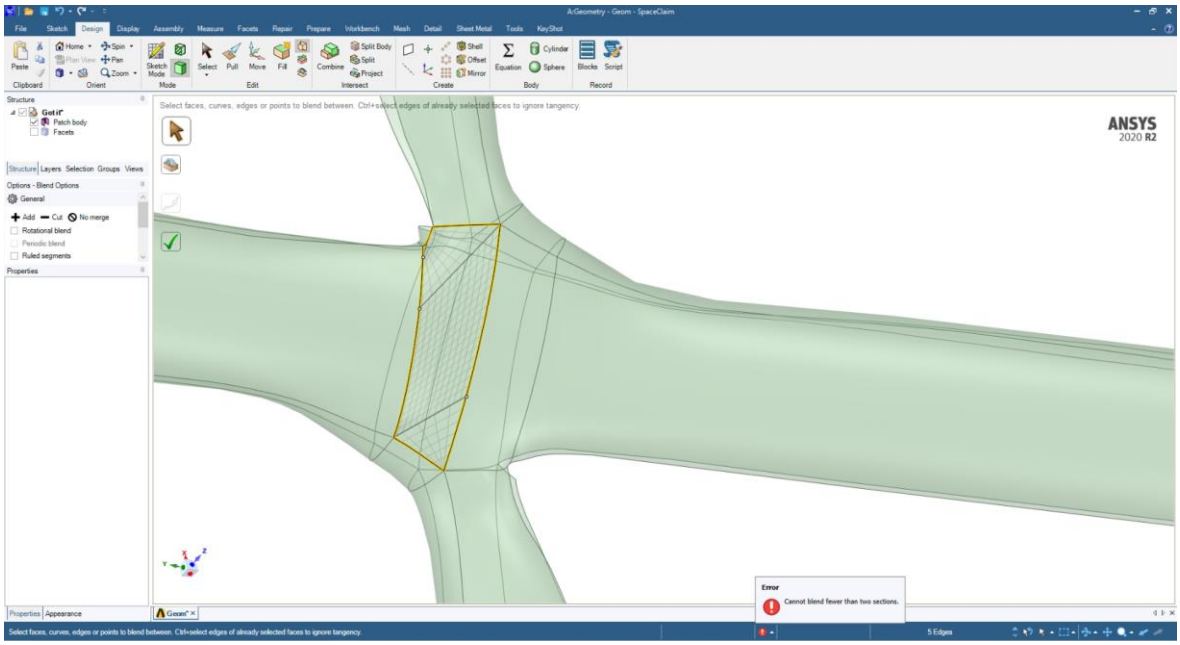
ANSYS
2020 R2
Error
Cannot blend fewer than two sections.

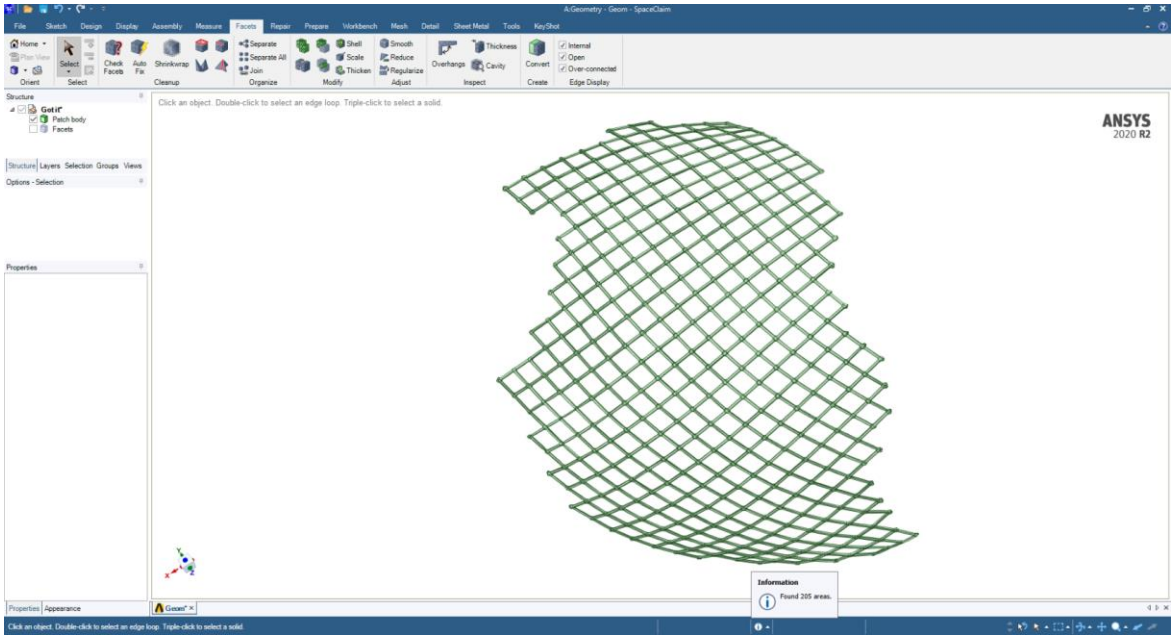

15. Detect Bad Faces and Sharp Edges. The CAD geometry still likely has bad features at this point that may be removed in one of three ways. In the case of small faces and edges, they may be either merged with another face, or a ‘repair sphere’ may be placed that merges with the flow diverter geometry and covers up the problematic geometry. In the case of very large sharp edges or faces, nearby faces must be deleted and replaced as in step 16.

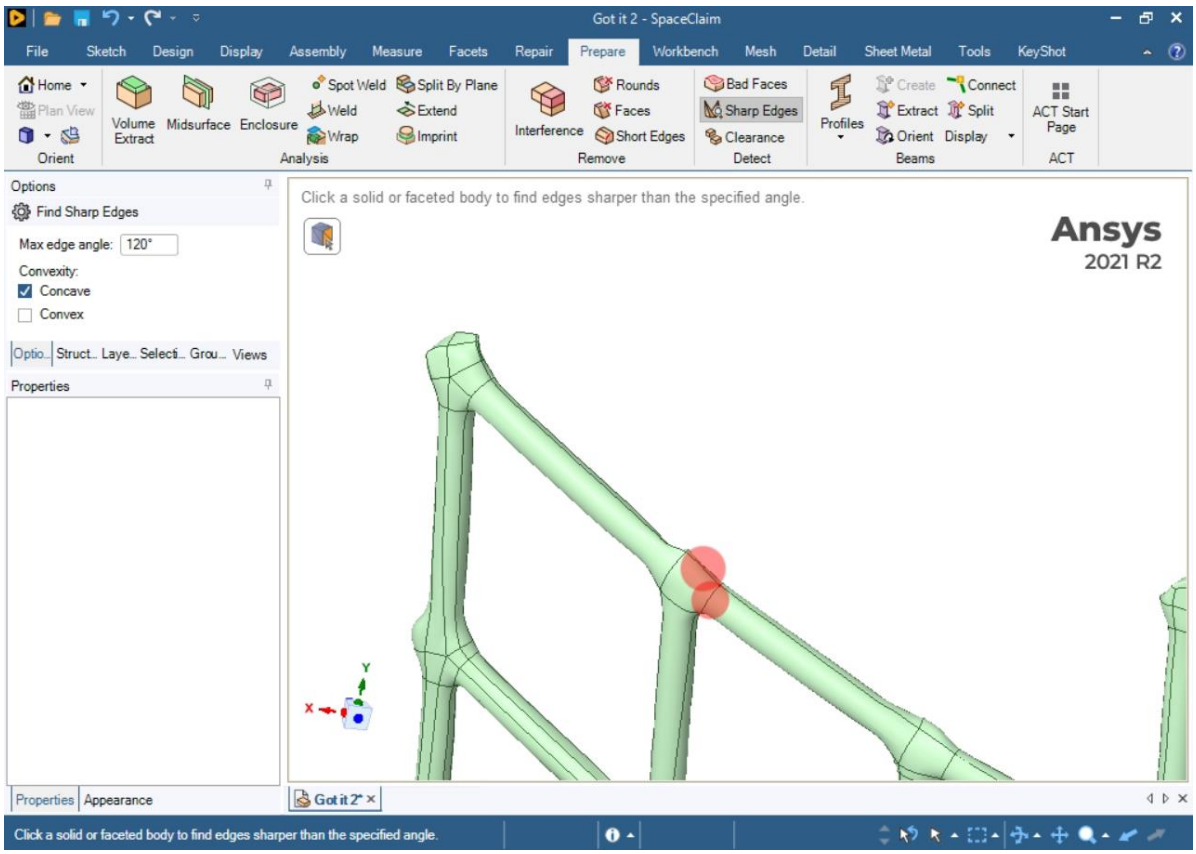

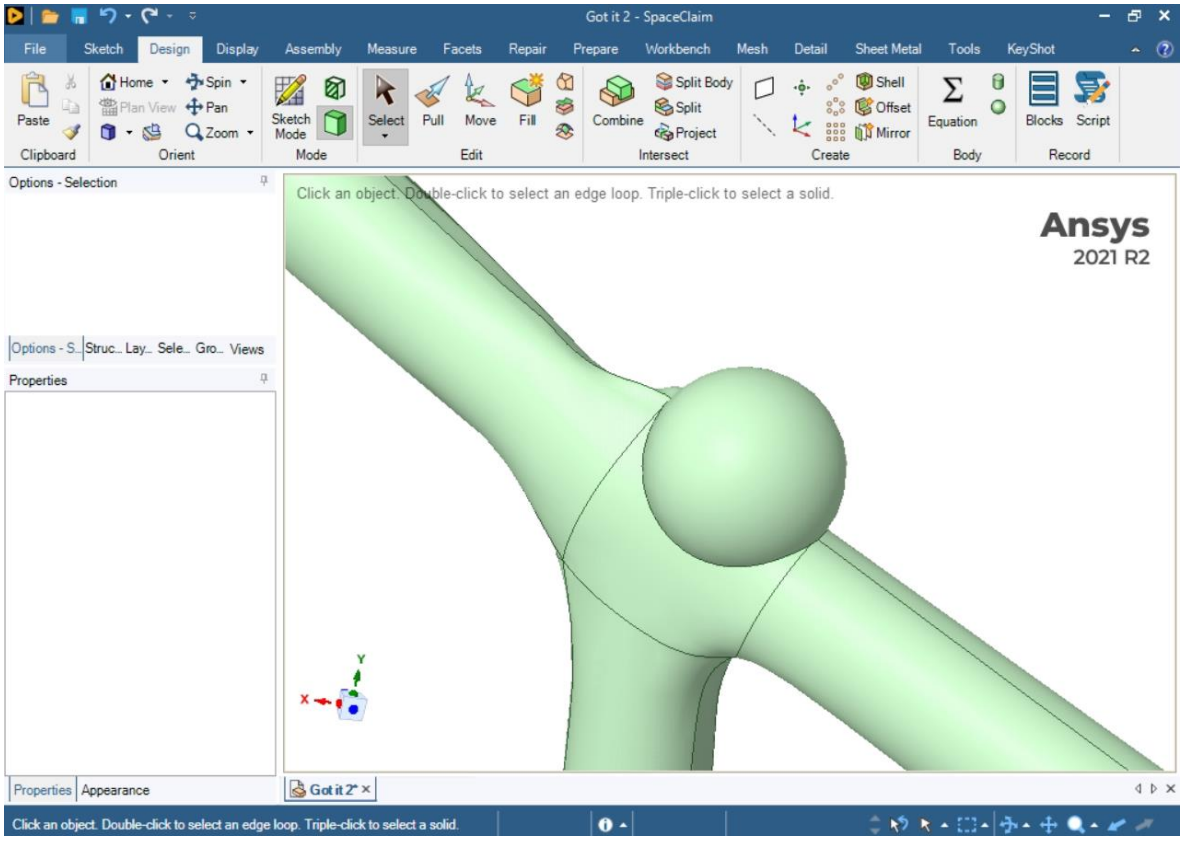

16. Fix split edges
17. Add processed CAD patient geometry as an assembly part

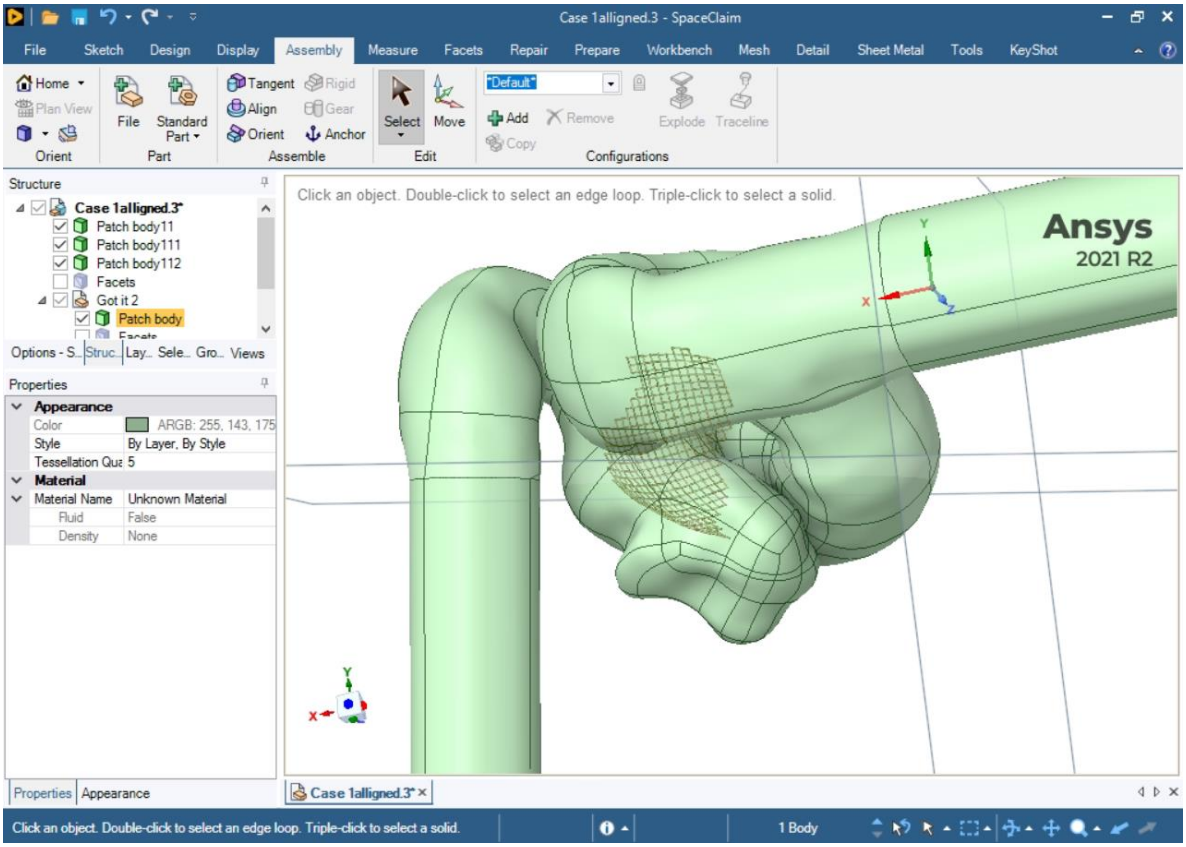

18. Subtract flow diverter CAD geometry from patient artery CAD geometry. If this step is unsuccessful, either trim faces from the flow diverter cad geometry and repeat step 16, or go back to step 11 and trim the geometry there.

APPENDIX B

UDF Code

```
#include "udf.h"
#include "prf.h"
#define bulge_th 9
DEFINE_PROFILE(AneurysmWall,th,i)
{
 face_t a;
 real h = 2.7272e0;
 real PEAK = 160;
 real TTP = 3.02;
 real ETP = 800.0e0;
 begin_f_loop(a,th)
  {
                F_PROFILE(a, th, i) = (h)*(PEAK)*exp(-h*((CURRENT_TIME / 60) - (TTP)))*(PEAK /
ETP)*exp(-exp(-h*((CURRENT_TIME / 60) - (TTP)))*(PEAK / ETP));
  }
 end_f_loop(a,th)
}
DEFINE_PROFILE(ThrombinInjection,th,i)
{
 face_t a;
 begin_f_loop(a,th)
  {
                if (CURRENT_TIME >=3)
                F_PROFILE(a,th,i) = 2.174;
                else
                                F_PROFILE(a,th,i) = 0;
  }
 end_f_loop(a,th)
}
DEFINE_SOURCE(Source_of_UDS2, c, t, dS, eqn)
{
                real kcat = 59.0;
                real Km = 3160.0;
                real Fnmax = 10000.0;
                real source2;
                real Fbng = C_UDSI(c, t, 1);
                real Thr  = C_UDSI(c, t, 0);
                real Fbrn = C_UDSI(c, t, 2);
                real gen =1050.0*kcat * Thr * Fbng / (Km + Fbng);
                if (Fbrn < Fnmax)
                                source2 = gen;
                else
                                source2 = 0.0;
                return source2;
}
DEFINE_SOURCE(Sink_of_UDS1, c, t, dS, eqn)
{
                real source1;
                real kcat = 59.0;
                real Km = 3160.0;
```

```
		real Fbng_min = 0.1;
		real Thr =  C_UDSI(c, t, 0);
		real Fbng = C_UDSI(c, t, 1);
		real Fbrn = C_UDSI(c, t, 2);
		real gen = 1050.0*kcat * Thr * Fbng / (Km + Fbng);
		if (Fbng > Fbng_min)
			source1 = gen*-1;
		else
			source1 = 0.0;
		return source1;
}
DEFINE_PROFILE(vis_resx, t, nv)
{
		real b;
		cell_t c;
		begin_c_loop(c, t)
		{
				if (C_UDSI(c, t, 3) != 1e0)
				b = 1.0e-12;
			else
				b = 1.0e+12;
			C_PROFILE(c, t, nv) = b;
		}
		end_c_loop(c, t)
}
 DEFINE_PROFILE(porosity_function_2, t, nv)
{
		real f;
		cell_t c;
		begin_c_loop(c, t)
		{
			real dudy;
			real dwdy;
			real dudz;
			real dvdz;
			real dvdx;
			real dwdx;
			real x_grad;
			real y_grad;
			real z_grad;
			real shear_rate;
			real fibrin;
			dudy = C_DUDY(c,t);
			dwdy = C_DWDY(c,t);
			dudz = C_DUDZ(c,t);
			dvdz = C_DVDZ(c,t);
			dvdx = C_DVDX(c,t);
			dwdx = C_DWDX(c,t);
			x_grad = pow((dvdx*dvdx)+(dwdx*dwdx),0.5);
			y_grad = pow((dudy*dudy)+(dwdy*dwdy),0.5);
			z_grad = pow((dudz*dudz)+(dvdz*dvdz),0.5);
```

```
                        shear_rate =
pow((x_grad*x_grad)+(y_grad*y_grad)+(z_grad*z_grad),0.5);
                        fibrin = C_UDSI(c, t, 2);
                        if (C_UDSI_M1(c, t, 3) == 1.0)
                        {
                                f = 0.75e0;
                                C_UDSI(c, t, 3) = 1.00e0;
                        }
                        else
                        {
                                if (C_UDSI(c, t, 2) >= 600 && shear_rate < 100)
                                {
                                        f = 0.75e0;
                                        C_UDSI(c, t, 3) = 1.0e0;
                                }
                                else if (C_UDSI(c, t, 2) > 0 && C_UDSI(c, t, 2) < 600 &&
shear_rate < 100)
                                {
                                        f = 1 - ((fibrin / 600) / 4);
                                        C_UDSI(c, t, 3) = (fibrin / 600);
                                }
                                else
                                {
                                        f = 1e0;
                                        C_UDSI(c, t, 3) = 0e0;
                                }
                        }
                        C_PROFILE(c, t, nv) = f;
                }
                end_c_loop(c, t)
}
 DEFINE_PROFILE(inlet_z_velocity_original,th,i)
{
  double x[ND_ND];
  double xx, y;
 face_t f;
 double a1,f1,ph1,a2,f2,ph2,a3,f3,ph3,offset;
  begin_f_loop(f,th)
   {
                double t = (CURRENT_TIME);
    F_CENTROID(x,f,th);
                xx = x[0];
    y = x[1];
a1 = 14.598;
a2 = -7.46;
a3 = 2.509;
ph1 = 15.031;
ph2 = 0.805;
ph3 = -0.782;
f1 = 0.9;
f2 = 1.8;
```

```
f3 = 2.7;
offset = 20.804;
                                F_PROFILE(f,th,i) = ((a1*sin(2*3.141592*f1*t+ph1)) +
(a2*sin(2*3.141592*f2*t+ph2))+(a3*sin(2*3.141592*f3*t+ph3))+offset)/100;
   }
  end_f_loop(f,th)
 }
DEFINE_PROFILE(pressure_profile_original,th,i)
{
  double x[ND_ND];
  double xx, y;
 face_t f;
int n;
double a1,f1,ph1,a2,f2,ph2,a3,f3,ph3,offset;
  begin_f_loop(f,th)
   {
                double t = (CURRENT_TIME);
    F_CENTROID(x,f,th);
                xx = x[0];
                y = x[1];
a1 = -26.298;
a2 = -13.633;
a3 = 5.891;
ph1 = 24.082;
ph2 = 12.730;
ph3 = -1.789;
f1 = 0.9;
f2 = 1.8;
f3 = 2.7;
offset = 74.982;
                                                F_PROFILE(f,th,i) = ((a1*sin(2*3.141592*f1*t+ph1)) +
(a2*sin(2*3.141592*f2*t+ph2))+(a3*sin(2*3.141592*f3*t+ph3))+offset)*(101325/760);
   }
end_f_loop(f,th)
 }
```